UNIVERSITÄT BAYREUTH

Method Development and Data-Driven Analysis for Thermal Management and Heat Monitoring

Dissertation

to be awarded the degree of
Doctor of Natural Sciences (Dr. rer. nat.)

at the Faculty of Biology, Chemistry & Earth Sciences
University of Bayreuth

submitted by
Thomas Quang Vinh Tran
born in Dieburg

Bayreuth, 2023

The work described in this thesis was carried out between October 2019 and December 2022 at the Chair of Physical Chemistry 1 at the University of Bayreuth under the supervision of Prof. Dr. Markus Retsch.

This is a full reprint of the dissertation submitted to obtain the academic degree Doctor of Natural Sciences (Dr. rer. nat.) and approved by the Faculty of Biology, Chemistry & Earth Sciences at the University of Bayreuth.

Thesis submitted:	10.01.2023
Acceptance by the Exam Commission:	25.01.2023
Date of Scientific Colloquium:	15.09.2023

Acting Dean:

Prof. Dr. Benedikt Westermann

Doctoral Commitee:

Prof. Dr. Markus Retsch (1st Reviewer)
Prof. Dr. Jürgen Senker (2nd Reviewer)
Prof. Dr. Peter Strohriegl (Chairman)
Prof. Dr. Holger Ruckdäschel

List of Publications

I wrote my thesis as a cumulative dissertation and present the results of the following publications in peer-reviewed journals:

[1] Qimeng Song,* Thomas Tran,* Kai Herrmann, Tobias Lauster, Maximilian Breitenbach, and Markus Retsch, A Tailored Indoor Setup for Reproducible Passive Daytime Cooling Characterization, *Cell Reports Physical Science*, **2022**, *3*(8), 100986.
**These authors contributed equally to the work.*

[2] Qimeng Song, Thomas Tran, Kai Hermann, Holger Schmalz, and Markus Retsch, Upcycling Chips-Bags for Passive Daytime Cooling, *Advanced Materials Technologies*, **2023**, 2300444.

[3] Thomas Tran, Charly Kodisch, Marius Schöttle, Nelson W. Pech-May, and Markus Retsch, Characterizing the Thermal Diffusivity of Single, Micrometer-Sized Fibers via High-Resolution Lock-In Thermography, *The Journal of Physical Chemistry C*, **2022**, *126*(32), 14003–14010.

[4] Simon Bard,* Thomas Tran,* Florian Schönl, Sabine Rosenfeldt, Martin Demleitner, Holger Ruckdäschel, Markus Retsch, and Volker Altstädt, Relationship Between the Tensile Modulus and the Thermal Conductivity Perpendicular and in the Fiber Direction of PAN-Based Carbon Fibers, *Carbon Letters*, **2023**.
**These authors contributed equally to the work.*

[5] Marius Schöttle, Thomas Tran, Tanja Feller, and Markus Retsch, Time-Temperature Integrating Optical Sensors Based on Gradient Colloidal Crystals, *Advanced Materials*, **2021**, *33*(40), 2101948.

[6] Marius Schöttle,* Thomas Tran,* Harald Oberhofer, and Markus Retsch, Machine Learning Enabled Image Analysis of Time-Temperature Integrating Colloidal Arrays, *Advanced Science*, **2023**, *10*(8), 2205512.
**These authors contributed equally to the work.*

The results from the following publications in peer-reviewed journals are not included in this thesis:

[7] Qiang Gao, Thomas Tran, Xiaojian Liao, Sabine Rosenfeldt, Chao Gao, Haoqing Hou, Markus Retsch, Seema Agarwal, and Andreas Greiner, Ultralight Heat-Insulating, Electrically Conductive Carbon Fibrous Sponges for Wearable Mechanosensing Devices with Advanced Warming Function, *ACS Applied Materials & Interfaces*, **2022**, *14*(17), 19918–19927.

[8] Xiaojian Liao, Jakob Denk, Thomas Tran, Nobuyoshi Miyajima, Lothar Benker, Sabine Rosenfeldt, Stefan Schafföner, Markus Retsch, Andreas Greiner, Guenter Motz, Seema Agarwal, Extremely Low Thermal Conductivity and High Electrical Conductivity of Sustainable Carbon-Ceramic Electrospun Nonwoven Materials, *Science Advances*, **2023**, *9*(13), eade6066.

Abstract

Scientific progress relies on the reproducible preparation and accurate characterization of novel materials. In today's laboratories, research would not be possible without harnessing the power of modern computers. Still, chemists spend a lot of time manually carrying out repetitious tasks and analyzing data. As a Ph.D. candidate, I utilized modern frameworks to automate experimental setups and streamline the subsequent data analysis. By doing so, I made previously impossible projects viable and expanded the methods present in our group.

All of the projects I worked on revolved around heat transport and its resulting effects. I established two new characterization methods investigating thermal diffusivity and passive cooling behavior. The thorough investigation of thermal properties enables the design of materials for thermal management. In addition, I refined a time-temperature integrator, allowing its evaluation based on single photographs taken with a smartphone camera. Thus, monitoring temperature events is possible either to control the thermal management systems or to detect events when management strategies are infeasible. In the following paragraphs, I will shortly present the results of each project.

Passive daytime cooling is a promising candidate to reduce global CO_2 emissions. It is based on devices with tailored optical properties to direct heat flow. A method is required to compare the characterization results of passive cooling materials measured at different times and locations. My colleagues and I developed an indoor measurement instrument able to characterize the cooling performance of investigated samples with outstanding reproducibility. It is a cornerstone for future research because it enables the characterization of new materials independent of weather and climate. We used our instrument to demonstrate the potential application of post-consumer waste as a passive cooling material. Polymer-coated aluminum laminate spontaneously cools below ambient temperatures. Our simulations estimate that large-scale employment can reduce the energy consumption of a four-story building by tens of GJ per year.

Besides tailoring the radiative properties, another possibility to manipulate heat transport is to control the thermal conduction of materials. Lock-in thermography is an established method to characterize the thermal diffusivity of 2D and 3D samples. However, little work has been done on the characterization of 1D samples. We created a measurement setup for fibers with diameters of a few micrometers and exhaustively investigated the impact of different measurement parameters. We proved that the investigation of samples smaller than the pixel resolution of the deployed camera system is possible, even

if the investigated fiber is not aligned with the detector orientation. Furthermore, we investigated the effect of different heating powers and how they introduce measurement errors. Our results facilitate the robust measurement of micrometer-sized fibers and filaments.

Fiber-reinforced composites are an example of a system benefitting from the characterization of single fibers. In cooperation with the engineering department, we investigated different fiber types embedded in a polymer matrix. The composite material exhibits anisotropic properties by aligning the fibers in one direction. Our research shows how the thermal properties of the composite material correlate with these of the fibers and their mechanical strength. We attribute the correlation of thermal and mechanical properties to the microstructure of the fibers.

Structures on yet smaller length scales are the basis for my final two publications. They introduce monitoring systems for temperature events. In the first project, we demonstrated the fabrication of a colloidal crystal assembled from a continuous gradient of different nanoparticles. The resulting structure is a time-temperature integrator, i.e., it records the thermal history by irreversibly changing its optical properties. In a follow-up publication, we built upon this concept and created an array of colloidal crystals with different compositions. By automating the fabrication process, we could measure large amounts of data that we analyzed with an artificial neural network. The evaluation of the sensor is based solely on photographs and is thus accessible to non-specialists. Our sensor enables a fast and tamper-proof way of analyzing the thermal history of an object. Possible applications include monitoring perishable goods such as food and medicine and technical applications for batteries.

Zusammenfassung

Wissenschaftlicher Fortschritt basiert auf der reproduzierbaren Herstellung und genauen Charakterisierung neuer Materialien. Heutzutage wäre Forschung ohne die Leistung moderner Computer undenkbar. Nichtsdestotrotz verbringen Chemiker viel Zeit damit, manuell monotone Aufgaben zu bearbeiten und Daten zu analysieren. Als Doktorand habe ich moderne Frameworks eingesetzt, um Messaufbauten zu automatisieren und die anschließende Datenanalyse zu vereinfachen. Dadurch habe ich vorher unmögliche Projekte machbar gemacht und die in unserer Gruppe vorhandenen Methoden erweitert.

Die von mir bearbeiteten Projekte drehten sich um Wärmetransport und den damit verbundenen Auswirkungen. Ich habe zwei neue Messapparate entwickelt, um die thermische Diffusivität und das passive Kühlverhalten zu charakterisieren. Eine umfassende Charakterisierung der thermischen Eigenschaften ermöglicht es, Materialien für das Wärmemanagement zu entwickeln. Außerdem habe ich Zeit-Temperatur-Integratoren weiterentwickelt und es ermöglicht, ihre Auswertung anhand einzelner Fotos eines Smartphones durchzuführen. Dies ermöglicht die Überwachung von Temperaturereignissen, um das eingesetzte Wärmemanagement zu kontrollieren oder Systeme zu überprüfen, bei denen Wärmemanagement nicht praktikabel sind. In den folgenden Absätzen werde ich kurz die Ergebnisse meiner Projekte vorstellen.

Passive Tageskühlung ist ein vielversprechender Kandidat, um die globalen CO_2-Emissionen zu verringern. Sie basiert auf Systemen mit maßgeschneiderten optischen Eigenschaften, die den Wärmefluss gezielt lenken. Um das optimale Material zu finden, wird eine Methode benötigt, um Messergebnisse von verschiedenen Orten und Zeiten vergleichbar zu machen. Daher haben meine Kollegen und ich ein Laborinstrument entwickelt, das die Kühlleistung mit herausragender Reproduzierbarkeit messen kann. Es legt den Grundstein für zukünftige Forschung, weil es die Charakterisierung neuer Materialien unabhängig von Wetter und Klima ermöglicht. Wir haben unser Instrument benutzt, um die potenzielle Anwendung von Post-Consumer-Abfällen als passive Kühlelemente zu demonstrieren. Polymerbeschichtetes Aluminiumlaminat kühlt spontan unter Raumtemperatur. Unsere Simulation zeigen, dass eine großflächige Anwendung den Energiebedarf eines vierstöckigen Gebäudes um einige Dutzend GJ pro Jahr senken kann.

Neben Strahlungseigenschaften ist die gezielte Kontrolle von Wärmeleitung eine weitere Möglichkeit, den Wärmefluss zu manipulieren. Lock-in-Thermografie ist eine etablierte Methode, um die thermische Diffusivität von 2D- und 3D-Proben zu bestimmen. Bis jetzt wurde die Charakterisierung von 1D-Materialien jedoch wenig untersucht. Wir haben einen Messaufbau für Fasern mit wenigen Mikrometern Durchmesser entwickelt und ausführlich den Einfluss unterschiedlicher Messparameter untersucht. Wir konnten zeigen, dass die Charakterisierung von Proben kleiner als der Pixelgröße der Kamera möglich ist, selbst wenn die Faser nicht parallel zum Detektor ausgerichtet ist. Außerdem haben wir experimentell den Einfluss unterschiedlicher Laserleistungen und die damit verbundenen Messungenauigkeiten untersucht. Unsere Ergebnisse sind ein Beitrag zur robusten Messung mikrometergroßer Fasern und Filamente.

Faserverbundwerkstoffe sind ein Beispiel für Systeme, die von einer besseren Charakterisierung von Fasern profitieren. In Kooperation mit dem Lehrstuhl für Polymere Werkstoffe haben wir unterschiedliche Fasern und ihre Matrixkomposite untersucht. Wenn die Fasern orientiert sind, haben die Komposite anisotrope Eigenschaften. Unsere Forschung hat gezeigt, wie die thermischen Eigenschaften der Komposite mit denen der Fasern und deren mechanischen Eigenschaften korrelieren. Wir führen die Korrelation der thermischen und mechanischen Eigenschaften auf die Mikrostruktur der Fasern zurück.

Strukturen auf noch kleineren Längenskalen sind die Grundlage meiner letzten beiden Veröffentlichungen. Sie stellen Sensoren für Temperaturereignisse vor. Im ersten Projekt haben wir die Herstellung eines Kolloidkristalls demonstriert, der aus einem kontinuierlichen Gradienten einer binären Nanopartikelmischung besteht. Die entstehende Struktur ist ein Zeit-Temperatur-Integrator, d. h., dass sie die thermische Historie aufzeichnet, indem sie irreversibel ihre optischen Eigenschaften ändert. In einer Folgeveröffentlichung haben wir auf diesem Konzept aufgebaut und eine Matrix von Kolloidkristallen unterschiedlicher Zusammensetzungen präsentiert. Durch die Automatisierung des Herstellungsprozesses konnten wir große Mengen an Daten messen, die wir mit Hilfe eines künstlichen neuronalen Netzwerks analysiert haben. Die Auswertung unseres Sensors basiert ausschließlich auf Fotos und ist somit auch Fachfremden zugänglich. Unser Sensor ermöglicht eine schnelle und manipulationssichere Auswertung der thermischen Historie. Mögliche Anwendungen sind die Überwachung verderblicher Güter wie Lebensmittel und Medikamente sowie der technische Einsatz für Batterien.

Acknowledgments

A Ph.D. thesis is a large, multi-year project that consists of many ups and downs. A lot of people supported me during my journey and I want to thank them.

I am grateful to my supervisor, Prof. Dr. Markus Retsch, for his guidance and support throughout my Ph.D. journey. I am especially thankful for the freedom he gave me to explore my research interests. He also gave me the opportunity to have a research trip to Barcelona. This was a great experience for which I am very grateful.

Working alone is neither possible nor desirable. Hence, I want to thank all my colleagues in the group. They made working enjoyable and provided valuable insights and ideas for my research. In particular, I want to express my appreciation to Marius, with whom I had long and fruitful discussions about all aspects of my studies.

But life consists of more than only work. I am grateful to my friends from school, volunteering, and university for their support and encouragement. They helped in maintaining a good balance during my studies by having interesting conversations, exploring the world, playing games together, and just generally having fun.

Finally, I want to thank my family for their unwavering support and encouragement throughout my academic journey and life in general. Their love and support made it possible for me to be where I am today. I feel very lucky to have such a strong foundation that I can always rely on. Thank you!

Contents

Part I

Fundamentals

Introduction

1

1.1 Motivation

Humans strive to understand the world and harness this knowledge to improve their lives. As scientists, we are responsible for gathering and widening our understanding. We propose models to describe nature, conduct experiments based on these models, and finally analyze the data to reject or validate our models. It is detrimental that the experiments and subsequent data analysis are reliable. It is even better if the whole process takes the shortest time possible. Utilizing computers allows us to reach these goals.

Since the first general computers were developed during the 1940s, they have been indispensable tools for scientists.[1] Many routine characterization methods in chemistry labs rely on specialized software.[2–6] Consequently, a growing amount of chemists demand teaching basic programming principles in undergraduate study programs.[7–10] Chemistry 4.0 and the general trend towards more digitalization are clear indications that the boundaries between chemistry and computer science will dilute even further. Recent advances include remote-controlled laboratories,[11] automatic synthesis robots,[12,13] and even fully autonomous laboratories.[14,15] While these technologies have an immense potential, they have a high barrier to entry. Still, it is possible to automate many experiments and data evaluation tasks on a small scale. This allows more thorough investigations, eventually leading to new insights.

During my Ph.D., I employed programming skills in various ways, from digital communication with laboratory instruments to the automatic evaluation of measurement data. I aimed to make new measurement techniques possible and to accelerate existing ones. In the following Section 1.2, I will briefly introduce heat transport because it accompanies all of my research projects. Afterward, Chapter 2 explains the most important concepts that I worked with, namely daytime passive cooling, lock-in thermography, and machine learning. It lays out the basic principles and gives an overview of current measurement implementations. In Chapter 3, I will discuss the publications included in this thesis and how I contributed to them. Finally, the remaining chapters contain all publications discussed in this thesis.

1.2 Heat Transport

Heat is an ambiguous term and is used in many different situations. In thermodynamics, heat describes the energy transfer from one system to another.[16,17] Therefore, it is helpful to have a brief look at temperature and thermal energy before talking about heat in more detail.

Every system consists of particles, e.g., molecules, atoms, ions, or electrons. Even if a system is stationary at a macroscopic scale, its particles possess kinetic energy. Depending on the system and the particle of interest, this kinetic energy can take the form of random translational, vibrational, or rotational movement. This microscopic kinetic energy is the thermal energy of the system. On a macroscopic scale, we use temperature to measure the average kinetic energy of a system's particles relative to their center of mass.[17] The faster the particles move, the higher the system's temperature. Consequently, the lowest[1] conceivable temperature, *absolute zero*, is reached when all particles are completely stationary. However, absolute zero does not occur naturally. Even deep space has a temperature of 2.8 K due to the cosmic background radiation. The coldest observed place in the universe is the Boomerang Nebula with an estimated temperature of 0.3–1.0 K.[20] Artificially, the temperature can be reduced even further. In 2021, researchers were able to cool a sample to only 38×10^{-12} K for a duration of two seconds.[21]

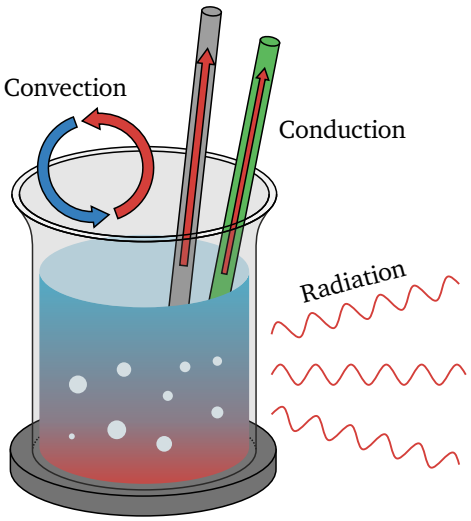

Figure 1.1.: Heat transport mechanisms.

Keeping samples at temperatures far below or above their surroundings is exceptionally challenging because the sample will interact with its surroundings. An interaction between two systems with different thermal energies eventually leads to both systems having the same temperature. They equilibrate by transferring heat from the high-energy system to the low-energy system. This transfer of thermal energy is possible via three different mechanisms: conduction, convection, and radiation (Figure 1.1). In the following paragraphs, each transfer mechanism is explained shortly.

Imagine putting two rods in a warm water bath, one made of metal and the other made of a polymer. After leaving the rods in the water for a while, we touch them and can feel

[1] Due to the definition of temperature also containing entropy, negative absolute temperatures are possible and have been demonstrated experimentally.[18,19] Nevertheless, these systems have higher thermal energy than objects with positive absolute temperatures and consequently transfer heat to them.

the warmth of the bath. Although both rods have the same temperature, the metal one seems to be warmer. In this example, we experience thermal conduction. Conduction occurs between systems that are in direct contact with each other. The collision between particles leads to the transfer of kinetic energy. First, the random motion of the water molecules heats the rods that finally warm our hands.

Thermal conduction is not identical for all materials. The metal rod feels warmer because it is a good thermal conductor, i.e., it transfers more heat. In this specific case, the conduction through the polymer is based on phonons, i.e., the vibration of the polymer's atoms. The atoms themselves are stationary, and as a result, the heat transfer is slow. In contrast, thermal conduction in metals is mainly based on electrons. The delocalized electrons of the outer shell can move through the metal and carry the heat faster.[17,22]

A mathematical description of conduction is Fourier's law. It describes the conductive heat transfer, $\vec{q}$, as[23,24]

$$\vec{q} = -\kappa \vec{\nabla} T \tag{1.1}$$

with κ being the thermal conductivity, and $\vec{\nabla} T$ the temperature gradient. There are two important features: (1) Heat flows in the opposite direction of the temperature gradient, i.e., from high to low temperature. (2) The heat flow is directly proportional to the temperature gradient. The constant[2] of proportionality is the thermal conductivity, κ. In our example above, the metal has a higher thermal conductivity than the polymer, thus, feeling warmer.

Fourier's law describes heat flow for steady-state phenomena, i.e., when the temperatures stay constant. However, in most situations the temperature changes with time. We need additional characteristics to describe the heat flow, most importantly the thermal diffusivity.[16] Usually, good thermal conductors are also good thermal diffusers. In fact, both quantities are related via

$$\alpha = \frac{\kappa}{\rho c}, \tag{1.2}$$

where α is the thermal diffusivity, ρ the density, and c the specific heat capacity. The product of ρ and c is the volumetric heat capacity that is almost constant for solids and liquids ($\approx 2 \times 10^6\,\mathrm{J\,m^{-3}\,K^{-1}}$). Hence, plotting κ against α follows a linear trend (Figure 1.2), and we can intuitively predict which materials are good thermal diffusers. An exception are gases that have a volumetric heat capacity three orders of magnitude lower than solids ($\approx 2 \times 10^3\,\mathrm{J\,m^{-3}\,K^{-1}}$). Therefore, gases can be good thermal diffusers

[2] Here, I assume an isotropic thermal conductivity. In general, κ is a second-rank tensor.

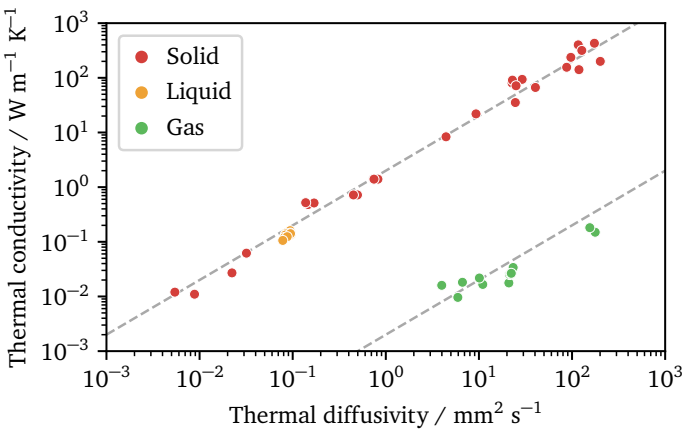

Figure 1.2.: Thermal diffusivities and conductivities of common materials. The volumetric heat capacity of solids and liquids is approximately constant and differs significantly from the one of gases. Data was taken from [25, 26].

without being good thermal conductors. The question arises of how to understand the difference between thermal diffusion and conduction.

We saw earlier that good thermal conductors are materials that can transport a lot of heat in steady-state conditions. Thermal diffusivity determines how fast these conditions are reached. Gases are very poor thermal conductors because the number of particles per unit volume is much lower than that of solids or liquids. On the other hand, their mean free path is significantly larger and thus, the temperature gradient establishes itself very quickly. This means that although a gas will extract very little energy from a thermal reservoir, this energy will disperse through the gas quickly.

In reality, the heat transfer in gases is higher than expected by conduction alone. Convection through the gas phase leads to additional heat transfer. If we think back to our two rods inside the warm water bath, we can feel the warmth even if we move our hands above the container without touching the rods. The air directly above the water is heated due to conduction. The rising temperature leads to a lower density of the air, and it rises upwards. Heat transfer by a moving medium is called convection.

There are two types of convection: natural and forced convection. Natural convection happens on its own due to temperature-induced density differences. This is the case in the example above. As the name suggests, forced convection is due to an externally applied velocity to the medium. Examples include cooling electronics via fans or heating with warm water in radiators. An important parameter for convective heat transport is the heat transfer coefficient between a solid and a liquid.[27] It determines how high the thermal resistance between both materials is and depends on many factors, e.g., the surface geometry, the fluid's material properties, and the flow rate. Even when including

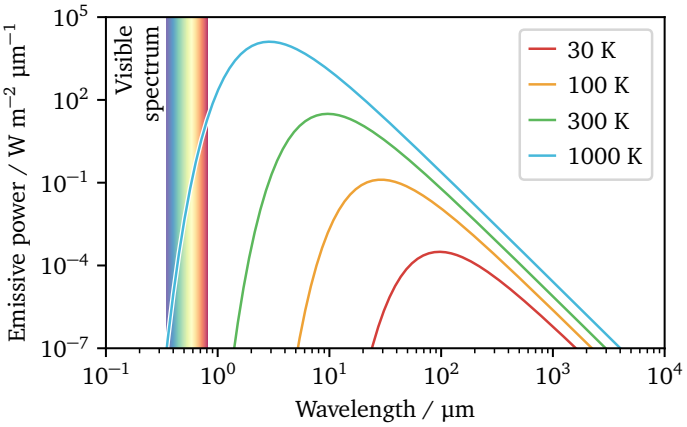

Figure 1.3.: Emission spectrum of a perfect black body. With increasing temperature, the overall power increases, and the emission maximum shifts to lower wavelengths. At sufficiently high temperatures, the thermal radiation reaches the visible spectrum.

convection in our model, gases show a higher heat transfer than expected because there is a third heat transfer method.

The last type of heat transfer is radiation. All materials emit thermal radiation. Radiation differs from conduction and convection because the heat transfer medium is electromagnetic radiation instead of matter. Common examples are standing next to a campfire or sitting outside and feeling the warmth of the sun. The emitted power, P, is described by the Stefan-Boltzmann law:[17,28]

$$P = \sigma A \varepsilon T^4. \tag{1.3}$$

Here, σ is the Stefan-Boltzmann constant, A the surface area of the body, and ε its emissivity. The emissivity is a dimensionless number between zero and one and indicates how similar a body's behavior is to the ideal black body with an emissivity of one. For this ideal black body, Planck's law describes the emitted radiation per unit area, E, as[27,29]

$$E(\lambda, T) = \frac{2\pi hc^2}{\lambda^5} \frac{1}{\exp\left(\frac{hc}{k_B T \lambda}\right) - 1} \tag{1.4}$$

with h being Planck's constant, c the speed of light, λ the wavelength, and k_B Boltzmann's constant. The wavelength of the thermal radiation is distributed over a wide spectrum. Its maximum strongly depends on the temperature, and at room temperature, it lies in the invisible infrared (IR) regime. With increasing temperature, the overall emission rises quickly ($\propto T^4$), and the maximum is shifted to lower wavelengths (Figure 1.3). Hence, hot objects irradiate a red glow, and increasing the temperature further will eventually lead to a white perception.

1.3 Thermal Management

Understanding the fundamentals of heat transport is essential to manipulate the heat flow. Thermal management is an active area of research and important on many length scales from buildings[30–33] over clothing[34–36] to integrated electronics.[37–39] The demands are as different as the application areas and include thermal insulation, heat dissipation, limiting the temperature to a narrow window, and efficient use of waste energy. The following section showcases some examples of thermal management research.

Energy use in buildings accounted for 29 % of global energy consumption in 2018, with thermal energy being 50–60 % thereof.[40] To achieve climate neutrality, reducing the energy usage of buildings is critical. In addition, living in energy-efficient homes is advantageous for human health. The increased healthy lifespan is a personal as well as societal benefit, adding several hundred million euros per year to a country's economy.[41] Considering the thermal energy, the perfect house needs neither active cooling nor heating and is thus net-zero. Passive houses are one standard for buildings with ideal heat management.[42] Achieving this goal is only possible with an architectural design incorporating highly insulating materials.

Traditional building materials for thermal insulation are polymer foams, most prominently polyurethane and polystyrene.[43] While the thermal conductivity of bulk polystyrene is reasonably low ($0.15\,\mathrm{W\,m^{-1}\,K^{-1}}$),[44] it can be lowered much further by changing its morphology. Foams drastically reduce possible conduction pathways by introducing pores filled with gas. The foam's thermal conductivity will be a value between that of the solid and gaseous phases. Commercial polystyrene foams have thermal conductivities between 0.03 and $0.04\,\mathrm{W\,m^{-1}\,K^{-1}}$,[43] close to the value of air ($0.026\,\mathrm{W\,m^{-1}\,K^{-1}}$).[25]

Besides the decreased conduction pathways, a closed-cell pore prevents convection through the wall. Nanopores can even lead to the Knudsen effect. Suppose the size of the air pockets is at the same order of magnitude as the mean free path of the individual molecules. In that case, the thermal conductivity of air inside the pores is reduced below its usual value. Aerogels are one material class utilizing the Knudsen effect. Cellulose-based aerogels for construction purposes usually have cell sizes far beyond one micrometer (Figure 1.4). Consequently, their thermal conductivity is very low, with values reaching a minimum of $0.015\,\mathrm{W\,m^{-1}\,K^{-1}}$.[45]

Completely removing the gas phase is the only option to reduce the thermal conductivity even further. Vacuum insulation panels consist of an open-celled foam as a core and a surrounding air-tight material. By evacuating the foam, the thermal conductivity reaches values as low as $0.002\,\mathrm{W\,m^{-1}\,K^{-1}}$.[47] A major drawback of vacuum insulation panels is their delicacy. If they are punctured, air fills the inner core, and they lose their superior

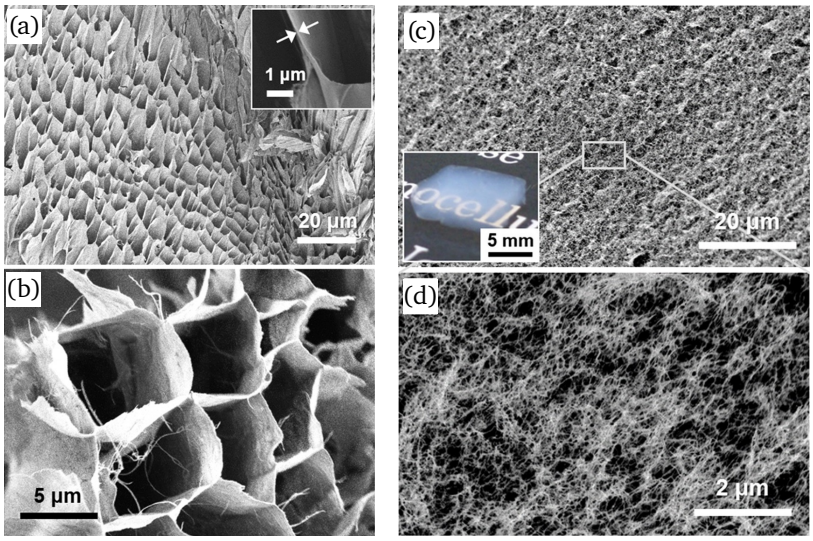

Figure 1.4.: Scanning electron images of foams with a solid content of (a, b) 1.04 vol% and (c, d) 0.60 vol%. Both aerogels have a thermal conductivity lower than air. Image reproduced with permission from [46].

insulation capacity. Even if they are not damaged, gas diffuses back into the foam over time and slowly increases the thermal conductivity. Vacuum insulation panels are not widespread due to the mentioned problems and their high costs.

A sustainable alternative is insulation based on natural or recycled materials. One example being both natural and recycled is sheep wool.[48] Many sheep are bred exclusively for their milk or meat and their wool is a byproduct that must be disposed of. Using the wool as building insulation utilizes this byproduct and prevents waste. Its insulation properties are as good as traditional building materials reaching thermal conductivities as low as $0.034\,\mathrm{W\,m^{-1}\,K^{-1}}$.[49] Other examples of sustainable insulation include cork, cotton fibers, textile waste, and ground tire rubber.[31]

Well insulated buildings can easily keep indoor temperatures high but they struggle with overheating issues in hot climates and need additional active cooling components.[50] One way to eliminate this remaining energy use is passive daytime cooling.[33] The concept is based on transferring heat to outer space via radiation and is explained in Section 2.1.

Manipulating the radiative properties is also relevant for personal heat management. IR transparent clothing allows the body to transfer heat to its surroundings.[51] However, this concept is limited to a narrow range of temperatures. If the ambient temperature is very high or low, equilibration with the surroundings will lead to an uncomfortable body temperature. For these temperatures, fabrics blocking the IR radiation are better suited. Jiang et al. reported a material that is opaque in the IR range due to its high emissivity.[52] As a downside, it still allows thermal equilibration between the fabric and

the surroundings, potentially leading to discomfort. An alternative is to create opaque fabrics by increasing their reflectivity. Gao et al. presented such a material made of polyimide and silver nanowires.[53] Their product is mainly suited for keeping the body warm. Therefore, it consists of a nonwoven with low thermal conductivity to further increase the insulation properties.

Increasing the thermal insulation ability is a general approach to creating novel clothing materials. Commercial materials such as Kevlar® and Nomex® are famous materials that can withstand high temperatures.[54,55] They are suitable for professional equipment, e.g., for firefighters. But their stiffness and heaviness render these materials inappropriate for everyday clothing. One strategy to increase thermal insulation without sacrificing comfort is controlling the fabric's weaving pattern and the fibers' shape.[56–58] Both determine the size of air gaps between the fabric and thus the thermal conductivity.

A natural example of trapping air inside fibers is polar bear fur. The freezing temperatures in the arctic led to the evolution of hollow fibers with good thermal insulation. Different artificial hollow fibers have been reported that mimic these properties.[59,60] As with building materials, aerogels are another option to include air in fabrics to decrease the thermal conductivity significantly.[61]

All fabrics mentioned so far have static properties. But since ambient temperatures can change in a matter of hours, responsive fabrics are desirable. An early example of a commercial application is Nike Sphere React.[62] The T-shirt made of a shape memory material reacts to humidity. When the wearer sweats due to exercise or hot weather, additional pores in the fabric open. The increased convection has a cooling effect on the wearer. The same idea can be used to create fabrics with automatically adjusting thickness.[63] For this, a memory shape polymer is sandwiched between two fabric layers. In its initial state, the polymer pushes the outer layers apart. The infiltrating air lowers the thermal conductivity of the composite material. When the wearer starts to sweat, the humidity increases, and the polymer flattens. Consequently, the thermal conductivity increases, and heat can escape (Figure 1.5).

Another option for personal heat management are active components. They are either based on Joule heating or the thermoelectric effect.[53,64] Both methods effectively regulate the micro-climate around the body. Regardless, they are not widespread yet because they include active electric components needing a power supply. This increases production costs, limits design possibilities, and makes washing difficult. Further improvements in this material class might eventually lead to general adoption, as is the case with other electronic components.

In many other areas, integrated circuits are vital to our technological progress. The miniaturization of computing equipment allows great computational power, e.g., for

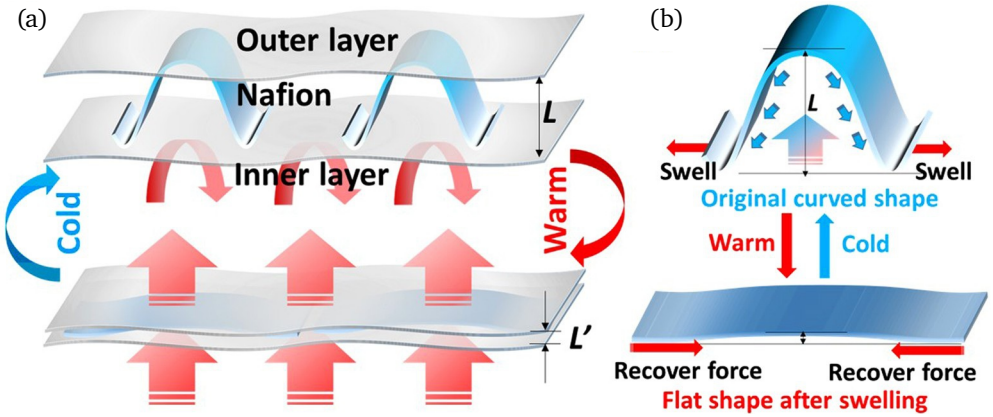

Figure 1.5.: Working principle of a smart textile. (a) The overall thickness of the textile governs the effective thermal conductivity. (b) The memory shape polymer changes depending on the humidity. Image reproduced with permission from [63].

smartphones, laptops, and data centers. Concentrating large processing capabilities in small spaces leads to a lot of concentrated waste heat. This negatively impacts device performance, demanding effective cooling solutions. Usually, the heat is dissipated to the surrounding by a heat sink with a large surface area. A major problem is the contact resistance between electronic components and heat sinks. Microscopic surface roughness decreases thermal conduction pathways and leads to high thermal barriers.[37,38]

Thermal interface materials decrease the thermal contact resistance between two materials. These materials must fulfill three major requirements: (1) They must have high thermal conductivity to efficiently transport the heat from the source to the sink. (2) They must have a low mechanical shear rate to fill microscopic gaps. (3) They must have a high electrical resistance to prevent shorting the electrical components. The last two requirements make polymers the perfect candidates because many polymers can deform easily and have high electrical resistance. However, their thermal conductivity is low, as discussed above. Mixing polymers with high thermal conductors creates composites with good thermal conductivities. Examples include metal- and boron-based materials.[65–67] Another option to increase the thermal conductivity of polymers is to control the polymer chain orientation. Xu et al. stretched polyethylene films, leading to the formation of oriented nanofibers. Their material had a thermal conductivity of the same order of magnitude as metals ($62\,\mathrm{W\,m^{-1}\,K^{-1}}$).[68] This facilitates a fast heat transfer between the heat source and sink.

Besides integrated circuits, rechargeable batteries are another cornerstone of modern machinery, including handheld devices, cars, and ships. The thermal demands of batteries are very different from other electronic equipment. There is a very narrow, optimal temperature window for the operation of batteries. If they are too cold, the chemical reactions inside the battery slow down, and both charging and discharging power

decrease, or the battery might stop working completely.[69] On the other hand, at high temperatures batteries can overheat. In the worst case, the battery reacts uncontrollably and spontaneously ignites.[39] The optimal temperature range for lithium ion batteries is 15–35 °C.[70,71] One particular research focus is the heat management for batteries for electric vehicles. They experience cold and hot temperatures alike while their efficiency is detrimental for commercialization.[39]

In addition to optimizing the internal battery cell architecture, there are four major thermal management systems for batteries based on air, liquids, thermoelectric devices, or phase change materials.[71] Air transfers heat through forced convection. While air management systems are easy to design, cheap, and lightweight, the heat transfer coefficient of air is low. This makes cooling/warming in extreme conditions difficult. Liquids such as water or oil offer a solution with better heat transfer but with the added risk of leaks. Peltier elements with thermoelectric properties are solid-state materials, eliminating the possibility of leaks. An applied current transfers heat from one side to the other. Reversing the current changes the heat transfer direction. Peltier elements can be used independently but are commonly combined with air or liquid as a transfer medium to prevent inhomogeneous temperature distributions. All three heat management methods depend on active components. The necessary fans, pumps, heaters, and coolers consume power. This reduces the energy available to the end user.

Passive thermal management for batteries is based on phase change materials and does not require energy. Instead of transporting all excess energy from the battery to the surroundings or vice versa, phase change materials undergo a phase transition at a temperature close to the operating temperature of the battery. Upon heating, the energy is reversibly stored inside the phase change material.[72] Therefore, it can be used for heating and cooling without needing active components. The biggest concerns with phase change materials are their low thermal conductivity and limited storage capacity. Solving these problems is a current research focus. Adding heat pipes to transfer the thermal energy between the battery and phase change material is a promising candidate for eliminating the conductivity issues.[73,74]

The presented topics are merely scratching the surface of heat transport research. They clearly demonstrate that further development of materials and the required characterization are important. During my Ph.D., one main focus was to improve characterization techniques. The second major focus was designing a heat monitoring system and its application-ready readout. The following section will introduce the topic.

1.4 Heat Monitoring

The last section showcased advances and ongoing research in the field of thermal management. To evaluate if the suggested strategies work, heat monitoring is necessary. During the scientific evaluation, the temperature of a system can be continuously monitored with temperature sensors. The three most common approaches are thermo-resistive devices, thermocouples, and thermography systems.[75,76] They enable detailed insight into the temperature evolution with local resolution.

The electrical resistance of materials changes with temperature. By knowing the temperature coefficient of the temperature change, the electrical resistance can be directly related to the temperature. Measuring the electrical resistance with high accuracy is easy and thus allows accurate temperature determination. Uncertainties of typical systems range from ±1 K for cheap systems down to below ±1 mK for high-precision systems. Most commonly used are platinum wires with resistances of 100 Ω or 1000 Ω because they show a linear temperature dependence in a wide range of temperatures (−260–960 °C).[77]

Thermocouples are another option based on electric measurements. They consist of two different materials with one junction as the reference and one as the sensor. The voltage across the device depends on the temperature difference between the two junctions.[78] Thus, thermocouples measure the temperature difference between two locations instead of the absolute temperature at one location. To get absolute readings, they are usually combined with thermo-resistive devices. The advantage of thermocouples is their low cost, high robustness, small size, and wide temperature range. Depending on the material, they can measure temperatures ranging from −270 °C up to 3000 °C. As shown in Table 1.1, common materials operate at lower temperatures.[75]

Table 1.1.: Commonly used thermocouples.

Type	Materials	Range / °C
T	copper / constantan	−262–850
J	iron / constantan	−196–700
E	chromel / constantan	−268–800
K	chromel / alumel	−250–1100
N	nicrosil / nisil	0–1250
B	platinum & 30 % rhodium / platinum & 6 % rhodium	100–1750
S	platinum & 10 % rhodium / platinum	0–1500
R	platinum & 13 % rhodium / platinum	0–1600

A last typical example of temperature sensors are thermography systems. They are explained in Section 2.2 in more detail. In contrast to thermo-resistive devices and thermocouples, they measure temperature non-invasively and at a distance. This makes them especially suited for the temperature detection of large surfaces or medical applications.[79–81]

Having complete data for the whole system is essential for a better understanding but places high demands on the monitoring system. Although cheaper manufacturing leads to more active monitoring, as evidenced by the growing popularity of the Internet of Things, the additional data create a need for data collection and analysis.[82] For many applications, simple and autonomous sensors are preferred. This is especially important when the readout must be faster or is done by non-specialists. In the following paragraphs, I will present example applications for passive sensors and current research efforts.

An estimated 17 % of all produced food are not consumed but discarded.[83] The needed resources to produce this food corresponds to 8–10 % of global greenhouse gas emissions. Still, the World Health Organization estimates that 600 million foodborne illnesses occur every year, resulting in more than 400 000 deaths.[84] Temperature is the most important factor contributing to food spoilage.[85] Simple, low-cost, autonomous sensors on food packaging can contribute to lowering food waste and preventing foodborne diseases. They indicate the shelf-life of products better than generic 'best-before' dates.

Research on time-temperature integrators for food products has been carried out for several decades.[86] Their working principle differs from the continuous temperature sensors presented above. Instead, time-temperature integrators change irreversibly above a specific temperature. On the one hand, this makes it impossible to get detailed information of the thermal history. On the other hand, the readout is significantly simpler, and information about the peak temperature is usually sufficient for food applications.

Optical indicators that record time-temperature events can be realized with different mechanisms. A change in color or color intensity can be induced by chemical, physical, or biological reactions.[87,88] An example of a chemical system are diacetylenes. Upon increasing the temperature, they polymerize, forming an extended, linear π-system. The degree of polymerization and the interaction with the sidechains govern the optical absorption.[87] Several commercial products based on polydiacetylenes have been developed. The labels are stored at low temperatures (−24 °C) before application to ensure a low reactivity.[87] As soon as they are brought in contact with the food packaging at a higher temperature, the color starts to change. Elevated temperatures will lead to faster reaction rates and, thus, a faster change.[89]

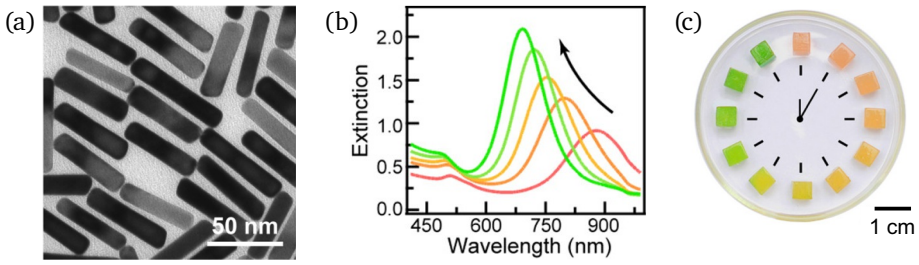

Figure 1.6.: Plasmonic nanorods as a time-temperature integrator. (a) Transmission electron microscopy images of the pristine gold nanorods. (b) Extinction spectra during the epitaxial growth of silver on the gold nanorods. (c) Photograph of nanorods after different time intervals. Image reproduced with permission from [94].

Spiro aromatic compounds are a second example of chemical systems used as time-temperature integrators in food packaging. Exciting these molecules with UV light will lead to a ring opening and the formation of a zwitterionic component. The reaction product is unstable and will slowly revert back to the original spiro component. The open and closed variants have different optical properties and can thus be easily distinguished.[90] One characteristic of this system is its reversibility. While this might facilitate recycling, it also opens the door to tampering with the indicator state and might be a possible security risk. Nevertheless, commercial systems based on spiro components exist. They usually employ a UV-resistant window to prevent accidental or malicious resetting of the sensor.[87]

Physical systems rely on phase changes or diffusion to indicate time and temperature. In diffusion-based systems, a colored substance slowly diffuses from one side of the sensor to the other. Since diffusion depends on temperature, the position of the colored fluid relates to time and temperature.[91,92] Commercial solutions based on fatty acid esters are available and used to monitor the temperature of perishable products.[93]

In the scientific community, research focuses on plasmonic and photonic systems. Zhang et al. presented plasmonic gold nanorods exhibiting red color.[94] By adding silver nitrate and ascorbic acid, the gold rods are slowly coated in a layer of silver. The epitaxial overgrowth changes the color of the system from red over yellow to green (Figure 1.6). Like with the polymerization systems above, the reaction kinetics change with temperature. The current color of the dispersion indicates the temperature history of the whole system. The visual readout is easy and straightforward, but the incorporation of solution chemistry poses a challenge to adoption.

Solid-state systems are better suited for labeling because they do not pose the risk of leaching chemicals into their surroundings. Nonwovens based on thermoplastic polyurethane (TPU) appear white because light is scattered at the many interfaces of the fibers. If the TPU contains aromatic disulfide groups, self-healing can occur.[95,96]

The self-healing converts the nonwoven into a film with significantly fewer interfaces. In turn, the scattering decreases, and the mat becomes transparent. The temperature and time response can be modified by changing the composition of the TPU.[97]

The softening of polymers around the glass transition temperature, T_g, is a common strategy for temperature-responsive optical sensors.[98] An example are inverse opals. First, a colloidal crystal template of silicon oxide particles is created. Subsequently, a precursor infiltrates the structure and polymerizes, creating a negative of the colloidal crystal. The template particles can be removed by controlled etching. The final structure shows the same color impression as the colloidal crystal. The polymer softens and the structure collapses when the temperature is raised to around and above T_g. In consequence, the reflectance shifts to lower wavelengths, and the color changes.[99] As before, the color change rate depends on both time and temperature.

Food packaging is only one example where autonomous time-temperature integrators are needed. Another important field of application is cool-chain monitoring in the medical sector for drugs, vaccines, and blood packages.[100] Since the temperature requirements are often similar to food, the same systems can be used. Other temperature regimes are also relevant for commercial applications, such as higher temperatures used to monitor the temperature history of batteries.[101] As discussed in Section 1.3, they have a narrow, optimal operation range. Before presenting my contributions to thermal management characterization and heat monitoring, I will introduce important concepts in the Chapter 2.

Concepts

2

2.1 Passive Daytime Cooling

With increasing global temperatures, the importance of energy-efficient cooling applications steadily increases.[102] Cooling an object describes the energy transfer from the object to a heat sink. As described in Section 1.2, there are three transfer mechanisms: conduction, convection, and radiation. Traditional air conditioning moves heat from the inside of a building to its immediate surroundings via conduction and convection. Especially in densely populated areas, air conditioning is a cause of local overheating.[103,104] One way to combat urban heat islands is to transfer the heat to a heat sink far away. Passive cooling materials achieve this by radiating heat to outer space.

At temperatures around 300 K, the thermal radiation maximum is about 10 µm. Coincidentally, the earth's atmosphere shows very high transmission between 8 and 13 µm (Figure 2.1). Therefore, a high emissivity material can radiate heat through the atmosphere directly to deep space with a temperature of around 3 K. Space is the ideal heat sink because it is far away and infinitely large for all practical purposes.

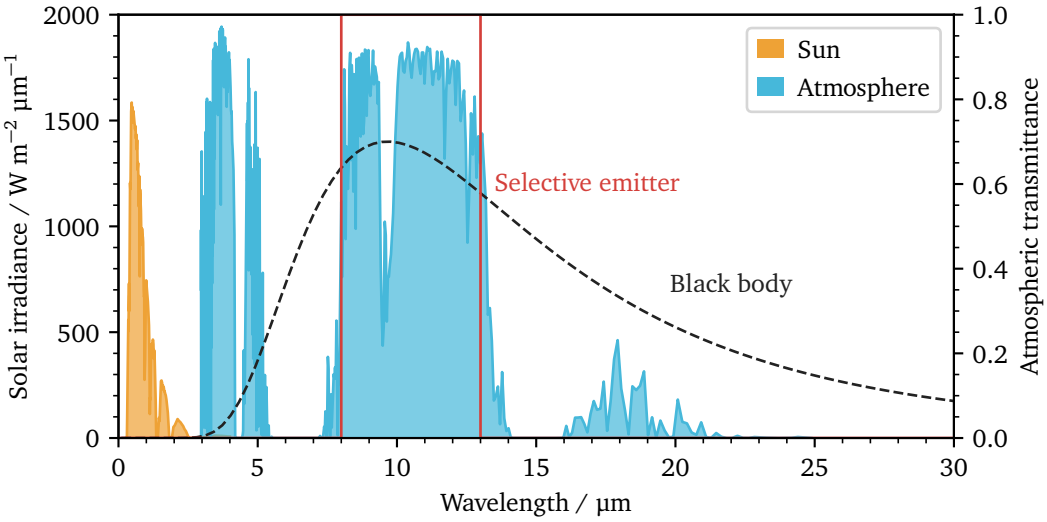

Figure 2.1.: Passive cooling basics. An ideal passive cooling material transmits thermal radiation through the atmosphere while reflecting solar irradiation.

Rephaeli et al. calculated the maximum cooling power under ideal conditions to be about 150 $W\,m^{-2}$.[105] The commonly used AM1.5 Global Tilt spectrum imitates the average solar irradiation in the contiguous United States and has a power of just below 1000 $W\,m^{-2}$. For a black body with unity emissivity at all wavelengths, heat absorption from the sun by far outweighs radiative cooling to outer space. Therefore, daytime passive cooling demands high reflectivity in the solar spectrum.

The first patent described radiative passive cooling and its application in 1962.[106] While Head identified the need for selective emissivity, his design simply included a sunshade to prevent solar heat absorption. Casting a shadow on large areas is unfeasible and prevents large-scale application. In 2014, Raman et al. presented a material with optimized optical properties to reach sub-ambient temperatures under solar illumination.[102] After the invention of the first working prototype, researchers designed a wide range of nanostructures with good passive cooling performances.[107–112] Their fabrication depends on precise morphology control, often based on lithography. Simpler and cheaper alternative designs based on polymers have been proposed to improve scalability.[113–115]

To decide which material design is optimal, a comparable and robust characterization method of the cooling performance is essential. One standard way to indicate the cooling performance is to characterize the optical properties of the material. All research articles mentioned above report the emission in the visible and IR spectrum.[102,107–115] Since spectrometry is well established, results from different groups can be easily compared. Despite the angle dependence of optical properties, they are often only reported at one specific angle.[116,117] This makes comprehensive simulations of the passive cooling power impossible.[118–120] For this reason, results of outdoor experiments usually accompany optical properties.[102,108–115] In field tests, the material experiences the same conditions like during the final application. The results indicate the actual cooling performance. But to obtain general results, field tests must be repeated at different locations and times to prevent local conditions, like weather, altitude, or humidity, from distorting the results. As with the characterization of solar cells,[121] a standard laboratory technique is desirable.

Zhou et al. developed the first indoor measurement setup to quantify shading effects on the cooling performance.[122] They coated the bottom of a styrofoam box with black aluminum and the walls with reflective aluminum (Figure 2.2a). Liquid nitrogen fills the bottom part of the box to provide a heat sink for the measurement. The sample is in a separate, insulated box above the heat sink and covered with a polyethylene (PE) foil to prevent convection. By changing the distance between the sample and the aluminum mirrors, different viewing angles for the sample are simulated. Increasing the angle from 30° to 180° changed the temperature difference between the sample and reference from 2 K to 9.5 K.[122] Their setup is very easy to replicate and demonstrates the angle

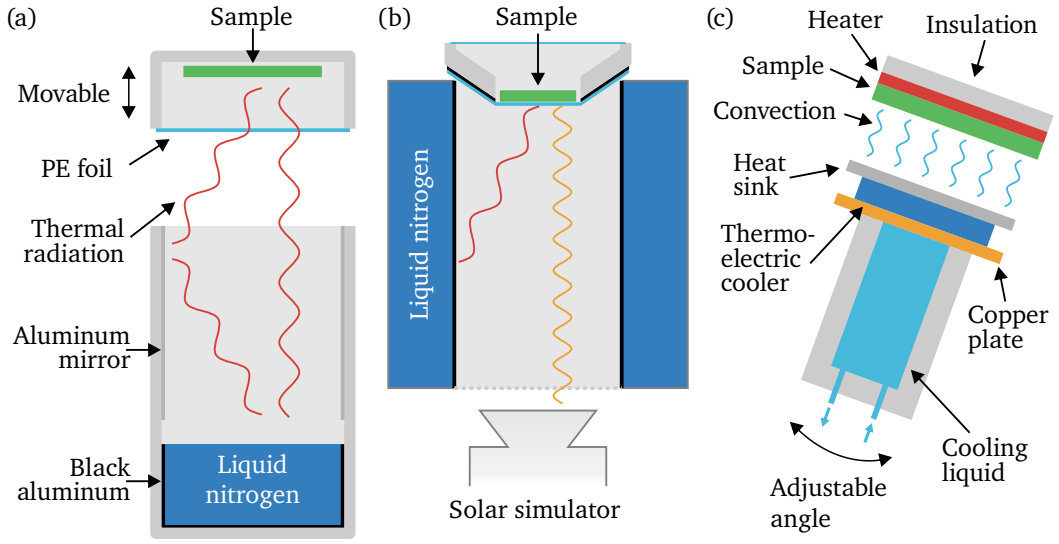

Figure 2.2.: Schematic representation of the indoor setups reported in [122–124].

dependency well. However, it is not universally applicable because it lacks both the sun and the selective transmittance of the atmosphere.

Park et al. followed a similar approach of using a black-coated cylinder cooled by liquid nitrogen.[123] Instead of filling liquid nitrogen inside the cylinder, they surrounded the cylinder walls with a container holding liquid nitrogen (Figure 2.2b). The sample is placed on top of the cylinder, and a solar simulator illuminates it from below. Including the solar simulator allows a comparison between daytime and nighttime performance.

A different approach compared to the two measurement setups above is to imitate the effect of passive cooling via convection. This method does not aim to measure a material's cooling performance but to simulate radiative cooling in the lab, allowing the investigation of devices. Wong et al. proposed a system where the passive cooling device faces a temperature-controlled heat sink (Figure 2.2c).[124] The angle between both surfaces determines the non-radiative heat transfer coefficient. In combination with the heat sink temperature, they simulate different cooling performances. To use the setup, prior knowledge of the material's cooling power is necessary to determine the correct heat sink temperature and sample angle. A follow-up study utilized the system to investigate power harvesting from cooled surfaces.[125]

It is evident that little research has been done on characterizing passive cooling materials under controlled conditions. Therefore, my colleagues and I invented a measurement setup. The respective publication is shown in Chapter 5. We used our setup to investigate the upcycling of post-consumer waste in Chapter 6.

2.2 Lock-in Thermography

Thermography is a widespread method to determine the temperature of objects. Its basic principle is to measure thermal radiation originating from the object under investigation. There are two detector types: microbolometers and photodetectors.[126] Microbolometers consist of an array of thermistors on silicon chips. The incoming thermal radiation heats these elements and thus changes the electrical resistance accordingly. From a previous calibration, the temperature can be obtained.[127] These detectors work at room temperature and are easy to fabricate. Hence, they are relatively cheap.

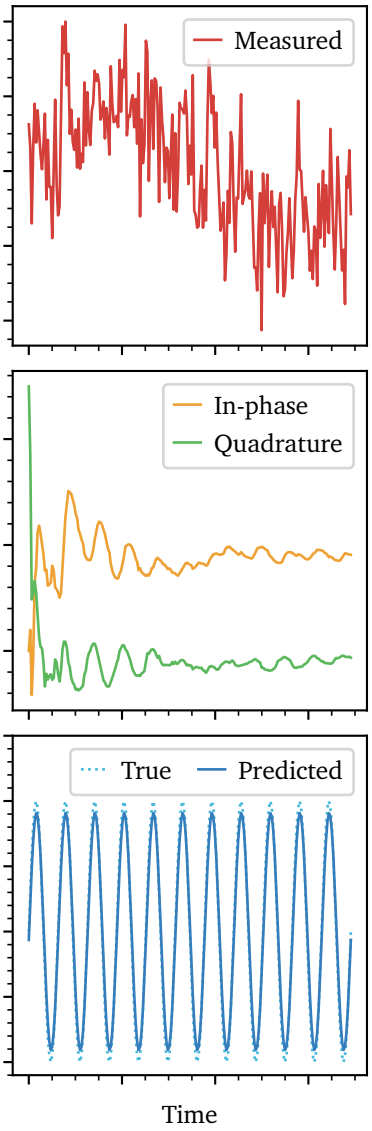

Figure 2.3.: Schematic demonstration of lock-in amplification.

Photodetectors are more expensive but offer a better signal-to-noise ratio. They are usually made of indium antimonide or mercury cadmium telluride.[126] Similar to photodetectors for visible light, incoming photons create a small electrical current that is multiplied and detected.[128] Besides the improved signal-to-noise ratio, the readout frequency can reach several thousand images per second compared to the maximum of sixty for microbolometers.[126] A disadvantage of photodetectors is the substantial dark current at room temperature. Hence, they must be cooled to around 80 K, e.g., by using a Stirling cooler.[129]

One distinct advantage of infrared thermography compared to other temperature sensors is the ability to determine temperature contactless and at large distances. This allows nondestructive measurements and the fast investigation of large areas. Therefore, infrared cameras are used in many areas, e.g., the investigation of buildings,[80,130] fault detection of wind turbines,[79,131] and medical diagnostics.[81,132] Since the detection principle relies on thermal radiation and not temperature itself, the sample emissivity influences the measurement result (see Equation 1.3). Without proper correction, objects will show an incorrect temperature. At the same time, the emissivity dependence can be an advantage for thermography. For example, it is possible to investigate structures behind a silicon wafer because silicon is almost transparent in the infrared regime.[126]

Applications are divided into passive and active thermography. The former measures the temperature of a system without interfering with it at all, while the latter records the temperature response due to an external stimulus. My research focused on a particular kind of active thermography, lock-in thermography. Here, a heat source excites the sample periodically. Special data analysis allows for increasing the sensitivity beyond the initially observed signal.

Lock-in amplification is a powerful technique to analyze periodic signals even if the noise floor is several magnitudes larger than the signal of interest. The time-dependent signal is transformed to the frequency domain via the discrete Fourier transform.[133] Most noise is either constant or at a frequency different from the lock-in frequency. Thus, only the relevant signal remains. Traditional lock-in amplification uses dedicated hardware.[134] With the computational power available today, a measured time series can be converted to the frequency domain digitally either in real-time or after acquisition. The measurement signal, $F(t)$, is multiplied with a weighting factor, $K(t)$, and the output signal, S, can be written as[126]

$$S = \frac{1}{t_{\text{int}}} \int_0^{t_{\text{int}}} F(t)K(t)\mathrm{d}t. \tag{2.1}$$

For narrow-band, two-channel correlation, there are two sets of weighting factors,

$$K^{0^\circ} = 2\sin(2\pi f_{\text{lock-in}} t) \quad \text{and} \quad K^{90^\circ} = 2\cos(2\pi f_{\text{lock-in}} t). \tag{2.2}$$

The resulting signals, S^{0° and S^{90°, are called in-phase and quadrature signal, respectively. From these, the amplitude, A, and phase, Ψ, of the measured signal relative to the reference can be determined as

$$A = \sqrt{(S^{0^\circ})^2 + (S^{90^\circ})^2} \tag{2.3}$$

$$\Psi = \arctan\left(\frac{S^{90^\circ}}{S^{0^\circ}}\right). \tag{2.4}$$

Figure 2.3 demonstrates how lock-in amplification can extract relevant information from a noisy signal. Lock-in amplification has been successfully applied to many measurement problems such as high-resolution microscopy,[135] atomic force microscopy,[136], and thermoelectric characterization of high-resistance samples.[137] In thermography, lock-in amplification is most commonly used in nondestructive testing for mechanical or electronic components.[138–142] I used quantitative lock-in thermography for the determination of the thermal diffusivity.

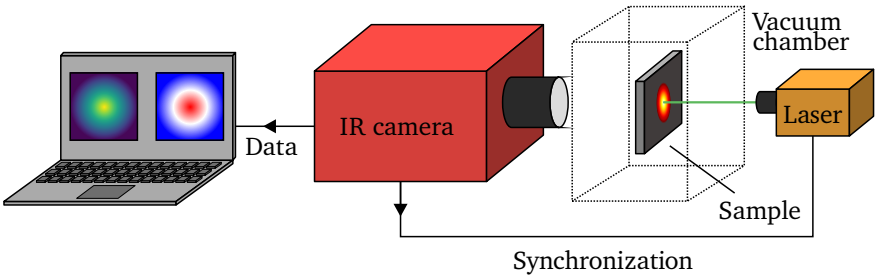

Figure 2.4.: Typical measurement geometry for lock-in thermography of thin films.

Ångström first used a periodic excitation to determine thermal properties in 1863.[143] In his experiment, Ångström measured the temperature with thermometers and controlled the temperature with steam and cold water. Nowadays, experimental setups consist of IR cameras as detectors and lasers as excitation sources.[144–147] In typical transmission geometry experiments, a thin, freestanding sample is heated by a laser from the back. The temperature at the entire front side is recorded as a video and converted to amplitude and phase (Figure 2.4). The sample is often placed inside a vacuum chamber to prevent thermal losses due to convection and conduction.

The data analysis is based on the amplitude and phase of the signal at the excitation frequency. Solving the differential heat transfer equation shows that the system behaves as one-dimensional at a sufficiently large distance from the laser spot.[148,149] The following steps extract the thermal diffusivity from the measurement data.

Fourier Transform The recorded temperature data is transformed to the amplitude and phase at the lock-in frequency, $f_{\text{lock-in}}$.

Center Determination The coordinates of the excitation have to be either set manually or detected automatically. They are essential for the next step.

Distance Calculation For each pixel, the distance to the center, r, is calculated using the Pythagorean theorem.

Amplitude Linearization For two-dimensional samples, e.g., thin films, the amplitude is multiplied with $\sqrt{r}$. Regardless of the dimensionality of the samples, the natural logarithm of the amplitude is calculated.

Linear Regression Both the linearized amplitude and the phase follow a linear trend with respect to r. The respective slopes are obtained by fitting the data.

Diffusivity Calculation The thermal diffusivity is the ratio between $\pi f_{\text{lock-in}}$ and the product of the slopes. If there are no thermal losses, the square of any one slope can be used instead of their product.

This evaluation procedure was experimentally validated for samples with different geometries and a wide range of thermal properties.[144,150–154] The data analysis assumes several conditions that must be fulfilled to obtain meaningful results. Samples must be homogeneous and have sufficient absorption/emission in the visible and IR range. In the visible range, the absorption is necessary for the excitation with the laser. In the IR range, the emission is necessary for detection with the IR camera. Low absorptivity/emissivity samples can be modified by adding thin layers of a high-emissivity material like carbon. For transmission experiments as discussed above, the samples are assumed to be thermally thin, i.e., the sample thickness is significantly smaller than the thermal decay length,

$$\mu = \sqrt{\frac{\alpha}{\pi f_{\text{lock-in}}}}. \tag{2.5}$$

At the same time, the samples must be sufficiently thick to ensure mechanical stability and withstand high gas flow rates when applying a vacuum. Lastly, samples are assumed to be infinitely large in the direction of heat transport, i.e., the height and width of 2D samples and the length of 1D samples must be much larger than μ. Since the thermal decay length depends on $f_{\text{lock-in}}$, it is recommended to investigate unknown samples at different frequencies. Evaluating the resulting data will ideally show a plateau regime in which the data evaluation is valid. If no such region can be found, either the sample or the measurement technique must be adapted.

While previous group members established lock-in thermography for films, I focused on measuring thin filaments. In 1998, Oksanen et al. reported the first measurements of fibers using the lock-in principle and IR detection.[155] For their experiments, they used a single-pixel IR detector and scanned the temperature along fiber bundles with a diameter of several millimeters. With advances in IR detection hardware, measuring fibers with diameters as low as 10 µm was possible.[153] However, the data acquisition took around 30 min because the measurement setup consisted of only a single-pixel detector but the whole fiber needed to be scanned. Therefore, analyzing samples under varying conditions or characterizing a large number of fibers was infeasible.

With the availability of IR cameras, the measurement times decreased significantly. Thus, more thorough investigations of convective heat losses were possible.[144,154] Researchers derived an analytical model to describe the heat distribution in thin fibers upon periodic excitation with a laser. They utilized their model to characterize fibers of different materials with diffusivities spanning four orders of magnitude.[154] Most importantly, they found that the surrounding atmosphere greatly influences the apparent thermal diffusivity.[144] Consequently, the highest quality results are obtained when the measurements are performed in a vacuum.

During the last 15 years, several alternative measurement methods to characterize the thermal properties of thin fibers have been proposed. They include the 3ω technique,[156] the transient electrothermal technique (TET),[157,158] time-domain thermoreflectance (TDTR),[159,160] and Raman thermometry.[161,162] Each has distinct strengths and weaknesses compared to lock-in thermography.

Measurement methods that detect electrical resistance instead of temperature (3ω, TET) have a very good signal-to-noise ratio. In 3ω measurements, an alternating current heats the sample. As a result, the electrical resistance of the sample will change. Repeating the measurement at several frequencies allows the characterization of the thermal properties of the sample.[156] The 3ω technique has two major drawbacks. It demands the knowledge of the temperature coefficient of resistance to transform the electrical signal into a thermal signal. This shifts the accuracy of the temperature measurement from the sensor to a temperature control unit. Moreover, the relation between current and voltage must be linear. Thus, the investigation of semiconductors and insulators is not possible.[157]

The second technique based on the change of electrical resistance with temperature, TET, alleviates these problems. It investigates the kinetics of the resistance change to determine the thermal diffusivity.[157] Therefore, no temperature calibration is needed. Insulators can be measured when they are coated with a thin conductive layer, e.g., gold. Since the thermal properties are calculated from the change in electrical resistance, the contact resistance between the sample and measurement electrodes strongly influences the results. Besides, high thermal conductivity samples reach their final temperature and thus final resistance very quickly. This can be detrimental to the measurement accuracy.

A commonly used method for the determination of cross-plane thermal properties is TDTR. Its primary advantage compared to other techniques is the very high spatial resolution limited by the spot size of a laser. Therefore, investigating fibers in the micrometer regime in both longitudinal and transverse directions is possible.[159,160] However, the sample preparation requires a precise cut along the fiber cross-section. This adds to the challenging measurement where two lasers must be perfectly aligned. Lastly, the data analysis model is based on many experimental parameters that have to be determined precisely for accurate measurements. Due to the high demands of sample preparation, experimental procedure, and data analysis, TDTR is very time-consuming and error-prone without extensive prior experience.

Raman thermometry is another alternative method to characterize the thermal properties of small structures. It detects temperature-induced changes in Raman peak frequency and shape.[161] Individual fibers as thin as 400 nm have been measured,[162] demonstrating

the capabilities of the technique. However, as with the 3ω method discussed above, a calibration relating the measurement signal to the temperature must be performed. If the material of interest shows no temperature-dependent Raman signal, the sample can be coated with a thin layer of carbon.

All presented characterization methods are appropriate for specific applications. TET and 3ω are particularly suitable for electrically conductive samples, TDTR is able to measure the transverse thermal properties, and Raman thermometry can characterize very small samples. Lock-in thermography is useful due to the simple sample preparation, measurement procedure, and data analysis. Furthermore, it can be applied at different length scales for electrically conductive and non-conductive samples.

Xie et al. utilized TET to determine the thermal properties of carbon nanotubes before and after current-induced thermal annealing.[163] By using in-situ characterization, they prevented errors due to sample-to-sample variation and sample transfer. They demonstrated the effects of the annealing step on the thermal diffusivity. Combining their results with Raman spectroscopy unveiled a correlation between the thermal and mechanical properties.

TDTR measurements show how mechanical strain influences the thermal conductivity of different polymer fibers in the axial direction. While the thermal conductivity of semi-crystalline and liquid crystalline polymers increases, amorphous polymers are unaffected by the strain.[164] These results expand our understanding of how different molecular arrangements influence the thermal transport properties.

A different study investigated the thermal properties of single spider silk fibers.[165] The authors reported a surprisingly high value of more than $80\,\mathrm{mm^2\,s^{-1}}$, using an electrothermal technique. However, this result is most likely wrong. Fuente et al. measured identical fibers with lock-in thermography and found a much more reasonable value of $0.2\,\mathrm{mm^2\,s^{-1}}$.[166] This example demonstrates the difficulty of accurately determining the thermal properties of individual fibers.

In Chapter 7, I present a lock-in thermography setup to determine the longitudinal thermal diffusivity of single, micrometer-sized fibers. Automating the measurement and data analysis allowed me to investigate the influence of several experimental parameters. In a subsequent study, I employed the setup to characterize carbon fibers and relate their mechanical and thermal properties with composites.

2.3 Machine Learning

In science, we try to find models to predict the behavior of a system. The underlying models are often rigorous, analytical descriptions but finding complete explanations is sometimes hard or impossible. Statistical methods can help us to predict the behavior of complex systems. Machine learning aims to teach machines decision-making based on previous experiences. Machine learning is a large field of research, with whole institutes dedicating all of their resources only to this topic. There are several different approaches suitable to distinct problem classes. The most important categories are below.

Supervised learning This is probably the first approach that comes to mind when thinking about machine learning. In supervised learning, a large set of labeled training data is available. The data consists of features describing a system as the inputs and their associated properties as outputs. The goal is to train a system to use unseen features as the input and predict the correct output. Supervised training itself consists of two subclasses, classification and regression. In classification problems, the set of possible outputs is finite and small, while for regression, the output is continuous. Examples include image classification,[167] the prediction of nanoparticle size,[168] and more efficient quantum mechanics simulations.[169]

Unsupervised learning For these types of problems, only input data is available, and the correct output is unknown. The system tries to find patterns or structures inherent to the data. The final model will either predict the probability of the observation belonging to an underlying distribution (density estimation), assign a category to the input (clustering), or reduce the data to the most important features without losing information (dimensionality reduction). Examples are movie recommendation systems,[170] the detection of protein concentration,[171] and the identification of chemical properties influencing power conversion efficiency.[172]

Reinforcement learning Here, an agent is presented with a current state and selects an action based on it. Afterward, the agent is rewarded or penalized based on the action and presented with a new state based on his previous action. The target is to find an optimal policy to maximize the rewards. An early example includes teaching computers to play tic-tac-toe.[173] More recently, this kind of machine learning received a lot of attention for the creation of chatbots,[174] playing more difficult games like Go,[175] and enabling self-driving cars.[176]

During the remainder of this chapter, I will focus on artificial neural networks (ANNs) for supervised learning because they were the method of choice for the image analysis presented in Chapter 10.

In materials science, researchers have used ANNs for more than 30 years.[177,178] With the newly gained general interest in machine learning, the last few years saw a surge in publications. One possible application is the substitution of ab initio simulations. Initially, ANNs and quantum mechanics simulations had to be combined to generate accurate results. Still, they decreased the computational cost by orders of magnitude.[169] Later, ANNs could predict interatomic potentials with comparable accuracies to molecular dynamics and Monte Carlo simulations for specific systems on their own.[179] Today, the availability of larger datasets allows models to predict potentials between any atoms.[180] These systems will support the discovery of new materials by steering experiments to the most promising candidates.

Besides finding new materials, neural networks also revolutionize data analysis. Often, physical models are computationally complex and contain many free parameters. This makes finding the correct values difficult and renders some evaluations impossible. ANNs can find solutions to complex equations quickly. They have been successfully applied for both time and frequency domain thermoreflectance.[181,182]

Several recent publications utilized ANNs to detect temperature with different kinds of optical sensors. All of them focused on the analysis of spectra. Azad et al. investigated fiber-optic sensor systems based on simulated Brillouin light scattering.[183] These sensors allow the determination of temperature in an optical fiber with several kilometers in length.[184] A pump and probe beam interact with each other, and the signal reaches a maximum at a particular frequency. This Brillouin frequency shift is proportional to the temperature. Compared to identifying the maximum with traditional curve fitting, evaluation with an ANN is faster and more accurate.[183]

A second application of ANNs for temperature sensors are fiber Bragg gratings. Their reflectance spectrum depends on the temperature due to the thermal expansion of the fiber. However, the reflectance spectra of neighboring Bragg gratings overlap, especially in high-density sensors. Conventional data analysis techniques try to identify the peak positions from the overlapping spectra. ANNs can directly correlate the whole spectrum to the temperature.[185] This allows resolving temperature distributions along the fiber.

For temperature detection in even smaller systems, quantum dots can be employed. Their fluorescence signal depends on temperature.[186] By embedding quantum dots next to a microfluidic channel, the temperature can be monitored in real-time and with very high local precision. The analysis of the fluorescence spectra with an ANN leads to higher accuracy than traditional analysis with errors as low as 0.1 K in a small temperature regime and 0.4 K in a large regime between 100 K and 300 K.[187]

The given examples demonstrate the capabilities of ANNs. In the following paragraphs, I will describe their basic principles to outline how they achieve this.

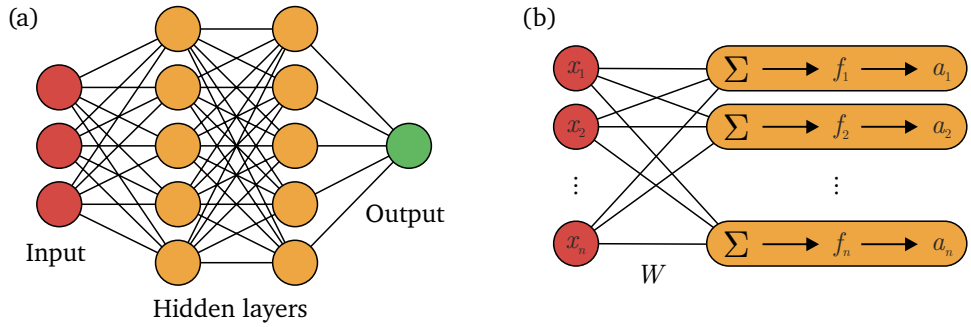

Figure 2.5.: Schematic view of an artificial neural network. (a) Overview of the whole network structure. (b) Detailed view of one layer.

ANNs imitate biological brains. Individual neurons are connected with each other and send outputs depending on the inputs they receive. In contrast to their biological counterpart, neurons in ANNs are organized in layers (Figure 2.5a). Each neuron receives inputs from all neurons in the previous layer and sends its output to all neurons in the following layer. Assuming a linear model, the output is simply the weighted sum of all inputs. Since linear models can only describe a fraction of phenomena, nonlinear models are usually employed. For these, a nonlinear activation function is applied to the weighted inputs to create the final output (Figure 2.5b). Mathematically, the input for a given layer l is a vector, X_l. It is the concatenation of the outputs, x, of the previous layer with N neurons,

$$X_l = \begin{pmatrix} x_1 \\ x_2 \\ \vdots \\ x_N \end{pmatrix}. \tag{2.6}$$

For each neuron n, the input is the product of X_l with a weight matrix, W_n. Finally, the activation function, f_n, is applied to obtain the output,

$$a_n = f_n(W_n \circ X_l). \tag{2.7}$$

The activation function can be any mathematical function. A common choice is the rectified linear unit because it is nonlinear and requires very little computational power.[188] Its definition is

$$\mathrm{ReLU}(z) = \max(0, z) = \begin{cases} 0 & \text{if } z < 0 \\ z & \text{otherwise} \end{cases} \tag{2.8}$$

Before we can train the model by updating the weights, we need to define our goal. Two criteria are important: (1) How well does our model describe the training data? (2) Can the model correctly predict the results for unseen data? Both of these questions are quantified with loss functions. Like activation functions, loss functions can be any mathematical function. Depending on the problem statement, several loss functions are commonly used. A simple example is the mean squared error (MSE). For a data set of size S, predicted outputs, a, and correct labels, y, the MSE is

$$\text{MSE} = \frac{1}{S}\sum_{i=1}^{S}(y_i - a_i)^2. \tag{2.9}$$

The MSE works well for continuous, numerical data, like in regression tasks. For classification problems, the MSE is ill-suited, and other loss functions are necessary. A common choice is the cross-entropy loss (CEL). Let us first consider only two distinct classes. The correct data labels are one if the feature belongs to the first class and zero otherwise. The predictions are a real number in the range [0, 1] and can be interpreted as the probability of a feature belonging to the first class. One way to define the best result is to maximize the probability that a label is predicted correctly by maximizing

$$\prod_{i=1}^{S}\begin{cases} a_i & \text{if } y_i = 1 \\ 1 - a_i & \text{otherwise} \end{cases} \tag{2.10}$$

$$= \prod_{i=1}^{S} a_i^{y_i}(1 - a_i)^{1-y_i}. \tag{2.11}$$

Taking the natural logarithm transforms the product into a computationally easier-to-manage sum,

$$\sum_{i=1}^{S} y_i \log(a_i) + (1 - y_i)\log(1 - a_i). \tag{2.12}$$

The sum can be extended to tasks with C classes via one-hot encoding, i.e., each label is a vector of dimension C where each component, $y^{(c)}$, is the probability of the feature set to belong to class c. By inverting the sign, the loss function will get smaller, the better the predictions are. This leads to the final equation for the cross-entropy loss,

$$\text{CEL} = -\sum_{i=1}^{S}\sum_{c=1}^{C} y_i^{(c)} \log\left(a_i^{(c)}\right) + \left(1 - y_i^{(c)}\right)\log\left(1 - a_i^{(c)}\right). \tag{2.13}$$

To ensure that our predictions are compatible with one-hot encoding, we need to transform our final output from arbitrary numbers to a probability density. We can do this by using the softmax function as the activation function of our final layer,

$$a = \text{softmax}(z) = \frac{1}{\sum_{n=1}^{N} \exp(z_n)} \begin{pmatrix} \exp(z_1) \\ \exp(z_2) \\ \vdots \\ \exp(z_N) \end{pmatrix}. \tag{2.14}$$

For the final layer, the number of neurons, N, must equal the number of classes, C. We use the exponential function instead of the simple sum because this will cancel the logarithm in Equation 2.13, making calculations easier.

We have defined how our network calculates outputs and how to score the results. The next step is to train the model. Training is similar to fitting data with a given function via gradient descent. In essence, we try to minimize the loss function. The initial weights are random numbers, and the model uses them to calculate the result for the first input vector. We use the predicted output to calculate the loss function with regard to the correct label. To optimize the weights, we take the partial derivative of the loss function regarding each weight. Depending on the sign and magnitude of the derivative, we update the individual labels to minimize the loss function, i.e., we follow the gradient of the loss function. Afterward, we proceed with the next feature vector and adjust the weights again. The whole procedure is repeated until the loss function reaches a target value or its change becomes insignificant. Ideally, we want to reach the global minimum of the function because at that point the weights are optimal for the given network architecture. In practice, the number of weights for typical ANNs can be millions of parameters.[167] This makes it very tedious to find the global minimum. Luckily, finding the optimal parameters is not necessary because local minima usually are sufficient for a good prediction quality.

To visualize gradient descent, we can imagine a surface in multi-dimensional space where the height corresponds to the magnitude of the loss function. The algorithm starts at an arbitrary point and follows the gradient towards the minimum (Figure 2.6). Effective and efficient learning depends on how accurate and fast we find the minimum. Several hyperparameters govern the learning process. The size of the steps is determined not only by the derivative but also by the learning rate. Training will be faster with higher learning rates, but too high rates can lead to uncontrolled behavior. Since we expect to get progressively closer to the minimum, the needed steps should decrease gradually. It can be useful to dynamically adjust the learning rate to prevent taking too large steps and skipping over minima. Two hyperparameters are used to change the

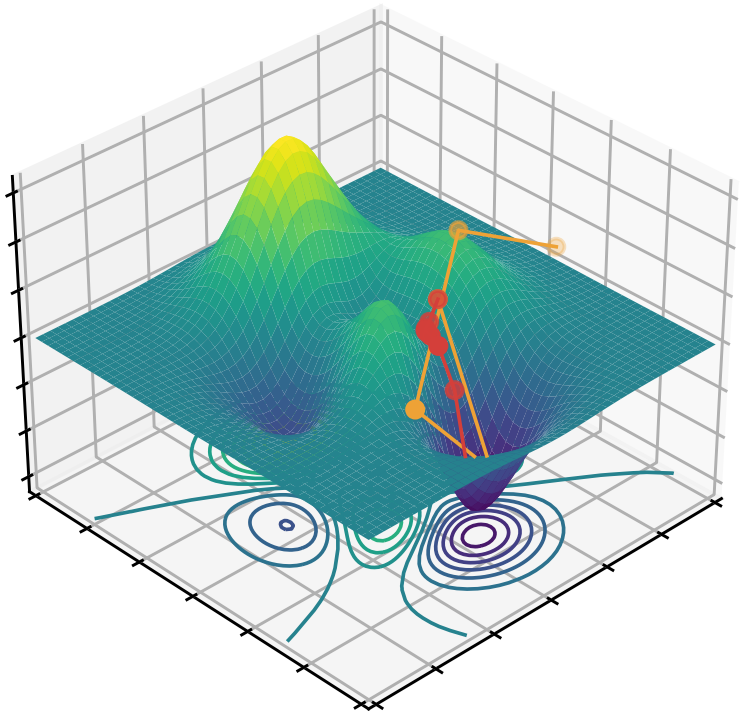

Figure 2.6.: Optimization path taken by gradient descent for a given loss function and different learning rates. A high rate (orange) can lead to uncontrolled behavior. Small rates (red) take longer to converge but can be more accurate.

learning rate during training, the weight decay and the momentum. The weight decay systematically decreases the learning rate over time and is independent of the current state of the network. The momentum uses the history of previous optimization steps to calculate the next step. By doing so, oscillations of gradient updates are reduced, and the path is smoothed.

Another technique to achieve better training results is to standardize the inputs. It prevents very large numbers that could lead to difficult optimization and, in the worst case, even overflow errors. One normalization method is to compute the z-score that transforms the feature vectors to have zero mean and unit variance by applying[189,190]

$$x_{\text{norm}} = \frac{x - \bar{x}}{\sigma}, \tag{2.15}$$

where $\bar{x}$ is the mean value and σ the standard deviation.

After we trained the network to achieve the best results on our training data, the final step is to investigate how well the model predicts unseen data. A second data set, the validation set, is necessary. The validation loss measures the generalization performance of the model. If the validation loss is significantly higher than the training loss, the model is overfitting the training data.

We can train the model with additional features to improve its generalization. However, adding training data is often not possible because acquiring the data is time-consuming. Another option to improve generalization is to introduce dropout layers. In these layers, a certain percentage of neurons is randomly deactivated. Thus, the model has less information available, and each node depends less on specific inputs. This has a comparable effect to adding random noise to the training data. Dropout layers are only used during training and deactivated for the final model execution. I used these regularization techniques in Chapter 10 to evaluate time-temperature integrators.

Outline

3

3.1 Synopsis

My research as a Ph.D. candidate focused on two main aspects: method development and data-driven analysis. By utilizing them individually or in combination, I contributed to the fields of thermal transport characterization and heat monitoring (Figure 3.1). Three main projects form the basis of my thesis. In the first project, I developed an indoor measurement instrument to characterize passive daytime cooling materials. In a follow-up study, the device is used to characterize the performance of a passive cooling system based on upcycled materials. My second project centers around lock-in thermography and fiber measurements in particular. I investigated in detail how different measurement parameters influence the evaluation results. Equipped with this knowledge, I studied carbon fibers and compared the thermal properties of pure fibers with their composites. My final project covered heat monitoring with the application of time-temperature integrators. After examining a gradient system, we applied the new insights to create an array-based sensor. I developed an artificial neural network to evaluate the data and predict time and temperature simultaneously.

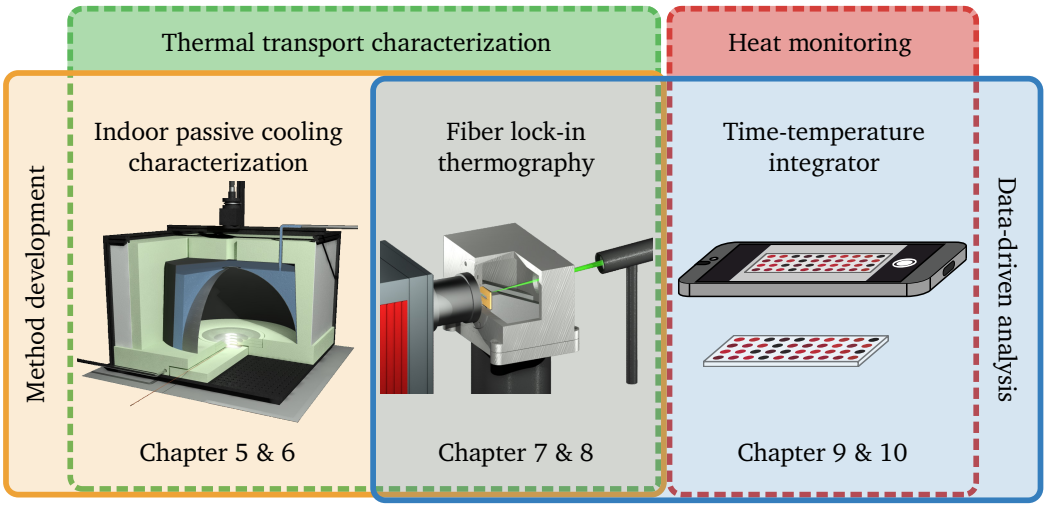

Figure 3.1.: Graphical overview of my main research projects. I developed methods and used advanced data analytics techniques to work on three projects contributing to the fields of thermal transport characterization and heat monitoring.

Heat management with passive cooling materials can contribute to lower power consumption while maintaining and even elevating our living conditions.[41,102,117] The cooling performance is usually characterized by outdoor measurements whose results depend on the climate and weather at the respective research facility. Therefore, comparing different materials measured at different times or locations is impossible, and reproducible characterization methods are needed.[122,123] In Chapter 5, my colleagues and I designed a measurement apparatus that mimics outdoor conditions inside a laboratory.

The sample is placed inside a closed chamber below a black-coated aluminum dome (Figure 3.2). Liquid nitrogen surrounds the dome and cools it to 80 K. The radiative heat transfer between the sample and the heat sink simulates radiation to outer space. Several layers of polyethylene foil prevent convection between the sample and the dome. In addition, a temperature-adjustable gas flow flushes this layered convection shield and thus enables setting the ambient temperature. Lastly, a solar simulator at the top of the dome illuminates the sample. The light intensity is adjustable and allows investigation of the influence of yet another environmental parameter on the cooling performance.

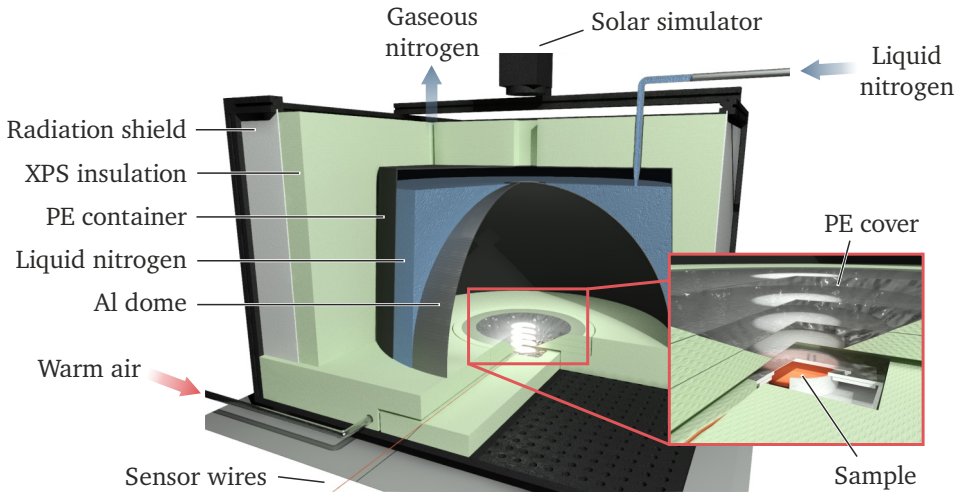

Figure 3.2.: Indoor characterization setup for daytime passive cooling materials.

Graphite is a material with a high emissivity across a large wavelength regime. It is a capable passive cooling material at night, but its cooling power is outweighed by solar absorption during the daytime. We used it as an example material to show both the temperature difference to ambient conditions and the cooling power with varying intensities of our solar simulator. In a second demonstration, we compared the theoretically expected temperature for a polydimethylsiloxane (PDMS) film with indoor measurements at different ambient temperatures. Although an offset is visible, the trends agree well (Figure 3.3). Overall, the results show that our setup is suited to investigate the impact of ambient conditions on the passive cooling performance of novel materials.

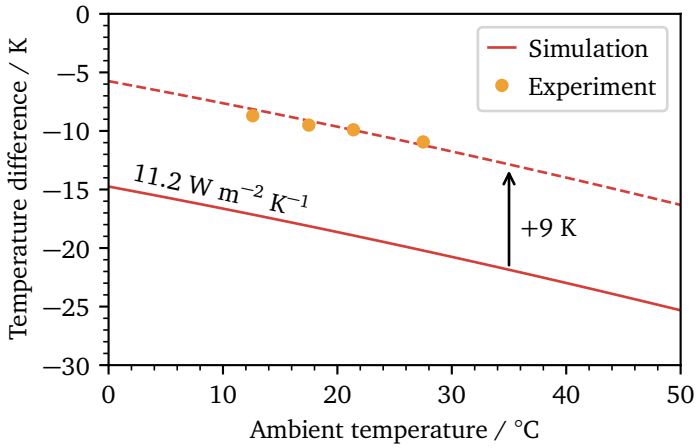

Figure 3.3.: Experimental and simulated temperature difference for a PDMS film at different ambient temperatures.

A validation experiment compares our indoor measurements to field tests and found a qualitative agreement. Quantitative differences are mainly attributed to the absence of atmospheric absorption in our indoor setup. A possible solution is to adjust the transmission of the convection shield to simulate atmospheric transmission. In our publication, we showed first measurements that allow us to distinguish the selectivity of PDMS samples.

In summary, we designed a measurement instrument for passive cooling characterization under controlled laboratory conditions. This enables the reproducible and, thus, comparable measurement of new material systems. The influence of environmental parameters, namely the illumination intensity and ambient temperature, can be investigated. Our setup can be the foundation of future research and material development.

In a follow-up study, we utilized our indoor setup to investigate the potential upcycling of aluminum-plastic laminates (APLs). Due to their excellent barrier properties, they are widely used for packaging applications in the food and medical industry.[191–194] However, the recycling of APLs is difficult, and the two most common post-consumer strategies are energetic recycling and the deposition in landfills.[195,196]

We investigated the reflectance spectrum in the visible range of APLs from packaging materials for three different goods: chips, coffee, and face masks. With their inherent high solar reflectance, APLs are a prime candidate for passive cooling applications. Besides a high solar reflectance, emission in the infrared regime is needed for passive cooling. The emissivity depends on the outermost material and its thickness. Fourier-transform infrared spectroscopy reveals different properties for the three APLs. While the chip bag has a relatively low emissivity, the bag of the face masks shows promising properties.

We measured all three pristine samples in our indoor setup to investigate the interplay between solar reflectance and infrared (IR) emission on the cooling performance.

All three samples showed a cooling effect in the dark, but with illumination, only the face mask bag kept a temperature below the ambient (Figure 3.4). With the ability to adjust the light intensity, we could determine at which intensity the solar absorption outweighed the cooling power of the APLs. This revealed a relative intensity of 50 % for the chip bag and 75 % for the coffee bag as the turnover points.

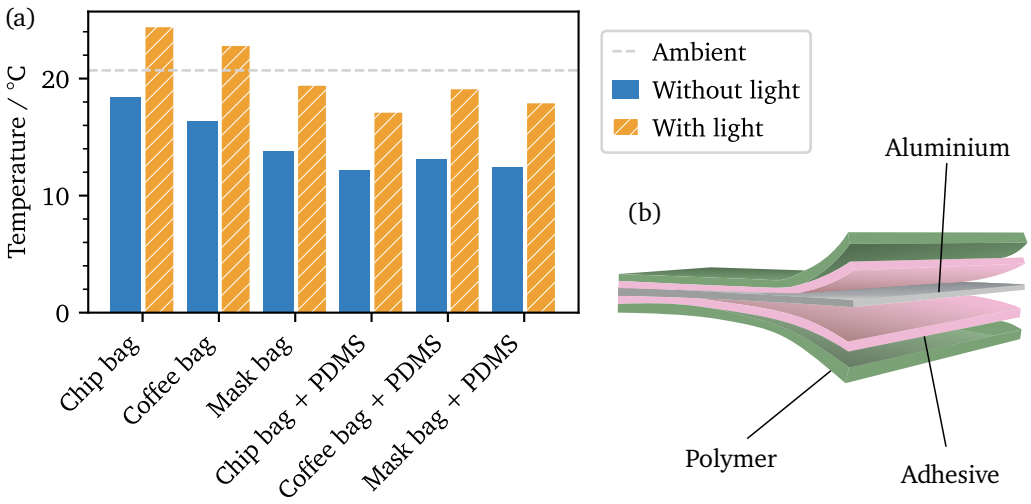

Figure 3.4.: (a) Cooling performance of different APLs with and without illumination as determined by our indoor setup. (b) Structure of an APL consisting of three different materials.

An additional layer with high IR emission can increase the cooling performance. By doctor blading PDMS on the APLs, the emission in the IR regime is significantly improved for all three samples. Consequently, the cooling performance increases, and all samples reach temperatures below ambient even under full illumination. In contrast to commonly reported materials, the fabrication of APL-based devices does not depend on sophisticated nano- or microstructuring. Thus, APLs have the potential to contribute to the widespread application of passive daytime cooling.

Calculating the yearly energy savings for a standard building highlights the potential benefits of our upcycling approach. We used hourly weather data to simulate the energy savings for a typical midrise apartment building at 1020 locations across the USA and 270 locations across China. Depending on the location, APL-based passive cooling foils can save up to 106 GJ per building and year if the foils are applied throughout the entire year (Figure 3.5). In cold regions, the passive cooling leads to negligible power savings and sometimes even to additional energy needed for heating. More sophisticated application of the APLs as retractable covers will increase power savings throughout all locations since the cooling can be stopped during cold seasons.

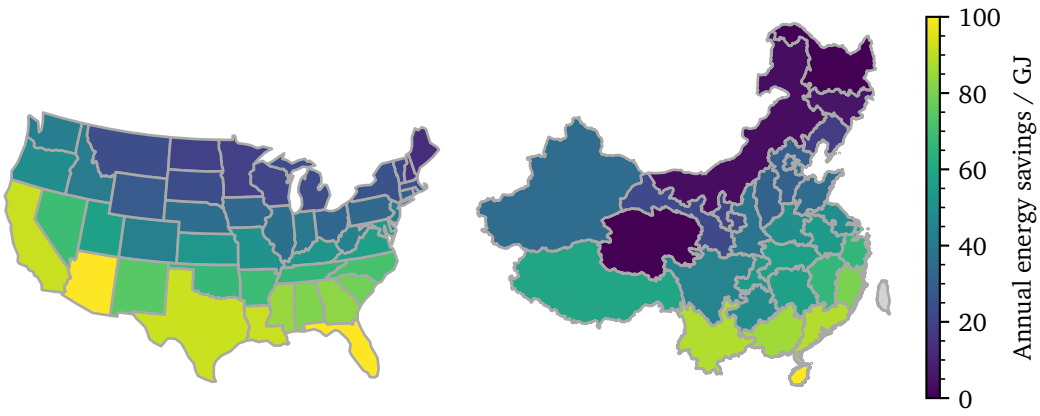

Figure 3.5.: Potential yearly energy savings for a typical apartment house located in different regions across the USA and China.

Passive daytime cooling centers around heat transport through radiation, while another transportation mode is conduction. Thermal conduction is essential for heat management involving insulation as well as heat spreading. Materials based on fibers are interesting due to their flexibility as fabrics or nonwovens and their added mechanical strength in composites. However, the characterization of single fibers is challenging, and measurement methods often rely on electrically conductive samples or complex measurement instruments. In Chapter 7, I present a lock-in thermography setup suitable to measure fibers with diameters ranging from several to hundreds of micrometers.

My colleagues and I designed an experimental setup with a sample holder facilitating the easy change of fibers (Figure 3.6). In addition, we developed software interfaces between the different instruments to enable automatic measurements once the laser is focused on the fiber. Previously, every experiment had to be started manually by changing parameters at various instruments. This approach was error-prone and time-consuming, rendering comprehensive measurement series unfeasible. Combining the semi-automatic measurement procedure with an almost fully automated data evaluation process, we could systematically investigate the influence of various experimental parameters on the resulting thermal diffusivities.

Before carrying out the experiments, we validated the measurement and evaluation with commonly found materials. The results agreed well with literature values. Subsequently, we investigated the influence of four experimental parameters: laser power, focal distance, optical magnification, and fiber alignment. During the validation, we could see a strong decreasing trend of the thermal diffusivity with increasing laser power. The trend was only apparent for some fibers, well reproducible, and most pronounced when including the amplitude for the evaluation (Figure 3.7). At higher powers, a plateau was visible, and one might erroneously conclude that this indicates the true value.

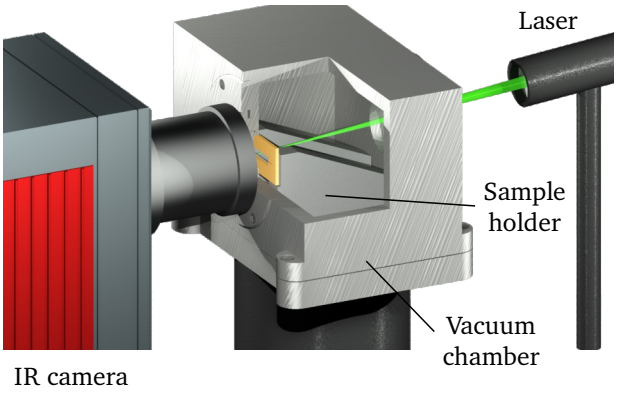

Figure 3.6.: Schematic image of the experimental setup for single fiber lock-in thermography.

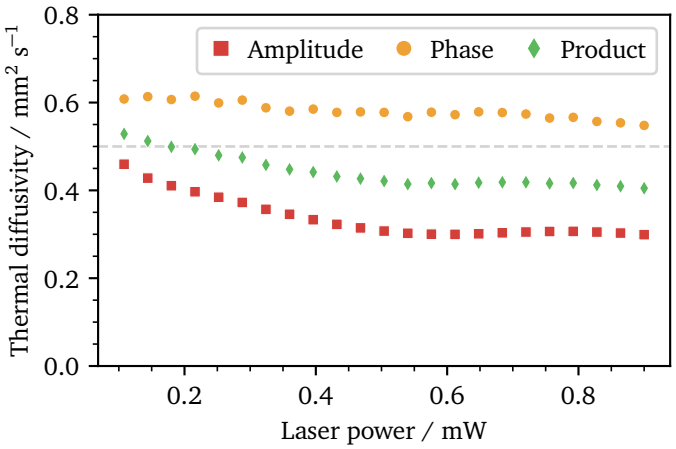

Figure 3.7.: Apparent thermal diffusivity of a single, 30 µm PEEK fiber measured at varying laser powers.

Further measurements and comparisons between fibers with small and large diameters revealed that, in fact, the diffusivity obtained at the smallest powers is correct. We attribute this power dependence to the high temperature fluctuations that thin fibers experience even if the laser power is below 1 mW. Our assumption is supported by the varying apparent thermal diffusivity with changing the focal distance where the same trend can be observed. The maximum linearized amplitude is an indicator of the periodic temperature fluctuation. Plotting it against the apparent thermal diffusivity for varying powers and focal distances reveals a good overlap (Figure 3.8).

Few previous publications measured single fibers via lock-in thermography.[144,154] Their setup consisted of a single optical system to investigate fibers that were in part smaller than the pixel resolution. This poses the question if these measurements are to be trusted and how the relative size of the fiber influences the results. We compared two lenses with a magnification of 1× and 8× resulting in pixel sizes of 10 µm and 1.3 µm, respectively.

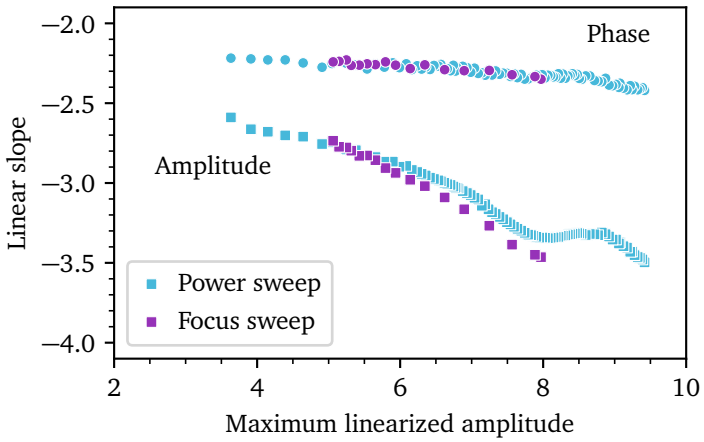

Figure 3.8.: Slope of the amplitude and phase of the same fiber at different laser powers and focal distances.

We found no difference between the thermal diffusivities calculated from the different measurements. Thus, we could verify previous studies.

Another interesting aspect of single fiber measurements is the fiber's alignment relative to the camera's pixel grid. Our evaluation software can automatically detect the orientation of the fiber and correct the data accordingly. For fibers with a size smaller than a single pixel, discrete jumps in the data are visible. They originate from the fiber traversing from one pixel line to the next. We could show that this seemingly unusable data leads to the same thermal diffusivity as a perfectly aligned fiber. Therefore, the tedious alignment of a fiber is not necessary when using our evaluation software.

In summary, we showed that lock-in thermography is a robust and powerful evaluation technique. With the software that we created and made publicly available, measurement series under different conditions are feasible, and the evaluation is highly automated. I applied single-fiber lock-in thermography in a project investigating carbon fibers.

Carbon fibers play an important role commercially, with applications ranging from thermal insulation over heat spreading to increasing mechanical stability.[53,197,198] Their thermal and mechanical properties depend on the source material and processing conditions. The influence of production temperature on morphology and mechanical strength has been investigated extensively.[199] However, no study regarding the impact on thermal properties has been conducted. In Chapter 8, we investigated four different kinds of carbon fibers with varying tensile moduli.

An initial morphological characterization showed that one type, HR40, has a higher crystallinity than the other investigated fibers. HR40 also possesses the highest mechanical

strength with a tensile modulus of 390 GPa. Without single fiber measurement techniques, the thermal conductivity of the carbon fibers can only be estimated. By varying the fiber content of laminates and assuming a linear mixture model, extrapolation leads to the best estimate of the single fiber conductivity (Figure 3.9a).

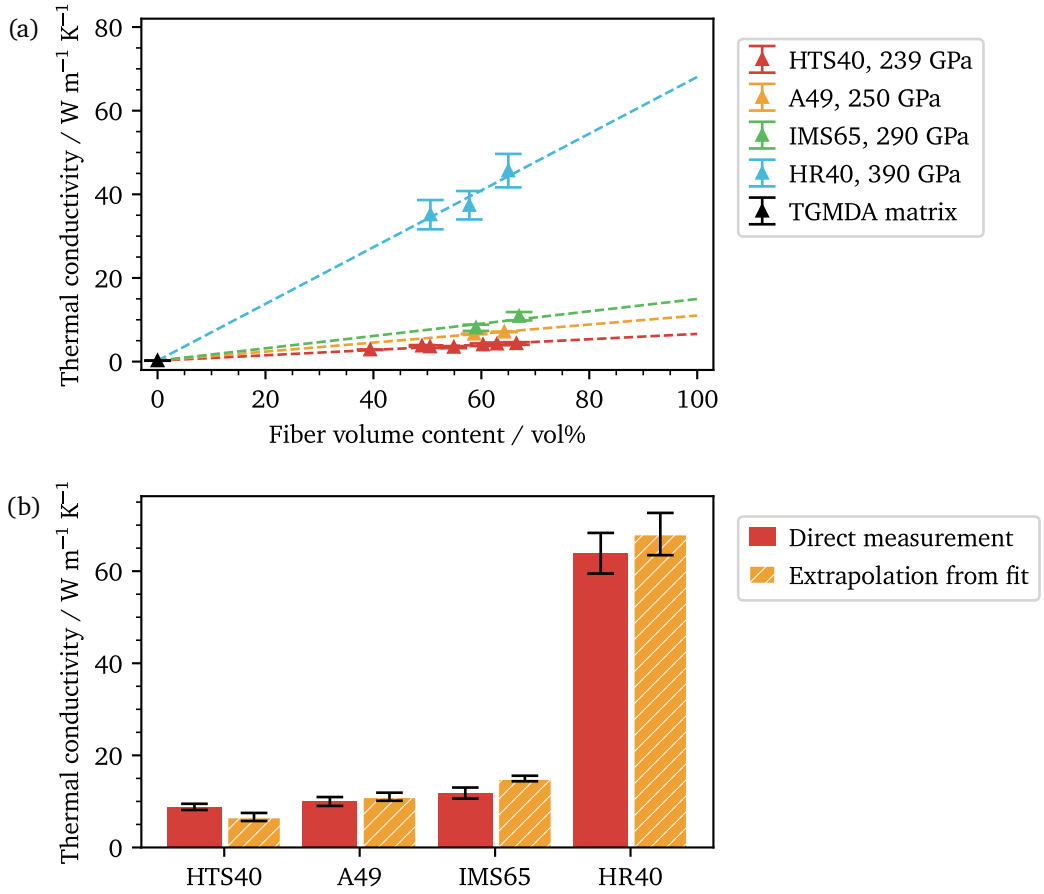

Figure 3.9.: (a) Thermal conductivity of carbon fiber laminates and extrapolation to the pure fiber. (b) Comparison between extrapolated and directly measured thermal conductivities.

In our study, we compared these results with single-fiber lock-in thermography. The results agree reasonably well, but the direct measurements show a thermal diffusivity in better agreement with the morphological investigation and mechanical properties (Figure 3.9b). This demonstrates that lock-in thermography is suitable for verifying models calculating the thermal properties of a composite based on the constituents' values, and potentially even leads to the development of improved models. Alternatively, the results for single fibers can be used with existing models to predict compound properties.

Predicting the thermal properties of fiber-incorporating materials allows the development of materials suited for heat management. As with passive daytime cooling, the aim is to keep the temperature in a well-defined range. Heat monitoring is needed to control if

these management strategies are successful or to inspect systems where management approaches are impractical or impossible. My final two publications introduce time-temperature integrators based on photonic systems.

The periodic arrangement of particles in colloidal crystals leads to pronounced structural colors. Changing colors due to changes in the lattice constant are clearly visible to the naked eye. This facilitates the application of colloidal crystals as optical sensors for a multitude of physical and chemical quantities, including temperature.[200–202] In Chapter 9, we introduced a new method to create a time-temperature integrating colloidal crystal based on a continuous gradient of a nanoparticle mixture. Integrators are irreversible sensors, i.e., they record the history of a system instead of the current state. Time-temperature integrators in particular record temperatures above a certain threshold and will not revert to their initial state even if the temperature falls again. This makes them ideal for indicating if a system stayed within the maximum allowed temperature regime and how substantial potential deviations were.

Colloidal crystals based on polymer particles lose their structural color at a sufficiently high temperature. This film-formation process starts around the glass transition temperature, T_g. The sintering kinetics are narrowly centered around T_g for systems based on a single polymer. This limits applications to a small range around a specific temperature. Mixing particles with identical sizes but different T_g changes the kinetics of the sintering kinetics. We created mixtures of low- and high-T_g particles and could show that a readout is possible in a 50 K range depending on the composition.

Infusion-withdrawal-coating allows the creation of a continuous gradient of binary nanoparticle compositions on a single substrate. The process starts with a flask filled with a dispersion of a single kind of particle. A syringe pump slowly removes the dispersion from the flask and thus leads to the formation of a colloidal crystal on a substrate inside the flask. At the same time, a second syringe pump introduces a second particle type (Figure 3.10). Due to the identical size and slow deposition, the different particles still form a colloidal crystal and show the same stopband position over the whole substrate. Using simple simulations and electron microscopy images, we proved that both particle types mix randomly and no phase segregation occurs. This allows the creation of a sample with a single stopband but varying film formation kinetics across its length.

Heating the gradient crystal to a given temperature leads to the film formation starting at the end where the majority of particles have a low T_g. The discoloration continuously moves along the gradient with longer sintering time (Figure 3.11). This allows us to access the full potential of the binary mixture and evaluate temperature events over a greater range than possible with a single particle type. While we based the evaluation of

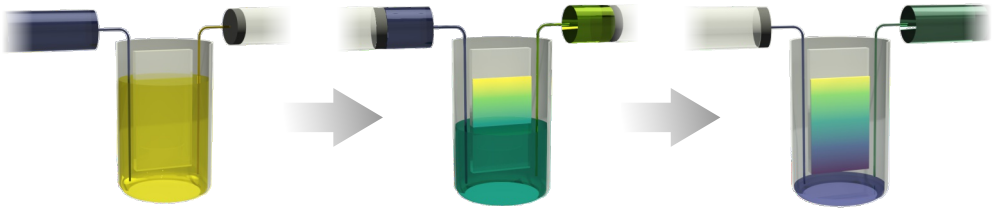

Figure 3.10.: Infusion-withdrawal-coating creates a colloidal crystal with a continuous gradient of the particle mixture. The color indicates the composition and is not related to the optical impression of the system.

the sintering kinetics on spectroscopic measurements, we gave a short outlook that the optical evaluation of colors based on microscopic images might be feasible.

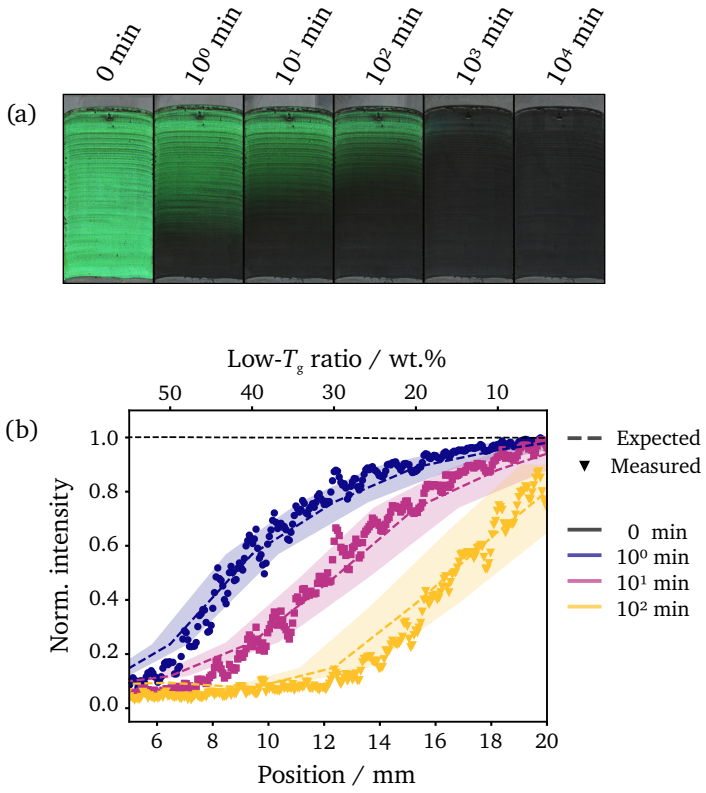

Figure 3.11.: (a) Microscopy images of the gradient colloidal crystal after different times. (b) Corresponding stopband intensity at different positions and times.

The gradient structures that we created were scientifically impressive but not suited for large-scale production. The infusion-withdrawal technique is very slow, and creating a single substrate takes several hours. Furthermore, the majority of the particle dispersion is neither deposited on the substrate nor suitable for reuse because of the mixture of particles now present in the dispersion. A solution to these shortcomings is printing as a commercially scalable process to create colloidal crystals.[203,204]

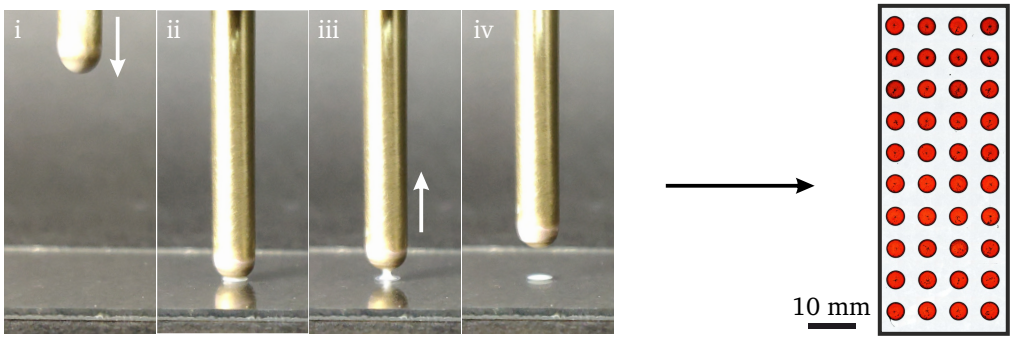

Figure 3.12.: Drop-casting of a single spot and final sample. Each spot has a distinct composition of nanoparticles.

For our next project, we created arrays of spots where each spot has a distinct mixture of particles with a different T_g. Our printing procedure is based on drop-casting single spots and utilizes a metal rod mounted to a 3-axis stage (Figure 3.12). The automation of the setup cut down the sample creation time by several hours. Thus, we could measure samples back-to-back. In addition to the increased fabrication speed, the array-printing procedure substantially decreased the required dispersion volume. Only a minuscule amount of dispersion is needed for each spot, and the remainder is not contaminated with other particles and is thus reusable. The last major advantage is the possibility of using dispersions with arbitrary compositions. Only two components with a monotonically changing ratio could be used for the gradient. In contrast, we used ternary mixtures of four different particle types for the array printing.

The gradient samples showed that image analysis is a feasible detection mechanism. Thus, we analyzed our arrays with an off-the-shelf smartphone camera. This has two major advantages: (1) We were able to characterize the intensity evolution of all spots simultaneously by capturing a series of images showing the whole substrate. (2) The evaluation of our sensors is widely accessible because no specialized hardware like spectrometers is needed.

Because our system shows a highly complex sintering behavior, an analytical description is not feasible. Instead, empirical or statistical methods should be used. Machine learning is a powerful method to predict the properties of unknown data and has been applied to different sensors in the past.[171,187,205,206] With the automated fabrication and simple characterization, our system is ideally suited for machine learning. We used supervised learning to train a model that can independently predict time and temperature.

We validated the trained model over the whole parameter space with a second data set containing samples at each temperature and time. The results resemble the training data very well and indicate the high generalizability of our model (Figure 3.13). While the predictions are not perfect, the validation across all possible parameters allows

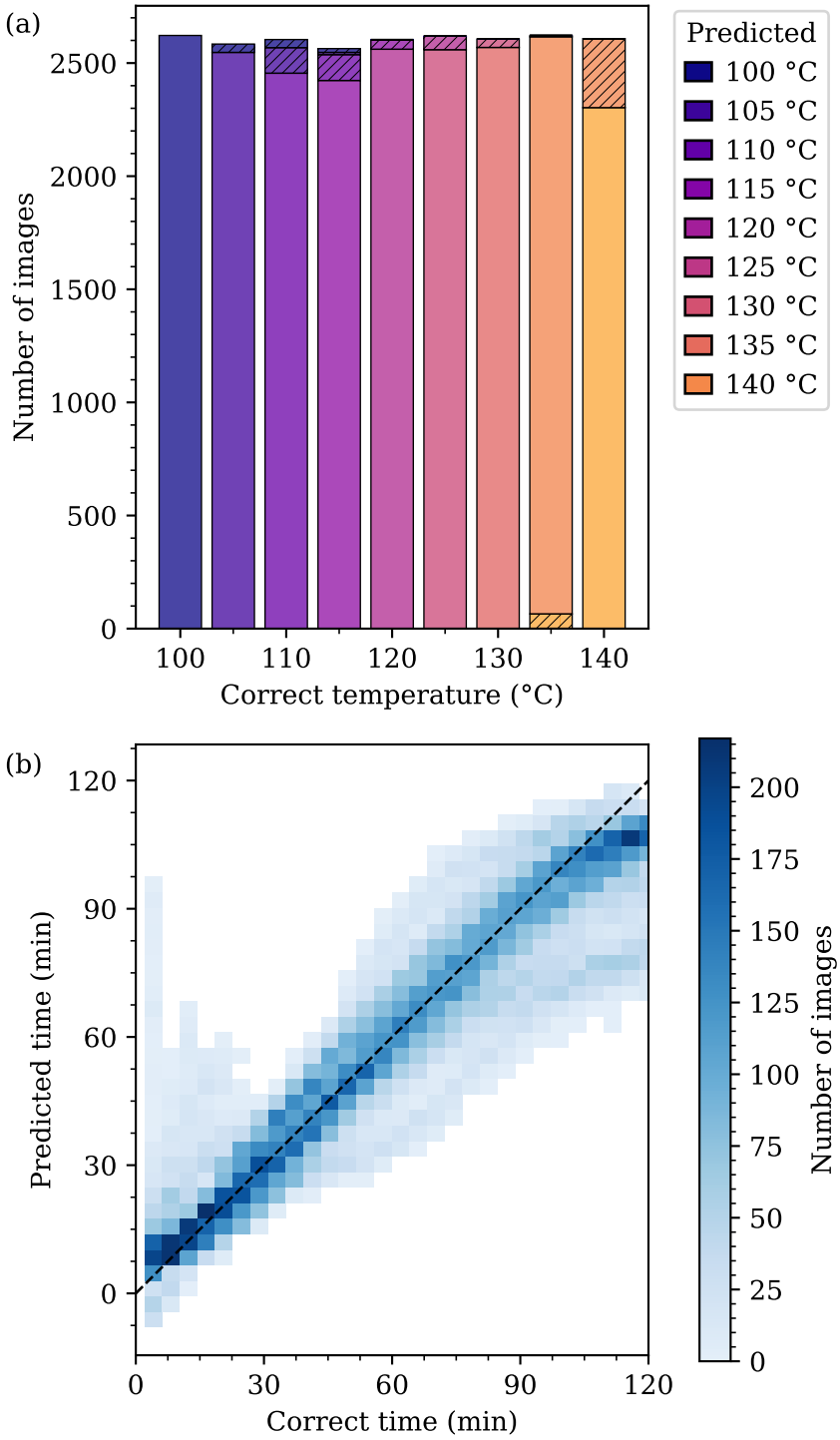

Figure 3.13.: (a) Temperature categorization and (b) time prediction of the validation data set of our array-based time-temperature integrator.

stating individual errors and shows where the system needs to be optimized. Only the two highest investigated temperatures show systematic errors. Their prediction quality can be further increased by adding additional particle types with higher T_g to the system. A higher resolution can be achieved by increasing the number of mixtures on the substrate.

The combination of automated fabrication and image analysis based on machine learning allows the application of a photonic system as temperature sensors. The readout is simple and can be done by non-specialists. Possible further optimizations of our system include the miniaturization of the individual spots to increase the information density. In addition, the fabrication can be sped up by either using a stamp or moving from drop-casting to inkjet printing.

In conclusion, I developed two measurement instruments to characterize thermal transport properties. The passive cooling measurement setup allows the reproducible comparison between materials aiming to reduce energy consumption for cooling. At the same time, the ability to easily characterize thin fibers allows designing materials with specific thermal properties. Both characterization methods facilitate the design of materials for heat management applications and will be the foundation for further research. In addition, my advanced data analytics skills allowed me to establish photonic systems as possible heat monitoring systems. They are needed to validate that the heat management strategies worked as expected.

In the next section, I briefly outline my contributions to the presented publications. Finally, the second part of my thesis contains all publications.

3.2 Contribution to Joint Publications

Chapter 5: A Tailored Indoor Setup for Reproducible Passive Daytime Cooling Characterization

Qimeng Song, Thomas Tran, Kai Herrmann, Tobias Lauster, Maximilian Breitenbach, and Markus Retsch

We published this article in *Cell Reports Physical Science*, **2022**, *3*(8), 100986.

Qimeng Song and I were leading the conceptualization and investigation. I designed the measurement apparatus, established the communication between hardware components, analyzed the data, and visualized the data. Qimeng Song used the setup to characterize the steady-state temperatures and cooling powers. Maximilian Breitenbach was involved in the investigation by supporting Qimeng Song with the measurements. Kai Herrmann contributed formal analysis and validation by doing the theoretical calculations. Tobias Lauster contributed validation and resources, creating samples. Markus Retsch led supervision, project administration, and funding acquisition. All authors contributed to the original draft writing.

Chapter 6: Upcycling chips-bags for passive daytime cooling

Qimeng Song, Thomas Tran, Kai Hermann, Holger Schmalz, and Markus Retsch

We submitted this article to a peer-reviewed journal.

Qimeng Song led the investigation and wrote the original draft. He created the samples and carried out the optical and thermal characterization. I visualized the data together with him. Additionally, I contributed to the investigation and formal analysis. I did the energy-saving simulations to show the potential impact of passive cooling materials in the United States and China. Kai Herrmann carried out investigations regarding the cooling power predictions by utilizing theoretical models. Holger Schmalz performed the Raman experiments and analyzed the resulting data. Markus Retsch supervised the project. All authors contributed to the editing of the draft.

Chapter 7: Characterizing the Thermal Diffusivity of Single, Micrometer-Sized Fibers via High-Resolution Lock-In Thermography

Thomas Tran, Charly Kodisch, Marius Schöttle, Nelson W. Pech-May, and Markus Retsch

We published this article in *The Journal of Physical Chemistry C*, **2022**, *126*(32), 14003–14010.

I lead the project, including conceptualization, investigation, software development, and formal analysis. I designed the vacuum chamber after discussions with Marius Schöttle and all remaining parts of the hardware setup. I developed all software parts, i.e., the automatic measurement and evaluation scripts. Charly Kodisch was involved in the investigation by preparing samples and measuring the fiber diameters. I measured all thermal diffusivities and visualized the data in cooperation with Marius Schöttle. Nelson W. Pech-May and Markus Retsch supervised the project. Markus Retsch acquired the necessary funds and provided resources. All authors contributed to the original draft writing.

Chapter 8: Relationship Between the Tensile Modulus and the Thermal Conductivity Perpendicular and in the Fiber Direction of PAN-Based Carbon Fibers

Simon Bard, Thomas Tran, Florian Schönl, Sabine Rosenfeldt, Martin Demleitner, Holger Ruckdäschel, Markus Retsch, and Volker Altstädt

We submitted this article to a peer-reviewed journal.

Simon Bard was responsible for the original draft and project administration. He created the composite materials and characterized them. I investigated the thermal properties of the single fibers and analyzed the resulting data. Sabine Rosenfeldt did the scattering experiments. I visualized the data for all experiments. Florian Schönl was responsible for the data curation and validation. All authors took part in the writing process.

Chapter 9: Time-Temperature Integrating Optical Sensors Based on Gradient Colloidal Crystals

Marius Schöttle, Thomas Tran, Tanja Feller, and Markus Retsch

We published this article in *Advanced Materials*, **2021**, *33*(40), 2101948.

Marius Schöttle led the conceptualization, investigation, formal analysis, and data curation. This included sample creation and characterization regarding optical properties and sintering behavior. He also wrote the original draft. I supported the investigation and formal analysis by creating software solutions for analyzing the time-dependent optical data. Tanja Feller was involved in the investigation by doing SEM measurements. Markus Retsch supervised the project and acquired the funds.

Chapter 10: Machine Learning Enabled Image Analysis of Time-Temperature Integrating Colloidal Arrays

Marius Schöttle, Thomas Tran, Harald Oberhofer, and Markus Retsch

Accepted for publication in *Advanced Science*.

Marius Schöttle and I were responsible for the conceptualization, investigation, formal analysis, and data curation. Marius Schöttle focused on chemical synthesis, sample creation, and traditional analysis, i.e., UV-Vis spectroscopy, SEM and DSC measurements. My main tasks were software development and image-based analysis. In detail, I prepared the image data for the neural network, trained and validated the network. Marius Schöttle and I wrote the original draft and visualized the data together. Harald Oberhofer and Markus Retsch supervised the project, reviewed and edited the manuscript.

References

4

[1] M. Campbell-Kelly, W. Aspray, N. Ensmenger, J. R. Yost, *Computer: A History of the Information Machine*, 3rd ed., Routledge, New York, **2018**.

[2] B. C. DeFelice, S. S. Mehta, S. Samra, et al., *Analytical Chemistry* **2017**, *89*, 3250–3255.

[3] J. C. Houck, L. A. DeNicola, *Astronomical Data Analysis Software and Systems Ix* **2000**, *216*, 591–594.

[4] B. Ravel, M. Newville, *Journal of Synchrotron Radiation* **2005**, *12*, 537–541.

[5] C. Simmler, J. G. Napolitano, J. B. McAlpine, S. N. Chen, G. F. Pauli, *Current Opinion in Biotechnology* **2014**, *25*, 51–59.

[6] W. F. Vranken, W. Boucher, T. J. Stevens, et al., *Proteins* **2005**, *59*, 687–696.

[7] L. Baptista, *ChemRxiv* **2021**, DOI `10.26434/chemrxiv.13656665.v1`.

[8] E. J. Menke, *Journal of Chemical Education* **2020**, *97*, 3899–3903.

[9] M. van Staveren, *Journal of Chemical Education* **2022**, *99*, 2604–2609.

[10] C. J. Weiss, *Journal of Chemical Education* **2020**, *98*, 489–494.

[11] R. A. Skilton, R. A. Bourne, Z. Amara, et al., *Nature Chemistry* **2015**, *7*, 1–5.

[12] B. Burger, P. M. Maffettone, V. V. Gusev, et al., *Nature* **2020**, *583*, 237–241.

[13] P. S. Gromski, J. M. Granda, L. Cronin, *Trends in Chemistry* **2020**, *2*, 4–12.

[14] B. P. MacLeod, F. G. L. Parlane, T. D. Morrissey, et al., *Science Advances* **2020**, *6*, eaaz8867.

[15] L. M. Roch, F. Hase, C. Kreisbeck, et al., *Science Robotics* **2018**, *3*, eaat5559.

[16] A. Salazar, *European Journal of Physics* **2003**, *24*, 351–358.

[17] R. A. Serway, J. W. Jewett, *Physics for Scientists and Engineers with Modern Physics*, 9th ed., Brooks/Cole, Boston, MA, **2014**.

[18] P. Medley, D. M. Weld, H. Miyake, D. E. Pritchard, W. Ketterle, *Physical Review Letters* **2011**, *106*, 195301.

[19] S. Braun, J. P. Ronzheimer, M. Schreiber, et al., *Science* **2013**, *339*, 52–55.

[20] R. Sahai, L.-Å. Nyman, *The Astrophysical Journal* **1997**, *487*, L155–L159.

[21] C. Deppner, W. Herr, M. Cornelius, et al., *Physical Review Letters* **2021**, *127*, 100401.

[22] R. Franz, G. Wiedemann, *Annalen der Physik und Chemie* **1853**, *165*, 497–531.

[23] J. B. J. Fourier, *Théorie Analytique de la Chaleur*, Cambridge University Press, Cambridge, **1822**.

[24] H. S. Carslaw, J. C. Jaeger, *Conduction of Heat in Solids*, 2nd ed., Oxford University Press, London, **1959**.

[25] *Handbook of Heat Transfer*, 3rd ed., McGraw-Hill, New York, NY, **1998**.

[26] *CRC Handbook of Chemistry and Physics*, CRC Press, Boca Raton, FL, **2005**.

[27] J. H. Lienhard IV, J. H. Lienhard V, *A Heat Transfer Textbook*, 5th ed., Version 5.10, Phlogiston Press, Cambridge, MA, **2020**.

[28] S. Basu, Z. M. Zhang, C. J. Fu, *International Journal of Energy Research* **2009**, *33*, 1203–1232.

[29] M. Planck, *The Theory of Heat radiation*, 2nd ed., Presley Blakiston, Son and Co., Philadelphia, PA, **1914**.

[30] H. Wang, P.-C. Chiang, Y. Cai, et al., *Sustainability* **2018**, *10*, 3331.

[31] B. Abu-Jdayil, A.-H. Mourad, W. Hittini, M. Hassan, S. Hameedi, *Construction and Building Materials* **2019**, *214*, 709–735.

[32] R. Arivazhagan, N. B. Geetha, P. Sivasamy, et al., *Materials Today: Proceedings* **2020**, *22*, 419–431.

[33] M. Chen, D. Pang, X. Chen, H. Yan, Y. Yang, *EcoMat* **2021**, *4*, e12153.

[34] L. Peng, B. Su, A. Yu, X. Jiang, *Cellulose* **2019**, *26*, 6415–6448.

[35] R. Hu, Y. Liu, S. Shin, et al., *Advanced Energy Materials* **2020**, *10*, 1903921.

[36] Z. Ma, D. Zhao, C. She, Y. Yang, R. Yang, *Materials Today Physics* **2021**, *20*, 100465.

[37] Y. Cui, M. Li, Y. Hu, *Journal of Materials Chemistry C* **2020**, *8*, 10568–10586.

[38] C.-P. Feng, L.-Y. Yang, J. Yang, et al., *Composites Communications* **2020**, *22*, 100528.

[39] X. Zhang, Z. Li, L. Luo, Y. Fan, Z. Du, *Energy* **2022**, *238*, 121652.

[40] D. Ürge-Vorsatz, R. Khosla, R. Bernhardt, et al., *Annual Review of Environment and Resources* **2020**, *45*, 227–269.

[41] S. Chatterjee, D. Ürge-Vorsatz, *Journal of Cleaner Production* **2021**, *318*, 128535.

[42] A. Moreno-Rangel, *Encyclopedia* **2020**, *1*, 20–29.

[43] B. P. Jelle, *Energy and Buildings* **2011**, *43*, 2549–2563.

[44] J. Liu, S. Ju, Y. Ding, R. Yang, *Applied Physics Letters* **2014**, *104*, 153110.

[45] D. Illera, J. Mesa, H. Gomez, H. Maury, *Coatings* **2018**, *8*, 345.

[46] K. Sakai, Y. Kobayashi, T. Saito, A. Isogai, *Scientific Reports* **2016**, *6*, 20434.

[47] S. E. Kalnæs, B. P. Jelle, *Applied Energy* **2014**, *116*, 355–375.

[48] D. Bosia, L. Savio, F. Thiebat, et al., *Energy Procedia* **2015**, *78*, 315–320.

[49] M. C. M. Parlato, S. M. C. Porto, *Sustainability* **2020**, *12*, 761.

[50] J. Schnieders, W. Feist, L. Rongen, *Energy and Buildings* **2015**, *105*, 71–87.

[51] J. K. Tong, X. Huang, S. V. Boriskina, et al., *ACS Photonics* **2015**, *2*, 769–778.

[52] S. Jiang, D. Miao, J. Xu, et al., *Journal of Materials Science: Materials in Electronics* **2016**, *28*, 3542–3547.

[53] Q. Gao, T. Lauster, B. A. F. Kopera, et al., *Advanced Functional Materials* **2021**, *32*, 2108808.

[54] S.-y. Zhao, J.-j. Li, X.-d. He, *International Journal of Thermophysics* **2014**, *35*, 90–104.

[55] S. Mandal, G. Song, *Journal of Industrial Textiles* **2016**, *47*, 622–639.

[56] D. Bhattacharjee, V. K. Kothari, *International Journal of Heat and Mass Transfer* **2009**, *52*, 2155–2160.

[57] Z. Wang, Y. Zhong, S. Wang, *Textile Research Journal* **2011**, *82*, 454–462.

[58] P. Lizák, J. Legerská, S. C. Mojumdar, *Journal of Thermal Analysis and Calorimetry* **2013**, *112*, 1013–1018.

[59] P. Lizák, A. Murárová, S. C. Mojumdar, *Journal of Thermal Analysis and Calorimetry* **2012**, *108*, 851–857.

[60] Y. Cui, H. Gong, Y. Wang, D. Li, H. Bai, *Advanced Materials* **2018**, *30*, 1870098.

[61] Y. Jiang, L. Zhang, H. Xu, Y. Zhong, Z. Mao, *Journal of Sol-Gel Science and Technology* **2017**, *82*, 370–379.

[62] J. Hu, H. Meng, G. Li, S. I. Ibekwe, *Smart Materials and Structures* **2012**, *21*, 053001.

[63] Y. Zhong, F. Zhang, M. Wang, et al., *Scientific Reports* **2017**, *7*, 44208.

[64] J. A. Lee, A. E. Aliev, J. S. Bykova, et al., *Advanced Materials* **2016**, *28*, 5038–5044.

[65] C. Yuan, B. Duan, L. Li, et al., *ACS Applied Materials and Interfaces* **2015**, *7*, 13000–13006.

[66] D. Suh, C. M. Moon, D. Kim, S. Baik, *Advanced Materials* **2016**, *28*, 7220–7227.

[67] J. S. Kang, H. Wu, Y. Hu, *Nano Letters* **2017**, *17*, 7507–7514.

[68] Y. Xu, D. Kraemer, B. Song, et al., *Nature Communications* **2019**, *10*, 1771.

[69] J. Jaguemont, L. Boulon, Y. Dube, F. Martel, *IEEE Transactions on Energy Conversion* **2016**, *31*, 1110–1120.

[70] S. Ma, M. Jiang, P. Tao, et al., *Progress in Natural Science: Materials International* **2018**, *28*, 653–666.

[71] J. R. Patel, M. K. Rathod, *Journal of Power Sources* **2020**, *480*, 228820.

[72] X. Zhang, X. Kong, G. Li, J. Li, *Energy* **2014**, *64*, 1092–1101.

[73] A. Wei, J. Qu, H. Qiu, C. Wang, G. Cao, *International Journal of Heat and Mass Transfer* **2019**, *135*, 746–760.

[74] Z. Y. Jiang, Z. G. Qu, *Applied Energy* **2019**, *242*, 378–392.

[75] P. R. N. Childs, J. R. Greenwood, C. A. Long, *Review of Scientific Instruments* **2000**, *71*, 2959–2978.

[76] L. H. J. Raijmakers, D. L. Danilov, R. A. Eichel, P. H. L. Notten, *Applied Energy* **2019**, *240*, 918–945.

[77] Q. Cai, Y.-C. Chen, C. Tsai, J. F. DeNatale, *Journal of Micromechanics and Microengineering* **2012**, *22*, 085012.

[78] A. Tong, *Sensor Review* **2001**, *21*, 193–198.

[79] F. P. García Márquez, A. M. Peco Chacón, *Renewable Energy* **2020**, *161*, 998–1010.

[80] Y. Kumar, J. Rahul, R. Harikrishnan, A. Mohan T P, P. Sreedharan, *Journal of Physics: Conference Series* **2021**, *2070*, 012242.

[81] S. Rajagopal, W. Arpan, S. Thomas, G. Gomare, R. Soangra, *ECS Transactions* **2022**, *107*, 9403–9416.

[82] J. F. C. B. Ramalho, L. D. Carlos, P. S. André, R. A. S. Ferreira, *Advanced Photonics Research* **2021**, *2*, 2000211.

[83] H. Forbes, T. Quested, C. O'Connor, UNEP Food Waste Index Report 2021, Report, United Nations Environment Programme, Nairobi, **2021**.

[84] Foodborne Disease Burden Epidemiology Reference Group, WHO Estimates of the Global Burden of Foodborne Diseases, Report, World Health Organization, Geneva, **2015**.

[85] M. Weston, S. Geng, R. Chandrawati, *Advanced Materials Technologies* **2021**, *6*, 2001242.

[86] P. S. Taoukis, T. P. Labuza, *Journal of Food Science* **1989**, *54*, 783–788.

[87] S. Wang, X. Liu, M. Yang, et al., *Packaging Technology and Science* **2015**, *28*, 839–867.

[88] T. Gao, Y. Tian, Z. Zhu, D.-W. Sun, *Trends in Food Science & Technology* **2020**, *99*, 311–322.

[89] T. F. M. Endoza, B. A. Welt, S. Otwell, et al., *Journal of Food Science* **2006**, *69*, FMS90–FMS96.

[90] *Organic Photochromic and Thermochromic Compounds*, 1st ed., (Eds.: J. C. Crano, R. J. Guglielmetti), Springer, New York, NY, **2002**.

[91] J. U. Kim, K. Ghafoor, J. Ahn, et al., *LWT - Food Science and Technology* **2016**, *67*, 143–150.

[92] P. Suppakul, D. Y. Kim, J. H. Yang, S. B. Lee, S. J. Lee, *Journal of Food Engineering* **2018**, *223*, 22–31.

[93] M. Ellouze, J. C. Augustin, *International Journal of Food Microbiology* **2010**, *138*, 119–29.

[94] C. Zhang, A. X. Yin, R. Jiang, et al., *ACS Nano* **2013**, *7*, 4561–4568.

[95] J. Wu, L. H. Cai, D. A. Weitz, *Advanced Materials* **2017**, *29*, 1702616.

[96] S. M. Kim, H. Jeon, S. H. Shin, et al., *Advanced Materials* **2018**, *30*, 1705145.

[97] S. Choi, Y. Eom, S. M. Kim, et al., *Advanced Materials* **2020**, *32*, 1907064.

[98] Y. Foelen, A. Schenning, *Advanced Science* **2022**, *9*, 2200399.

[99] S. Y. Lee, J. S. Lee, S. H. Kim, *Advanced Materials* **2019**, *31*, 1901398.

[100] D. Y. Youn, U. Jung, M. Naqi, et al., *ACS Applied Materials and Interfaces* **2018**, *10*, 44678–44685.

[101] L. H. J. Raijmakers, D. L. Danilov, R. A. Eichel, P. H. L. Notten, *Applied Energy* **2019**, *240*, 918–945.

[102] A. P. Raman, M. A. Anoma, L. Zhu, E. Rephaeli, S. Fan, *Nature* **2014**, *515*, 540–544.

[103] A. M. Rizwan, L. Y. C. Dennis, C. Liu, *Journal of Environmental Sciences* **2008**, *20*, 120–128.

[104] B. Tremeac, P. Bousquet, C. de Munck, et al., *Applied Energy* **2012**, *95*, 102–110.

[105] E. Rephaeli, A. Raman, S. Fan, *Nano Letters* **2013**, *13*, 1457–1461.

[106] A. K. Head (C. Scientific, I. R. O. CSIRO), *US Pat.*, US3043112A, **1962**.

[107] M. M. Hossain, B. Jia, M. Gu, *Advanced Optical Materials* **2015**, *3*, 1047–1051.

[108] L. Zhu, A. P. Raman, S. Fan, *Proceedings of the National Academy of Sciences* **2015**, *112*, 12282–12287.

[109] Z. Chen, L. Zhu, A. Raman, S. Fan, *Nature Communications* **2016**, *7*, 13729.

[110] S.-H. Wu, M. Chen, M. T. Barako, et al., *Optica* **2017**, *4*, 1390–1396.

[111] H. Zhang, K. C. S. Ly, X. Liu, et al., *Proceedings of the National Academy of Sciences* **2020**, *117*, 14657–14666.

[112] T. Wang, Y. Wu, L. Shi, et al., *Nature Communications* **2021**, *12*, 365.

[113] Y. Zhai, Y. Ma, S. N. David, et al., *Science* **2017**, *355*, 1062–1066.

[114] J. Mandal, Y. Fu, A. C. Overvig, et al., *Science* **2018**, *362*, 315–319.

[115] T. Li, Y. Zhai, S. He, et al., *Science* **2019**, *364*, 760–763.

[116] M. M. Hossain, M. Gu, *Advanced Science* **2016**, *3*, 1500360.

[117] Z. Li, Q. Chen, Y. Song, B. Zhu, J. Zhu, *Advanced Materials Technologies* **2020**, *5*, 1901007.

[118] B. Bhatia, A. Leroy, Y. Shen, et al., *Nature Communications* **2018**, *9*, 5001.

[119] R. Zhu, D. Hu, Z. Chen, et al., *Nano Letters* **2020**, *20*, 6974–6980.

[120] K. Herrmann, T. Lauster, Q. Song, M. Retsch, *Advanced Energy and Sustainability Research* **2021**, *3*, 2100166.

[121] B. H. Hamadani, B. Dougherty in *Semiconductor Materials for Solar Photovoltaic Cells*, (Eds.: M. Paranthaman, W. Wong-Ng, R. Bhattacharya), Springer Series in Materials Science, Springer, Cham, **2016**, Chapter Chapter 8, pp. 229–245.

[122] L. Zhou, H. Song, J. Liang, et al., *Nature Sustainability* **2019**, *2*, 718–724.

[123] G. Park, K. Roh, H. Kim, et al., *Advanced Materials Technologies* **2021**, *7*, 2101205.

[124] R. Y. M. Wong, C. Y. Tso, C. Y. H. Chao, *International Journal of Heat and Mass Transfer* **2021**, *174*, 121341.

[125] R. Y. M. Wong, C. Y. Tso, C. Y. H. Chao, *Renewable Energy* **2021**, *180*, 700–711.

[126] O. Breitenstein, W. Warta, M. C. Schubert, *Lock-in Thermography*, 3rd ed., Springer, **2018**.

[127] D. P. Neikirk, W. W. Lam, D. B. Rutledge, *International Journal of Infrared and Millimeter Waves* **1984**, *5*, 245–278.

[128] A. Einstein, *Annalen der Physik* **1905**, *322*, 132–148.

[129] P. Klipstein, D. Aronov, M. b. Ezra, et al., *Infrared Physics & Technology* **2013**, *59*, 172–181.

[130] E. Barreira, S. S. de Freitas, V. P. de Freitas, J. M. P. Q. Delgado in *Industrial and Technological Applications of Transport in Porous Materials*, (Ed.: J. M. P. Q. Delgado), Advanced Structured Materials, Springer, Berlin, Heidelberg, **2013**, Chapter Chapter 4, pp. 91–117.

[131] H. Sanati, D. Wood, Q. Sun, *Applied Sciences* **2018**, *8*, 2004.

[132] K. Khaksari, T. Nguyen, B. Hill, et al., *Journal of Medical Imaging* **2021**, *8*, 010901.

[133] S. Winograd, *Mathematics of Computation* **1978**, *32*, 175–199.

[134] W. C. Michels, N. L. Curtis, *Review of Scientific Instruments* **1941**, *12*, 444–447.

[135] R. D. Muir, S. Z. Sullivan, R. A. Oglesbee, G. J. Simpson, *Review of Scientific Instruments* **2014**, *85*, 033703.

[136] J. M. R. Weaver, *Journal of Vacuum Science & Technology B: Microelectronics and Nanometer Structures* **1991**, *9*, 1559–1561.

[137] Z. Pan, Z. Zhu, J. Wilcox, et al., *Advanced Electronic Materials* **2020**, *6*, 1901340.

[138] C. Meola, G. M. Carlomagno, A. Squillace, G. Giorleo, *Measurement Science and Technology* **2002**, *13*, 1583–1590.

[139] N. W. Pech-May, A. Oleaga, A. Mendioroz, et al., *Measurement Science and Technology* **2014**, *25*, 115601.

[140] R. Celorrio, A. J. Omella, N. W. Pech-May, et al., *Measurement Science and Technology* **2014**, *25*, 115602.

[141] O. Breitenstein, M. Langenkamp, F. Altmann, et al., *Review of Scientific Instruments* **2000**, *71*, 4155–4160.

[142] O. Breitenstein, J. P. Rakotoniaina, M. H. A. Rifai, *Progress in Photovoltaics: Research and Applications* **2003**, *11*, 515–526.

[143] A. J. Ångström, *The London Edinburgh and Dublin Philosophical Magazine and Journal of Science* **1863**, *25*, 130–142.

[144] A. Mendioroz, R. Fuente-Dacal, E. Apinaniz, A. Salazar, *Review of Scientific Instruments* **2009**, *80*, 074904.

[145] T. Ishizaki, H. Nagano, *International Journal of Thermophysics* **2014**, *36*, 2577–2589.

[146] N. W. Pech-May, A. Mendioroz, A. Salazar, *NDT & E International* **2016**, *77*, 28–34.

[147] P. W. Nolte, T. Malvisalo, F. Wagner, S. Schweizer, *Quantitative InfraRed Thermography Journal* **2017**, *14*, 218–225.

[148] L. Fabbri, P. Fenici, *Review of Scientific Instruments* **1995**, *66*, 3593–3600.

[149] B. Zhang, R. E. Imhof, *Applied Physics A Materials Science & Processing* **1996**, *62*, 323–334.

[150] J. Martan, N. Semmar, C. Boulmer-Leborgne, P. Plantin, E. Le Menn, *Nanoscale and Microscale Thermophysical Engineering* **2006**, *10*, 333–344.

[151] Á. Cifuentes, A. Mendioroz, A. Salazar, *International Journal of Thermal Sciences* **2017**, *121*, 305–312.

[152] A. Philipp, N. W. Pech-May, B. A. F. Kopera, et al., *Analytical Chemistry* **2019**, *91*, 8476–8483.

[153] C. Pradère, J. M. Goyhénèche, J. C. Batsale, S. Dilhaire, R. Pailler, *International Journal of Thermal Sciences* **2006**, *45*, 443–451.

[154] A. Salazar, A. Mendioroz, R. Fuente, R. Celorrio, *Journal of Applied Physics* **2010**, *107*, 043508.

[155] M. Oksanen, R. Scholz, L. Fabbri in *Review of Progress in Quantitative Nondestructive Evaluation, Vol. 17*, Springer, Boston, MA, **1998**, Chapter Chapter 157, pp. 1217–1221.

[156] Z. L. Wang, D. W. Tang, W. G. Zhang, *Journal of Physics D: Applied Physics* **2007**, *40*, 4686–4690.

[157] J. Guo, X. Wang, T. Wang, *Journal of Applied Physics* **2007**, *101*, 063537.

[158] C. Xing, T. Munro, C. Jensen, et al., *Measurement Science and Technology* **2014**, *25*, 115604.

[159] X. Wang, V. Ho, R. A. Segalman, D. G. Cahill, *Macromolecules* **2013**, *46*, 4937–4943.

[160] X. Ji, S. Matsuo, N. R. Sottos, D. G. Cahill, *Carbon* **2022**, *197*, 1–9.

[161] J. Liu, H. Wang, Y. Hu, W. Ma, X. Zhang, *Review of Scientific Instruments* **2015**, *86*, 014901.

[162] J. Liu, H. Liu, Y. Hu, X. Zhang, *International Journal of Heat and Mass Transfer* **2019**, *135*, 511–516.

[163] Y. Xie, T. Wang, B. Zhu, et al., *Carbon* **2018**, *139*, 445–458.

[164] Y. Lu, J. Liu, X. Xie, D. G. Cahill, *ACS Macro Letters* **2016**, *5*, 646–650.

[165] X. Huang, G. Liu, X. Wang, *Advanced Materials* **2012**, *24*, 1482–1486.

[166] R. Fuente, A. Mendioroz, A. Salazar, *Materials Letters* **2014**, *114*, 1–3.

[167] S. Xie, R. Girshick, P. Dollar, Z. Tu, K. He in Proceedings of the IEEE Conference on Computer Vision and Pattern Recognition (CVPR), **2017**, pp. 1492–1500.

[168] J. Kimmig, T. Schuett, A. Vollrath, S. Zechel, U. S. Schubert, *Advanced Science* **2021**, *8*, e2102429.

[169] L. Shen, J. Wu, W. Yang, *Journal of Chemical Theory and Computation* **2016**, *12*, 4934–4946.

[170] J. Bennett, S. Lanning in Proceedings of KDD Cup and Workshop, **2007**, p. 35.

[171] S. Pandit, T. Banerjee, I. Srivastava, S. Nie, D. Pan, *ACS Sensors* **2019**, *4*, 2730–2737.

[172] Y. Huang, J. Zhang, E. S. Jiang, et al., *The Journal of Physical Chemistry C* **2020**, *124*, 12871–12882.

[173] D. Michie, *The Computer Journal* **1963**, *6*, 232–236.

[174] H. Cuayáhuitl, D. Lee, S. Ryu, et al., *Neurocomputing* **2019**, *366*, 118–130.

[175] D. Silver, J. Schrittwieser, K. Simonyan, et al., *Nature* **2017**, *550*, 354–359.

[176] B. R. Kiran, I. Sobh, V. Talpaert, et al., *IEEE Transactions on Intelligent Transportation Systems* **2022**, *23*, 4909–4926.

[177] M. Tusar, J. Zupan, J. Gasteiger, *Journal de Chimie Physique* **1992**, *89*, 1517–1529.

[178] B. G. Sumpter, C. Getino, D. W. Noid, *The Journal of Chemical Physics* **1992**, *97*, 293–306.

[179] J. Weinreich, A. Römer, M. L. Paleico, J. Behler, *The Journal of Physical Chemistry C* **2020**, *124*, 12682–12695.

[180] C. Chen, S. P. Ong, *Nature Computational Science* **2022**, *2*, 718–728.

[181] W. Shen, D. Vaca, S. Kumar, *Nanoscale and Microscale Thermophysical Engineering* **2020**, *24*, 138–149.

[182] Y. Pang, P. Jiang, R. Yang, *Journal of Applied Physics* **2021**, *130*, 084901.

[183] A. K. Azad, L. Wang, N. Guo, C. Lu, H. Y. Tam, *Electronics Letters* **2015**, *51*, 1578–1580.

[184] M. A. Soto, G. Bolognini, F. Di Pasquale, L. Thevenaz, *Optics Letters* **2010**, *35*, 259–61.

[185] A. Kokhanovskiy, N. Shabalov, A. Dostovalov, A. Wolf, *Sensors* **2021**, *21*, 6188.

[186] W. Liu, S. Xu, Z. Li, et al., *Chemistry of Materials* **2016**, *28*, 5426–5431.

[187] C. Lewis, J. W. Erikson, D. A. Sanchez, et al., *ACS Applied Nano Materials* **2020**, *3*, 4045–4053.

[188] T. E. H. Allen in *Machine Learning in Chemistry*, (Ed.: H. M. Cartwright), Theoretical and Computational Chemistry Series, The Royal Society of Chemistry, Croydon, **2020**, Chapter Chapter 2, pp. 16–36.

[189] M. Kubat, *An Introduction to Machine Learning*, 3rd ed., Springer, Coral Gables, FL, **2021**.

[190] S. Vishnoi, H. Matre, P. Garg, S. K. Pandey, *Chemical Biology & Drug Design* **2020**, *96*, 902–920.

[191] M. Lamberti, F. Escher, *Food Reviews International* **2007**, *23*, 407–433.

[192] *Food Packaging Materials: Testing & Quality Assurance*, (Eds.: P. Singh, A. A. Wani, H.-C. Langowski), CRC Press, Boca Raton, FL, **2017**.

[193] J. Patel, A. Parhi, S. Al-Ghamdi, et al., *Journal of Food Science* **2020**, *85*, 2843–2851.

[194] F. Ali, I. Khan in *Essentials of Industrial Pharmacy*, AAPS Advances in the Pharmaceutical Sciences Series, Springer, Cham, **2022**, Chapter Chapter 5, pp. 55–66.

[195] O. Horodytska, F. J. Valdes, A. Fullana, *Waste Management* **2018**, *77*, 413–425.

[196] A. S. Bauer, M. Tacker, I. Uysal-Unalan, et al., *Foods* **2021**, *10*, 2702.

[197] Q.-Q. Kong, Z. Liu, J.-G. Gao, et al., *Advanced Functional Materials* **2014**, *24*, 4222–4228.

[198] T. K. Das, P. Ghosh, N. C. Das, *Advanced Composites and Hybrid Materials* **2019**, *2*, 214–233.

[199] X. Qin, Y. Lu, H. Xiao, Y. Wen, T. Yu, *Carbon* **2012**, *50*, 4459–4469.

[200] J. H. Holtz, S. A. Asher, *Nature* **1997**, *389*, 829–832.

[201] K. Ueno, K. Matsubara, M. Watanabe, Y. Takeoka, *Advanced Materials* **2007**, *19*, 2807–2812.

[202] M. Tsuchiya, Y. Kurashina, H. Onoe, *Scientific Reports* **2019**, *9*, 17059.

[203] K. Burkert, T. Neumann, J. Wang, et al., *Langmuir* **2007**, *23*, 3478–3484.

[204] L. Bai, Z. Xie, W. Wang, et al., *ACS Nano* **2014**, *8*, 11094–11100.

[205] Y. Zhang, L. Yu, Z. Hu, et al., *Journal of Lightwave Technology* **2021**, *39*, 1537–1543.

[206] A. Döring, A. L. Rogach, *ACS Applied Nano Materials* **2022**, *5*, 11208–11218.

Part II

Publications

5

A Tailored Indoor Setup for Reproducible Passive Daytime Cooling Characterization

Qimeng Song,[1, 3] Thomas Tran,[1, 3] Kai Herrmann,[1] Tobias Lauster,[1] Maximilian Breitenbach,[1] and Markus Retsch[1, 2, 4, *]

1 Department of Chemistry, Physical Chemistry I, University of Bayreuth, 95447 Bayreuth, Germany
2 Bavarian Polymer Institute, Bayreuth Center for Colloids and Interfaces, and Bavarian Center for Battery Technology (BayBatt), University of Bayreuth, 95447 Bayreuth, Germany
3 These authors contributed equally to the work
4 Lead contact
* Corresponding author

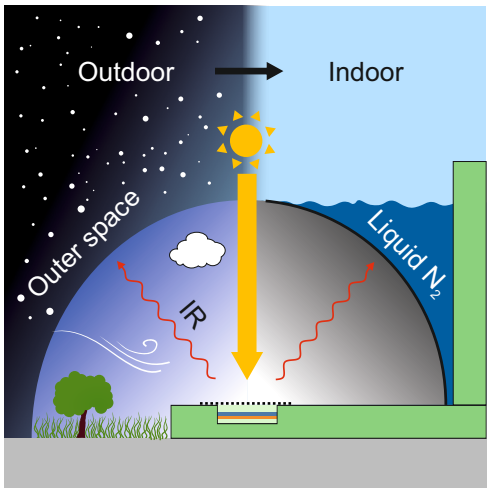

Published in *Cell Reports Physical Science*, **2022**, *3*(8), 100986.

5.1 Summary

Passive daytime cooling materials can lower global energy consumption owing to their autonomous cooling capability. Although a significant number of passive cooling materials have been developed recently, their performance characterization is still challenging. Field tests experience high variability due to uncontrollable changes in environmental conditions. Here, we design an indoor setup to characterize the performance of passive cooling materials reproducibly and independently of weather and season. Outdoor measurement conditions are approximated using a liquid-nitrogen-cooled aluminum dome, a solar simulator, and a wavelength-selective inverse sky-window filter. In contrast to outdoor measurements, the results of various reference materials show remarkable precision and repeatability. Additionally, the impact of solar light intensity and temperature on the passive cooling performance can be experimentally investigated. Our setup is a first step in the development of a standardized test method to bring accuracy, reproducibility, and comparability to the emerging field of passive cooling materials.

5.2 Introduction

Passive daytime cooling has emerged as a strong candidate to alleviate the global energy demand for cooling.[1,2] It conveys heat from a material to outer space through the atmospheric window (8–13 µm) without external energy consumption. For an ideal daytime passive cooling performance, low absorption in the solar range (0.3–2.5 µm) and high emission over the mid-infrared (MIR) region is stringently required. In the last few years, advanced fabrication techniques have led to various novel materials, including photonically structured materials,[3–5] hybrid composites,[6–9] highly porous materials,[10–13] and hierarchically structured materials.[14–17] These classes of materials promote the development of devices for daytime passive cooling applications.

Two essential techniques are usually used to evaluate a material's passive cooling performance: optical spectroscopy and field testing.[2,18] The former determines the spectral absorption of a material in both the solar and MIR regions. Utilizing a theoretical model based on energy balance considerations, the net passive cooling power of a material can be calculated. Li et al. introduced a simple figure of merit to fairly assess the performance of distinct cooling materials based on their optical properties.[19] However, the comprehensive optical properties, including angle and temperature dependence, of a material, are rather hard to access, especially for complex materials, e.g., multilayer composites, self-adaptive metamaterials,[20,21] and materials with irregular surface topography, making it difficult to achieve a precise comparison.

During field testing, the steady-state temperature of a sample and its cooling power at ambient temperature are obtained. However, outdoor measurements are impressionable and uncontrollable, and the outcome strongly depends on measurement conditions,[22,23] e.g., geographical location, solar intensity, ambient temperature, humidity, wind speed, and air pressure. The uncontrollable and unsteady atmospheric conditions limit the comprehensive characterization of passive cooling materials firstly, and replication of the measurement results secondly. Due to this challenge, different materials cannot be compared reasonably. Therefore, a comparable and standardized test method is urgently required to push the development of passive daytime cooling materials forward. In contrast to outdoor environments, an indoor setup is independent of weather conditions and provides a stable and controllable environment for passive cooling characterization. A simple indoor setup for passive cooling characterization was reported by Zhou et al.[24] By using liquid-nitrogen-cooled black aluminum foil as a heat sink, the nighttime passive cooling behavior of a PDMS film was imitated. However, their indoor setup did not include a light source. The characterization was thus limited to nighttime conditions. A similar setup was also constructed by Park et al. in a glovebox.[25] With applying a solar simulator, the characterization can be performed in the presence of solar light. Very recently, a hybrid refrigerative thermoelectric cooling system was built by Wong et al. to simulate the radiative cooling effect artificially under controlled conditions.[26] Their sophisticated setup achieved a reasonable accuracy (deviation of 17 %–33 %). Still, a repeatable and comprehensive characterization method for passive daytime cooling materials remains an enormous challenge.

In this work, we present a tailored indoor setup for comprehensively characterizing the performance of daytime passive cooling materials. The setup allows measurements with and without illumination of the sample, analogous to daytime and nighttime field testing, respectively. It consists of a liquid-nitrogen-cooled, hemispherical aluminum (Al) dome as a heat sink and an air mass (AM) 1.5 solar simulator as a light source. To the best of our knowledge, our method is the first indoor setup for the experimental characterization of passive cooling materials in both nighttime and daytime, with outstanding repeatability showcased for three distinct materials, namely, a silver (Ag) mirror, a polydimethylsiloxane (PDMS) film, and a graphite coating. Furthermore, our setup can experimentally determine the impact of environmental changes, such as the ambient temperature or solar irradiation intensity, on the material's cooling performance. Such a parametric investigation is unfeasible with field tests due to uncontrollable environmental conditions. Lastly, our indoor setup is robust and simple to build, opening a promising pathway to quantitatively compare passive cooling materials designed in different research groups.

5.3 Results and Discussion

5.3.1 Indoor setup design

The most important aspects of passive cooling field testing that a feasible indoor setup must capture are (1) radiative heat transfer from the sample to outer space; (2) illumination of the sample by the sun; and (3) measurement at moderate temperatures. The realization of these key measurement aspects can each be attributed to distinct parts of the proposed setup.

Radiative heat transfer

The samples emit hemispherically to outer space, which acts as a heat sink, with a temperature of ∼3 K. To imitate this behavior, we utilize a hemispherical Al dome with a diameter of 60 cm. The high thermal diffusivity of Al ensures a homogeneous temperature distribution across the entire surface. The inner surface of the dome was coated with graphite to enhance its broadband absorption, thus resembling space as a heat sink for radiative heat transport. A polyethylene (PE) container is imposed on the hemisphere, creating a reservoir around the Al dome. Liquid nitrogen is filled inside this reservoir and cools the dome down to ∼80 K. The entire setup is thermally insulated using extruded polystyrene foam (XPS, Styrodur, BASF) with a thickness of 8 cm to prevent cold loss. A schematic of the indoor setup is shown in Figure 5.1. Detailed dimensions and a photograph are in Figure 5.S1. During the measurement, a small steady influx of liquid nitrogen compensates for all remaining heat losses to the environment. The sample is placed in a homemade measurement cell constructed by XPS under the center of the dome. Low-density polyethylene (LDPE) foils were applied above the sample to prevent convection.

Solar illumination

The average solar irradiation is generally presented by the AM 1.5 spectrum with a power of ∼1000 W m^{-2}, which is well established in the characterization of photovoltaic devices.[18] In the laboratory environment, a solar simulator was placed directly on the top of the dome to provide AM 1.5 solar light with an illumination area of 5 × 5 cm^2. The hole in the dome accounts for 0.8 % of the total area seen by the sample and is thus negligible. The similarity between the light of the solar simulator and the sun is shown in Figure 5.S2. The light hits the sample at an angle of 8° to prevent back reflection into the solar simulator.

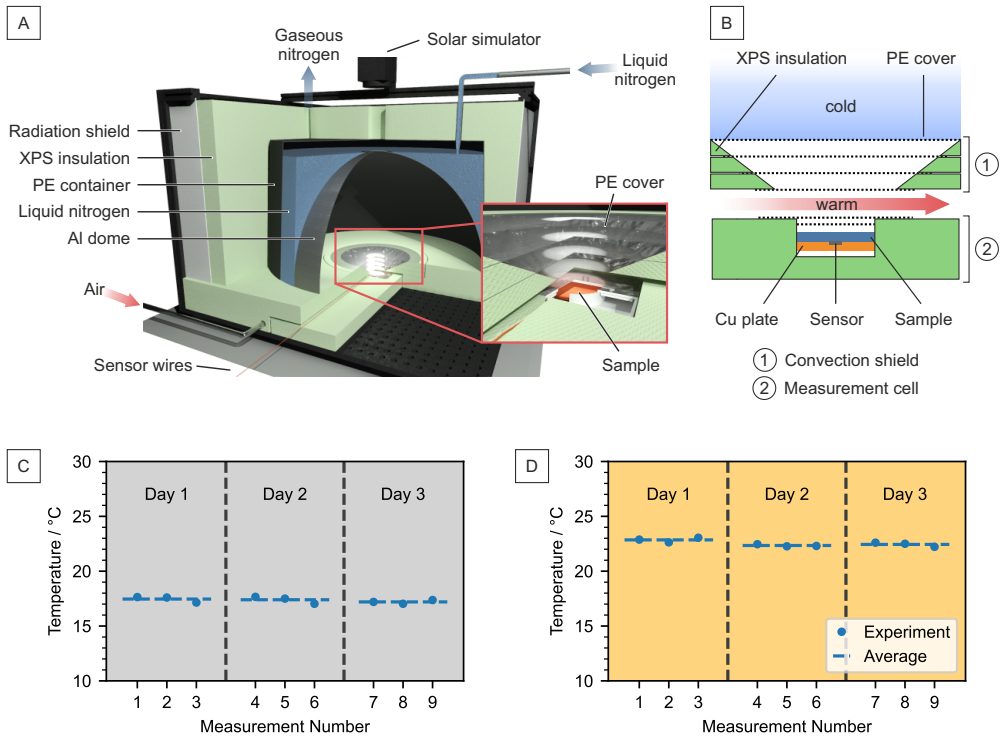

Figure 5.1.: Indoor setup design and repeatability. (A and B) Schematic of the indoor setup for characterizing passive daytime cooling. A liquid-nitrogen-cooled aluminum dome imitates outer space, while a solar simulator illuminates the sample. A convection shield in combination with XPS minimizes non-radiative heat transfer between the dome and sample. Detailed schematic of the sample holder (B). A warm gas flow between the convection shield and the sample holder allows controlling the temperature inside the measurement cell. (C and D) The steady-state temperature of an Ag mirror measured (C) w/o and (D) w/ solar light. Results show outstanding precision that cannot be achieved with outdoor measurements.

Sample temperature

The most challenging part of the indoor setup is to keep the sample at moderate temperatures while cooling the dome down to liquid nitrogen temperatures. The significant temperature difference across the short distance between the cooled dome and the sample holder naturally leads not only to the desired radiative heat transfer but also to undesired convection and conduction. Conduction is minimized by employing XPS insulation in combination with air gaps between the sample and the dome. Several LDPE foils (thickness ~15 µm), possessing a high solar and IR transparency, act as a convection barrier between the sample and the cold air inside the dome. These PE layers reduce the solar radiation intensity in the sample by 25 %, due to absorption, reflection, and scattering. Furthermore, the reduction of the transmittance is angle-dependent (Figure 5.S3). Previous reports showed that angles $< 60°$ have a dominant contribution to the emission of passive cooling materials.[4,27,28] Therefore, the convection shield made from XPS and LDPE has a cone-shaped inner part, with a zenith angle of 60° to reduce the thermal

loss (conduction and convection) area while marginally blocking the pathway of thermal radiation from the sample. Conductive heat transport from each gas compartment to the next would eventually cool the air below the convection shield. A heated flow of dry air offsets this effect. The constant airflow and the stable laboratory environment (Figure 5.S4) ensure highly stable and reproducible experiments. Moreover, controlling the temperature by tuning the airflow temperature allows for experimentally setting the ambient temperature and elaborating the temperature-dependent performance of passive cooling materials.

5.3.2 Performance assessment

We investigated the repeatability of the indoor setup without (w/o) and with (w/) solar light. Multiple measurements of the steady-state temperature of an Ag mirror on different days are shown in Figures 5.1C and 1D. An SD of ±0.24 K and ±0.26 K was obtained from nine measurements over three consecutive days w/o and w/ light, respectively. This minor deviation shows that our indoor setup possesses outstanding repeatability in both nighttime and daytime-like measurements. When shining solar light with one sun power on the Ag mirror, the temperature increased by about 6 K. Since a LDPE foil is applied to the measurement cell to prevent convection, we thus attribute the temperature increase to the greenhouse effect caused by the parasitic solar light absorption of the Ag mirror and sample holder. This phenomenon has also been observed in outdoor measurements.[29,30]

For outdoor measurements, an intuitive definition of the ambient temperature is the air temperature, which can be measured simultaneously with the sample temperature. For indoor measurements, however, the environment temperature results from the interplay between the cold dome and the warm gas flow. The large temperature gradient between the sample holder and the dome surface prevents a meaningful ambient temperature measurement in the vicinity of the actual sample. Therefore, an alternative way to define the ambient temperature is needed. Ag possesses a low emissivity in both the solar and IR region and, therefore, closely resembles the ambient temperature inside of the measurement cell without any major radiative heat losses or gains. We confirm this assumption by comparing the Ag mirror temperature with the ambient temperature in a field test (Figures 5.2A and 2B), where both temperatures almost overlap. The ambient temperature for the indoor setup is thus defined as the temperature obtained with an Ag mirror.

To verify the reliability of the indoor setup, we analyzed three reference materials: an Ag mirror, a PDMS film on an Ag mirror, and a graphite-coated silicon wafer. The chosen materials possess very different optical properties. Ag has a very low emissivity in both

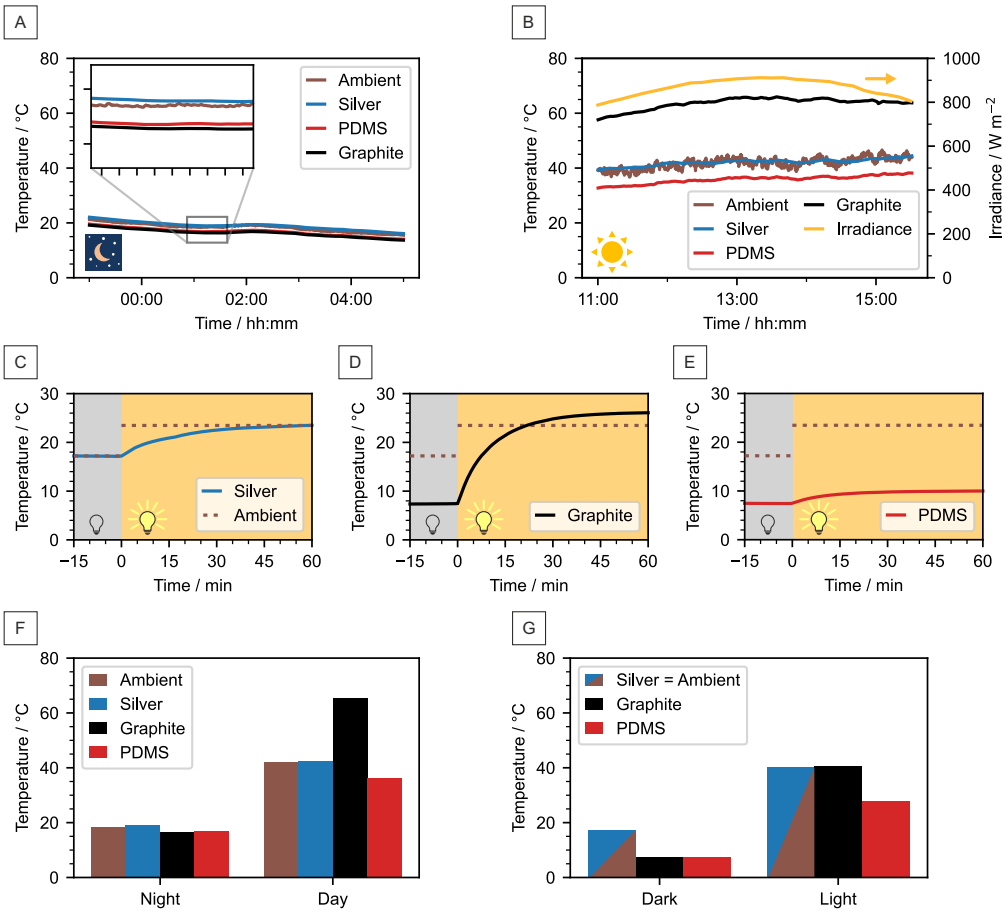

Figure 5.2.: Performance assessment. (A and B) Outdoor rooftop measurement for the reference materials at (A) nighttime and (B) daytime. The measurement was carried out under a clear sky, on June 17–18, 2021 in Bayreuth, Germany. (C–E) Indoor measurements of the (C) Ag mirror, (D) PDMS film, and (E) graphite coating. The turn-on point of the solar simulator was defined as 0 min. The dashed lines indicate the respective ambient temperatures for measurements w/o and w/ light. (F and G) The steady-state temperature of the reference materials in the (F) outdoor and (G) indoor measurements, respectively.

the visible and MIR regions, as outlined above. Furthermore, it has been widely applied to the backside of daytime passive cooling devices to minimize solar absorption.[6,31] PDMS is a good passive cooling material due to its inherent selective emissivity in the MIR region. By combining the PDMS film and an Ag mirror, a practical daytime passive cooler is easily constructed.[24,32] As the last sample, we use a graphite coating exhibiting broadband absorption in the solar and MIR regions. The spectral emissivity of all reference materials is shown in Figure 5.S5.

Measurements of the reference materials were carried out w/o and w/ light irradiation (Figures 5.2C–2E). For measurements w/o light, a steady-state temperature of 17.2 °C, 7.5 °C, and 7.4 °C was observed for the Ag mirror, the PDMS film, and the graphite coating, respectively. The PDMS film and graphite coating show a steady-state temperature ∼ 10 K lower than the Ag mirror. This is caused by the emissivity dependence of the radiative heat transfer. In contrast to the PDMS film and graphite coating, the Ag mirror shows negligible emissivity in the MIR region.

Subsequently, the solar simulator was used to simulate daytime measurements. After the reference materials reached a steady-state temperature in the dark, the solar simulator with one sun power was switched on. The temperature of all reference samples increased, and a new steady-state temperature was reached within 1 h. Compared with the Ag mirror (+6.3 K) and the PDMS film (+2.6 K), the temperature increase of the graphite coating was substantial (+18.8 K). The temperature increase of the Ag mirror can be explained by the absorption of the sample holder and the greenhouse effect. The different light response of the reference materials occurs because graphite has a significantly higher absorption in the solar regime. In addition, more than a 10 K difference in the steady-state temperature was observed between the Ag mirror and the PDMS film. The much lower final temperature of PDMS film demonstrates the good passive daytime cooling performance of the PDMS film agreeing with field testing in the literature.[24,29]

To compare the results of the indoor experiment with the conventionally used field testing, outdoor measurements of the reference materials (Figures 5.2A and 2B) were conducted in both nighttime (23:00–05:00) and daytime (11:00–15:30). The setup for the outdoor measurements is shown in Figure 5.S6. The PDMS film and graphite coating show similar steady-state temperatures at nighttime, ∼ 2.5 K lower than the Ag mirror (Figure 5.2F). During the daytime, the Ag back mirror of the PDMS sample reflected most solar irradiation, while the PDMS transferred heat to outer space via IR radiation. Therefore, the PDMS film keeps its sub-ambient temperature even with an average solar intensity of around 850 W m^{-2}. In contrast, the graphite coating absorbed considerable solar energy and warmed up to ∼ 60 °C.

Indoor measurements were performed with the respective ambient outdoor temperatures, 17 °C and 40 °C (Figure 5.2G). We observe that the absolute values of steady-state temperature for the reference materials obtained from indoor and outdoor measurements do not agree with each other. A daytime sub-ambient cooling by 6.2 K was observed from an outdoor measurement of a PDMS film, while 12.1 K was obtained from the indoor setup. We attribute this difference to two main contributions. First, the black-coated Al dome represents a broadband black body. More radiative heat can be transferred to it compared with the higher selectivity of the atmospheric window in outdoor measurements. Hence, the sub-ambient cooling power is increased. Second, the irradiance in the outdoor measurement is 900 $W\,m^{-2}$, while the irradiance in the indoor measurement is only 750 $W\,m^{-2}$. Consequently, the absorbance in the visible spectrum leads to a higher heat input for the outdoor case. Considering these effects, the values agree reasonably well. The reproducible values of the indoor setup allow for better comparison between different measurements as displayed in the literature. PDMS samples measured at different locations and times show an even larger range of temperature reductions. For instance, Zhou et al. observed a sub-ambient cooling of 11 K at Buffalo, NY, USA (February 2018).[24] Zhu et al. reported 3.3 K at Nanjing, China (November 2019),[33] and our previous study showed 7.4 K at Bayreuth, Germany (April 2020).[29] The disparity in the investigation of similar PDMS films from different groups is attributed to the distinct measurement conditions, e.g., ambient air temperature, humidity, and solar irradiation. Even subsequent measurements with the same setup from one group at a fixed location are prone to fluctuations, due to the equilibration time and the natural changes in temperature, humidity, and solar radiation. Consequently, multiple tests are typically run simultaneously to allow for comparability among different samples. In contrast, the proposed indoor setup enables measurements with a predetermined condition and, thus, allows a quantitative comparison of measurements from different days.

5.3.3 Cooling power characterization

Besides the sub-ambient temperature that a passive cooling material can reach, its net cooling power is another important parameter for quantifying the cooling performance. The standard technique to measure the net cooling power is using a feedback-controlled electrical heater underneath the sample to maintain the ambient temperature. As a result, the recorded input heating power is equivalent to the net cooling power.[4] However, the cooling power obtained from outdoor measurements, in most cases, fluctuates over time due to the unstable conditions, mainly solar intensity, wind speed, and cloud coverage. Hence, such outdoor measurements are typically carried out for many hours and merely reach a temporary steady-state condition, making quantification of the cooling power

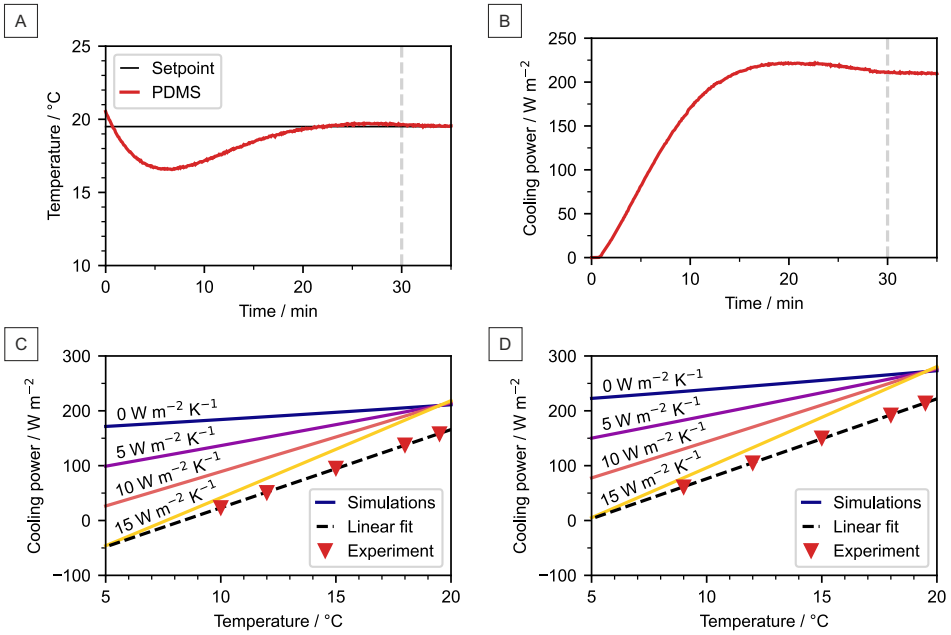

Figure 5.3.: Comparison with numerical calculations. (A and B) Temperature tracking (A) and net cooling power measurement (B) of a PDMS film (∼ 88.4 µm) via the indoor setup. (C and D) A steady net cooling power could be obtained within 30 min. Numerically calculated net cooling power as a function of emitter temperature with different non-radiative heat transfer coefficients (h_c) for (C) a thin PDMS film (∼ 19.2 µm) and (D) a thick PDMS film (∼ 88.4 µm), based on the configuration of the indoor setup. The respective experimental values are measured and plotted to estimate h_c for our setup. Values of 11.6 and 11.2 $W m^{-2} K^{-1}$ were obtained for the thin and thick PDMS samples, respectively. For the experiments, the setpoint was 19.5 °C and solar light was excluded.

difficult.[7,11,34] By contrast, a steady net cooling power can be measured with the presented indoor setup in a matter of minutes. The ambient temperature is set to the Ag mirror temperature determined under the same measurement condition. We assume that at this temperature, no non-radiative losses, i.e., convection and conduction, occur. As shown in Figures 5.3A and 5.3B, the net cooling power of a PDMS film (∼ 88.4 µm) was obtained within 30 min. The PDMS film exhibits a net cooling power of about 200 $W m^{-2}$ at an ambient temperature of 19.5 °C, w/o solar light. Compared with the net cooling power of the PDMS-based passive cooling devices reported in the literature, i.e., up to ∼ 130 $W m^{-2}$,[31] the value obtained from the indoor setup is relatively high. This is attributed to the absence of atmospheric thermal radiation outside of the sky-window range in the indoor setup.[35] Nevertheless, characterizing the passive cooling power with the indoor setup allows for a precise and defined measurement with a reasonably fast equilibration time.

For materials exposed to the clear sky, the net cooling power can be calculated with the radiative model, $P_{cool} = P_{mat} - P_{sun} - P_{atm} - P_{nonrad}$. Here, P_{mat} is the thermal

irradiation power of the emitter, P_{sun} is the solar power absorbed by the material, P_{atm} is the absorbed power from the atmosphere, and P_{nonrad} is the absorbed power due to conduction and convection. P_{nonrad} can be expressed as $P_{nonrad} = h_c \cdot (T_{atm} - T_{mat})$, where h_c is the non-radiative heat transfer coefficient. For the indoor setup, the inner space is filled with nitrogen and the path between the sample and the dome is short. Thus, P_{atm} can be omitted and the equation can be simplified to $P_{cool} = P_{mat} - P_{sun} - P_{nonrad}$ and $P_{cool} = P_{mat} - P_{nonrad}$ for daytime and nighttime, respectively. It needs to be noted that h_c varies from measurement to measurement, because of the distinct measurement conditions, and the estimation of h_c has been widely conducted,[4,36] whereas, it should not depend on the material optical properties.

To better understand our indoor setup and verify that h_c is indeed independent of the optical properties for all indoor setup measurements, we calculated the theoretical net cooling powers of PDMS films with various optical properties and compared them with the actual indoor measurements. The h_c-dependent net cooling power of PDMS films with two different thicknesses, 88.4 and 19.2 µm, was calculated via the radiative cooling model based on the indoor setup configuration. The model was thoroughly discussed in our previous work, which demonstrated the thickness dependence on optical properties and passive cooling performance.[29] The complex refractive index of PDMS films used in the calculation was obtained from the literature.[37,38] To determine h_c of our indoor setup measurements, the net cooling powers of the PDMS samples were measured at five different temperatures. We observed a linear relationship between the sample temperature and the cooling power that agreed with the expected trend obtained from the numerical calculations (Figures 5.3C and 5.3D). Based on the linear fitting of the measurement points, we estimate h_c of the indoor measurements to be 11.6 and 11.2 $W\,m^{-2}\,K^{-1}$ for the measurements of thin and thick PDMS films, respectively (Figure 5.S7). The consistent h_c value obtained from the indoor measurements with different samples proves the stability and reliability of the indoor setup. In addition, we observed a slight offset between the measured and calculated net cooling power. We attribute this to the approximations in the theoretical model, the adopted complex refractive index value from the literature,[29] and the uncertainty of the measurement.

5.3.4 Variation of environmental parameters

Solar irradiance and ambient temperature vary with time and location. They strongly influence the cooling capacity of passive daytime cooling devices. As shown in Figures 5.4A and 5.4B, solar irradiance changes from 0 to $\sim 950\,W\,m^{-2}$ during a summer day and ambient air temperature changes between about −10 °C to about 35 °C over a year in

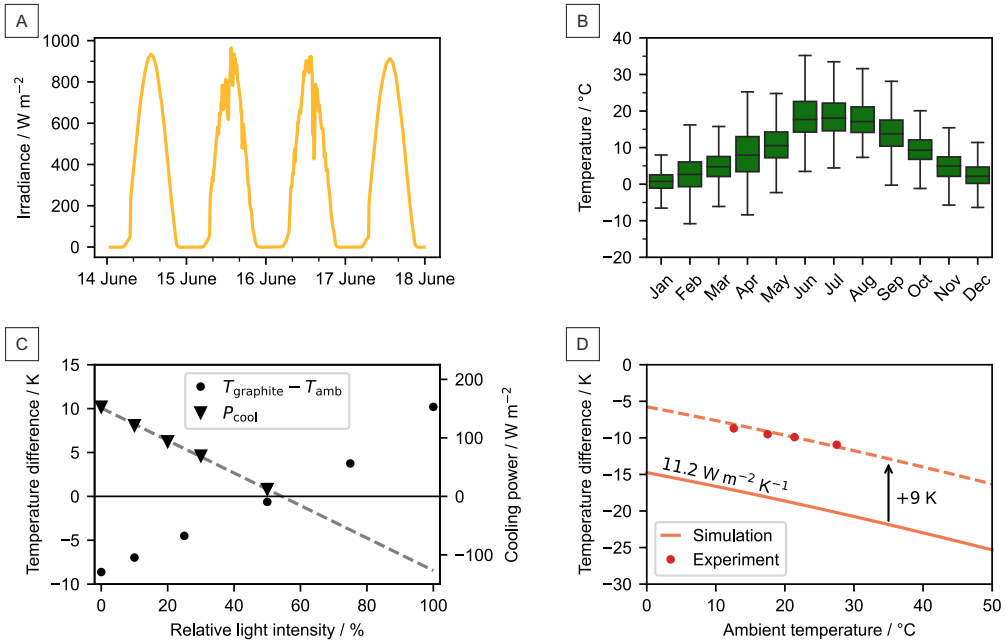

Figure 5.4.: Variation of environmental parameters (A) Solar irradiance over four days in Bayreuth, Germany. (B) Ambient air temperature of different months in Bayreuth, Germany, over the last three years. The error bars represent the standard deviation of the data. (C) Impact of solar intensity on the passive cooling performance of a graphite coating. The temperature difference ($T_{graphite} - T_{amb}$) and net cooling power (P_{cool}) show a linear trend when increasing the solar light intensity from 0 % to 100 % of one sun ($\sim$ 100 W m^{-2}). (D) The impact of ambient temperature (T_{amb}) on the cooling performance of a PDMS film. Both the simulation and experiment show that T_{amb} enhances the cooling performance leading to a decrease in the temperature difference ($T_{PDMS} - T_{amb}$).

Bayreuth, Germany. How do temperature and solar radiance influence the cooling performance? In our indoor setup, the solar irradiance can be changed between 0 and 100 % of one sun via the solar simulator. We, therefore, examined the sub-ambient cooling as well as the net cooling power of a graphite coating at various solar intensities, from 0 % to 100 %. As illustrated in Figure 5.4C, the temperature difference ($T_{graphite} - T_{amb}$) increased from about −10 K to 10 K with increasing solar intensity from 0 % to 100 %. Concomitantly, the net cooling power declined gradually. Moreover, the temperature difference and the net cooling power showed a linear trend with respect to the solar intensity.

The temperature controllable gas flow allows tuning of the ambient temperature in the measurement cell between 10 °C and 35 °C (Figure 5.S8). The temperature dependence of blackbody radiation is well known. An increasing emitter temperature enhances the thermal irradiation, and, therefore, the cooling performance. We measured the steady-state temperature of a PDMS film (88.4 µm) at various ambient temperatures. We found that with increasing the ambient temperature, the cooling performance was

also enhanced, as indicated by the increased sub-ambient cooling (Figure 5.4D). The sub-ambient cooling rose from 8.7 K to 11.0 K, with increasing the ambient temperature from 12.6 °C to 27.5 °C. We confirmed this temperature dependence by a numerical calculation with $h_c = 11.2\,\mathrm{W\,m^{-2}\,K^{-1}}$. Despite the offset between the experimental and theoretical values (~ 9 K), the trends agree well.

In general, passive cooling materials can be divided into two groups. The first group is selective emitters, which emit only at the atmospheric window (8–13 µm). These emitters transfer heat directly to outer space without interference from the atmosphere. The second one is broadband emitters. Broadband emitters emit not only at the atmospheric window but also outside, resulting in heat exchange with the atmosphere itself.[39] It is controversial which kind of emitter is better suited for passive cooling applications.[31,40] In its current form, our setup is best suited to compare emitters of the same type, i.e., compare broadband with broadband and selective with selective emitters. However, the discrimination between broadband and selective emitters is limited due to the lack of an atmospheric window. Directly simulating the atmosphere within the indoor setup is rather challenging.

Instead of equipping the indoor setup with a direct MIR filter with a transmission similar to the atmosphere to further imitate the field testing, an inverse MIR filter that emits only in the atmosphere window regime can be introduced. By placing the inverse MIR filter, which possesses ambient temperature, between the sample and the cold dome during the measurement, only the spectral radiation outside the atmosphere window regime can reach the cold dome (Figure 5.5A). The filter will block the rest. Selective emitters can thus be distinguished from broadband emitters by comparing the proportion of cooling power loss in a two-step measurement without and with the inverse MIR filter installed. The radiation in the atmosphere window regime contributes distinctly to the radiative cooling ability of broadband emitters and selective emitters.

We demonstrate such an inverse MIR filter by coating an LDPE foil with a thin layer of PDMS. A thin PDMS film with the desired thickness on an LDPE foil ensures a high absorption in the regime of 8–13 µm and simultaneously high transmission in the remaining spectral range (Figure 5.5B). The cooling power of PDMS films with different thicknesses, i.e., 712 nm and 8.6, 13.1, and 88.4 µm, is determined w/o and w/ the PDMS-PE filter to prove the concept (Figures 5.5C and 5.S9). The optical properties of the PDMS films show that with increasing film thickness, they gradually transition from a selective to a broadband emitter (Figure 5.S10). Consequently, the cooling power without the MIR filter increased gradually. This is in good agreement with our previous work based on outdoor measurements.[29] The cooling power reduces dramatically when applying the PDMS-PE filter. The decrease varies for the differently thick PDMS films. To highlight the cooling power difference caused by the PDMS-PE filter, the relative power

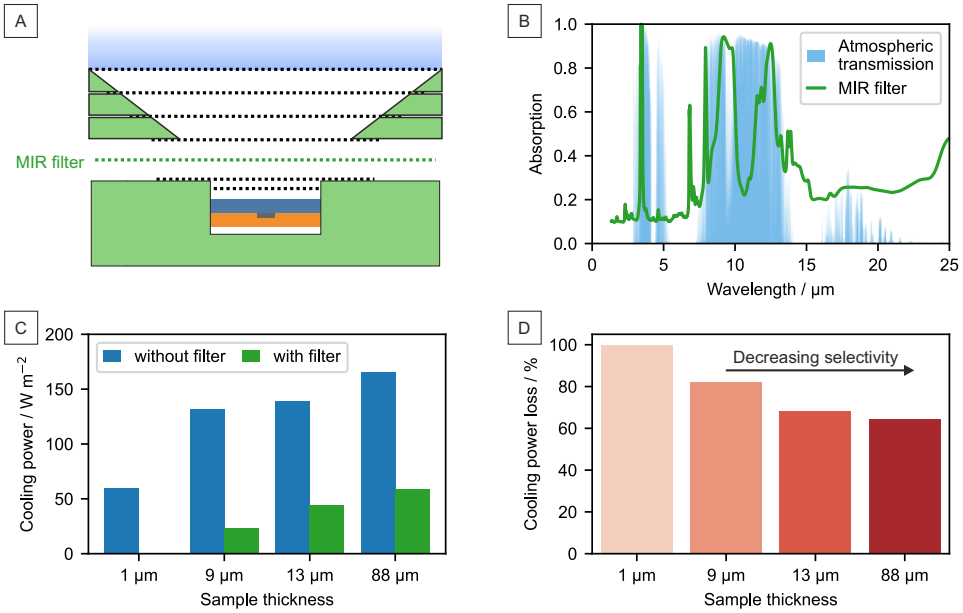

Figure 5.5.: Distinguishing broadband and selective emitters. (A) An MIR filter consisting of PDMS on PE is inserted between the sample and the convection shield. (B) The absorption spectrum of the PDMS-PE filter is comparable with the transmission of the atmosphere. (C) Cooling power measurements of differently thick PDMS samples with and without the filter. With increasing thickness, the cooling power rises. The introduction of the MIR filter results in a significant reduction of cooling power. (D) The relative cooling power loss decreases with increasing PDMS film thickness. The loss correlates with the emission selectivity of the samples.

loss was calculated as power loss $= (P_{w/o} - P_{w/})/P_{w/o}$ and is shown in Figure 5.5D. The increasing thickness of the PDMS films reduces the cooling power loss, which indicates that the PDMS-PE filter affects selective emitters more importantly than broadband emitters. Besides, we also calculated the cooling power loss of the PDMS films w/and w/o atmosphere with outdoor conditions (Figure 5.S11). Despite the deviation of the absolute value between the experiment and the simulation, the trend agrees well. The deviation is mainly attributed to the imperfect match between the PDMS-PE filter and the atmosphere. The inverse MIR filter design can assess the influence of the sky-window transmission on the cooling power but is not suitable to compare the temperature reduction with outdoor measurements. A direct temperature comparison required a filter matching the sky-window properties.

Although it is hard to imitate the atmosphere in the indoor setup, with the inverse MIR filter, the indoor setup can distinguish between selective and broadband emitters. The possibility to add a tailor-made filter to our setup further expands the scope for its applicability to characterize passive daytime cooling materials close to field testing conditions. Further additions may include filters that account for a specific relative humidity or cloud coverage. Another class of filters may address the angular dependence

of the thermal emission of a given material by controlling the view factor of the dome in dependence on the polar angle. Such a measurement capability is highly demanded to characterize emissive materials with diffusive reflectance properties. For instance, the heat management properties of smart textiles can be investigated with such a sample-dome layout, when operated at body heat and room temperature, respectively.[41]

In summary, we constructed a versatile indoor setup to thoroughly characterize the performance of passive cooling materials for both daytime and nighttime. Our setup combines a liquid-nitrogen-cooled Al dome with a solar simulator. Unlike conventional outdoor measurements, our setup allows controlling the measurement conditions, leading to outstanding reproducibility and time-saving measurements. Characterizing materials in a laboratory environment makes measuring and comparing materials independent of weather, time, and location. Additionally, the impact of solar intensity and ambient temperature on the cooling performance can be practically studied. Such comprehensive investigations are impossible for outdoor measurements due to the uncontrollable atmospheric conditions. We are convinced that our test setup is a first step toward a standardized passive cooling test routine. A standardized method to practically compare the cooling performance of various innovative materials from research groups all over the world is, however, a gatekeeper to turning passive cooling into a widespread and applied technology.

5.4 Experimental Procedures

5.4.1 Resource availability

Lead contact

Further information and requests for resources should be directed to and will be fulfilled by the lead contact, Markus Retsch (retsch@uni-bayreuth.de).

Materials availability

This study did not generate new unique reagents.

Data and code availability

All data from this study are available from the corresponding author upon reasonable request.

5.4.2 Preparation of reference materials

Ag mirrors

Ag with a thickness of 100 nm was thermally evaporated on a silicon wafer ($r = 2.5$ cm), followed by a deposition of 10 nm silicon oxide (SiO_2) with a sputter coating step.

PDMS films

PDMS films with different thicknesses (88.4, 13.1, and 8.6 µm and 712 nm) were prepared on top of the Ag mirrors. For this, a prepolymer of PDMS (Sylgard 184, Dow Chemical) was mixed with a curing agent in a ratio of 10:1 (by weight) and degassed in a desiccator under vacuum. Subsequently, films with a thickness of 88.4 and 13.1 µm were prepared via spin-coating (1000 and 3000 rpm) on the Ag mirror. For films with a thickness of 8.6 and 13.1 µm, the prepolymer/cross-linker mixture was diluted to 75 wt% and 25 wt% solutions, respectively, with n-hexane. The films were then prepared via spin coating (3000 and 4000 rpm) on the Ag mirror. The PDMS layers were cured at room temperature for 48 h.

Graphite coating

The graphite coating is prepared by spray coating graphite (Cramolin, ITW Spraytec, Germany) onto a precleaned silicon wafer ($r = 2.5$ cm), followed by evaporation of the solvent at ambient temperature.

The layer thickness of the reference samples, namely PDMS films and graphite, was determined by using a three-dimensional (3D) laser scanning microscope (LEXT OLS5000, Olympus). A thickness of 88.4 µm, 13.1 µm, 8.6 µm, 712 nm, and 3.2 µm was obtained for the four PDMS films and the graphite coating, respectively.

PDMS-PE window

A prepolymer of PDMS (Sylgard 184, Dow Chemical) was mixed with a curing agent in a ratio of 10:1 (by weight) and degassed in a desiccator under a vacuum. The resulting mixture was diluted to a 50 wt% solution with n-hexane. A PDMS thin film was spin-coated (3500 rpm) on an LDPE foil (thickness of around 15 µm), which was evenly attached to a silicon wafer ($r = 7.5$ cm). A PDMS-PE window was obtained by detaching the PDME-PE foil from the silicon wafer.

5.4.3 Optical characterization with UV-Vis and FTIR spectroscopy

Broadband optical properties of the reference materials were characterized by ultraviolet-visible (UV-Vis) and Fourier transform infrared (FTIR) spectroscopy. UV-Vis reflectance of the reference materials was measured with a UV-Vis spectrometer (Cary 5000, Agilent Technologies) equipped with an integrating sphere accessory (Labspheres). A Spectralon diffuse reflectance standard (Labspheres) was used as a reference. The FTIR spectroscopy measurements were carried out on an IR spectrometer (Vertex 70, Bruker) coupled with a gold-coated integrating sphere accessory (A562, Bruker). A gold mirror was used as a reference. The absorptance (emittance) was calculated as absorptance (emittance) = 1 - reflectance. We assume that the transmission can be neglected because of the Ag layer at the back.

5.4.4 Transmittance characterization of the convection shield

We used a pyroelectric sensor (FieldMaxII, Coherent) to measure the power of the solar simulator irradiation. Triplicate measurements were performed with and without the convection shield between the simulator and the sensor. The transmittance was calculated as $1 - P_{\text{w/ shield}}/P_{\text{w/o shield}}$.

5.4.5 Indoor measurements

Daytime measurements are imitated by applying solar light provided by a solar simulator (AX-LAN400, Sciencetech, Canada) with an illumination area of $5 \times 5\,\text{cm}^2$. For nighttime measurements, the solar simulator was turned off. For all indoor measurements, dried air was warmed up by a water bath with a controlled temperature and flushed the area between the convection shield and measurement cell. Liquid nitrogen was filled into the setup to cool down the Al dome. Before filling the liquid nitrogen into the setup, the inner space of the dome is flushed with N_2 to remove air. Thus, no pronounced water condensation was observed on the convection shield. The temperature of the dome is maintained during the entire measurement by continuously filling liquid nitrogen into the setup. The sample temperature is measured with a thermocouple (type T) and collected by a digital multimeter (DAQ6510, Tektronix, Germany) every 5 s. To determine the steady-state temperature, data from the last 5 min of the measurement were averaged.

For the indoor measurements with the PDMS-PE window, the prepared PDMS-PE foil was placed above the sample holder at a distance of around 5 mm.

Repeatability test

An Ag mirror was used to check the repeatability of the setup. The temperature of the airflow was controlled by setting the water bath to 40 °C. The steady-state temperature of the Ag mirror was measured three times per day on three different days, w/ and w/o one sun power of solar light ($\sim 1000\,\mathrm{W\,m^{-2}}$).

Solar intensity dependence test

The graphite coating was measured to highlight the influence of solar intensity on the cooling performance. The temperature of the airflow was set to 40 °C. The intensity of the solar light was varied from 0 % to 100 % of one sun power ($\sim 1000\,\mathrm{W\,m^{-2}}$). The steady-state temperature and the cooling power of the graphite coating were then obtained under each condition. The net cooling power was measured by actively heating the graphite coating to keep it at the same temperature as an Ag mirror under the same conditions (water bath temperature and solar irradiance).

Ambient temperature dependence test

A PDMS film (88.4 µm) was applied to prove the temperature dependence of the thermal irradiation. The temperature of the airflow was set to 35 °C, 40 °C, 50 °C, and 60 °C. Subsequently, the steady-state temperature of the Ag mirror and the PDMS film was measured w/o the solar light.

5.4.6 Rooftop measurements

Rooftop measurements for daytime and nighttime were carried out on the roof of a four-floor building (June 17–18, 2021, University of Bayreuth, Bayreuth, Germany) under a clear sky. The reference samples were each placed in identical homemade sample holders. The holders were thermally insulated by Styrofoam and covered with Mylar Al foil. Convective heat transfer was prevented by applying an LDPE foil, with a thickness of approximately 15 µm. The emitter temperatures were measured by Pt100 temperature sensors and recorded with a digital multimeter (DAQ6510, Tektronix, Germany) every 5 s. Temperatures between 1:00–1:30 and 13:00–13:30 were averaged to obtain steady-state temperatures. One sample holder covered with Al foil but without LDPE foil was used to obtain the ambient temperature. The solar irradiance data were collected from the weather station at the University of Bayreuth (Ecological-Botanical Garden, 400 m away from the rooftop measurement).

5.4.7 Numerical calculations

The numerical calculations for theoretically estimating the steady-state temperature and cooling power of the PDMS films are based on a model that is described in our previous study.[29] The broadband optical properties of the PDMS film are obtained from the literature.[37,38,42] The sample was tilted 8° to avoid direct reflection of the solar light. For simplicity, this has been neglected in numerical calculations. A polar angle θ of 60° and an azimuthal angle of 360° was applied to the calculation based on the configuration of the indoor setup. We assume that no thermal radiation was emitted by the liquid-nitrogen-cooled dome.

To calculate the cooling powers of PDMS films with different thicknesses, i.e., 88.4, 13.1, 8.6 µm and 712 nm, with the outdoor condition, a polar angle θ of 90° and an azimuthal angle of 360° were applied. The ambient temperature of the emitter is set to 18.5 °C, which is the preset temperature of PDMS films for indoor cooling power measurement. For emitters with a temperature as same as ambient temperature, the nighttime cooling power is calculated as $P_{\text{mat}} - P_{\text{atm}}$. P_{mat} is the total power emitted by the sample. P_{atm} is the absorbed power from the atmosphere. The cooling power loss is calculated as $(P_{\text{mat}} - P_{\text{atm}})/P_{\text{mat}}$.

5.5 Acknowledgments

The authors gratefully thank Stefan Rettinger and the mechanical and electrical workshop (University of Bayreuth) for technical support and Klaus Müller for the metal evaporation. We are indebted to Prof. Christoph Thomas for kindly providing the solar radiance and air temperature data. T.T. and T.L. acknowledge support from the Elite Network Bavaria (ENB). The authors acknowledge financial support from the European Research Council (ERC) under the European Union's Horizon 2020 research and innovation program (grant agreement no. 714968).

5.6 References

[1] M. Santamouris, J. Feng, *Buildings* **2018**, *8*, 168.

[2] Z. Li, Q. Chen, Y. Song, B. Zhu, J. Zhu, *Advanced Materials Technologies* **2020**, *5*, 1901007.

[3] E. Rephaeli, A. Raman, S. Fan, *Nano Letters* **2013**, *13*, 1457–1461.

[4] A. P. Raman, M. A. Anoma, L. Zhu, E. Rephaeli, S. Fan, *Nature* **2014**, *515*, 540–544.

[5] D. Chae, M. Kim, P.-H. Jung, et al., *ACS Applied Materials & Interfaces* **2020**, *12*, 8073–8081.

[6] Y. Zhai, Y. Ma, S. N. David, et al., *Science* **2017**, *355*, 1062–1066.

[7] X. Wang, X. Liu, Z. Li, et al., *Advanced Functional Materials* **2019**, *30*, 1907562.

[8] B. Zhu, W. Li, Q. Zhang, et al., *Nature Nanotechnology* **2021**, *16*, 1342–1348.

[9] S. Zeng, S. Pian, M. Su, et al., *Science* **2021**, *373*, 692–696.

[10] A. Leroy, B. Bhatia, C. C. Kelsall, et al., *Science Advances* **2019**, *5*, eaat9480.

[11] J. Mandal, Y. Fu, A. C. Overvig, et al., *Science* **2018**, *362*, 315–319.

[12] J. Wang, J. Sun, T. Guo, et al., *Advanced Materials Technologies* **2021**, *7*, 2100528.

[13] H. Zhong, P. Zhang, Y. Li, et al., *ACS Applied Materials & Interfaces* **2020**, *12*, 51409–51417.

[14] N. N. Shi, C.-C. Tsai, F. Camino, et al., *Science* **2015**, *349*, 298–301.

[15] H. Zhang, K. C. S. Ly, X. Liu, et al., *Proceedings of the National Academy of Sciences* **2020**, *117*, 14657–14666.

[16] T. Wang, Y. Wu, L. Shi, et al., *Nature Communications* **2021**, *12*, 365.

[17] S. Wang, Y. Wang, Y. Zou, et al., *ACS Applied Materials & Interfaces* **2021**, *13*, 21888–21897.

[18] B. Zhao, M. Hu, X. Ao, N. Chen, G. Pei, *Applied Energy* **2019**, *236*, 489–513.

[19] X. Li, J. Peoples, Z. Huang, et al., *Cell Reports Physical Science* **2020**, *1*, 100221.

[20] S. Wang, T. Jiang, Y. Meng, et al., *Science* **2021**, *374*, 1501–1504.

[21] K. Tang, K. Dong, J. Li, et al., *Science* **2021**, *374*, 1504–1509.

[22] M. M. Hossain, M. Gu, *Advanced Science* **2016**, *3*, 1500360.

[23] M. Dong, N. Chen, X. Zhao, S. Fan, Z. Chen, *Optics Express* **2019**, *27*, 31587.

[24] L. Zhou, H. Song, J. Liang, et al., *Nature Sustainability* **2019**, *2*, 718–724.

[25] G. Park, K. Roh, H. Kim, et al., *Advanced Materials Technologies* **2022**, *7*, 2101205.

[26] R. Y. Wong, C. Tso, C. Y. Chao, *International Journal of Heat and Mass Transfer* **2021**, *174*, 121341.

[27] Z. Huang, X. Ruan, *International Journal of Heat and Mass Transfer* **2017**, *104*, 890–896.

[28] U. Banik, A. Agrawal, H. Meddeb, et al., *ACS Applied Materials & Interfaces* **2021**, *13*, 24130–24137.

[29] K. Herrmann, T. Lauster, Q. Song, M. Retsch, *Advanced Energy and Sustainability Research* **2021**, *3*, 2100166.

[30] S. Y. Jeong, C. Y. Tso, J. Ha, et al., *Renewable Energy* **2020**, *146*, 44–55.

[31] J.-l. Kou, Z. Jurado, Z. Chen, S. Fan, A. J. Minnich, *ACS Photonics* **2017**, *4*, 626–630.

[32] I. Haechler, H. Park, G. Schnoering, et al., *Science Advances* **2021**, *7*, eabf3978.

[33] Y. Zhu, Y. Ye, D. Wang, Y. Cao, *OSA Continuum* **2021**, *4*, 416.

[34] T. Li, Y. Zhai, S. He, et al., *Science* **2019**, *364*, 760–763.

[35] M. Chen, D. Pang, X. Chen, H. Yan, *Journal of Physics D: Applied Physics* **2021**, *54*, 295501.

[36] T. M. Nilsson, G. A. Niklasson, *Solar Energy Materials and Solar Cells* **1995**, *37*, 93–118.

[37] X. Zhang, J. Qiu, X. Li, J. Zhao, L. Liu, *Applied Optics* **2020**, *59*, 2337.

[38] X. Zhang, J. Qiu, J. Zhao, X. Li, L. Liu, *Journal of Quantitative Spectroscopy and Radiative Transfer* **2020**, *252*, 107063.

[39] D. Zhao, A. Aili, Y. Zhai, et al., *Applied Physics Reviews* **2019**, *6*, 021306.

[40] Y. Li, L. Li, L. Guo, B. An, *Optical Materials Express* **2020**, *10*, 1767.

[41] Q. Gao, T. Lauster, B. A. F. Kopera, et al., *Advanced Functional Materials* **2021**, *32*, 2108808.

[42] M. R. Querry, Optical Constants of Minerals and Other Materials from the Millimeter to the Ultraviolet, **1987**.

5.7 Supplemental Information

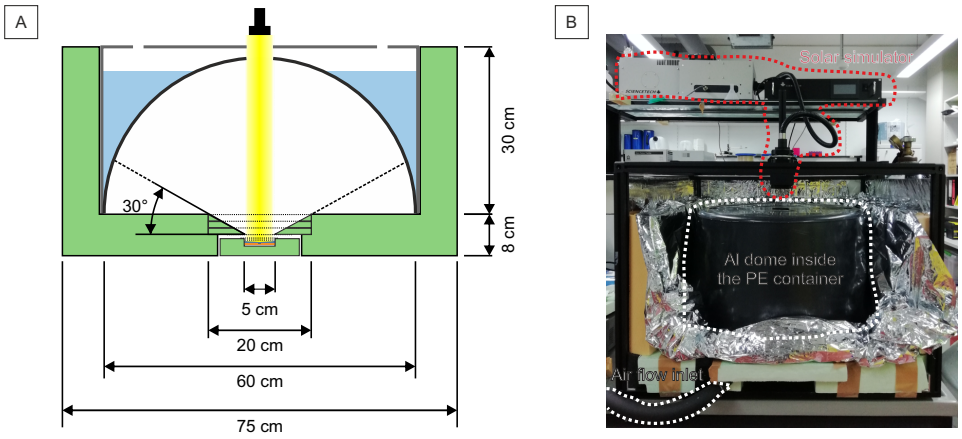

Figure 5.S1.: Indoor setup design. (A) Detailed dimensions and (B) photograph of the indoor setup. Related to Figure 5.1 and Indoor Setup Design.

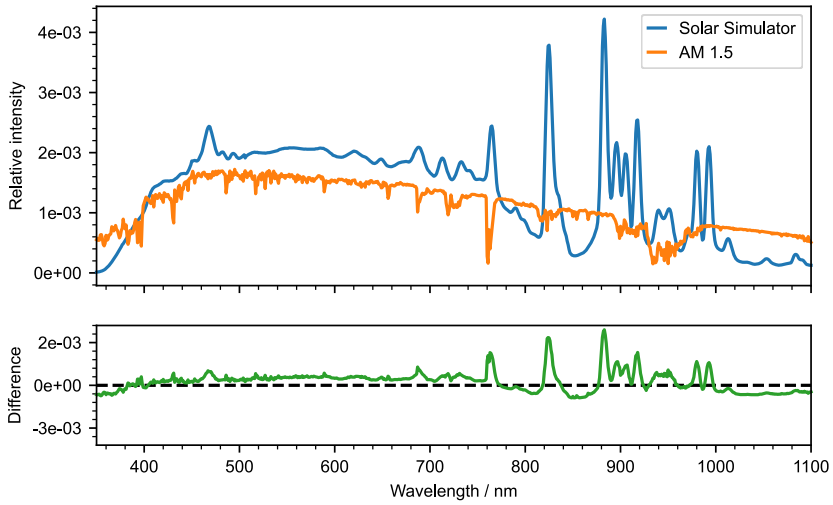

Figure 5.S2.: Comparison between the solar light from the sun (AM 1.5) and the solar simulator. The intensity shown is relative to the total intensity of the light source, i.e., the integral from 0 to infinity is 1 for each individual curve. Related to Indoor Setup Design.

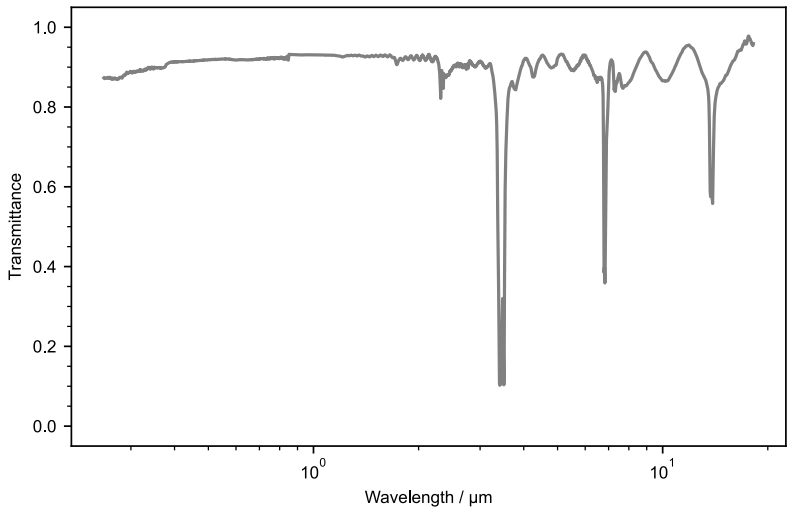

Figure 5.S3.: Angle-dependent optical properties in (A) UV/Vis and (B) IR regime for a single, 15 µm thick PE window used in the convection shield. Related to Indoor Setup Design.

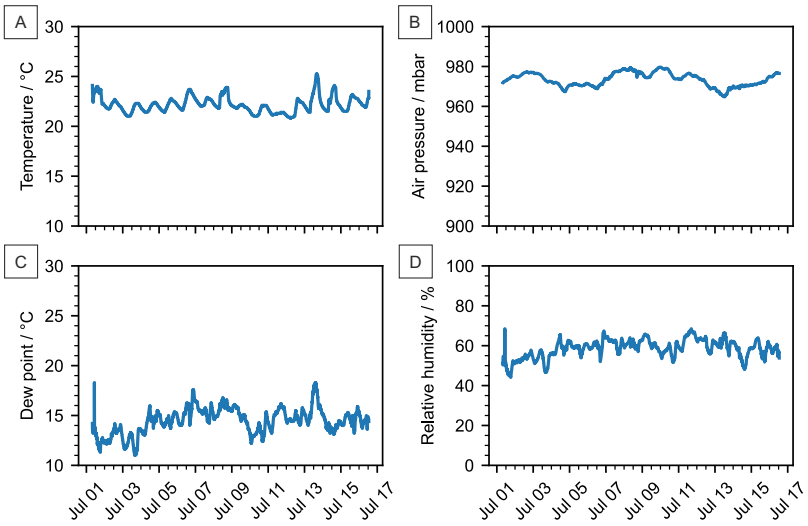

Figure 5.S4.: Laboratory conditions. (A) Ambient temperature, (B) air pressure, (C) dew point, and (D) relative humidity in the laboratory over a week. Related to Indoor Setup Design.

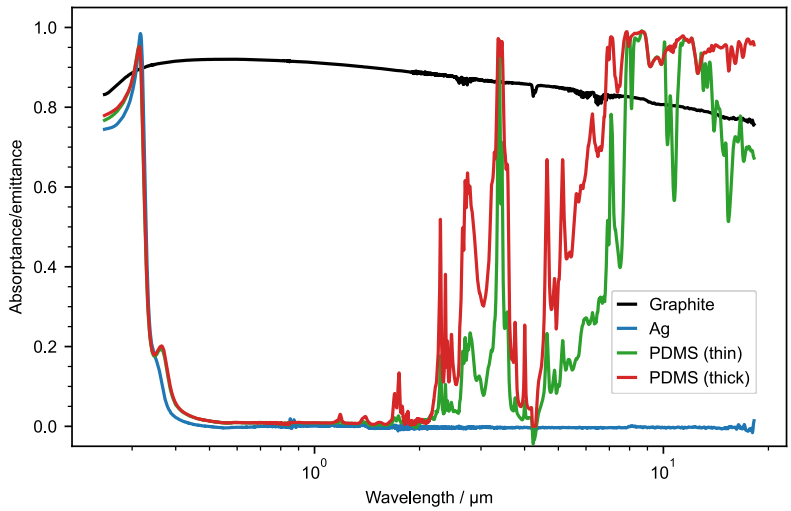

Figure 5.S5.: Optical properties of the reference materials used in this work, i.e., PDMS, Ag, and graphite, in the UV/Vis and MIR region. Related to Figure 5.2 and Performance Assessment.

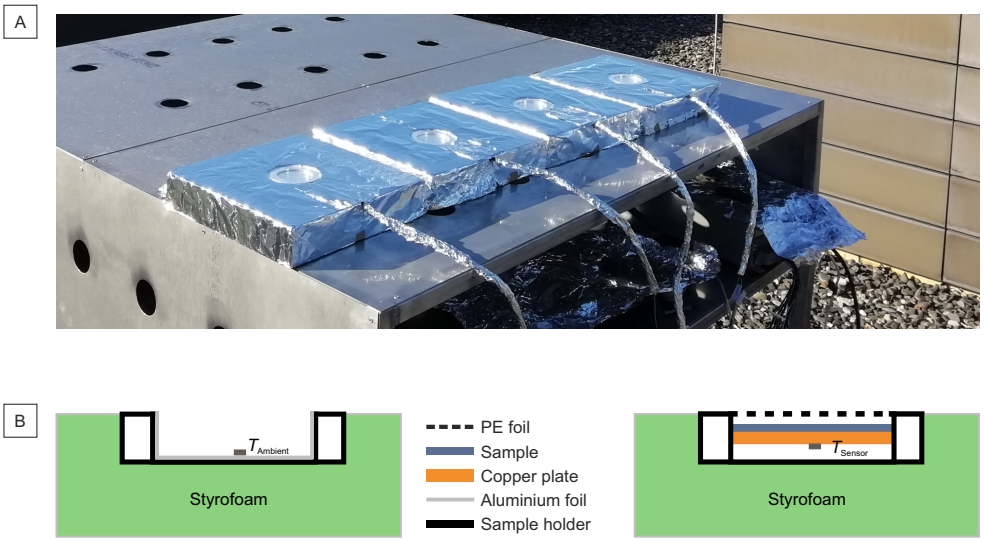

Figure 5.S6.: Outdoor setup design. (A) Photograph and (B) schematic of the setup for outdoor measurements. Related to Figure 5.2 and Performance Assessment.

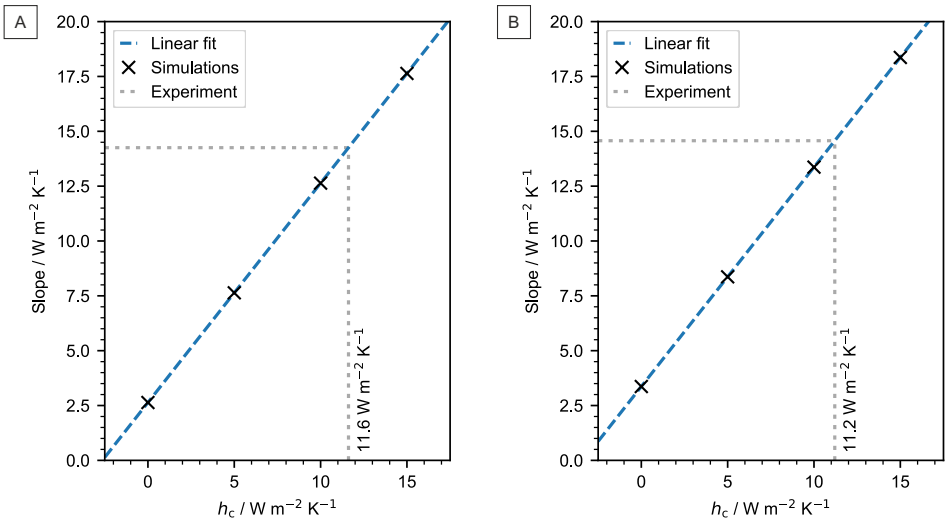

Figure 5.S7.: Determination of h_c for the thin (A) and thick (B) PDMS samples in the indoor setup measurement. The linear fit shows how the slope of the simulated cooling power behaves for different values of h_c. Calculating the slope of the experimental cooling powers leads to h_c values of 11.6 and 11.2 W m^{-2} K^{-1} for the thin and thick PDMS samples, respectively. Related to Figure 5.3 and Cooling Power Characterization.

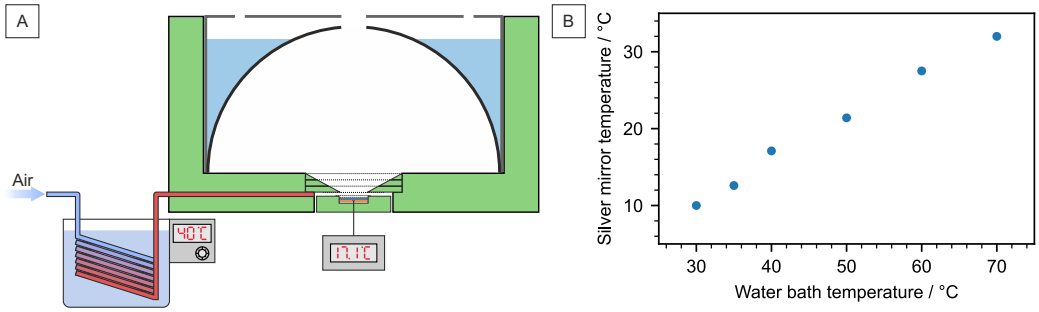

Figure 5.S8.: Tunable ambient temperature of the indoor setup. (A) Schematic of a part of the indoor setup. (B) Ambient temperature of the indoor setup as a function of water bath temperature. Related to Figure5.4 and Variation of Environmental Parameters.

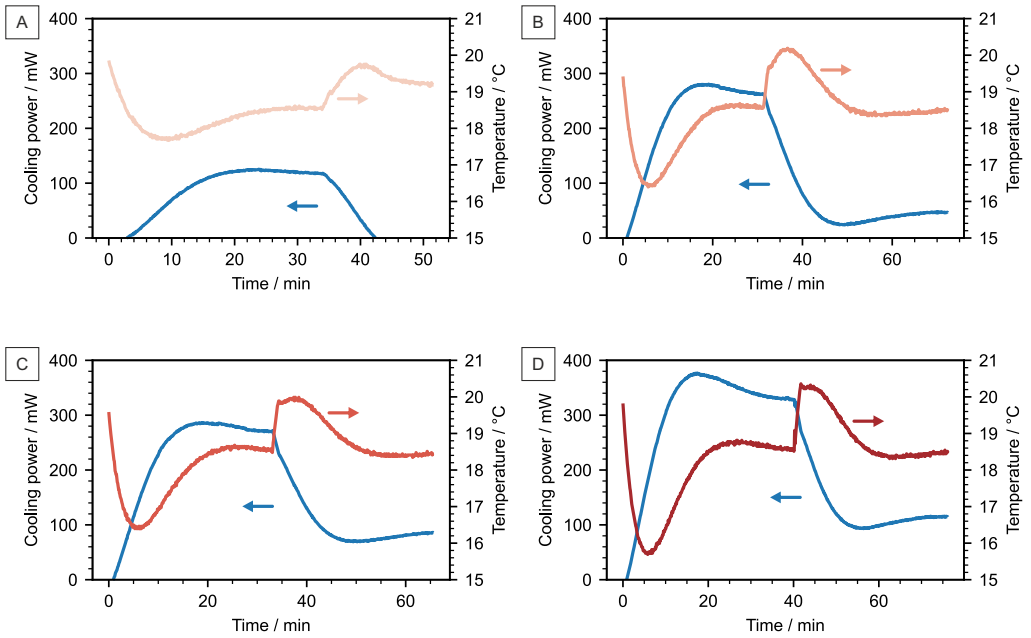

Figure 5.S9.: Cooling power measurements with and without a MIR filter for PDMS samples with a thickness of (A) 712 nm, (B) 8.6 µm, (C) 13.1 µm, and (D) 88.4 µm. The MIR filter is inserted into the indoor setup after temperature and cooling power reach a steady state. The insertion of the MIR filter leads to a significant decrease in cooling power for all samples.

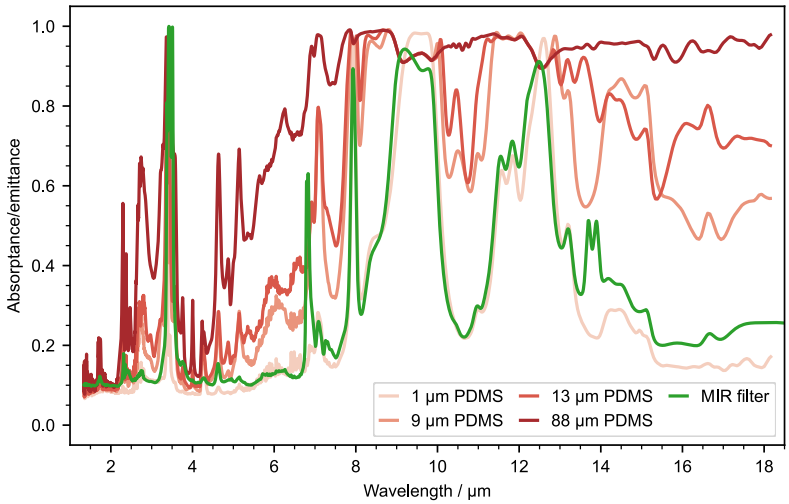

Figure 5.S10.: Absorption spectra for PDMS films of different thicknesses and the MIR filter. Decreasing thickness leads to higher emission selectivity.

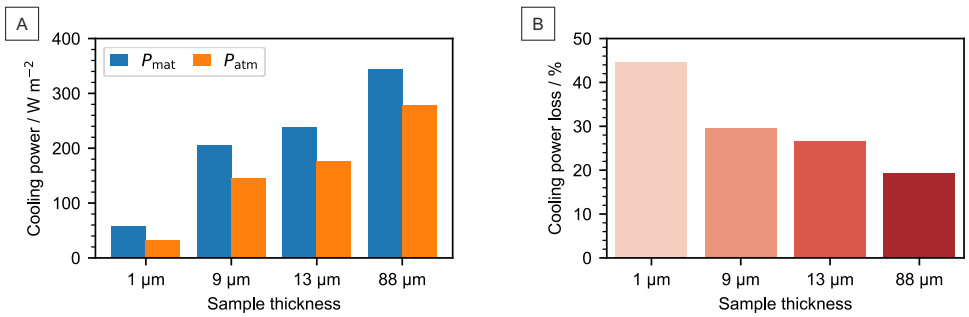

Figure 5.S11.: Simulation results for PDMS samples with different thicknesses in outdoor conditions. (A) Absolute contributions to the cooling power. (B) Cooling power loss. The loss is calculated as $(P_{\mathrm{mat}} - P_{\mathrm{atm}})/P_{\mathrm{mat}}$.

Upcycling chips-bags for passive daytime cooling

6

Qimeng Song,[1,*] Thomas Tran,[1] Kai Hermann,[1] Holger Schmalz,[2] and Markus Retsch[1,3,*]

1 Department of Chemistry, Physical Chemistry I, University of Bayreuth, Universitätsstraße 30, 95447 Bayreuth, Germany
2 Department of Chemistry, Macromolecular Chemistry II, Bavarian Polymer Institute, University of Bayreuth, Universitätsstraße 30, 95447 Bayreuth, Germany
3 Bavarian Center for Battery Technology (BayBatt), Bavarian Polymer Institute, and Bayreuth Center for Colloids and Interfaces, University of Bayreuth, Universitätsstraße 30, 95447 Bayreuth, Germany
∗ Corresponding author

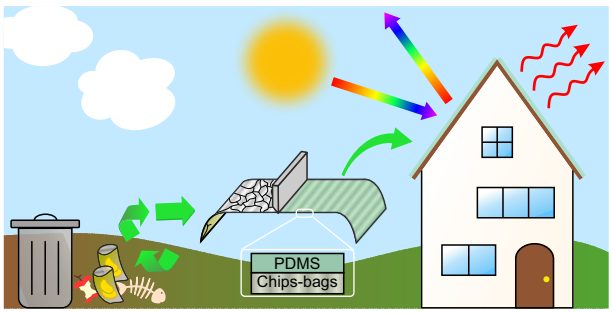

Published in *Advanced Materials Technologies*, **2023**, 2300444.

6.1 Abstract

Plastic pollution has caused numerous environmental issues in recent decades. As one of the most commonly used packaging materials, aluminum-plastic laminates (APL) are particularly challenging for recycling purposes due to their sophisticated materials components. This work reveals a new strategy to upcycle such post-consumer APL packaging waste, e.g., chips-bags, for passive daytime cooling applications. This opens an attractive route to reuse APLs while at the same time reducing global energy consumption and carbon emissions. The mirror-like appearance of the APLs possesses a strong solar reflection, up to 86 %. By coating, this reflective layer of the APL waste with a high emissive polydimethylsiloxane layer, a simple but effective passive daytime cooling foil is constructed, which shows promising passive cooling performance theoretically and practically. More importantly, the passive cooling foil based on APL waste is flexible and can be applied to any target object, protecting it from harsh sunlight. The low-cost APL waste-based passive cooling foil proposed in this work will significantly contribute to both energy and environmental issues that humans face today.

6.2 Introduction

aluminum-plastic laminates (APL) have been massively used as packaging materials to extend the shelf-life of products like chips, roasted, and powdered coffee, as well as milk and juices.[1] Besides, APL has extended its applications dramatically in the pharmaceutical packaging of FFP2 masks and rapid tests over the last few years because of the COVID-19 pandemic. With aluminum as a barrier layer, the APL provides satisfactory product protection from various deteriorating factors, including oxygen, moisture, and light.[2] However, the complex construction, consisting of aluminum and multiple layers of polymer, makes this sort of packaging foil exceedingly challenging to recycle.[1,3–5] Consequently, most APL waste is treated by incineration or discarded in landfills, causing severe environmental sustainability issues, including the release of greenhouse gas emission, air pollution, and soil infertility.[6,7]

The industrial recycling of APL faces several challenges, such as the segregation of the different layers as well as cleaning and sorting issues.[4,5] One technique for recovery of aluminum and individual polymer components is chemical delamination, where the individual polymer layer is dissolved with the corresponding solvent.[8,9] Besides, thermal and catalytic pyrolysis have also been developed to extract aluminum and energy from APLs.[10,11] More recently, various innovative strategies for APL recycling have been reported. For instance, thermal delamination[12] and enzymatic bioleaching recycling

methods.[13] Despite the progress in material and energy extraction from APL, it is still considered unrecyclable due to its low recycling efficiency. The European plastic strategy aims for all used packaging to be recyclable or reusable by 2030.[14] For this to be successful and to reduce the impact of APL waste on the environment, advanced strategies for cost-effective recycling or repurposing of APL are urgently desired.

Another rising concern is global warming, caused by the overuse of fossil fuels and resulting greenhouse gas emissions.[15] As one of the consequences, the frequency of intense heat waves has increased worldwide, threatening human and ecological health.[16–18] Passive daytime radiative cooling (PDRC) is regarded as a promising strategy to combat global warming by reducing the energy demand for cooling.[19,20] By emitting thermal irradiation to cold outer space (3 K) through the atmospheric transparency window (8–13 µm), terrestrial materials with engineered optical properties autonomously cool down to subambient temperatures in the nighttime, without external energy input. By minimizing the absorption of a material in the solar regime (0.3–2.5 µm), the passive cooling properties can be preserved during the daytime, even under direct sunlight illumination. A passive cooling device can be readily constructed by combining a highly solar transparent and emissive layer, like polydimethylsiloxane (PDMS), with a back reflector, e.g., silver (Ag) or aluminum (Al).[21,22] To circumvent the usage of the metallic back reflector, in recent years, advanced structured materials have been fabricated to strongly scatter sunlight,[23] including micro-/nanoporous materials,[24,25] and nanoparticles-based composites.[26,27] Though an increasing number of passive cooling devices with remarkable daytime cooling performance have been reported, the transition from fundamental scientific studies to a widely distributed cooling technology is still missing. Scalability, practicality, durability, and manufacturing costs are insurmountable problems restricting this technique from practically transitioning to real-life applications. Considering that the amount of energy saved with PDRC is proportional to the applied area, it is imperative to design a cost-effective, scalable, and easily applicable PDRC foil.

In our contribution, we outline a comprehensive upcycling strategy to repurpose APL waste and to access PDRC foils in a cost-effective manner. This combination has a twofold beneficial consequence for the environment due to the reduction of APL waste, and the fabrication of PDRC foils with already available materials. Optical property characterization elucidates that the plain APL possesses a substantial solar light reflection (up to 86 %), owing to the presence of the Al layer, which makes APL a promising candidate for the back reflector of the PDRC material. By adding an emissive layer, e.g., PDMS, to enhance the radiative heat release, the cooling capacity of APL waste-based foils is theoretically and experimentally demonstrated. Moreover, the cooling foil is scalable, flexible, and can be readily applied to various surfaces, protecting the target

object from harsh sunlight and heat. Our approach is the first step toward a widespread and low-cost utilization of optically engineered passive cooling foils.

6.3 Results and Discussion

APL is generally constituted by several polymer layers and aluminum laminated with adhesives, as illustrated in Figure 6.1a. A scanning electron microscope (SEM) image of a cross-section of APL used for a chip bag shows its multilayer structure. A thickness of about 18.9, 2.7, 1.7, 3.2, and 31.2 µm is observed for respective layers (from the top, goods contacting side, to bottom, ink side). By using confocal Raman spectroscopy, we determined the chemical composition of each layer. The Raman spectra show that both polymer layers are polypropylene (PP) for the tested APL.[28] APL shows a mirror-like appearance due to the presence of Al laminated at the core, demonstrating its potential as a back reflector. To reveal the capability of APL as a back reflector for PDRC, we examined the solar reflectance of APL from various packaging bags, as shown in Figure 6.1d and Figure 6.S1. As representative samples, APLs from bags originally used for potato chips, coffee, and face masks are mainly focused on in this work due to their widespread usage in the market. An impressive solar reflectance is observed for most of the APLs. As shown in Figure 6.1d, an average solar reflectance of 0.86, 0.81, and 0.83 was obtained from the chip, coffee, and mask bags, respectively. The decent solar reflectance verifies that APL holds considerable potential as the back reflector for passive daytime cooling materials. Moreover, APLs, especially the chip bag and the mask bag, exhibit a constant reflectance at a large incident angular range (Figure 6.1e). This stable and high solar reflectance allows them to face and reflect the sun at various angles. Even when substantially wrinkled, as expected from waste stream collection, the APL foils retain their high solar reflectance (Figure 6.S2.

For PDRC materials, absorption in the solar range determines the energy uptake from the sun in the daytime, while mid-infrared (MIR) emissivity controls the radiative heat release. Therefore, both aspects of the material need to be optimized to achieve a net passive cooling performance in the daytime. In the market, various polymers have been utilized to compose the APL, including PP, low-density polyethylene (PE), and polyethylene terephthalate (PET).[7] APL varies in composition and layer thickness depending on the end-use product, resulting in different MIR emissivities. To reveal the MIR emissivity of the tested plain packaging bags, we measured their absorptance (1 − reflection) spectra at a wavelength range of 2–18 µm by using Fourier-transform infrared spectroscopy (FTIR) (Figure 6.2a). Average MIR absorptances of 0.23, 0.51, and 0.70 were obtained for the plain chip bag, coffee bag, and mask bag, respectively, which are related to the layer composition (Figure 6.S3 and 6.S4) and thickness. The

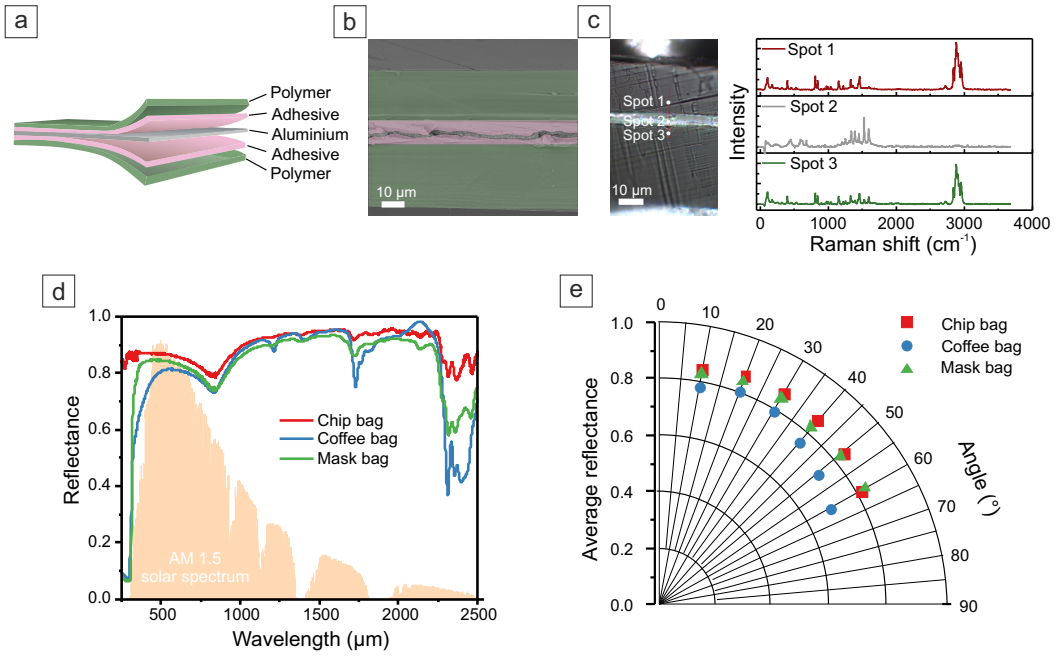

Figure 6.1.: a) Schematic of the multilayer structure of an APL used for packaging. b) SEM image of the cross-section of an APL from a chip bag. c) Raman spectra of the cross-section of the APL. d) Solar reflectance of the goods contacting side of the APLs collected from different packaging bags: chip bag, coffee bag, and FFP2 mask bag, with an incidence angle of 8°. The AM 1.5 solar spectrum is plotted as the background.[29] e) Average solar reflectance of the goods contacting side of the chip bag, coffee bag, and FFP2 mask bag at different incidence angles.

impact of the layer thickness on material optical properties in both the solar and MIR ranges has been investigated in a previous study.[30]

To experimentally demonstrate the capability of the plain APL for PDRC, the passive cooling performance of the APLs, i.e., chip bag, coffee bag, and mask bag, was determined with a homemade indoor setup. Figure 6.2b shows the schematic of the indoor setup, and detailed information on the design is presented in our previous work.[31] Compared to conventional field testing under uncontrollable weather conditions, indoor measurements ensure reproducible measurements under controlled and stable conditions, providing better cooling performance evaluation, especially for comparing different samples. In addition, various parameters, such as solar intensity and ambient temperature, are independent and can be tuned individually with the designed indoor setup. By contrast, the study of the influence of a single parameter on material cooling performance is not possible for conventional field testing due to the time-varying weather conditions.

The indoor measurement was first carried out without (w/o) solar light. A steady-state temperature of 18.4, 16.4, and 13.8 °C was observed for the chip bag, coffee bag, and mask bag, respectively (Figure 6.2c–e). Compared to the 'ambient temperature' (20.7 °C), obtained with an Ag mirror under identical measurement conditions without

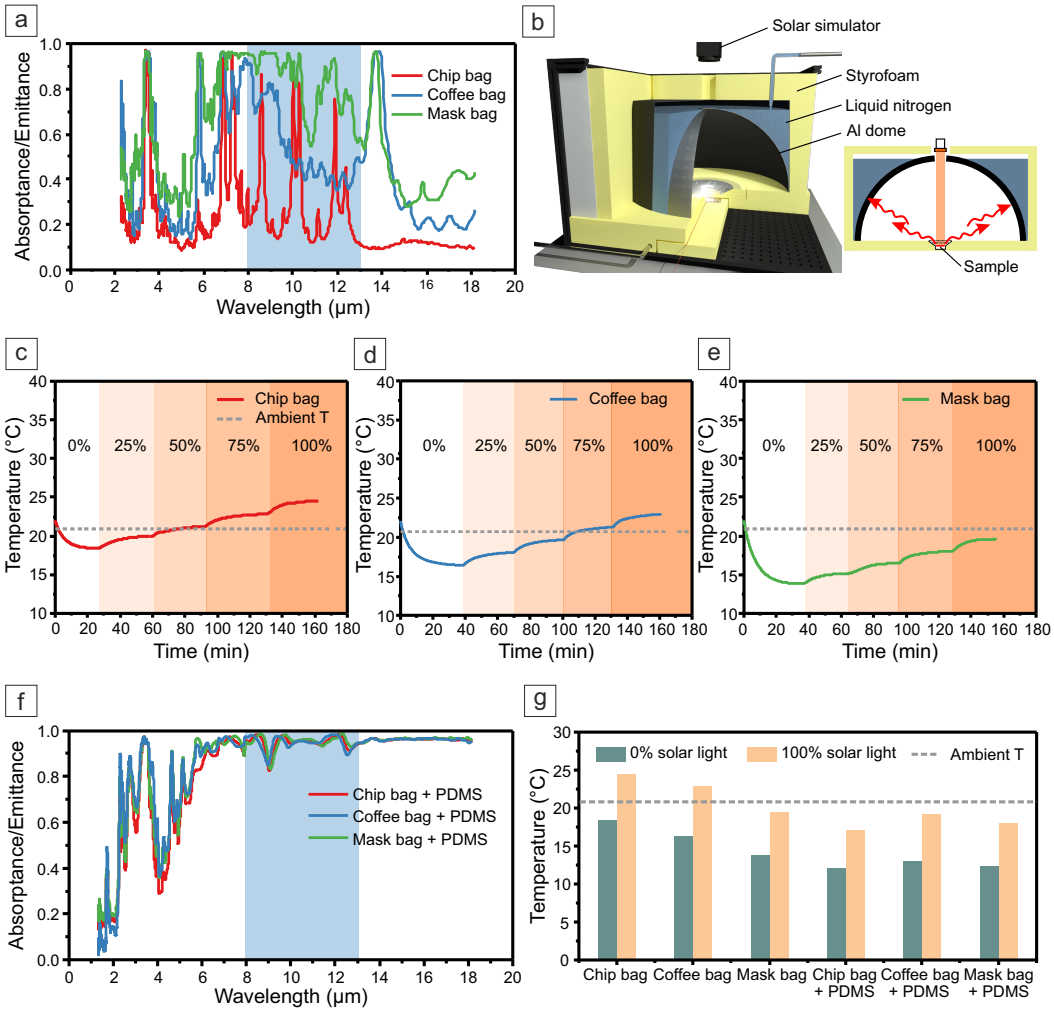

Figure 6.2.: Indoor characterization of plain and PDMS modified APL bags: chip bag, coffee bag, and FFP2 mask bag. a) Optical properties of plain APL bags in the MIR range. The blue shaded area indicates the atmosphere window (8–13 µm). b) Schematic of the setup for indoor measurements. Continuous temperature measurements of the APL bags with stepwise increase of the solar intensity from 0 % to 100 % of one sun for a c) chip bag, d) coffee bag, and e) FFP2 mask bag. f) Optical properties of PDMS (thickness ≈200 µm) coated APL bags. g) Steady-state temperature of plain and PDMS-coated laminated Al packaging bags with and without 100 % solar light. The dotted line indicates the ambient temperature.

solar light, all the APLs show varying degrees of passive cooling performance. The mask bag provides the best subambient cooling, 6.9 K, followed by the chip bag (2.3 K) and coffee bag (4.3 K), owing to the higher emittance in the MIR regime. Subsequently, AM 1.5 solar light was applied to the samples by a solar simulator to imitate the cooling performance characterization in the daytime. To reveal the impact of the solar radiation intensity on the passive cooling performance, the solar intensity was increased stepwise from 0 % to 25 %, 50 %, 75 %, and 100 % of one sun power (1000 W m^{-2}), after the sample's temperature reaches a steady state. Note that our previous study showed that the intensity of the light reaching the sample is about 75 % of the initial power due to the absorption, scattering, and reflection of the convection shield in the indoor setup.[31] As shown in Figure 6.2c–e, the solar illumination increases the temperature of all APL samples until a steady state is reached. Moreover, the solar energy uptake exceeds the radiative heat loss at a certain level of solar intensity for the chip bag and coffee bag. As a result, the steady-state temperature is higher than the ambient temperature, for instance, 50 % solar intensity for the chip bag and 75 % solar intensity for the coffee bag, which follows the degree of emittance of those sample in the sky-window range. This observation implies that a net heat loss can only be achieved under a certain solar intensity level for the chip bag and the coffee bag due to their inherently low MIR emittance. By contrast, the mask bag allows net passive cooling even under a sunlight power of 100 %.

To enhance the radiative heat release by increasing the MIR emittance, we introduced PDMS onto the APLs. PDMS, a widespread and easily processable polymer, has been widely used as standard material for fabricating passive daytime cooling devices, ensuring a direct comparison between the APL waste-based cooling foil and PDMS-based cooling devices reported in the literature. Furthermore, its optical transparency is ideal for retaining the reflective properties of the APL support structure and its flexibility ensure a good adhesion to the APL foil. In particular, a PDMS layer (≈200 µm) was coated onto the APLs via the doctor blading technique. The IR absorption spectra illustrate the significant enhancement of the APLs in the MIR region (Figure 6.2f). An average emittance of up to 0.94 was obtained for all PDMS-coated APLs. The cooling performance of plain APLs and PDMS-coated APLs, determined by the indoor setup, is summarized in Figure 6.2g. Compared to plain APLs, a promising PDCR performance is obtained with all PDMS-coated APLs. A subambient cooling was observed with all PDMS-coated APLs for both dark and light conditions. Furthermore, no pronounced difference was observed between the PDMS-coated chip bag, coffee bag, and mask bag for measurements in the dark. However, with the presence of 100 % solar light, the PDMS-coated chip bag shows a slightly lower temperature, owing to its high solar reflectance (Figure 6.1d) compared to the coffee and mask bag.

Apart from the steady state temperature reduction measurements, the indoor setup also allows for determining the net cooling power. To measure the net cooling power of the plain and PDMS-coated APLs, the samples were heated to the 'ambient' temperature. The required heating power at this temperature represents the net cooling power of the emitter. An observation similar to the steady-state temperature measurements was obtained for the cooling power measurements (Figures 6.S6 and 6.S8). Solar illumination decreases the net cooling power of all tested samples. The plain chip bag and coffee bag only possess net cooling power below a certain level of solar intensity. In contrast, the plain mask bag shows net cooling power even under illumination with full power. The solar light intensity follows a linear dependency for the steady-state temperature (Figure 6.S5), and the net cooling power (Figure 6.S7), indicating the stable and constant measurement conditions. In addition, the PDMS coating dramatically enhances the net cooling power for all APLs. Due to the absence of the atmospheric window in the indoor setup, the net cooling power measurements only allow an indirect comparison to the outdoor field tests. To illustrate the cooling performance of PDMS-coated APLs more clearly, we normalized the cooling power of the plain and PDMS-coated APLs by the cooling power measured with a standard passive daytime cooling sample namely a PDMS-coated Ag mirror (Figure 6.S9). Compared to this standard passive cooling sample, a comparable cooling power can be observed for all PDMS-coated APLs in the dark. With the full power of solar light, the PDMS-coated APLs could still provide up to 25 % of the net cooling power of the reference material.

To further verify the potential of APL waste as PDRC material for energy saving, we determined the cooling performance of plain and PDMS-coated APLs with field testing under a clear sky in Bayreuth, Germany. Figure 6.3a illustrates the schematic of the homemade setup, and a photograph of the setup is shown in Figure 6.S10. During the measurement, the samples were placed into identical sample holders surrounded by styrofoam to block undesired thermal conduction. A highly transparent, low-density polyethylene (LDPE) foil suppresses convective heat losses. Besides the tested sample APLs, the temperature of the ambient and a graphite sample were also collected for comparison. Figures 6.3b, c shows the real-time temperature of the tested plain and PDMS-coated APLs under direct sunlight. Due to substantial solar reflectance, the plain APLs exhibit a much lower temperature than graphite. The temperature difference was 18.1, 19.7, and 21.2 K between graphite and the chip bag, coffee bag, and mask bag, respectively, under average solar irradiation of 866.2 W m^{-2}. The significant temperature difference confirms the potential of APLs as a back reflector for PDRC. However, due to inadequate radiative heat release, the temperature of all tested packaging bags is slightly higher than the ambient. With the introduction of the PDMS coating, thermal radiation is greatly facilitated for all APLs. This leads to coinciding ambient and sample temperatures under average solar irradiation of 847.8 W m^{-2}. In addition, a temperature

difference of about 22.5 K between graphite and the PDMS-coated APLs is obtained. Despite the deviation of the absolute value between the indoor measurement and the field testing, the trend agrees well. The deviation is mainly attributed to the absence of the atmosphere for the indoor setup and the inconsistent conditions between indoor and outdoor measurements, such as solar intensity and humidity.

The cooling foils based on APL waste are flexible, possess excellent mechanical strength, and can be scaled up. In the first step to accessing large area foils, stitching multiple packaging bags via plastic joining techniques, including welding and adhesive bonding,[32] are expected to be suitable processes that need to be adapted to APL waste. Concomitant with the areal scale-up, a consistent high solar reflectance of the patches also needs to be realized. These engineering challenges are beyond the scope of this work. In the second step, an emitter layer, such as PDMS, can be coated with well-established processing techniques, like blade coating and roll-to-roll coating.[33] Figure 6.3d shows a whole piece of a chip bag coated with PDMS via blade coating. Such low-cost, flexible, and free-standing cooling foils can be practically applied to any target surface. To emphasize this point, we applied the PDMS-coated chip bag to a standard transparent container using double-sided adhesive tape. Subsequently, we monitored the temperature inside the cooling foil-covered container (C1) under direct sunlight. The inside temperature of an identical container (C3) and a plain chip bag-covered box (C2) were also recorded for comparison. Figure 6.3e shows the schematic and a photograph of the measurement. All samples were placed on an Al foil-covered styrofoam plate to avoid undesired thermal conduction. In Figure 6.3f, we plotted the continuous inner temperature of different containers and the temperature difference relative to C3, along with the solar irradiation during the measurement. With reflecting most of the solar light, the plain chip bag-coated container (C2) shows a much lower temperature than the bare container (C3), which exhibits a substantial amount of greenhouse warming. The average temperature difference is 7.2 K from 11:30 to 13:30, under an average solar irradiation of 668 W m^{-2}. Furthermore, the cooling foil-covered container (C1) maintained its temperature close to the open air temperature and is much lower than C2 and C3 due to the high solar reflection and superior heat release via MIR radiation. The average temperature difference between C1 and C3 is 12.6 K. The much lower temperature achieved with APL-based cooling foil proves that it can effectively protect the target object from overheating under intensive solar light. In addition, the protection will be more pronounced when applying the cooling foil on surfaces of solar light-absorbing materials.

To theoretically quantify the cooling performance of the plain and PDMS-coated APLs, i.e., chip bag, coffee bag, and mask bag, we calculated their net cooling power for both daytime, and nighttime (Figures 6.S11 and 6.S12), based on the radiative model,[34] $P_{cool} = P_{mat} - P_{sun} - P_{atm} - P_{nonrad}$. Here, P_{mat} is the emitter thermal irradiation power,

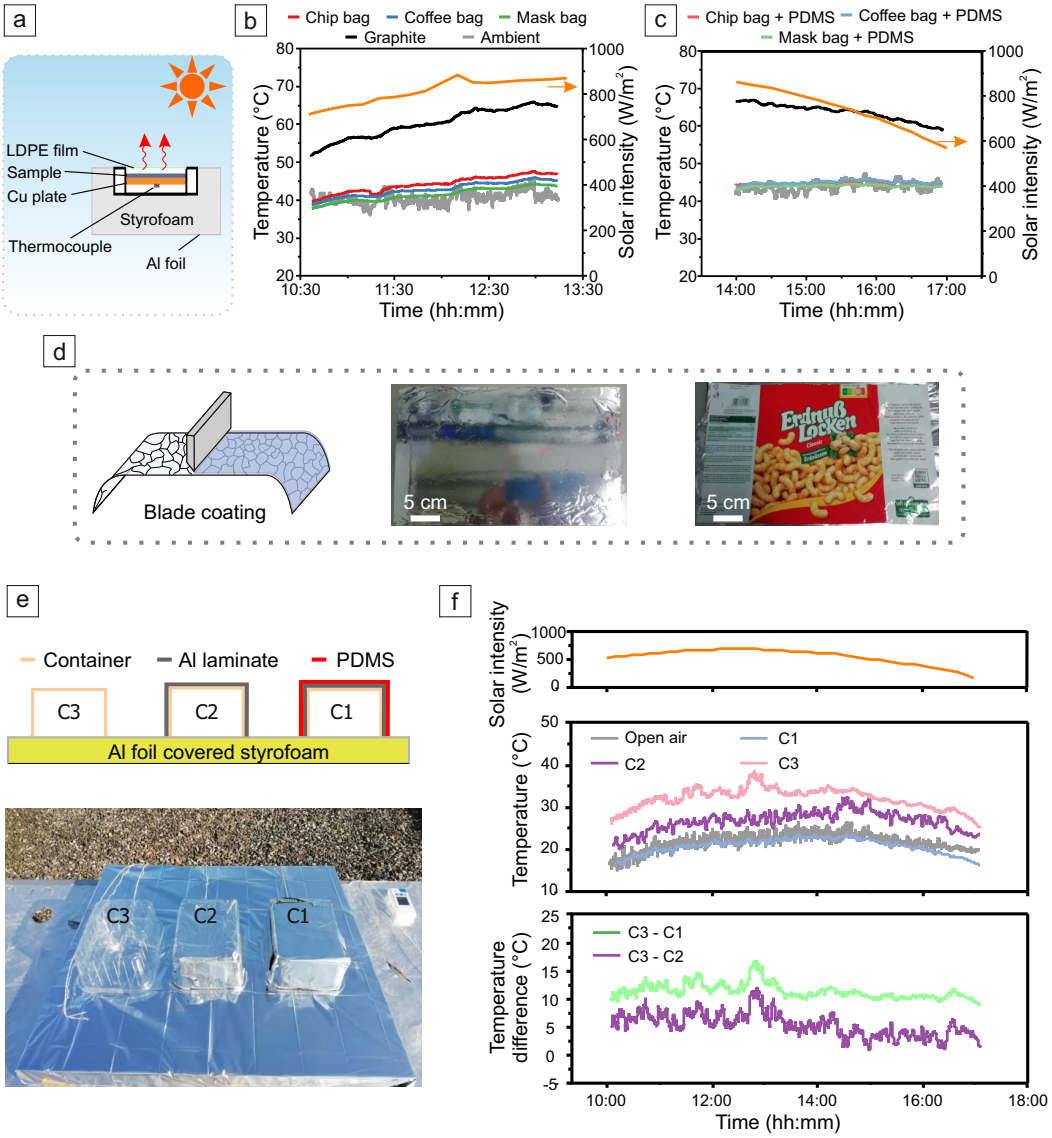

Figure 6.3.: a) Schematic of the setup used for outdoor measurements. Outdoor measurements for b) plain and c) PDMS-coated APL bags. The measurement was carried out under a clear sky on 18.06.2022 in Bayreuth, Germany. d) Schematic of the blade coating technique and photographs of the entire piece of the PDMS-coated chip bag, goods contacting side (left) and ink side (right). Application of the APL waste-based cooling foil on a target surface. e) Schematic and photograph of temperature measurements for different samples. C1, transparent PET box covered with PDMS-coated chip bag; C2, transparent PET box covered with plain chip bag; C3, transparent PET box. f) Temperature tracking of different samples and temperature differences shown in e). The measurement was carried out under a clear sky on 24.03.2022 in Bayreuth, Germany.

P_{sun} is the solar power absorbed by the emitter, P_{atm} is the emitter absorbed power from the atmosphere, and P_{nonrad} is the absorbed power caused by conduction and convection, which is defined as $P_{nonrad} = h_c \cdot (T_{atm} - T_{mat})$, and h_c is the nonradiative heat transfer coefficient. Solar irradiation varies over the daytime. An average solar irradiation of 500 W m^{-2} is thus applied to the daytime calculations (see the Supporting Information for calculation details). For the plain APLs, a net cooling power of −33.7, −12.3, and 38.3 W m^{-2} are expected for the chip, coffee, and mask bags, respectively. Because of the distinct inherent optical properties, only the mask bag exhibits decent PDRC performance due to its high emissivity in the MIR regime. Still, a promising PDRC performance is obtained for all APLs when coated with PDMS. The net cooling power for the PDMS-coated chip, coffee, and mask bag is 71.3, 45.1, and 50.4 W m^{-2}, respectively. Moreover, when the net cooling power is zero, a subambient cooling of 4.9, 3.1, and 3.5 K could be expected for the PDMS-coated chip bag, coffee bag, and mask bag, respectively, with $h_c = 10$ W m^{-2} K^{-1}. In the nighttime, without the uptake energy from solar light, cooling performance, in terms of net cooling power and subambient cooling, is greatly enhanced for all cooling foils (Figures 6.S11 and 6.S12). The combination of indoor testing with controlled parameters, the outdoor field tests under realistic conditions, and the theoretical description all confirm the adequate optical properties of upcycled APL waste to be reused as (daytime) passive cooling material.

In this work, PDMS is introduced as an exemplary emitter to enhance the thermal radiation of the plain APLs. Various other emitters could be applied to APLs, too, as long as they possess low solar absorption and high mid-infrared emissivity. Generally, PDRC emitters can be classified into two categories: broadband emitters and selective emitters. Figure 6.4a plots the absorptance/emittance spectra of an ideal broadband emitter ($E_{\lambda>4\,\mu m} = 1$, $E_{\lambda<4\,\mu m} = 0$) and a selective emitter ($E_{8\,\mu m<\lambda<13\,\mu m} = 1$, $E_{\lambda<8\,\mu m \vee \lambda>13\,\mu m} = 0$) both with zero solar absorption. The ideal broadband emitter has unit emittance over the entire MIR range, while the ideal selective emitter exhibits unit emittance only in the atmosphere window (8–13 µm). To reveal the impact of the emitter selectivity on the PDRC performance of APL waste-based cooling foils, we calculated the net cooling power as a function of average emissivity for both APL-supported broadband emitters and selective emitters. For simplicity, the absorptance of the APL support layer has been taken as constant (14 %), and its emissivity in the mid-infrared range was excluded from the calculation. Due to the fact that the solar intensity varies over the daytime, the influence of solar intensity on cooling performance is also considered in the calculation. As shown in Figure 6.4b, in the nighttime, at an emitter temperature of 26.85 °C (300 K), an increase of the average emissivity of the entire cooling foil from 0 to 1 increases the net cooling power from 0 to 215 and 132 W m^{-2} for the broadband emitter and selective emitter modified APL, respectively. During daytime, the APL cooling foil reduces the net cooling power by absorbing about 14 % of solar energy. With

a solar radiation of 1000 W m^{-2}, a selective emitter-modified APL cannot exhibit a net passive cooling performance. To achieve a net cooling performance with broadband emitter-modified APL, the average MIR emissivity of the emitter layer should be larger than 0.73. With an average emissivity of 1, a net cooling power of 51.5 W m^{-2} can be achieved by the cooling foil under a solar illumination of 1000 W m^{-2}. Since solar light intensity varies over the daytime and barely exceeds 900 W m^{-2} we firmly believe that all APL-based cooling foils will ensure an appealing PDRC performance throughout the entire day. Furthermore, these calculations confirm the solar radiance-dependent measurements (Figure 6.1c-–e) and demonstrate that a reflectance of ≈ 86 % of the APL waste foil is sufficient for passive daytime cooling depending on the interplay between solar radiance and emissivity of the emitter layer.

The upcycling of APL waste for the fabrication of passive daytime cooling foils will significantly alleviate the predicament of the current recycling of aluminum-laminated packing foils. In addition, the APL-based passive daytime cooling foils are low-cost, scalable, and flexible, allowing their widespread worldwide application. To predict the energy-saving potential of APL-based cooling foils on building energy efficiency, we predicted the year-round cooling energy consumption for the United States and mainland China using EnergyPlus (Version 9.6.0).[36–38] For the simulations, 1020 and 270 locations across the United States and mainland China, respectively, were included in the calculations. The optical properties of the traditional material (acquired from EnergyPlus) and APL-based cooling foils that are input into the model are listed in Table 6.1. The energy-saving is obtained by comparing the energy consumption between the traditional material and APL-based cooling foil-covered outer walls and roof of a building. An energy-saving map is created for the United States and mainland China, respectively, as shown in Figure 6.4d. APL-based foils allow promising energy savings in most areas, with expectedly higher energy savings in the hotter southern areas. With the upcycling of APL waste for PDRC, we believe that a substantial amount of cooling energy can be saved annually, while simultaneously avoiding the large-scale fabrication of additional APLs for this sustainable cooling technology.

6.4 Conclusions

This work introduced a promising strategy to turn postconsumer APL waste into high-value PDRC applications. We experimentally and theoretically verified the potential of laminated Al foils for passive daytime cooling. Due to the inherent presence of the Al layer, APLs enable a high solar reflection, up to 86 %. Using the laminated Al foil as the back reflector and PDMS as an infrared emittance enhancer, a simple but effective passive daytime cooling foil is fabricated, exhibiting remarkable cooling performances. Moreover,

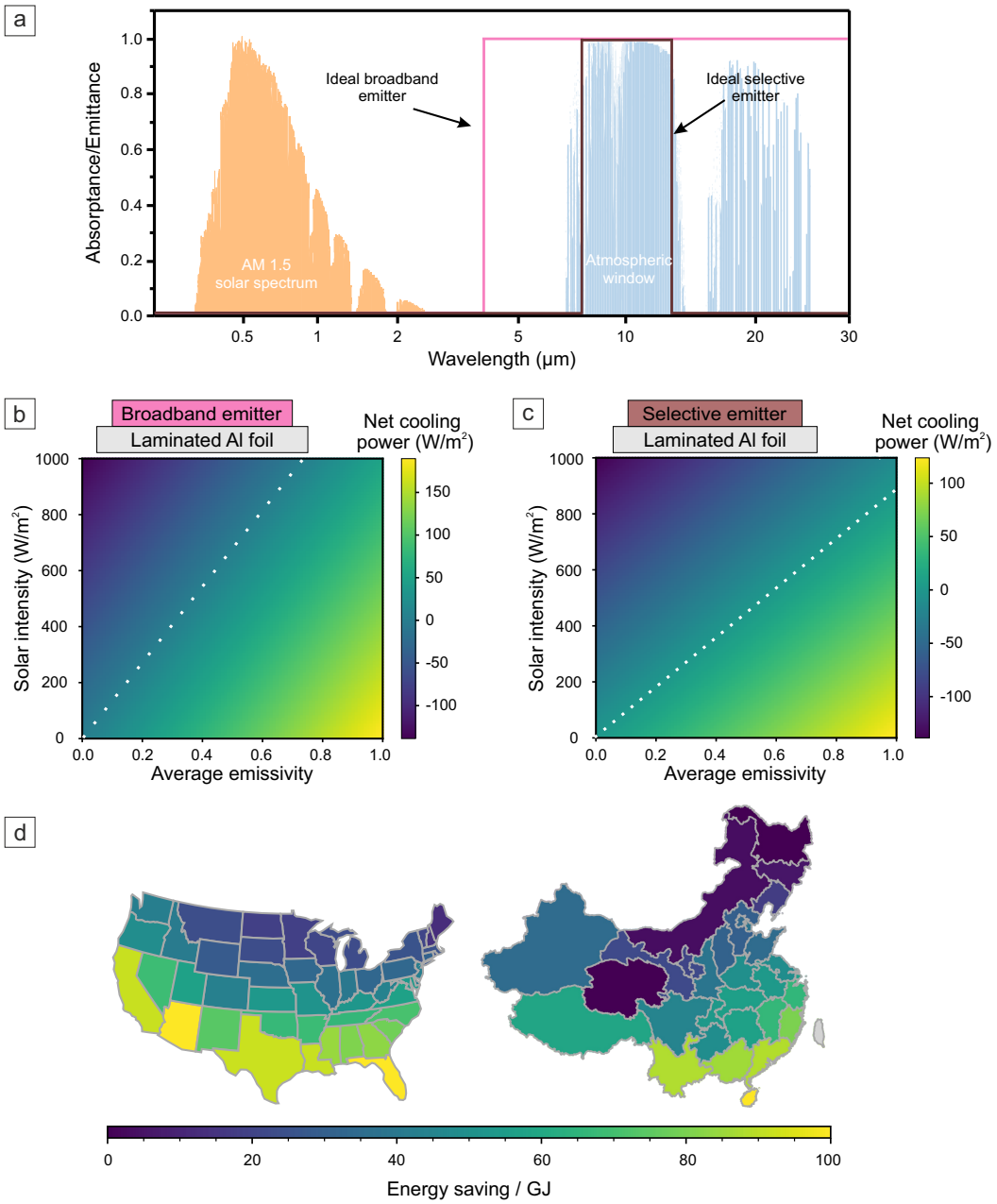

Figure 6.4.: a) Optical properties of an ideal broadband emitter and selective emitter. The gray dotted line indicates the solar absorption of the APL foil. AM 1.5 solar spectrum[29] and atmosphere transparency[35] are plotted as background. Predicted net cooling power for APL supported b) broadband emitter and c) selective emitter with varying solar intensity and emissivity. The ambient temperature is 300 K. The average solar reflectance of the cooling foils is assumed as 0.86. The dotted lines indicate zero net cooling power. d) Predicted annual energy savings across the United States and mainland China with APL-supported broadband emitter coating on walls and roofs for a typical midrise apartment building.

such flexible cooling foils can be readily applied on any target surface, protecting it from harsh sunlight. We believe sustainable, low-cost, and scalable APL waste-based passive daytime cooing foils can significantly contribute to environmental protection while ensuring a substantial reduction in global energy consumption for cooling applications.

6.5 Experimental Section

Sample Fabrication –Laminated Al Foil

Various laminated Al packaging bags were collected from plastic waste, followed by cleaning with standard detergent and adequate water. Subsequently, the samples were rinsed with ethanol and Milli-Q water and dried for further application.

PDMS-Coated Laminated Al Foil

A prepolymer of PDMS (Sylgard 184, Dow Chemical) was mixed with a curing agent in a ratio of 10:1 (by weight) and degassed in a desiccator under a vacuum. Subsequently, films with a thickness of around 200 µm were prepared via doctor blading on the laminated Al foil. The PDMS layer was cured at room temperature for 48 h.

All the samples were cut to a size of dia. = 5 cm for the indoor and rooftop measurements.

SEM

The cross-section of a chip bag was prepared by cryo-fracturing and cutting at RT with a razor blade. SEM images were taken with a Zeiss Ultra plus (Carl Zeiss AG, Germany) at an operating voltage of 3 kV and with in-lens detection.

Raman Spectroscopy Measurement

A confocal WITec Alpha 300 RA+ Raman imaging system equipped with a UHTS 300 spectrometer and a back-illuminated Andor Newton 970 EMCCD camera together with the WITec Suite FIVE 5.3 software package was employed for Raman spectroscopy measurements. Typically, laser intensities of 2–5 mW and an integration time of 0.5 s (grating: 600 g mm^{-1}) were employed. Single spectra were acquired with an excitation wavelength of $\lambda = 532$ nm, and 50 measurements were accumulated for a spectrum. For line scans, a 100× objective (Zeiss EC Epiplan-Neofluar 100×, NA = 0.9) was used, and the step size was 0.2 µm. All spectra were corrected for cosmic ray spikes and subjected to

a background removal routine. The WITec TrueMatch Raman spectra database software in combination with a self-created polymer database was applied to identify the polymer layer based on the obtained spectra.

Optical Properties Characterization with UV–Vis and FTIR Spectroscopy

Solar reflectance was measured by using a UV–vis spectrometer (Cary 5000, Agilent Technologies), equipped with an integrating sphere accessory (Labspheres), with a fixed incident angle of 8°. A Spectralon diffuse reflectance standard (Labspheres) was applied as the reference. Angular reflectance measurements were carried out with samples placed inside the integrating sphere at various angles with respect to the incident light. The optical property of samples in the MIR regime was determined with an FTIR spectroscopy (Vertex 70, Bruker) equipped with a gold-coated integrating sphere accessory (A562, Bruker). A gold mirror was applied as the reference. The absorptance (emittance) was calculated with absorptance (emittance) = 1− Reflectance. Transmission is assumed to be negligible due to the presence of the Al layer.

Indoor Measurement for Cooling Performance Characterization

For all indoor measurements, dried air was warmed up by a water bath to 40 °C and flushed in the area between the convection shield and measurement cell with a volumetric flow rate of 80 L min^{-1}. The Al dome was cooled with liquid nitrogen to about −190 °C. Before filling the liquid nitrogen into the setup, the inner space of the dome is flushed with nitrogen to avoid water condensation. The temperature of the dome is maintained constant during the entire measurement by continuously filling liquid nitrogen into the setup. A thermocouple (type T) is used for recording the temperature, and data are collected by a digital multimeter (DAQ6510, Tektronix, Germany) every 5 s.

For the measurements with different solar intensities AM 1.5 solar light is provided by a solar simulator (AX-LAN400, SCIENCETECH, CANADA) with an illumination area of 5 × 5 cm^2. The solar intensity was changed stepwise from 0 % to 25 %, 50 %, 75 %, and 100 % of one sun (≈1000 W m^{-2}) after the sample temperature reached a steady state.

The cooling power measurement was conducted with a homemade feedback heater. Samples were placed on the feedback heater and heated to a predetermined temperature. The required heating power represents the cooling power of the sample.

Rooftop Measurement

Rooftop measurements for the plain and PDMS coated APLs were carried out on the roof of a three-floor building (18.06.2022, University of Bayreuth, Bayreuth, Germany) under a clear sky. All the test samples were each placed in identical homemade sample holders. The holders were thermally insulated by Styrofoam and covered with Mylar aluminum foil. A LDPE foil with a thickness of ≈15 µm is applied to prevent convective heat transfer. The temperatures of the samples were determined by Pt-100 temperature sensors and recorded with a digital multimeter (DAQ6510, Tektronix, Germany) every 5 s. One sample holder covered with Al foil instead of LDPE foil was used to obtain the ambient temperature. The solar irradiance data were collected from the weather station at the University Bayreuth (Ecological-Botanical Garden, 400 m away from the rooftop measurement).

6.6 Acknowledgements

The authors gratefully thank Stefan Rettinger and the mechanical and electrical workshop (University of Bayreuth) for their technical support. They acknowledged support by the Bavarian Polymer Institute and the KeyLabs 'Electron Microscopy' and 'Synthesis and Molecular Characterization'. They are indebted to Prof. Christoph Thomas for kindly providing the solar radiance and air temperature data. The authors acknowledged financial support from the European Research Council (ERC) under the European Union's Horizon2020 research and innovation program (Grant Agreement No. 101082087). Open access funding enabled and organized by Projekt DEAL.

6.7 References

[1] O. Horodytska, F. J. Valdes, A. Fullana, *Waste Manage.* **2018**, *77*, 413–425.

[2] M. Lamberti, F. Escher, *Food Rev. Int.* **2007**, *23*, 407–433.

[3] J. N. Hahladakis, E. Iacovidou, *Sci. Total Environ.* **2018**, *630*, 1394–1400.

[4] A. S. Bauer, M. Tacker, I. Uysal-Unalan, et al., *Foods* **2021**, *10*, 2702.

[5] G. Robertson, *Recycling* **2021**, *6*, 20.

[6] A. Ahamed, A. Veksha, A. Giannis, G. Lisak, *Curr. Opin. Chem. Eng.* **2021**, *32*, 100684.

[7] A. Farrukh, S. Mathrani, A. Sajjad, *Sustainability* **2022**, *14*, 4737.

[8] S. F. Zhang, L. L. Zhang, K. Luo, Z. X. Sun, X. X. Mei, *Waste Manage. Res.* **2014**, *32*, 317–22.

[9] T. W. Walker, N. Frelka, Z. Shen, et al., *Sci. Adv.* **2020**, *6*, eaba7599.

[10] A. Korkmaz, J. Yanik, M. Brebu, C. Vasile, *Waste Manage.* **2009**, *29*, 2836–41.

[11] J. Haydary, D. Susa, J. Dudas, *Waste Manage.* **2013**, *33*, 1136–41.

[12] S. Yin, R. Rajarao, B. Gong, et al., *J. Clean. Prod.* **2019**, *211*, 321–329.

[13] K. Kremser, P. Gerl, A. B. Borrás, et al., *Resour. Conserv. Recy.* **2022**, *185*, 106444.

[14] European Commission, A European strategy for plastics in a circular economy, Generic, **2018**.

[15] L. Al-Ghussain, *Environ. Prog. Sustain.* **2019**, *38*, 13–21.

[16] V. Thompson, A. T. Kennedy-Asser, E. Vosper, et al., *Sci. Adv.* **2022**, *8*, eabm6860.

[17] G. A. Meehl, C. Tebaldi, *Science* **2004**, *305*, 994–7.

[18] S. E. Perkins-Kirkpatrick, S. C. Lewis, *Nat. Commun.* **2020**, *11*, 3357.

[19] X. Yin, R. Yang, G. Tan, S. Fan, *Science* **2020**, *370*, 786–791.

[20] M. M. Hossain, M. Gu, *Adv. Sci.* **2016**, *3*, 1500360.

[21] Y. Zhu, Y. Ye, D. Wang, Y. Cao, *OSA Contin.* **2021**, *4*, 416.

[22] L. Zhou, H. Song, J. Liang, et al., *Nat. Sustain.* **2019**, *2*, 718–724.

[23] X. Yu, J. Chan, C. Chen, *Nano Energy* **2021**, *88*, 106259.

[24] J. Mandal, Y. Fu, A. C. Overvig, et al., *Science* **2018**, *362*, 315–319.

[25] D. Li, X. Liu, W. Li, et al., *Nat. Nanotechnol.* **2021**, *16*, 153–158.

[26] X. Li, J. Peoples, Z. Huang, et al., *Cell Rep. Phys. Sci.* **2020**, *1*, 100221.

[27] J. Song, W. Zhang, Z. Sun, et al., *Nat. Commun.* **2022**, *13*, 4805.

[28] A. Gopanna, R. N. Mandapati, S. P. Thomas, K. Rajan, M. Chavali, *Polym. Bull.* **2018**, *76*, 4259–4274.

[29] Solar Spectral Irradiance: Air Mass 1.5, Web Page, `http://rredc.nrel.gov/solar/spectra/am1.5` (accessed June, 2022), **2022**.

[30] K. Herrmann, T. Lauster, Q. Song, M. Retsch, *Adv. Energy Sustain. Res.* **2022**, *3*, 2100166.

[31] Q. Song, T. Tran, K. Herrmann, et al., *Cell Rep. Phys. Sci.* **2022**, *3*, 100986.

[32] D. Grewell, A. Benatar, *International polymer processing* **2007**, *22*, 43–60.

[33] K. Lin, L. Chao, T. C. Ho, et al., *Energ. Buildings* **2021**, *252*, 111400.

[34] B. Zhao, M. Hu, X. Ao, N. Chen, G. Pei, *Appl. Energy* **2019**, *236*, 489–513.

[35] Spectral atmospheric transmittance, Web Page, https://www.gemini.edu/observing/telescopes-and-sites/sites#Transmission (accessed June, 2022), **2022**.

[36] X. Li, B. Sun, C. Sui, et al., *Nat. Commun.* **2020**, *11*, 6101.

[37] Y. Peng, L. Fan, W. Jin, et al., *Nat. Sustain.* **2021**, *5*, 339–347.

[38] S. Wang, T. Jiang, Y. Meng, et al., *Science* **2021**, *374*, 1501–1504.

6.8 Supplemental Information

6.8.1 Numerical Simulation

Calculation of average solar reflection and MIR absorptance/emittance

Average solar reflectance ($\bar{R}_{\text{solar}}$) is calculated by:

$$\bar{R}_{\text{solar}} = \frac{\int_{0\,\mu\text{m}}^{2.5\,\mu\text{m}} I_{\text{solar}}(\lambda) \cdot R_{\text{solar}}(\lambda)\mathrm{d}\lambda}{\int_{0\,\mu\text{m}}^{2.5\,\mu\text{m}} I_{\text{solar}}(\lambda)\mathrm{d}\lambda} \tag{6.1}$$

Where λ is the wavelength, $I_{\text{solar}}(\lambda)$ is the ASTM G173 Global solar intensity spectrum,[1] and $R_{\text{solar}}(\lambda)$ is the surface spectral reflectance.

Average absorptance/emittance ($\bar{\varepsilon}$) is calculated by:

$$\bar{\varepsilon} = \frac{\int_{0\,\mu\text{m}}^{30\,\mu\text{m}} I_{\text{BB}}(T,\lambda) \cdot \varepsilon(T,\lambda)\mathrm{d}\lambda}{\int_{0\,\mu\text{m}}^{30\,\mu\text{m}} I_{\text{BB}}(T,\lambda)\mathrm{d}\lambda} \tag{6.2}$$

Where $I_{\text{BB}}(T,\lambda)$ is the spectral emittance of a blackbody at temperature T ($T = 300\,\text{K}$ is applied to all $\bar{\varepsilon}$ calculations) and $\varepsilon(T,\lambda)$ is the surface spectral emittance.

Calculation of net cooling power

Cooling power calculation:

The net cooling power P_{cool} is defined as

$$P_{\text{cool}} = P_{\text{mat}} - P_{\text{sun}} - P_{\text{atm}} - P_{\text{nonrad}} \tag{6.3}$$

P_{mat} is the power radiated by the material, which is given by

$$P_{mat} = 2\pi \int_0^{\pi/2} \sin\theta \cos\theta \mathrm{d}\theta \int_0^{\infty} I_b(\lambda, T_{mat}) \cdot \varepsilon_{mat}(\lambda, \theta)\mathrm{d}\lambda \tag{6.4}$$

$$I_b = \frac{2hc^2}{\lambda^5} \cdot \frac{1}{e^{\frac{hc}{\lambda k_B T}} - 1} \tag{6.5}$$

Where h is Planck's constant, k_B is Boltzmann's konstant and c is the light speed.

$$P_{sun} = \int_0^{\infty} I_{AM1.5}(\lambda) \cdot \varepsilon_{mat}(\lambda)\mathrm{d}\lambda \tag{6.6}$$

$$P_{atm} = 2\pi \int_0^{\pi/2} \sin\theta \cos\theta \int_0^{\infty} I_b(\lambda, T_{atm}) \cdot \varepsilon_{atm}(\lambda, \theta)\mathrm{d}\lambda\mathrm{d}\theta \tag{6.7}$$

Where $\varepsilon_{atm}(\lambda, \theta) = 1 - \tau_{atm}(\lambda, 0)^{\frac{1}{\cos\theta}}$,[2] with $\tau_{atm}(\lambda, 0)$ being the spectral transmittance of the atmosphere.[3]

Nonradiative power exchange is calculated with:

$$P_{nonrad} = h_{nonrad} \cdot (T_{atm} - T_{mat}) \tag{6.8}$$

Where h_{nonrad} is the non-radiative heat transfer coefficient.

$\varepsilon_{mat}(4\,\mu m < \lambda) = 1$ and $\varepsilon_{mat}(8 < \lambda < 13\,\mu m) = 1$, else $\varepsilon_{mat} = 0$, is applied for the net cooling power calculation of APLs-supported broadband emitter and selective emitter, respectively. We assume that the emissivity of the broadband and selective emitter and APLs-based cooling foil are directional-independent.

Simulation of energy saving for China and US

We used EnergyPlus v9.6.0 for the evaluation of annual energy consumption.[4] The modeled building is based on a midrise apartment building defined by the American National Standards Institute.[5] We created two versions of this building: One with traditional materials as included in EnergyPlus and one with our material properties for the wall and roof, as shown in Table 6.1.

Table 6.1.: Material properties used for energy saving simulations.

Absorptance	Traditional material	Our material
Visible ($0.37\,\mu m < \lambda < 0.78\,\mu m$)	0.7	0.152
Solar ($0.3\,\mu m < \lambda < 2.5\,\mu m$)	0.7	0.14
Thermal ($2.5\,\mu m < \lambda$)	0.9	1

The weather for the USA is the Typical Meteorological Year 3 data set.[6] It includes hourly data for 1020 locations across the USA for a 1-year period. For China, the Chinese Standard Weather Data collected by the China Meteorological Bureau[7] has been used, consisting of data for 270 locations. For each location, two yearly simulations were run: one with the traditional and one with ideal APL-based cooling foil. Afterward, the total yearly energy consumption was averaged for all locations in each state or province. The energy saving is the difference between the averaged data of the traditional materials and our materials.

6.8.2 Supporting Figures

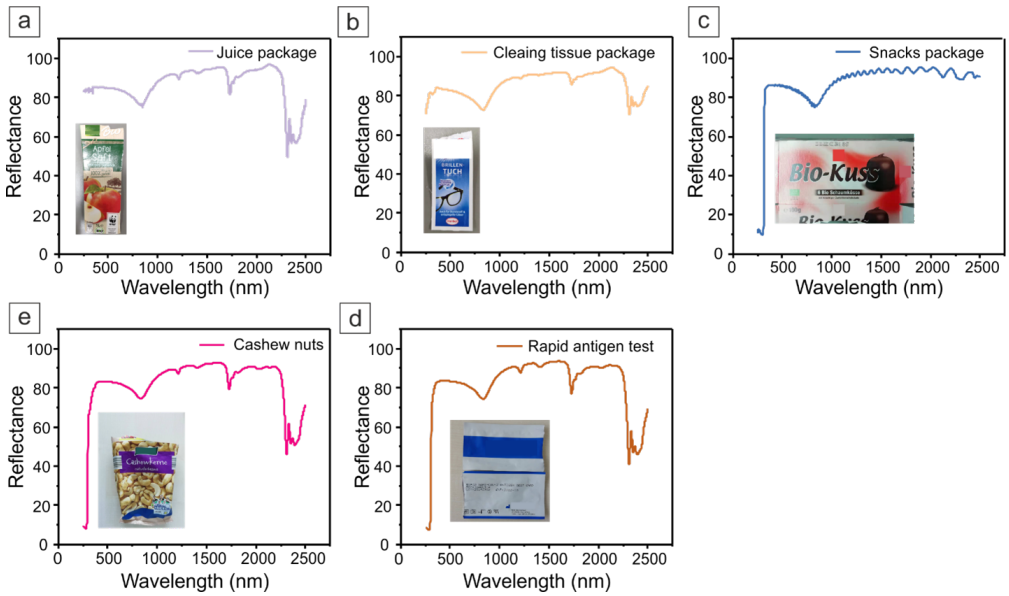

Figure 6.S1.: Solar reflectance of various packaging laminated Al foils: a) juice package, b) cleaning tissue package, c) snacks package, d) Cashew nuts bag, and d) rapid antigen test bag.

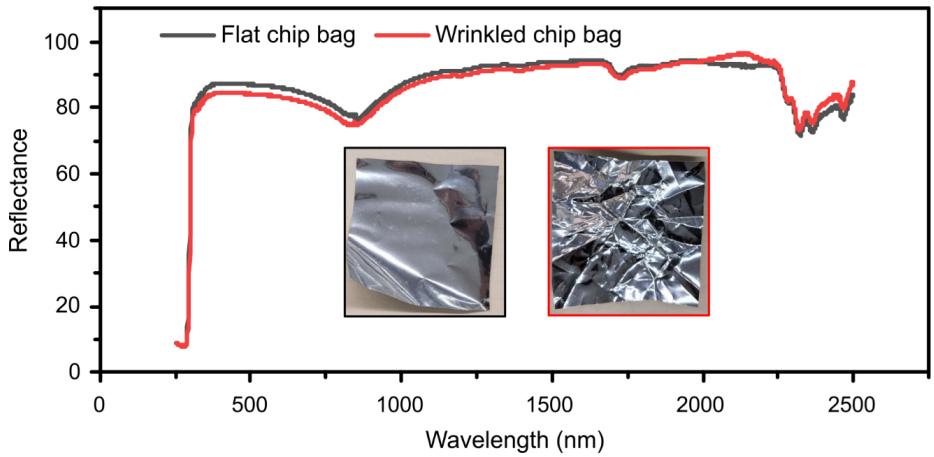

Figure 6.S2.: Diffuse solar reflectance of a chip bag before (flat chip bag) and after wrinkling (wrinkled chip bag). The insets show the photography of the flat and wrinkled chip bag.

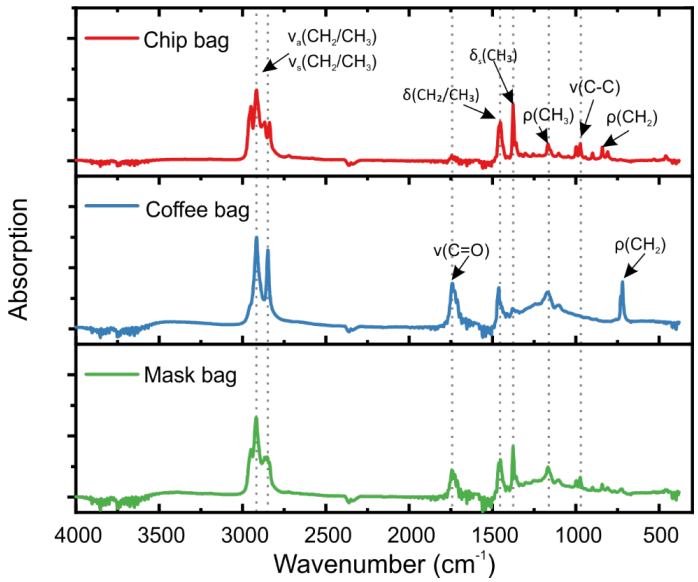

Figure 6.S3.: FTIR absorption spectra of the chip bag, coffee bag and FFP2 mask bag.

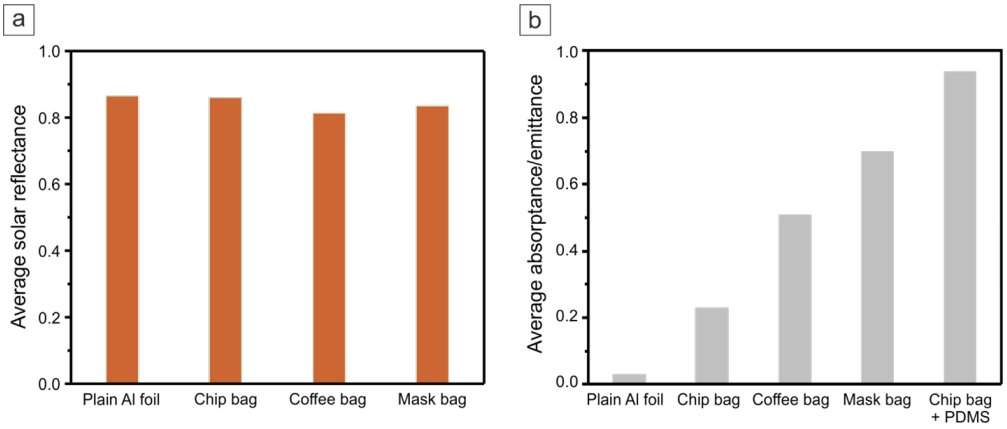

Figure 6.S4.: a) Average solar reflectance b) average MIR absorptance/emittance of different PALs: chip bag, coffee bag, and FFP2 mask bag. Plain Al foil is plotted as a reference.

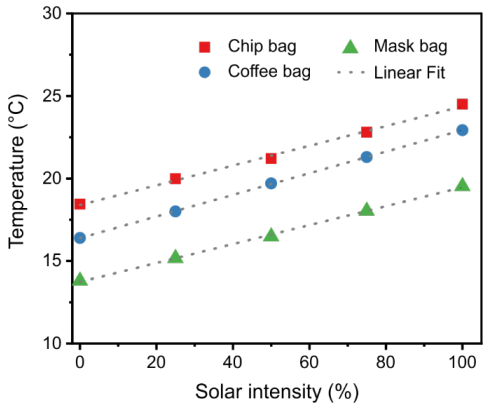

Figure 6.S5.: Steady-state temperature of different APLs: chip bag, coffee bag, and FFP2 mask bag, as a function of solar intensity.

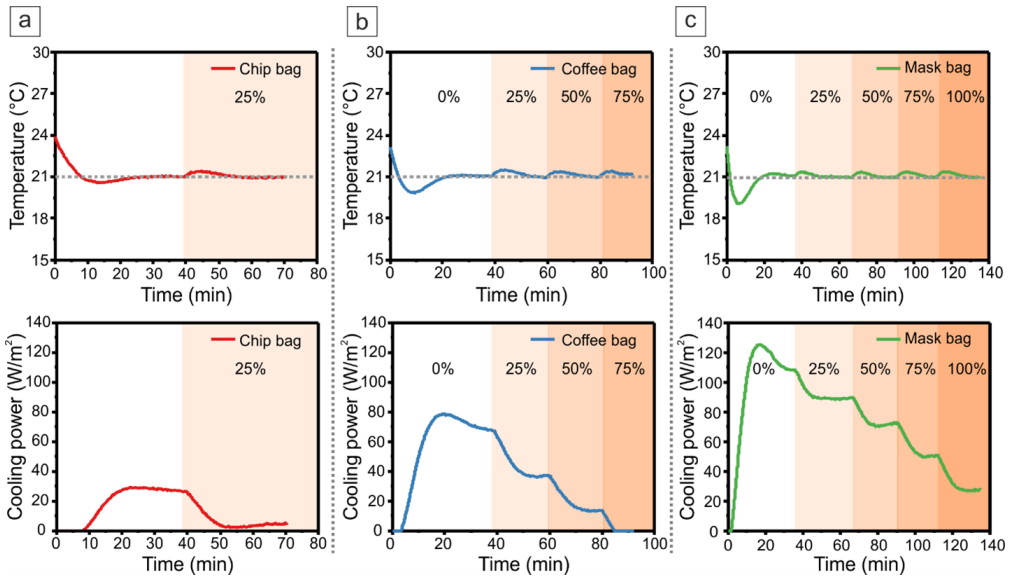

Figure 6.S6.: Cooling power measurements of different laminated Al packaging bags: a) chip bag, b) coffee bag, and c) FFP2 mask bag, with increasing solar intensity from 0 % to 100 % via the indoor setup.

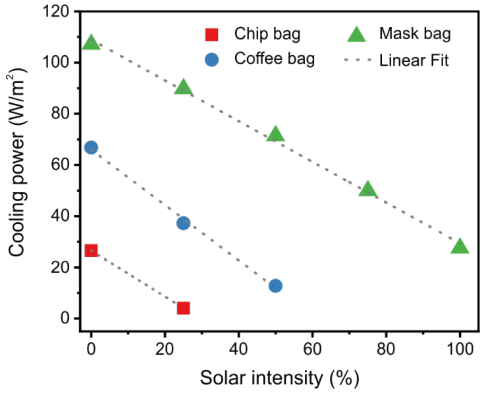

Figure 6.S7.: Cooling power of different APLs: chip bag, coffee bag, and FFP2 mask bag, as a function of solar intensity.

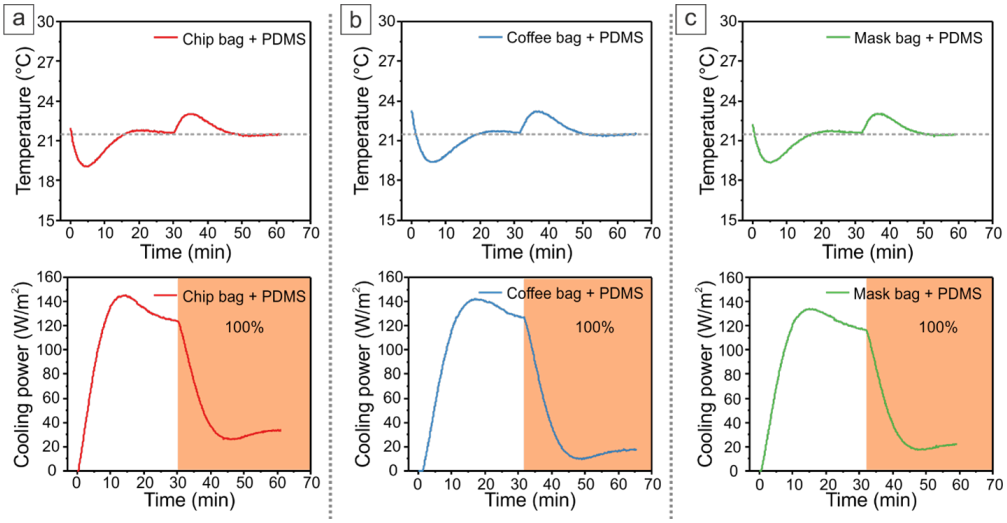

Figure 6.S8.: Cooling power measurements of different PDMS-coated APLs: a) chip bag, b) coffee bag, and c) FFP2 mask bag, with increasing solar intensity from 0 % to 100 % via the indoor setup.

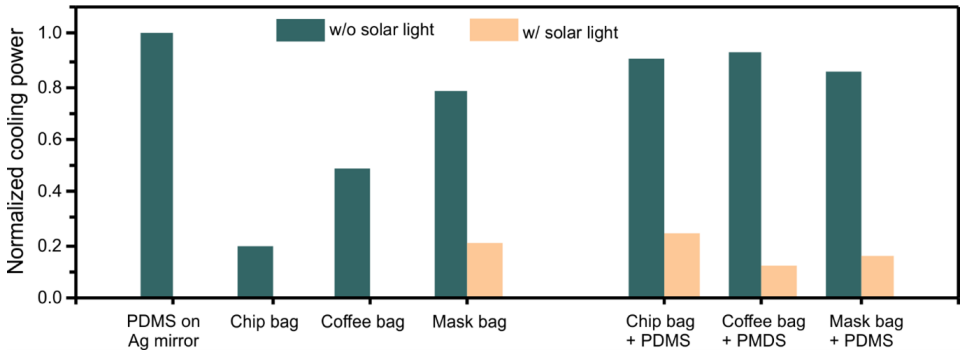

Figure 6.S9.: Cooling power of different plain and PDMS coated APLs normalized by the cooling power of a PDMS-coated (~100 µm) Ag mirror (w/o solar light), for both w/o and w/ 100 % solar light.

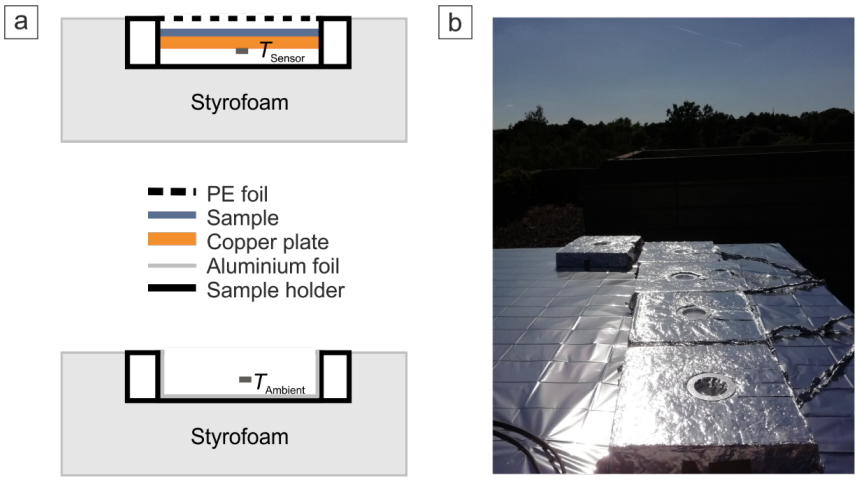

Figure 6.S10.: a) Schematic and b) photography of the homemade setup for field testing.

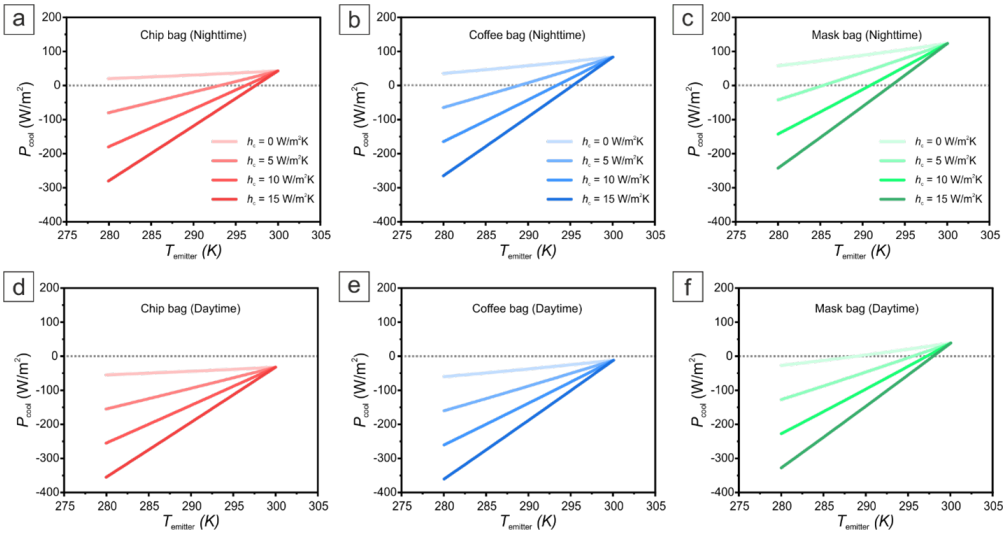

Figure 6.S11.: Predicted net cooling power of the plain APLs, a, d) chip bag, b, e) coffee bag, and c, f) mask bag for both nighttime and daytime with various non-radiative heat transfer coefficients, 0, 5, 10 and 15 $W\,m^{-2}\,K^{-1}$. An average solar intensity of 500 $W\,m^{-2}$ is applied for daytime calculation.

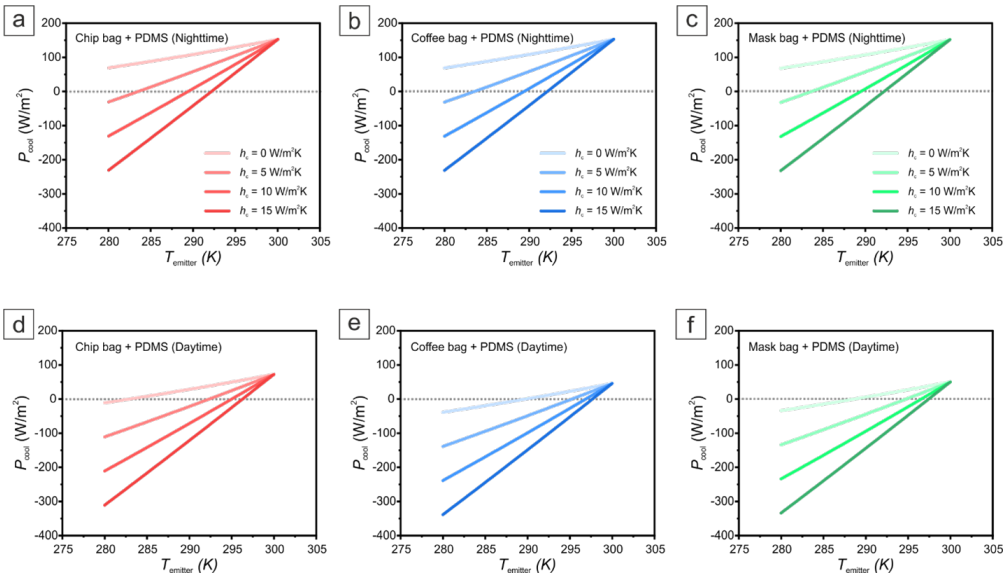

Figure 6.S12.: Predicted net cooling power of the PDMS coated APLs, a, d) chip bag, b, e) coffee bag, and c, f) mask bag for both nighttime and daytime with various non-radiative heat transfer coefficient, 0, 5, 10 and 15 $W\,m^{-2}\,K^{-1}$. The average solar intensity of 500 $W\,m^{-2}$ is applied for daytime calculation.

6.8.3 References

[1] Solar Spectral Irradiance: Air Mass 1.5, Web Page, `http://rredc.nrel.gov/solar/spectra/am1.5` (accessed June, 2022), **2022**.

[2] C. Granqvist, A. Hjortsberg, *Journal of Applied Physics* **1981**, *52*, 4205–4220.

[3] Spectral atmospheric transmittance, Web Page, `https://www.gemini.edu/observing/telescopes-and-sites/sites#Transmission` (accessed June, 2022), **2022**.

[4] D. B. Crawley, L. K. Lawrie, F. C. Winkelmann, et al., *Energy and Buildings* **2001**, *33*, 319–331.

[5] American National Standards Institute, *ANSI/ASHRAE/IES Standard 90.1-2019: Energy Standard for Buildings Except Low-Rise Residential Buildings*, Atlanta, GA (United States), **2019**.

[6] S. Wilcox, W. Marion, *Users Manual for TMY3 Data Sets (Revised)*, National Renewable Energy Lab. (NREL), Golden, CO (United States), **2008**.

[7] China Meteorological Bureau, C.I.C., Climate Data Office and Tsinghua University, Department of Building Science and Technology, *China Standard Weather Data for Analyzing Building Thermal Conditions*, China Building Industry Publishing House, Beijing, China, **2005**.

7

Characterizing the Thermal Diffusivity of Single, Micrometer-Sized Fibers via High-Resolution Lock-In Thermography

Thomas Tran,[1] Charly Kodisch,[1] Marius Schöttle,[1] Nelson W. Pech-May,[2,*] and Markus Retsch[1,3,*]

1 Department of Chemistry, Physical Chemistry I, University of Bayreuth, Universitätsstraße 30, 95447 Bayreuth, Germany
2 Bundesanstalt für Materialforschung und -prüfung (BAM), Unter den Eichen 87, 12205 Berlin, Germany
3 Bavarian Polymer Institute, Bayreuth Center for Colloids and Interfaces, and Bavarian Center for Battery Technology (BayBatt), University of Bayreuth, Universitätsstraße 30, 95447 Bayreuth, Germany
* Corresponding author

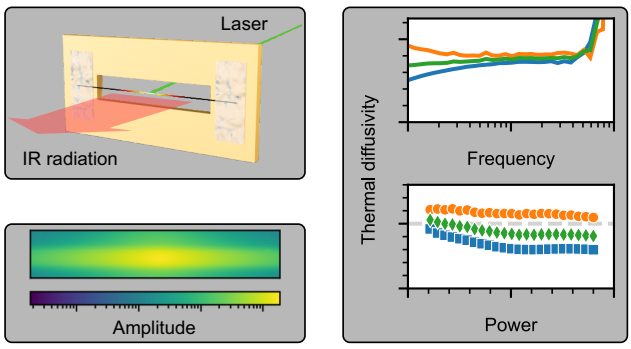

Published in *The Journal of Physical Chemistry C*, **2022**, *126*(32), 14003–14010.

7.1 Abstract

Many advanced materials consist of fibers. They are used as nonwovens, fabrics, or in composite materials. Characterization of individual fibers allows us to predict resulting material properties. We present a measurement setup and analysis software to characterize individual, micrometer-sized fibers fast and reliably. The setup is based on the lock-in thermography principle. Thermal diffusivity values of seven reference samples agree very well with previously reported values. We use our setup to investigate critical measurement parameters like excitation frequency, excitation power, pixel size, and fiber orientation. Our results show that fibers with subpixel diameters can be measured even if they are not aligned. However, special care has to be taken to choose an adequate excitation power. Measurements at high intensities can underestimate thermal diffusivity even though the raw data looks reasonable. By automatically measuring at different excitation powers, our setup solves this issue.

7.2 Introduction

Fiber-based materials play an important role in a range of heat management applications, such as thermal insulation,[1,2] heat dissipation,[3,4] heat spreading,[5] and thermoelectric power generation.[6,7] Fibers can be used without additional material as nonwovens or fabrics, or in composite materials with an enclosing matrix. The effective thermal properties depend on the interplay between the individual fiber properties and their arrangement in a composite material, nonwoven, or knitted structure. In either case, a precise knowledge of the thermal properties is essential to understanding and designing advanced materials with heat control. Knowing the properties of single fibers enables the design of the resulting material properties of fabrics and composite materials, taking into account appropriate models.[8–10] Measuring individual fibers gets excessively difficult the smaller the fiber diameter is.

Early experimental setups to determine the thermal properties of fibers utilized steady-state measurements.[11–15] These techniques measure either the temperature difference along the fiber or the corresponding heat flux. A significant disadvantage of steady-state methods is the measurement time. The sample must be in thermal equilibrium before relevant data can be recorded. A second disadvantage is heat losses. They must be either prevented or taken into consideration for the data evaluation. Therefore, experimental setups are challenging to create and operate.

An alternative to steady-state methods are transient or periodic techniques. In transient measurements, a single heating event is recorded. Afterward, an appropriate model

analyzes the resulting data. Vignoles et al. presented a transient method to characterize fibers.[16] They compared different evaluation models and showed a good agreement between all models. However, they exclusively measured a 450 µm thick silica fiber bundle with a low diffusivity ($\approx 0.2\,\mathrm{mm^2\,s^{-1}}$). The signal-to-noise ratio for fibers with high thermal conductances might be too small to evaluate because only a single heating event is considered. Recently, dual laser flash Raman spectroscopy was introduced to characterize the thermal diffusivity of individual nanowires.[17,18] They achieved a better signal-to-noise ratio by averaging multiple, identical heating events.

Periodic state techniques provide an even higher signal-to-noise ratio. Besides averaging multiple heating events, the signal occurs with a defined excitation frequency. Hence, a Fourier transformation can eliminate noise very effectively. Wang et al. presented a 3ω method adapted to micrometer-sized wires.[19] They apply an alternating current to the wire. As a result, the temperature and thus the electrical resistance changes periodically. The resistance change can be detected as a voltage change at the third harmonic, 3ω. While their measurement setup characterizes single wires well, it works exclusively for electrically conducting materials. More general methods employ external heat sources. They can be either dedicated heating wires[8] or lasers.[20,21] Contactless measurements are possible by using infrared (IR) detectors or cameras

Lock-in thermography is a nondestructive characterization method used for qualitative and quantitative analysis.[22] A light source periodically heats the sample to determine the thermal diffusivity quantitatively. An IR camera detects temperature fluctuations. The time–temperature data is converted to an amplitude, $\tilde{T}_0$, and phase signal, Ψ, by applying a Fourier transformation. At a sufficient distance from the excitation spot, $\ln(\tilde{T}_0)$ and Ψ follow a linear trend with respect to the distance. In combination with the lock-in frequency, the respective slopes lead to the thermal diffusivity. This evaluation method has been proven for films as well as fibers.[21,23–25] By changing the excitation frequency, materials with diffusivities spanning several orders of magnitude can be measured.[26]

Major technological advances in thermography lead to higher magnifications and temperature sensitivities rendering this technique powerful and adaptable to characterize heat transport and temperature distributions on small length scales. We revisit the valuable contributions of lock-in thermography to characterize individual fibers. In particular, we focus on the interplay between measurable pixel size, fiber orientation, and fiber diameter, and their influence on the measured thermal diffusivity. We also outline how even small excitation powers lead to a considerable temperature rise and the resulting effect on the measurement.

In addition to investigating the measurement technique itself, we introduce an evaluation software that enables fast and easy characterization of single, micrometer-sized fibers.

Different experimental parameters, namely the lock-in frequency and excitation power, can be changed automatically. Subsequently, our software package analyzes the data with minimal user input required increasing the reproducibility of the data evaluation. Overall, our work highlights the valuable insights that lock-in thermography can provide to the quantitative heat transport characterization of small objects – even on length-scales that are smaller than the actual pixel resolution.

7.3 Methods

7.3.1 Measurement Principle

Lock-in thermography has been widely used to accurately determine the thermal diffusivity of solids. In particular, for a thin filament of radius r, which is heated periodically by a focused laser modulated at frequency f, one-dimensional heat diffusion occurs outside the illuminated region.[20] By solving the heat diffusion equation, the corresponding surface temperature oscillation can be written as[20,26]

$$\tilde{T}(\hat{z},t) = T_0 \exp(-\gamma\hat{z}) \exp(i \cdot 2\pi f t) \tag{7.1}$$

with

$$\gamma = \gamma_\mathrm{r} + i\gamma_\mathrm{i} \tag{7.2}$$

$$\gamma_\mathrm{r} = \frac{1}{\sqrt{\alpha}} \sqrt{\frac{h_0}{\rho c_p r} + \sqrt{\left(\frac{h_0}{\rho c_p r}\right)^2 + (\pi f)^2}} \tag{7.3}$$

$$\gamma_\mathrm{i} = \frac{1}{\sqrt{\alpha}} \sqrt{-\frac{h_0}{\rho c_p r} + \sqrt{\left(\frac{h_0}{\rho c_p r}\right)^2 + (\pi f)^2}}, \tag{7.4}$$

where α is the thermal diffusivity, $\hat{z}$ is the relative distance to the center of the laser beam, $i = \sqrt{-1}$ is the imaginary unit, T_0 is a term that depends on the heating power, the shape of the laser beam and the size of the fiber;[26] t is the time, h_0 is the radiative heat loss coefficient, ρ is the material density, and c_p is the specific heat. We can write the amplitude, $\tilde{T}_0$, and phase, Ψ, of the periodic signal as

$$\tilde{T}_0 = T_0 \exp(-\gamma_\mathrm{r}\hat{z}) \tag{7.5}$$

$$\Psi = -\gamma_\mathrm{i}\hat{z} - \arctan(\gamma_\mathrm{i}/\gamma_\mathrm{r}). \tag{7.6}$$

If heat losses are negligible, both the slope of the linearized amplitude and phase with respect to $\hat{z}$ are identical and depend only on the excitation frequency and the thermal diffusivity

$$\frac{\partial \ln \tilde{T}_0}{\partial \hat{z}} = -\gamma_\mathrm{r} = \sqrt{\frac{\pi f}{\alpha}} \tag{7.7}$$

$$\frac{\partial \Psi}{\partial \hat{z}} = -\gamma_\mathrm{i} = \sqrt{\frac{\pi f}{\alpha}}. \tag{7.8}$$

If heat losses are non-negligible, the product of the slopes can be used to determine the thermal diffusivity

$$\gamma_\mathrm{r}\gamma_\mathrm{i} = \frac{\pi f}{\alpha}. \tag{7.9}$$

In our experimental setup, heat losses by convection are negligible because the sample is kept in a high vacuum ($< 10^{-2}$ mbar) during the measurements. Since only the slopes of $\ln \tilde{T}_0$ and Ψ are needed, we can use the excitation point of the laser as the coordinate origin. This method is known in the literature as the *slope method* and has been confirmed for various samples.[20,21,25–27] We refer to $\ln \tilde{T}_0$ as the linearized amplitude.

7.3.2 Measurement Setup

Figure 7.1a shows a schematic overview of our measurement setup. Single fibers are attached to 3D-printed sample fixtures. A 20 nm thick carbon layer is deposited on the front and back of the sample (EM ACE600, Leica Microsystems GmbH). To measure the thermal diffusivity of an individual fiber, the fixture is placed inside an aluminum vacuum chamber ($p < 10^{-2}$ mbar) utilizing a sample holder (Figure 7.1b,c). Using a dedicated fixture for each sample makes swapping samples easy and fast. Photographs and laser microscope images of the samples are shown in Figure 7.S1. The vacuum chamber is on top of a three-axis translation stage and a tip-tilt rotation stage. This enables focusing and alignment of the fiber. A point laser (51nano-N-520-0.9-O05-P-12-4-28-0-150, Schäfter+Kirchhoff GmbH) enters the vacuum chamber through an optically transparent N-BK7 glass window in the back at an angle of about 5°. A coating on the camera lens blocks the laser from reaching the detector. Using an angled point laser prevents the reflection of the laser at the camera lens from creating a secondary heating spot on the fiber. A signal generator (DG1022A, RIGOL Technologies Co., Ltd.) controls the maximum power of the laser by applying a direct current (DC) voltage. The maximum power of 0.9 mW corresponds to a voltage of 2.5 V. At the same time, a control interface (BreakOut-Box, Infratec GmbH) modulates the power periodically. The

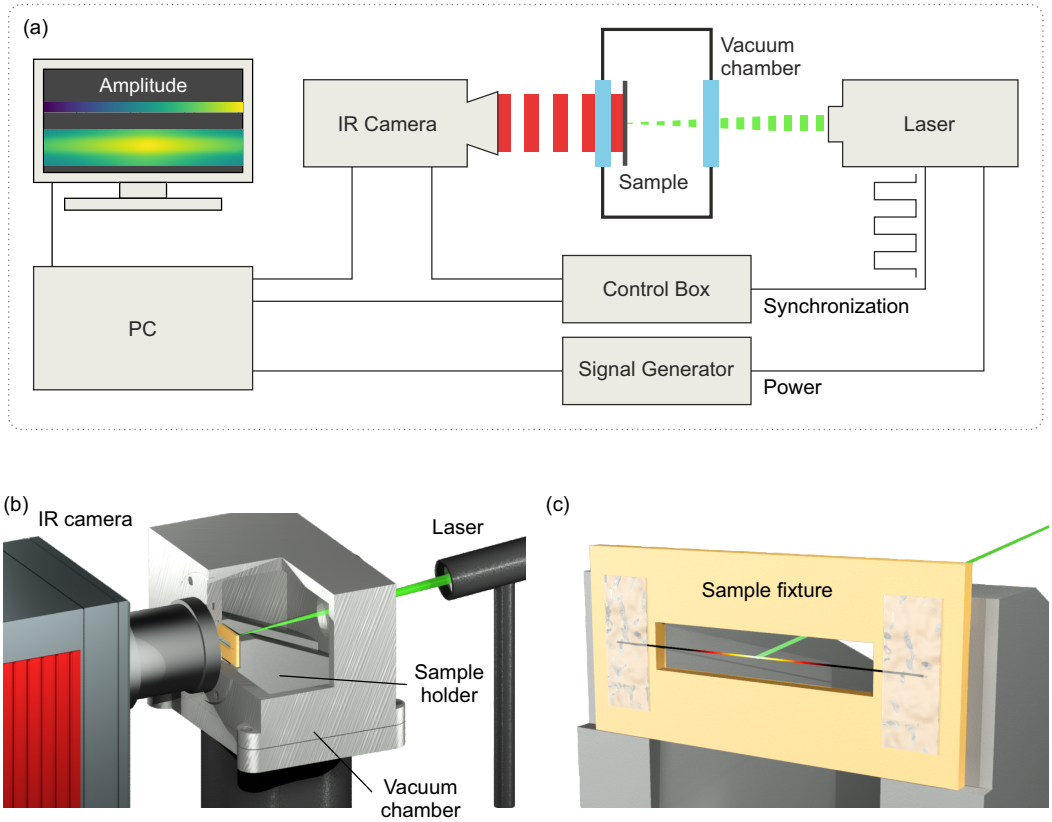

Figure 7.1.: Measurement setup. (a) A modulated laser heats the sample. An IR camera detects the resulting temperature distribution. A computer converts the signal to amplitude and phase data. (b) The sample is positioned inside a vacuum chamber at a pressure of $< 10^{-2}$ mbar. A glass window is in the back of the chamber, and in the front is an IR-transparent sapphire window. (c) The fiber is attached to a 3D-printed sample fixture and is thermally excited by the laser in the center.

duty cycle is set to 30 % to decrease the DC heating of the fiber.[28] The total thermal load on the fiber is determined by the laser power, the duty cycle, and the focused laser area. We will address the influence of laser power and focal area in a dedicated section. The control interface is synchronized with an IR camera (Image IR 9430, InfraTec GmbH) at the front of the vacuum chamber and a computer. InfraTec's IRBISactiveonline software handles the synchronization. The camera is set to a frame rate of 500 frames per second and detects the sample temperature through a sapphire window. We use a 1× and an 8× microscope lens resulting in pixel resolutions of 10 and 1.3 µm, respectively. Measurements are taken with the 8× lens if not stated otherwise.

For each measurement, the equilibration time is 60 s or 50 periods, whichever is longer. The measurement time is always set to 60 s corresponding to the analysis of 30 000 images. For frequency-dependent measurements, the excitation frequency is varied logarithmically between 0.1 and 125 Hz. For power-dependent measurements, powers are varied linearly between 0.108 mW and 0.9 mW.

7.3.3 Data Analysis

The amplitude and phase of the temperature are calculated in real-time. As shown in Figure 7.2a, the fiber only occupies part of the image. Thus, the camera view is cropped to a smaller area. We developed software to analyze the resulting amplitude and phase images semiautomatically.[31] Figure 7.S2 shows the workflow from sample preparation to data analysis utilizing our software. First, the software detects the position of the fiber and laser excitation. Pixels outside the fiber area are not used for the data evaluation. For the remaining pixels, the distance to the laser spot is calculated. The natural logarithm of the amplitude and the phase are plotted against the distance to the center (Figure 7.2b and Figure 7.S3). Afterward, linear regression determines the slope of the data in the linear regime. The respective slopes sufficiently far from the laser excitation are evaluated according to the theoretical model described above. Determining the boundaries of the linear regime is the only part requiring user interaction. From the slopes, the thermal diffusivity is calculated according to eqs 7.7 to 7.9. In addition to detecting the fiber position, the software automatically detects the fiber's orientation and aligns the fiber accordingly. As shown in Figure 7.S4, by rotating the image, the slope of the amplitude and phase match those of a straight fiber.

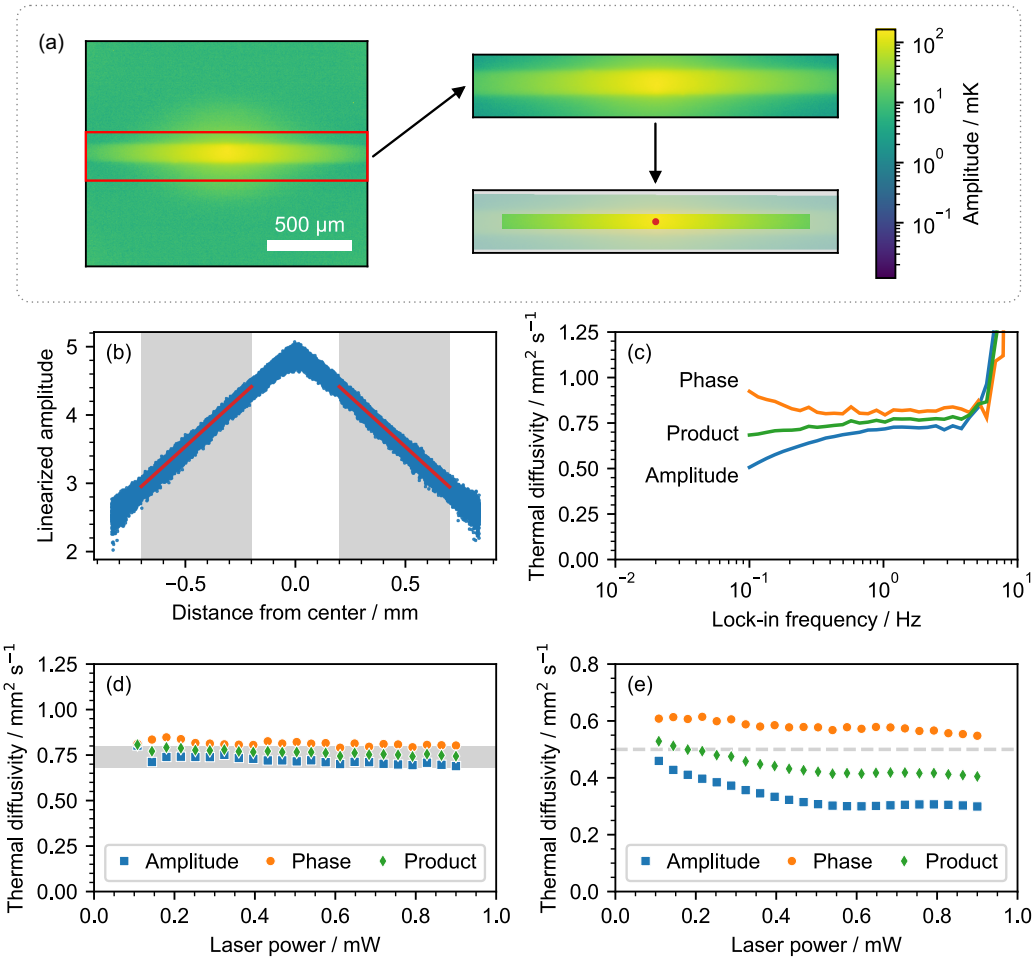

Figure 7.2.: Typical data and resulting diffusivities. (a) Raw amplitude data of a 100 µm quartz fiber detected by the camera. The raw amplitude image is cropped. The fiber (bright area) and laser spot (red circle) are detected using the cropped data. (b) For each pixel, the natural logarithm of the amplitude is plotted against the distance to the laser spot. The linear slope (red line) is calculated in the grey area. (c) From the amplitude and phase slope, the resulting diffusivities for different measurements are evaluated. By repeating the measurement at a constant laser power (0.9 mW) but at different frequencies, a plateau can be seen. (d) At a frequency of 2 Hz, a 139 µm quartz fiber was excited with different laser powers. Regardless of laser power, the same diffusivity is measured. The gray shaded area shows the range of values found in the literature.[29,30] (e) For a 30 µm PEEK fiber at 1 Hz, the thermal diffusivity decreases with increasing laser power. This change is caused mainly by the amplitude slope. The gray dashed line shows a value reported previously.[26]

Table 7.1.: Measurement Results for Thermal Diffusivities of Different Fibers and Comparison to Literature Values[a]

material	thickness / µm	excitation frequency / Hz	thermal diffusivity / $mm^2\,s^{-1}$ 1× lens	8× lens	lit.
quartz	139	2	0.76 ± 0.01	0.77 ± 0.02	0.68[b] - 0.8[c]
	100	2	0.80 ± 0.06	0.80 ± 0.04	0.68-0.8
	78	2	0.81 ± 0.01	0.77 ± 0.02	0.68-0.8
	70	2	-	0.78 ± 0.02	0.68-0.8
PEEK	210	1	-	0.46 ± 0.02	0.5[d]
	30	1	0.50 ± 0.01	0.52 ± 0.02	0.5
titanium	128	3	-	9.38 ± 0.46	8.85[e]

[a] The given errors are standard deviations of multiple measurements. All values agree well with the literature. [b] Reference [29]. [c] Reference [30]. [d] Reference [26]. [e] Reference [33].

7.4 Results and Discussion

7.4.1 Instrument Validation

To validate our setup, we characterized three different materials: amorphous quartz, polyether ether ketone (PEEK), and titanium. Each sample was measured at different frequencies at constant power. Figure 7.2c shows typical data for a 100 µm quartz fiber. At high frequencies, diffraction effects of the microscope lens lead to an overestimation of the thermal diffusivity.[32] At moderate frequencies, a plateau is visible, while at low frequencies, the values diverge from the actual value due to heat losses. This matches very well with the experimental results of Mendioroz et al.[26] Evaluating only the amplitude/phase leads to an under-/overestimation of the thermal diffusivity. This matches the expectation from the theoretical model and experimental values reported in the literature.[21] Heat losses are compensated using the product, and the correct value is obtained. Table 7.1 compares the measured values for the reference materials with values reported in the literature. The deviation is at most 6 % for all materials. Considering the standard deviations of our measurements and the differences to literature values, we estimate an uncertainty of 5 %. These results validate the measurements with our instrument.

7.4.2 Influence of Laser Power and Focal Distance

For each sample, measurements with varying power at a frequency in the plateau regime are conducted. As expected, the resulting diffusivities show a constant value for a 139 µm

quartz fiber matching the values found in the literature[29,30] (Figure 7.2d). However, a 30 µm PEEK fiber with a lower material diffusivity shows a power dependency. The trend is mainly driven by the amplitude slope while the phase slope stays almost constant (Figure 7.2e).

We propose that the power dependency is due to temperature effects. To confirm our hypothesis, we investigated the raw data of measurements at a wide range of laser powers between 0.05 mW and 0.9 mW more closely. The absolute value of the amplitude decreases with decreasing laser power (Figure 7.3a). This matches the expectation that a lower excitation power heats the fiber less during one period. However, subtracting the maximum amplitude from each measurement clearly shows that the slope of the amplitude changes (Figure 7.3c), compromising the thermal diffusivity evaluation. Individually, each measurement looks reasonable and shows a linear regime, but overall, a trend of the slopes becomes visible. For the phase, no such trend can be observed (Figure 7.3e). We rationalize this observation by effects introduced by the high temperature fluctuations of the fiber (Figures 7.S5 and 7.S6).

At the highest laser power of 0.9 mW, the peak-to-peak amplitude during one period is up to 43 K. A power of 0.108 mW leads to an amplitude of only 1.4 K (Figure 7.S5a,b). Meanwhile, the average absolute temperature is 22 °C throughout the whole fiber at a power of 0.108 mW, but it changes from 45 °C at the center to 34 °C at 0.3 mm for the highest power (Figure 7.S5c,d). As the thermal diffusivity decreases with increasing temperature,[34] this will lead to an additional downward trend. Since thick fibers have a higher heat capacity, the temperature change is attenuated and small even for high laser powers. A 210 µm thick PEEK fiber shows an amplitude of 1.4 K and a homogeneous average temperature of around 25 °C throughout the whole fiber even at the highest laser power (Figure 7.S6). Hence, no trend in the thermal diffusivity is visible (Figure 7.S7a). In contrast, a 5 µm thin carbon fiber shows a clear trend comparable to the thin PEEK fiber (Figure 7.S7b). Accordingly, our results on different fiber diameters and laser incidence powers suggest that reliable thermal diffusivity values can be obtained when the temperature rise is below 4 K (Figure 7.S6), provided that a good signal-to-noise ratio is achieved in the measurement.

Moving the fiber in and out of the focal plane of the laser at a constant laser power achieves a comparable effect to the power dependence (Figure 7.3h). Moving the sample by 4 mm changes the laser spot size from 10 µm to about 266 µm (Figure 7.S8). The resulting amplitude and phase data (Figure 7.3b,d,f) resemble the power sweep. Heating the fiber with a narrowly focused laser leads to the highest temperature amplitude. Consequently, the apparent thermal diffusivity has a minimum when the laser is at the focal point of the laser (Figure 7.S9). The laser spot size increases when moving the fiber out of the focal point. This leads to two effects: (1) The light hitting the fiber

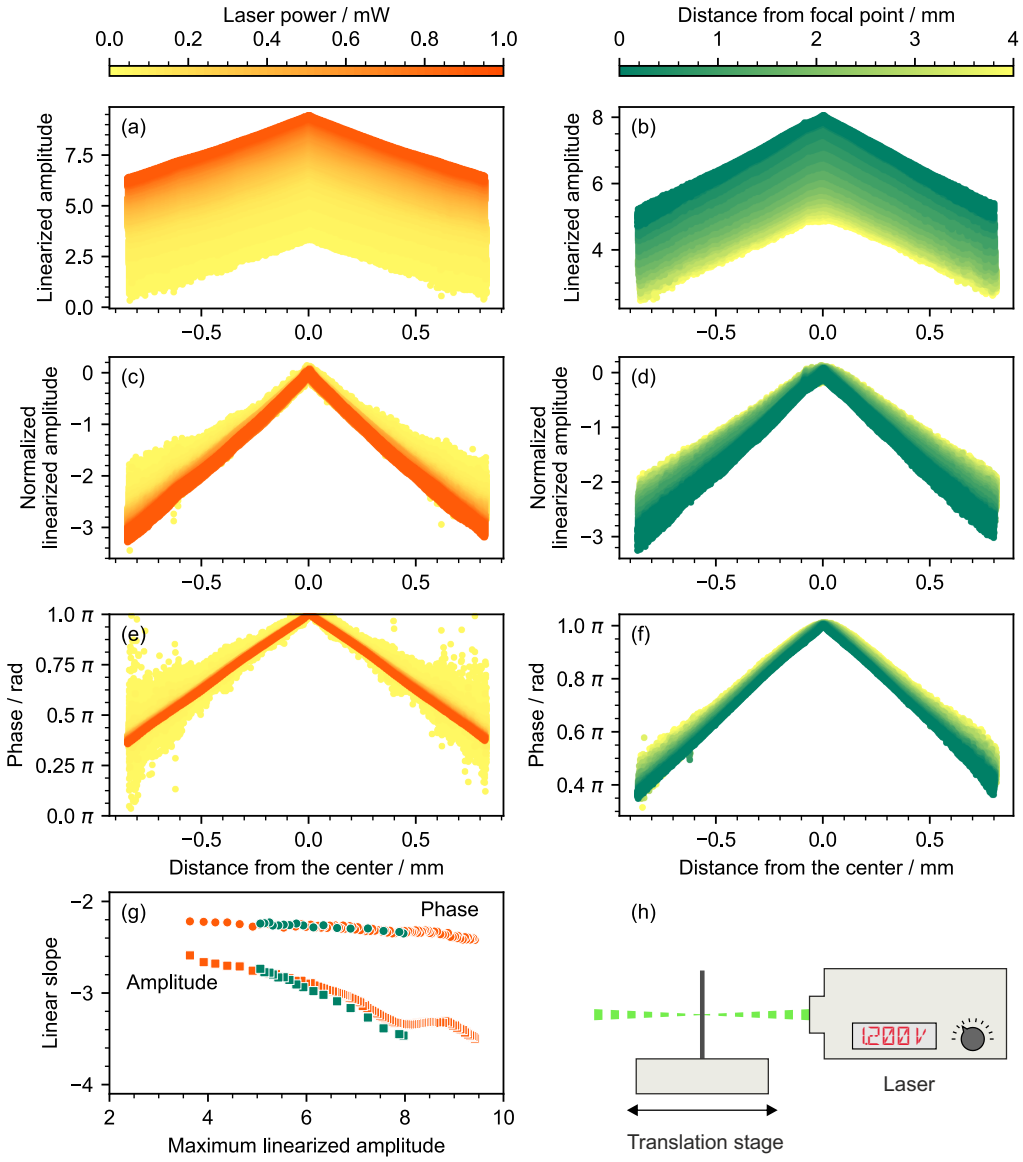

Figure 7.3.: Influence of the laser power and focal distance on the thermal diffusivity of a 30 µm PEEK fiber. Raw data at (a, c, e) different laser powers and (b, d, f) different distances from the focal point. (g) Slopes of the phase and amplitude against the maximum linearized amplitude. While the phase slope stays almost constant, the amplitude slope changes significantly. A steeper slope correlates with higher temperature differences leading to lower apparent thermal diffusivities. (h) Schematic drawing of the measurement setup. Applying different voltages changes the laser power. Moving the fiber in and out of the focal point of the laser achieves a comparable effect.

is distributed over a larger area. (2) After exceeding the fiber diameter, a part of the laser passes the fiber without contributing to the thermal excitation. As a result of both effects, the maxima in the linearized data are less sharp, and the temperature difference decreases from 2.7 to 0.5 K at a laser power of 0.180 mW.

Figure 7.3g shows the slopes of the linearized amplitude and phase versus the maximum linearized amplitude for each measurement. The maximum linearized amplitude indicates the temperature difference during one measurement period. The trends of the power sweep and focus sweep agree well. While the phase slope stays almost constant, the amplitude slope decreases with higher temperature amplitudes.

A third possibility to observe this effect is changing the duty cycle since the duty cycle has been shown to influence the absolute temperature during a lock-in measurement.[28] Figure 7.S10 shows a thick and thin PEEK fiber measured with different duty cycles. Again, the thick fiber shows no trend while the thin fiber shows a decreasing apparent thermal conductivity with increasing temperature.

7.4.3 Comparison of Different Magnifications

Researchers used the same detection hardware for all experiments when characterizing fibers via lock-in thermography in previous publications.[8,20,21,26] In contrast, our camera system can be equipped with different lenses to access pixel resolutions down to 1.3 µm. Consequently, we can now elucidate any potential influence of the camera resolution on the quantification of thermal diffusivity. At the same time, we address whether tilting a fiber relative to the pixel orientation significantly influences the evaluation. Figure 7.4 shows the thermal diffusivities measured with a 1× and 8× microscope lens for a thick and thin fiber. The thick quartz fiber is clearly visible with both lenses as it spans 14 pixel lines even for the 1× lens. For evaluating the thin PEEK fiber, 17 pixel lines were used for the 8× lens and only a single pixel line for the 1× lens (Figure 7.S11). The results for both lenses overlap, showing that either lens can be used to measure either fiber. Note that the slight power trend for the thin PEEK fiber is reproducible.

Next, we investigate a 5 µm carbon fiber. This fiber is half the camera's pixel size when equipped with the 1× lens. Intuitively, an evaluation of the fiber seems questionable due to its subpixel diameter. The fiber is aligned to a single pixel line. The measurement data shows the expected shape (Figure 7.5a,b), and the resulting thermal diffusivity agrees well with the 8× lens (Figure 7.5c–e).

When tilting the fiber at an angle of 3.2° (Figure 7.S12), the linearized amplitude data of the 1× lens shows discrete steps (Figure 7.5a). These arise from the fiber moving from one pixel line to the next in the original data. Nevertheless, the slope and hence

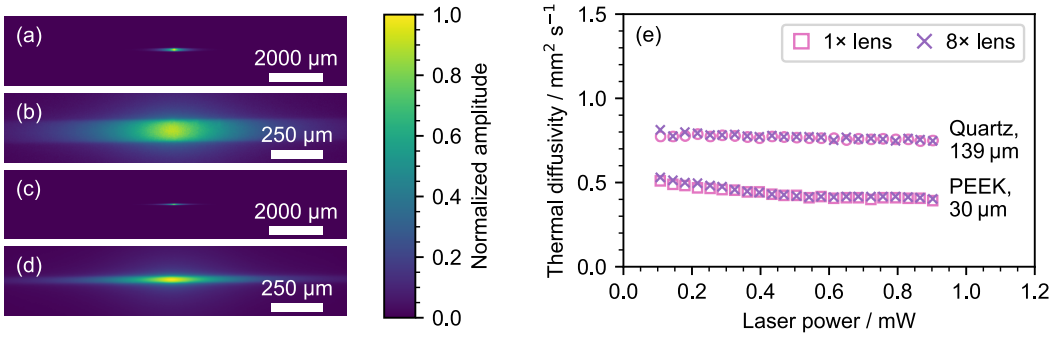

Figure 7.4.: Comparison of the two different lenses with a thick quartz fiber and a thin PEEK fiber. Amplitude of the (a, b) quartz fiber and (c, d) PEEK fiber with the 1× and 8× lens. (e) Resulting thermal diffusivity versus nominal laser power. The respective thermal diffusivities of both lenses agree very well.

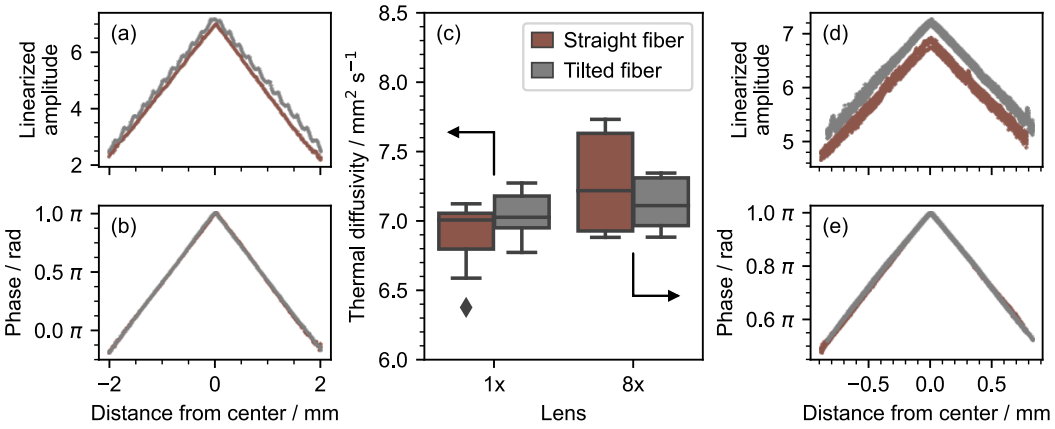

Figure 7.5.: Measurements of a 5 µm carbon fiber measured while straight and tilted. (a, b) Raw data for the 1× lens. The fiber size is half the pixel size. (c) Both the 1× and 8× lens lead to comparable results for the straight and tilted fiber. (d, e) Raw data for the 8× lens. Since the pixel size is smaller than the fiber diameter, both the straight and tilted fiber look identical.

the thermal diffusivity is not affected. Repeating the measurement five times for each configuration shows a maximum spread of 0.85 $mm^2 s^{-1}$ and a maximum deviation from the mean of 6.2 % (Figure 7.5c). This proves that measuring fibers with subpixel diameters is possible even if they are not perfectly aligned. Thus, our measurements confirm the results from previous publications in which fibers have been characterized even if their size was of subpixel resolution. Furthermore, our results are encouraging that lock-in thermography may be suitable to access the submicrometer range as long as the temperature excitation is sufficiently small.

7.5 Conclusions

We revisit lock-in infrared thermography to characterize individual, micrometer-sized fibers. Utilizing high-resolution thermography, we demonstrate that fibers with subpixel sizes can be accurately measured. In addition, tilted fibers can be evaluated straightforwardly without compromising the quantitative evaluation. Measuring with a minimum external heat load is of paramount importance to obtain the true thermal diffusivity of a specific fiber. This becomes particularly relevant for fibers of very thin cross sections and low intrinsic thermal conductivity. Measures to adjust the excitation energy are the laser power and the focused area. Considering these measurement parameters, we confirm the reported literature values for a range of reference materials. Furthermore, we provide a measurement and data evaluation platform with a high degree of automation. This software is openly available and allows for fast and accurate determination of the thermal diffusivity of fibers. Considering the advantages of lock-in thermography, we are convinced that this method will strongly contribute to developing advanced fibers for heat management applications.

7.6 Acknowledgments

The authors thank the mechanical workshop at the University of Bayreuth for manufacturing the vacuum chamber and fixtures for the IR camera and laser. T.T. and M.S. acknowledge support from the Elite Network Bavaria (ENB).

7.7 References

[1] Y. Cui, H. Gong, Y. Wang, D. Li, H. Bai, *Adv. Mater.* **2018**, *30*, e1706807.

[2] P. Lizák, A. Murárová, S. C. Mojumdar, *J. Therm. Anal. Calorim.* **2012**, *108*, 851–857.

[3] J. Wang, Q. Li, D. Liu, et al., *Nanoscale* **2018**, *10*, 16868–16872.

[4] T. Gao, Z. Yang, C. Chen, et al., *ACS Nano* **2017**, *11*, 11513–11520.

[5] D. D. L. Chung, Y. Takizawa, *J. Electron. Mater.* **2012**, *41*, 2580–2587.

[6] J. Liu, Y. Jia, Q. Jiang, et al., *ACS Appl. Mater. Inter.* **2018**, *10*, 44033–44040.

[7] Y. Kim, A. Lund, H. Noh, et al., *Macro. Mater. Eng.* **2020**, *305*, 1900749.

[8] A. A. Candadai, J. A. Weibel, A. M. Marconnet, *ACS Appl. Polym. Mater.* **2019**, *2*, 437–447.

[9] Y. Zhao, Y. Jiao, L. Song, Q. Jiang, J. Li, *J. Compos. Mater.* **2016**, *51*, 3041–3051.

[10] E. Oner, *Fiber. Polym.* **2019**, *20*, 2416–2425.

[11] B. M. Zawilski, R. T. Littleton, T. M. Tritt, *Rev. Sci. Instrum.* **2001**, *72*, 1770.

[12] B. Bouyer, X. Tardif, C. Mercader, D. Delaunay, *Int. J. Therm. Sci.* **2021**, *161*, 106740.

[13] L. Piraux, J. P. Issi, P. Coopmans, *Measurement* **1987**, *5*, 2–5.

[14] X. Zhang, S. Fujiwara, M. Fujii, *High Temp.-High Press.* **2000**, *32*, 493–500.

[15] J. L. Wang, M. Gu, X. Zhang, Y. Song, *J. Phys. D Appl. Phys.* **2009**, *42*, 105502.

[16] G. L. Vignoles, G. Bresson, C. Lorrette, A. Ahmadi-Sénichault, *J. Phys. Conf. Ser.* **2012**, *395*, 012079.

[17] J. H. Liu, H. Liu, Y. D. Hu, X. Zhang, *Int. J. Heat Mass Tran.* **2019**, *135*, 511–516.

[18] S. T. Luo, A. R. Fan, Y. F. Zhang, et al., *Int. J. Heat Mass Tran.* **2022**, *184*, 122271.

[19] Z. L. Wang, D. W. Tang, W. G. Zhang, *J. Phys. D Appl. Phys.* **2007**, *40*, 4686–4690.

[20] C. Pradere, J. M. Goyheneche, J. C. Batsale, S. Dilhaire, R. Pailler, *Int. J. Therm. Sci.* **2006**, *45*, 443–451.

[21] A. Salazar, A. Mendioroz, R. Fuente, R. Celorrio, *J. Appl. Phys.* **2010**, *107*, 043508.

[22] O. Breitenstein, W. Warta, M. Langenkamp, *Lock-in Thermography*, 3rd ed., Springer, **2018**.

[23] L. Fabbri, P. Fenici, *Rev. Sci. Instrum.* **1995**, *66*, 3593–3600.

[24] B. Zhang, R. E. Imhof, *Appl. Phys. A-Mater.* **1996**, *62*, 323–334.

[25] A. Philipp, N. W. Pech-May, B. A. F. Kopera, et al., *Anal. Chem.* **2019**, *91*, 8476–8483.

[26] A. Mendioroz, R. Fuente-Dacal, E. Apinaniz, A. Salazar, *Rev. Sci. Instrum.* **2009**, *80*, 074904.

[27] R. Fuente, A. Mendioroz, A. Salazar, *Mater. Lett.* **2014**, *114*, 1–3.

[28] B. A. F. Kopera, M. Retsch, *Rev. Sci. Instrum.* **2021**, *92*, 014902.

[29] S. W. Kieffer, I. C. Getting, G. C. Kennedy, *J. Geophys. Res.* **1976**, *81*, 3018–3024.

[30] T. Katsura, *Phys. Chem. Miner.* **1993**, *20*, 201–208.

[31] The source code for our software is available at `https://github.com/thomas-tran-de/lockinthermography`.

[32] J. F. Bisson, D. Fournier, *Journal of Applied Physics* **1998**, *83*, 1036–1042.

[33] K. Zhou, H. P. Wang, J. Chang, B. Wei, *Chem. Phys. Lett.* **2015**, *639*, 105–108.

[34] C. L. Choy, K. W. Kwok, W. P. Leung, F. P. Lau, *J. Polym. Sci. Pol. Phys.* **1994**, *32*, 1389–1397.

7.8 Supplemental Information

7.8.1 Materials

Quartz fibers with diameters of 139 µm and 100 µm, titanium fibers, and polyether ether ketone (PEEK) fibers were purchased from GoodFellow GmbH. Quartz fibers with diameters of 78 µm and 70 µm were created in-house by heating and stretching quartz glass rods. Carbon fibers with a diameter of 5 µm were supplied by Toho Tenax Co., Ltd. (IMS65).

7.8.2 Determination of Fiber Diameter

Each fiber was investigated with a 3D laser measuring microscope (LEXT OLS5000-SAF, OLYMPUS EUROPA SE & CO. KG). We obtained images of 1200 µm × 490 µm size with a 50× lens. The diameter of each fiber was measured at three positions (left, center, right) and averaged.

7.8.3 Supplemental Figures

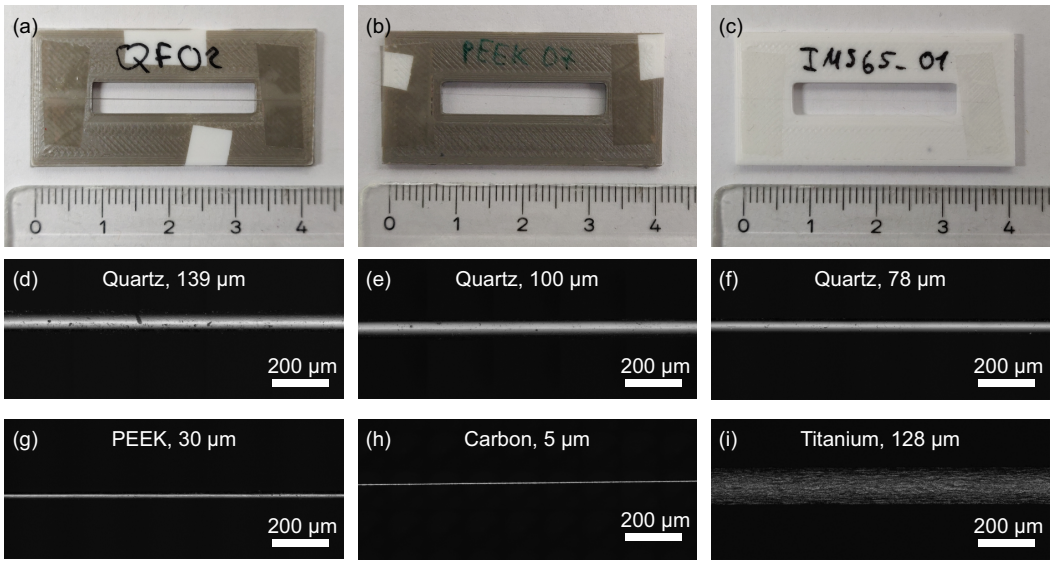

Figure 7.S1.: (a-c) Photographs of three samples with different thicknesses. (a) 139 µm quartz fiber, (b) 30 µm PEEK fiber, (c) 5 µm carbon fiber. (d-i) Laser microscopy images for different fibers.

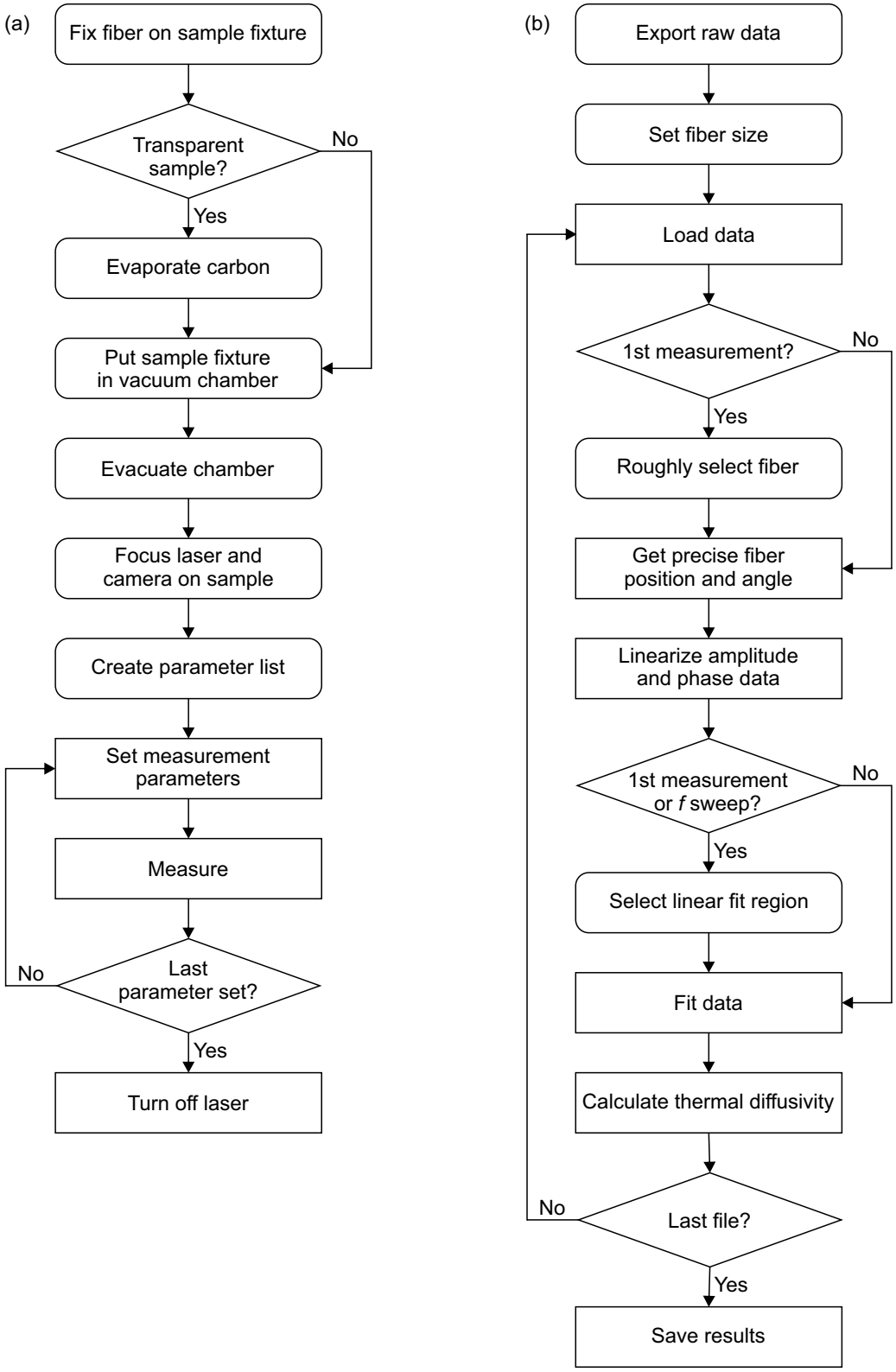

Figure 7.S2.: Flowcharts of (a) the measurement procedure and (b) the analysis software. Round rectangles are parts requiring human interaction, while sharp rectangles are fully automatic.

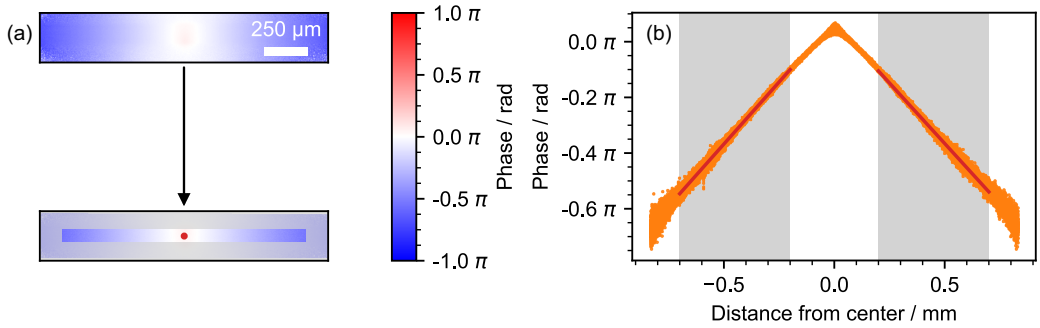

Figure 7.S3.: Phase data for a 100 µm quartz fiber. (a) The fiber and laser positions are identical to the corresponding amplitude measurements. Highlighted pixels are used for evaluation. (b) For each pixel, the distance to the laser excitation is determined. A clear linear trend (red line) of the phase is visible in the evaluated area (gray).

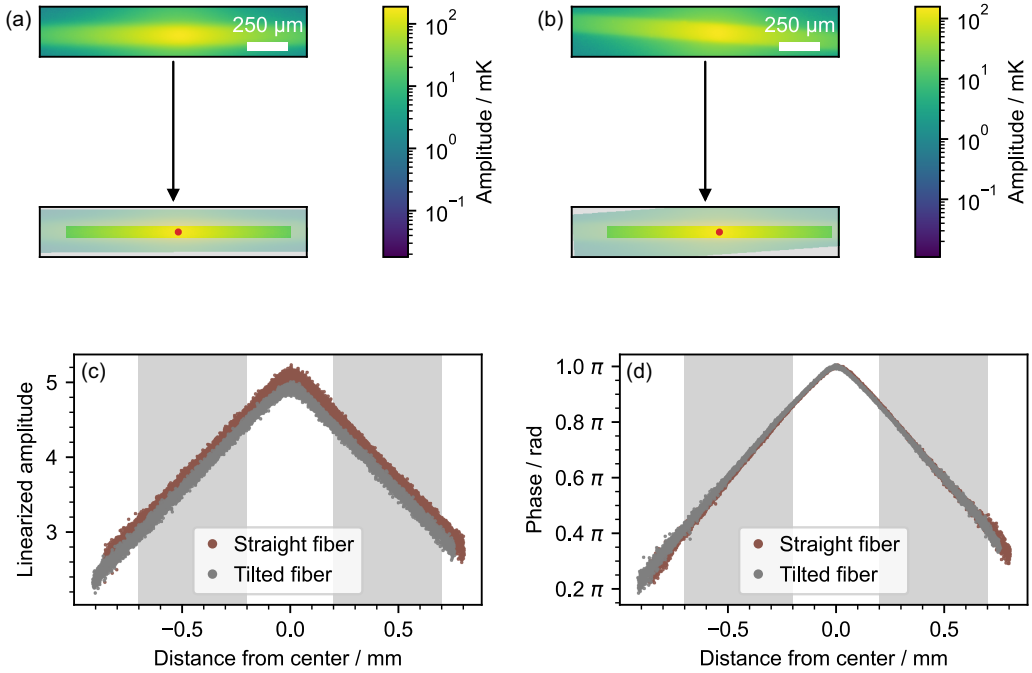

Figure 7.S4.: (a, b) 2D amplitude images of a 100 µm quartz fiber. When the fiber is straight, the software detects only the fiber and laser position. When the fiber is tilted, an additional tilt correction is applied. Here, the software determined an angle of 4°. (c) Linearized amplitude data, and (d) phase data. The data for the straight and tilted fiber overlap leading to the same slopes and thus the same thermal diffusivities.

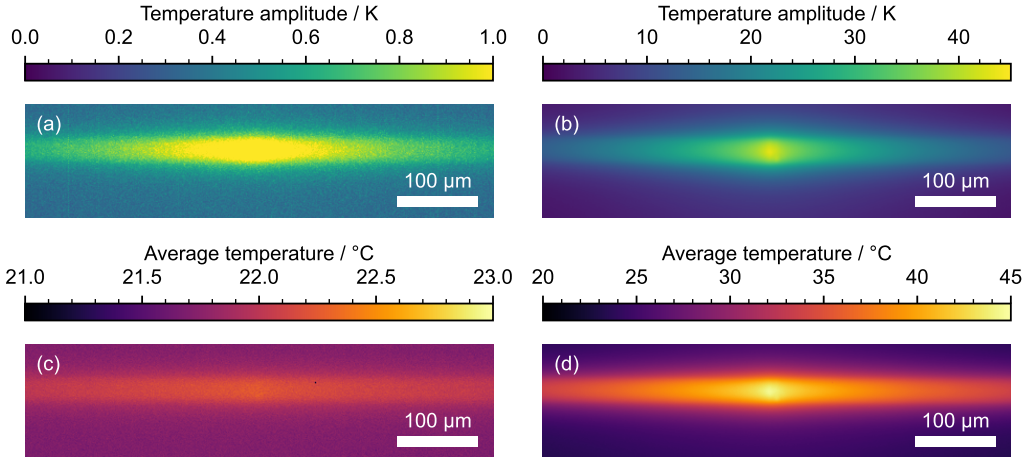

Figure 7.S5.: Temperature evolution of a 30 µm thick PEEK fiber with an excitation frequency of 1 Hz. Temperature change during one period at (a) 0.108 mW and (b) 0.9 mW. Average temperature during one period at (c) 0.108 mW and (d) 0.9 mW.

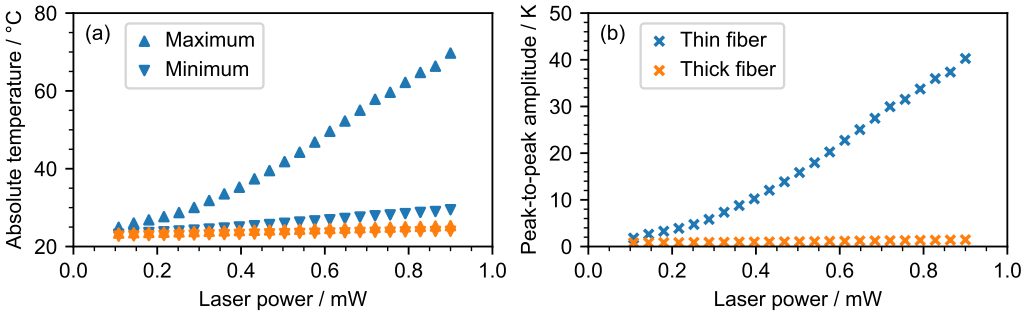

Figure 7.S6.: (a) Absolute temperature at the center of a 30 µm and 210 µm thick PEEK fiber during one 1 Hz period with a laser power of 0.9 mW. (b) Resulting peak-to-peak amplitude of the respective measurements. While the temperature of the thick fiber stays almost constant, the thin fiber heats up considerably during one period.

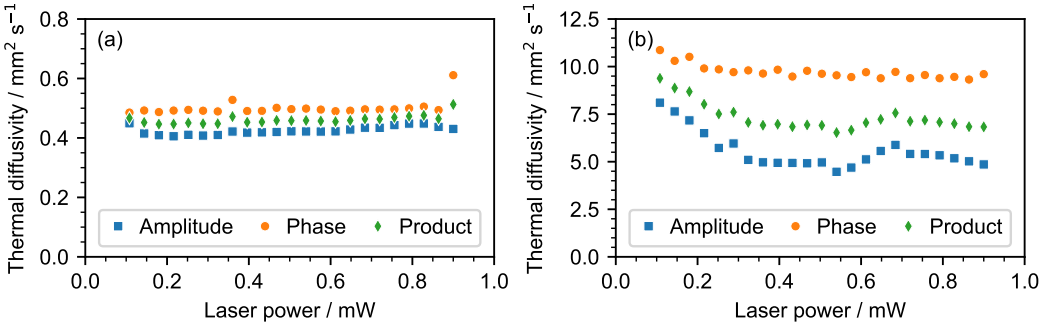

Figure 7.S7.: Thermal diffusivity at different laser powers for (a) a 210 µm thick PEEK fiber at 1 Hz and (b) a 5 µm thick carbon fiber at 10 Hz. For the thin fiber, a decrease in apparent thermal diffusivity is visible with increasing laser power.

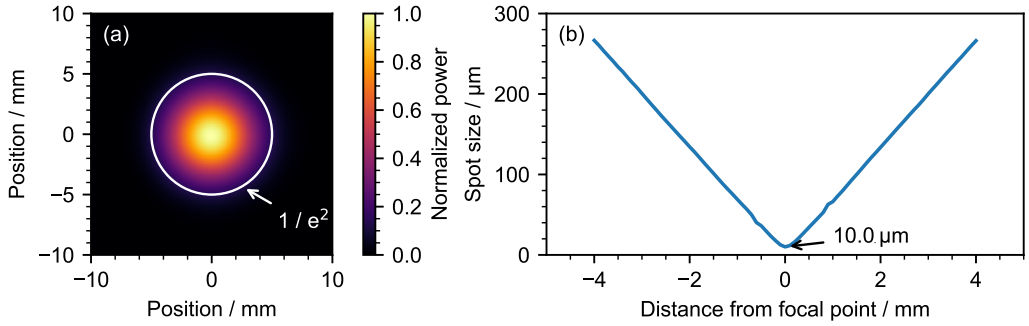

Figure 7.S8.: Laser spot size. (a) The laser spot size was measured with a beam profiler (DataRay BR2, DataRay Inc.). The size is given by the diameter of the laser at 13.5 % power. (b) At the focal point, the size of the laser is 10 µm. With increasing absolute distance, the spot size increases linearly up to a size of 266 µm at 4 mm.

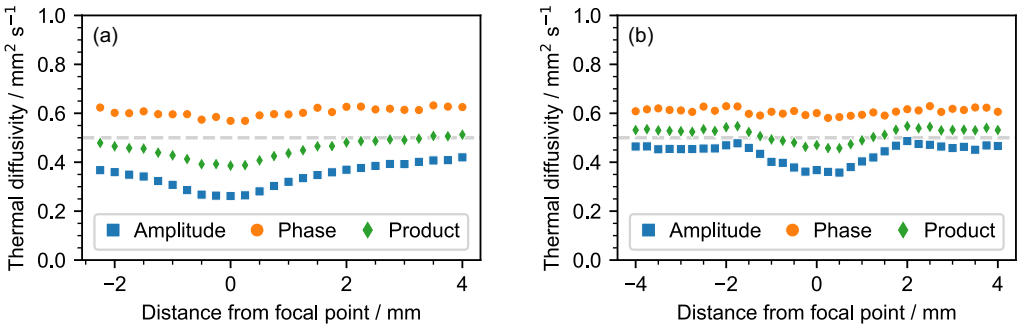

Figure 7.S9.: Focus sweep with the (a) 8× and (b) 1× lens. A laser power of 0.18 mW was used. The thermal diffusivity determined by the amplitude shows a clear minimum at the focal point. For the phase, no trend is visible.

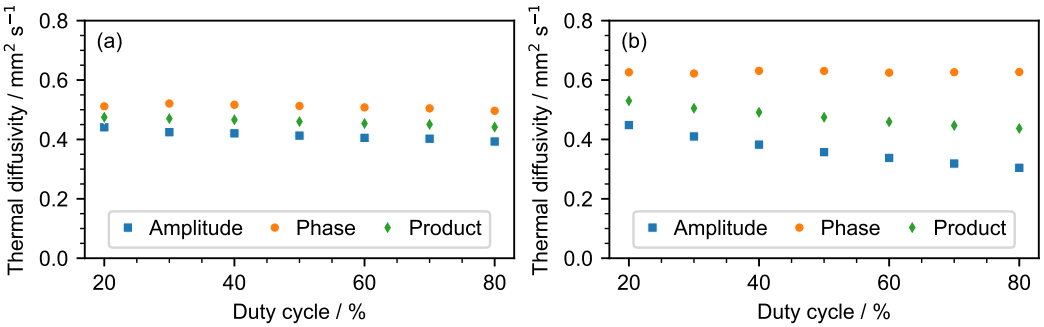

Figure 7.S10.: Effect of different duty cycles. Measurement results of (a) a 210 µm thick PEEK fiber at 1 Hz and 0.9 mW and (b) a 30 µm thick PEEK fiber at 1 Hz and 0.36 mW. For the thin fiber, a decreasing trend is visible.

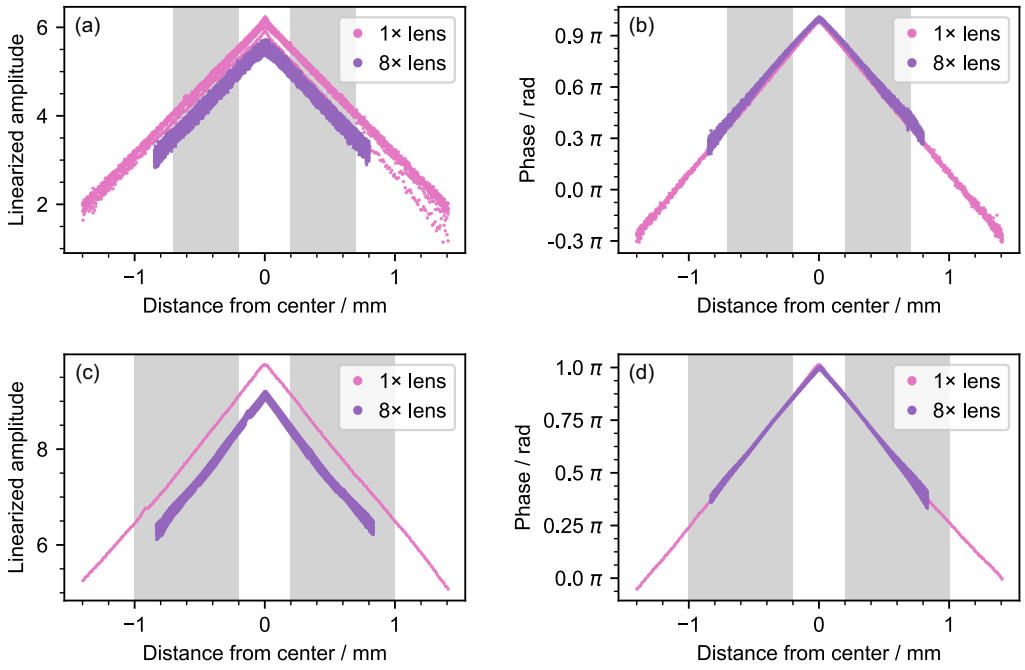

Figure 7.S11.: (a-b) Measurement data for a 139 µm quartz fiber. The slopes of the 1× and 8× lens are identical. (c-d) Measurements for a 30 µm PEEK fiber. Again, the slopes are identical. Note that only a single pixel line was evaluated for the 1× lens.

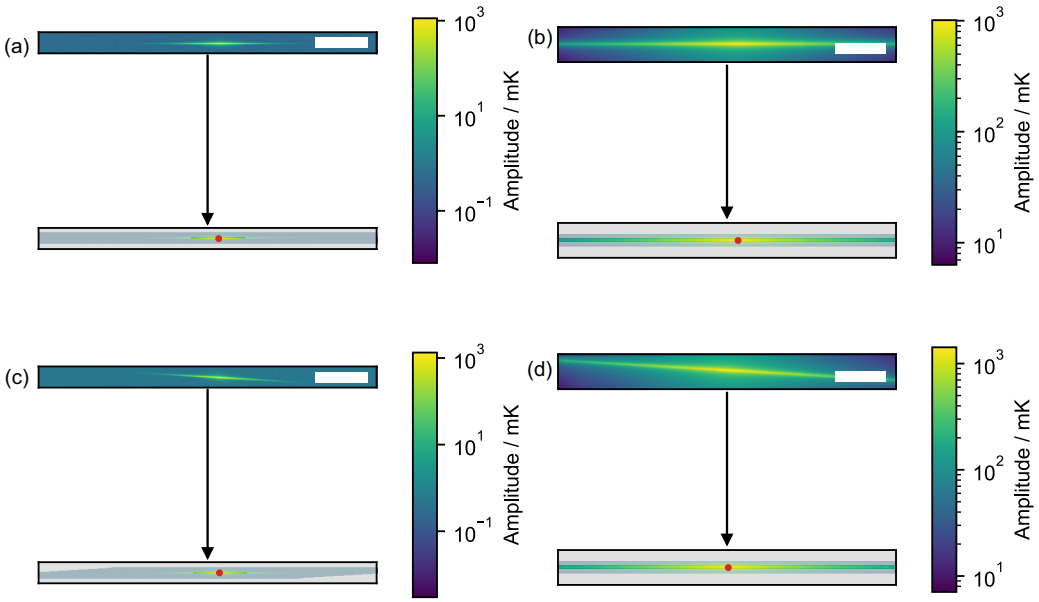

Figure 7.S12.: 2D amplitude images of a 30 µm PEEK fiber of (a, b) aligned and (c, d) tilted fibers. The scale bars for the 1× lens in (a) and (c) are 2000 µm, for the 8× lens in (b) and (d) 250 µm.

8

Relationship Between the Tensile Modulus and the Thermal Conductivity Perpendicular and in the Fiber Direction of PAN-Based Carbon Fibers

Simon Bard,[1, 3] Thomas Tran,[2, 3] Florian Schönl,[1] Sabine Rosenfeldt,[2] Martin Demleitner,[1] Holger Ruckdäschel,[1] Markus Retsch,[2] and Volker Altstädt[1, *]

1 Department of Polymer Engineering, University of Bayreuth, Universitätsstraße 30, 95447 Bayreuth, Germany

2 Bavarian Center for Battery Technology (BayBatt), Bavarian Polymer Institute, and Bayreuth Center for Colloids and Interfaces, Department of Chemistry, Physical Chemistry I, University of Bayreuth, Universitätsstraße 30, 95447 Bayreuth, Germany

3 These authors contributed equally to the work

∗ Corresponding author

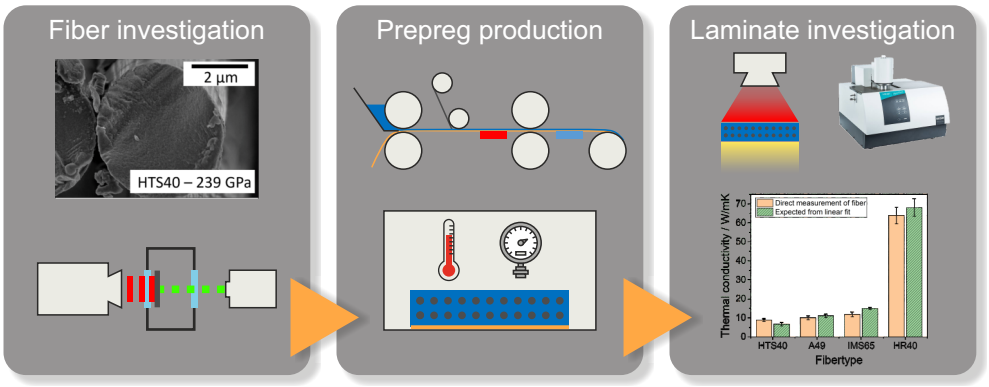

Published in *Carbon Letters*, **2023**.

8.1 Abstract

A thorough knowledge and understanding of the structure-property relationship between thermal conductivity and C-fiber morphology is important to estimate the behavior of carbon fiber components, especially under thermal loading. In this paper, the thermal conductivities of different carbon fibers with varying tensile modulus were analyzed perpendicular and parallel to the fiber direction. Besides the measurement of carbon fiber reinforced polymers, we also measured the thermal conductivity of single carbon fibers directly. The measurements clearly proved that the thermal conductivity increased with the tensile modulus both in fiber and perpendicular direction. The increase is most pronounced in fiber direction. We ascribed the increase in tensile modules and thermal conductivity to increasing anisotropy resulting from the orientation of graphitic domains and microvoids.

8.2 Introduction

Carbon fibers are usually made from cellulose, polyacrylonitrile (PAN), or mesophase pitch. Fibers with the precursor cellulose have low thermal and electrical conductivity due to the lattice defects in the carbon structure. Therefore, they are mainly used as insulating materials.[1] Fibers made from PAN or pitch play a more important role economically and are used in aircraft, wind turbine blades, and vehicles.

High temperature treatment of PAN precursors leads to dehydrogenation, cyclization reactions, N_2-elimination, and carbonization. Overall, these reactions lead to the high thermal stability and good mechanical properties of the resulting carbon fibers, especially if the fibers were aligned during the stabilization process. Microscopically, the high temperature processing leads to semicrystallinity due to the formation of graphitic domains. The fibers made from polyacrylonitrile have a circumferentially orthotropic structure, i.e., their properties depend on the direction in which they are measured. Heat transport takes place mainly within the graphitic basal planes, which are held together by covalent bonds. Only weak Van der Waals forces act between the basal planes, which reduces transversal heat transport.[2,3]

The anisotropic fiber morphology has a considerable influence on the fiber properties. The anisotropic behavior was extensively studied and compared to micromechanical models in other publications of the author.[4–6] The anisotropy affects tensile strength and Young's modulus, thermal expansion, and electrical and thermal conductivity.[7–10] Morgan[10] showed that the property profile can be adjusted by the temperature during the production of the fibers. The higher the oven temperature, the more the layers orient

themselves in the longitudinal direction of the fibers. This results in a more aligned structure, which significantly increases the anisotropy. As expected, this has an effect on the respective morphology of the carbon fiber.

In the PAN-based carbon fibers, there is mostly a random distribution of the individual layers, while more ordered structures result in the pitch-based ones. Qin et al.[11] investigated the effect of temperature treatment on the morphology of PAN-based carbon fibers and the effects on elemental composition, porosity and mechanical properties, tensile strength, and tensile modulus. In their work, the fibers were high-temperature treated over a range of 1300 °C to 2700 °C. They showed that the carbon content of the fibers increases with increasing processing temperature, while the remaining elements such as nitrogen and hydrogen are split off. In particular, the step from 1300 °C to 2000 °C stands out, where the nitrogen content is reduced from 4.96 % to 0.12 %, resulting in a carbon yield of 99.4 %. This results in an increased porosity of the fiber, since the elimination of nitrogen leads to the formation of pores and voids in the fiber. These are only eliminated with a further increase in temperature by rearrangements in the lattice structure. With the increase in temperature, an increasing orientation of the crystalline domains becomes apparent. In the case of the PAN-based carbon fibers, a largely unordered structure can be seen for the temperature treatment up to 1300 °C (see Figure 8.1). When treated up to 2700 °C, a clear orientation and growth of the graphitic lamellae can be seen.

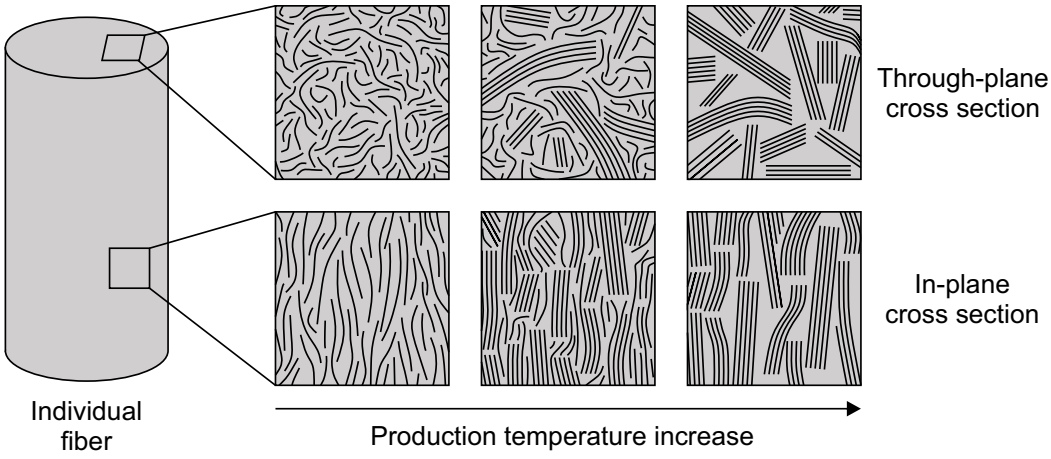

Figure 8.1.: Scheme of fiber microstructure based on PAN with increasing production temperature.

The different fiber morphologies also affect the mechanical and thermal properties, as shown by Qin et al.[11] Their findings show that especially the tensile modulus increases with increasing temperature as a result of the increased alignment and growth of the crystallites. However, when the tensile strength is considered, it shows a decrease with increasing high-temperature treatment. The reason for this is the orientation of the

graphene layers. With increasing temperature, the amount of entanglement and covalent cross-linking decreases, resulting in a decreased shear modulus. In addition, there is an increase in the microporosity within the fiber, mainly due to cleavage of the chemically bound nitrogen and consequent formation of defects in the crystal structure.[8,10,11]

Due to the morphology induced anisotropy of the fibers, there are significant differences between the thermal conductivity longitudinal (0°) and transversal (90°) to the main fiber axis. In this regard, Zhang[3] suggests that the transverse thermal conductivity is generally equivalent to about 1 % of the longitudinal thermal conductivity. Our findings in other publications show that this can only be seen as a rough estimation.[5] The literature review summarized in Tabelle 8.1 shows that the relation between thermal conductivity in fiber direction, $\kappa_{\parallel}$, and in transverse direction, $\kappa_{\perp}$, (the anisotropy factor) varies between different fibers.

Table 8.1.: Overview of thermal conductivities for PAN and pitch-based carbon fibers parallel and perpendicular to the longitudinal fiber axis.

Precursor	$\kappa_{\parallel}$	$\kappa_{\perp}$	Tensile modulus	Classification	Source
	$W\,m^{-1}\,K^{-1}$	$W\,m^{-1}\,K^{-1}$	GPa		
PAN (n. a.)	17	(n. a.)	(n. a.)	(n. a.)	[12]
PAN (n. a.)	10-20	(n. a.)	(n. a.)	(n. a.)	[13]
PAN (n. a.)	5	(n. a.)	(n. a.)	(n. a.)	[14]
PAN (n. a.)	16	3	(n. a.)	(n. a.)	[10]
PAN (T700S-12K)	10.2	1.3	230	HT	[15]
PAN (Toray T300)	7	2	230	HT	[2]

n. a. = not available HT = high tenacity

From the literature, it is well-known that the conditions during production of the fiber (mainly the temperature) lead to different morphology and different mechanical properties. So far, the effect on thermal conductivity in fiber and transverse direction has not been studied. The aim of this work is to investigate the influence of the morphology of carbon fibers with varying tensile modulus on the thermal conductivity of composites with a resin matrix made thereof.

8.3 Materials and methods

8.3.1 Materials

The resin tetraglycidylmethylenedianiline (TGMDA, Epikote™ RESIN 496, Hexion Inc., Columbus, OH, USA) is four-functional with an epoxy equivalent of 115 $g\,eq^{-1}$. The used

hardener was diethyltoluenediamine (DETDA, XB3473™, hydrogen equivalent weight 43 g eq^{-1}).

The used carbon fibers were HTS40 (Toho Tenax, Chiyoda, Japan), A49 (Dowaksa, Tucson, AZ, USA), IMS65 (Toho Tenax, Chiyoda, Tokyo, Japan), and HR40 (Mitsubishi, Tokyo, Japan). Further properties can be found in Tabelle 8.2.

Table 8.2.: Manufacturer data of fibers used in the underlying research.

Fiber	Manufacturer	Tensile strength	Tensile modulus
		MPa	GPa
HTS40	Toho Tenax	4620	239
A49	DowAksa	2900	250
IMS65	Toho Tenax	6000	290
Pyrofil HR40	Mitsubishi	4610	390

8.3.2 Resin preaparation and curing

TGMDA and DETDA were mixed stoichiometrically (72:28 m/m). Degassing followed at 10–20 mbar. The samples were cured in a laboratory oven at 120, 160, and 200 °C, at each temperature for 1 h with a heating rate of 10 K min^{-1}. A postcuring at 220 °C for 2 h followed.

8.3.3 Prepreg production and consolidation

The department of Polymer Engineering owns a industry-like processing line to produce prepregs (pre-impregnated fibers). The procedure is as follows: 12 K unidirectional carbon fiber rovings were pre-spread with rollers. A carrier paper was coated with a resin film at room temperature. In the last step, the fibers were compressed with the resin film to the final prepreg with calander rolls (25 °C). The prepregs were stored in a fridge at (−20 °C) before further processing. By hand lay-up the prepregs were stacked and air was removed. It followed a sealing in vacuum bags and curing under atmospheric pressure of 5 bar in a laboratory press at 120, 160, and 200 °C, at each temperature for 1 h with a heating rate of 10 K min^{-1}. Post-curing at 220 °C for 2 h before cooling at a rate of 5 K min^{-1} followed.

8.3.4 Determination of fiber volume content

Thermogravimetric analysis (TGA) was conducted with the TG 209 F1 Libra (Netzsch-Gerätebau GmbH, Selb, Germany).

The fiber volume content was determined by TGA according to DIN 16459:2019-12.[16] In the suggested routine, fibers were dried for 2 h at 120 °C in the TGA. Then the fibers were heated in the TGA from 20 °C to 800 °C, with a heating rate of 2 K min^{-1} under a nitrogen flux of 85 mL min^{-1}. Samples cut from the laminates and samples cut from neat resin plates were dried for 2 h in the TGA, then heated up to 450 °C with a heating ramp of 10 K min^{-1}. Finally, an isothermal step for 170 min at 450 °C was performed. All samples were handled with gloves to prevent possible contamination.

In the TGA, the fibers showed only a slight weight loss of 1.0(1) %, which could be attributed to the oxidation of the sizing. During the drying step, no significant weight loss could be detected.

The fiber volume content, Φ, could then be calculated as

$$\Phi = \frac{m_f}{\rho_f\left(\frac{m_f}{\rho_f} + \frac{1-m_r}{\rho_r}\right)}, \tag{8.1}$$

where m_f is the mass of the fibers, ρ_f is their density, and ρ_r represents the density of the resin. The mass of the fibers was calculated by

$$m_f = \frac{m_l - m_r}{1 - m_r}, \tag{8.2}$$

where m_l is the remaining mass of the laminate after the cycle, and m_r is the remaining mass of the resin.

The method was successfully verified and tested in comparison to the determination of the fiber volume content via density measurements.[5]

8.3.5 Thermal conductivity measurements of composites

The thermal conductivity was measured by the laser flash method (LFA) with LFA447 (Netzsch GmbH, Selb, Germany). Five shots were used with a duration of 30 ms each, the signal was fitted with the Proteus Analysis Software (Netzsch GmbH, Selb, Germany) by the Cape–Lehman algorithm. The tested samples had a diameter of 12.7 mm.

The density was measured with the AG245 (Mettler-Toledo International Inc., Columbus, Ohio, USA) using Archimedes' principle. The thermal heat capacity was measured

with the DSC 1 (Mettler-Toledo International Inc., Columbus, OH, USA), according to ASTM E1269–11, with a heating rate of 20 K min^{-1}.[17]

8.3.6 Nanostructural analysis of PAN fibers

For volume-averaged nanostructural analysis, small-angle (SAXS) and wide-angle X-ray (WAXS) scattering were performed on a bundle of parallelly aligned fibers using a Double Ganesha AIR system (SAXSLAB/Xenocs), equipped with a rotating copper anode (MicroMAx 007HF, Rigaku Corporation, wavelength of $\lambda = 0.154\,\text{nm}$). Data were recorded with a position-sensitive detector (Pilatus 100K for WAXS, PILATUS 300K for SAXS; Dectris). Two-dimensional scattering patterns were converted into one-dimensional intensity profiles of $I(q)$ vs q, where q is given as

$$q = \frac{4\pi}{\lambda} \sin\frac{\theta}{2}, \tag{8.3}$$

with the scattering angle θ. X-ray diffractograms (XRD) of the carbon fiber bundles were recorded in Bragg-Brentano geometry as coupled θ-2θ scans using an Empyrean system (PANalytical, Almelo, Netherlands) equipped with a sealed X-ray tube (Cu-K$_\alpha$), a PIXEL solid state detector, and a spinning stage.

8.3.7 Thermal conductivity measurements of single fibers

Thermal diffusivity of single fibers was determined via lock-in thermography in accordance with our previous publication.[18] All measurements were done in a vacuum ($p < 5 \times 10^{-2}\,\text{mbar}$). A laser beam (Genesis MX 532-1000 SLM OPS, Coherent, Dieburg, Germany, $\lambda = 532\,\text{nm}$) periodically heated the sample with a frequency of 2 Hz for HTS40, A49, and IMS65 fibers and 20 Hz for HR40 fibers. A higher frequency was chosen for HR40 fibers to decrease the thermal diffusion length and thus ensure the assumption of an infinite sample dimension. The laser power was set to 0.1 mW to heat the samples as little as possible while maintaining a suitable signal-to-noise ratio. An infrared (IR) camera (Image IR 9430, InfraTec GmbH, Dresden, Germany) equipped with an 8× microscope lens monitored the sample temperature for 60 s at 200 fps. The pixel resolution of this setup is 1.3 µm. Measurements were performed using Infratec's IRBIS active online software. The slope of the logarithm of the amplitude vs the distance from the excitation, m_A, and the phase vs the distance, m_Φ, were evaluated between 0.2

and 0.8 mm. The thermal diffusivity, α, was calculated utilizing the slope method,[19] i.e.,

$$\alpha = \frac{\pi f}{m_\Phi m_A}. \tag{8.4}$$

For each fiber type, 3 fibers were measured 3 times each.

The volume of at least 400 mg of fibers was measured with a pycnometer (Ultrapyc 1200e, Anton Paar QuantaTec Inc., Boynton, Florida, USA) by analyzing 100 runs. The weight of the samples was determined with an analytical balance (CP324S, Sartorius Lab Instruments GmbH & Co. KG, Göttingen, Germany). Heat capacity was measured via differential scanning calorimetry (Discovery DSC 2500, TA instruments, New Castle, USA) of 3 samples for each fiber type following the ASTM E1269–11 standard.[17]

8.4 Results and discussion

8.4.1 Morphology of fibers

The amount and spatial distribution of non-graphitizing and graphitizing carbons highly depends on the processing temperature. With increasing temperature, the graphitic domains grow and the layers orient parallel and equidistant to each other. While atoms are connected by strong covalent bonds inside a layer, only Van der Waals forces act perpendicular to the layers. As a result, physical properties such as the tensile modulus and thermal conductivity depend on the measurement direction. In pyrolytic graphite, the thermal conductivity parallel to the graphitic layers is about 2000 $W\,m^{-1}\,K^{-1}$, while it is only 5 $W\,m^{-1}\,K^{-1}$ perpendicular to the layers.[20] In general, both tensile modulus and thermal conductivity are expected to increase with increasing processing temperature. Tensile moduli for the investigated fibers are provided by the manufacturers (Tabelle 8.2), but neither thermal conductivity nor processing conditions are given.

To investigate the fiber morphology, we performed nanostructural analysis using scanning electron microscopy (SEM), small (SAXS) and wide (WAXS) angle X-ray scattering, as well as X-ray diffraction (XRD). SEM images (Abbildung 8.2a-d and Figure 8.S1a-b) of the fiber cross sections reveal a coarse grained pattern suggesting a porous structure. The structure is most dense for HTS40 and IMS65. A49 and HR40 have a less dense, more granular appearance. The increase in roughness seems to be unrelated to the increase in tensile modulus. The 2D-SAXS patterns (Abbildung 8.2e-f, Figure 8.S1c-d) of all fibers exhibit a comparable, barbell form. We attribute this pattern mainly to a preferential orientation of nano- and microvoids along the fiber axes. Assuming

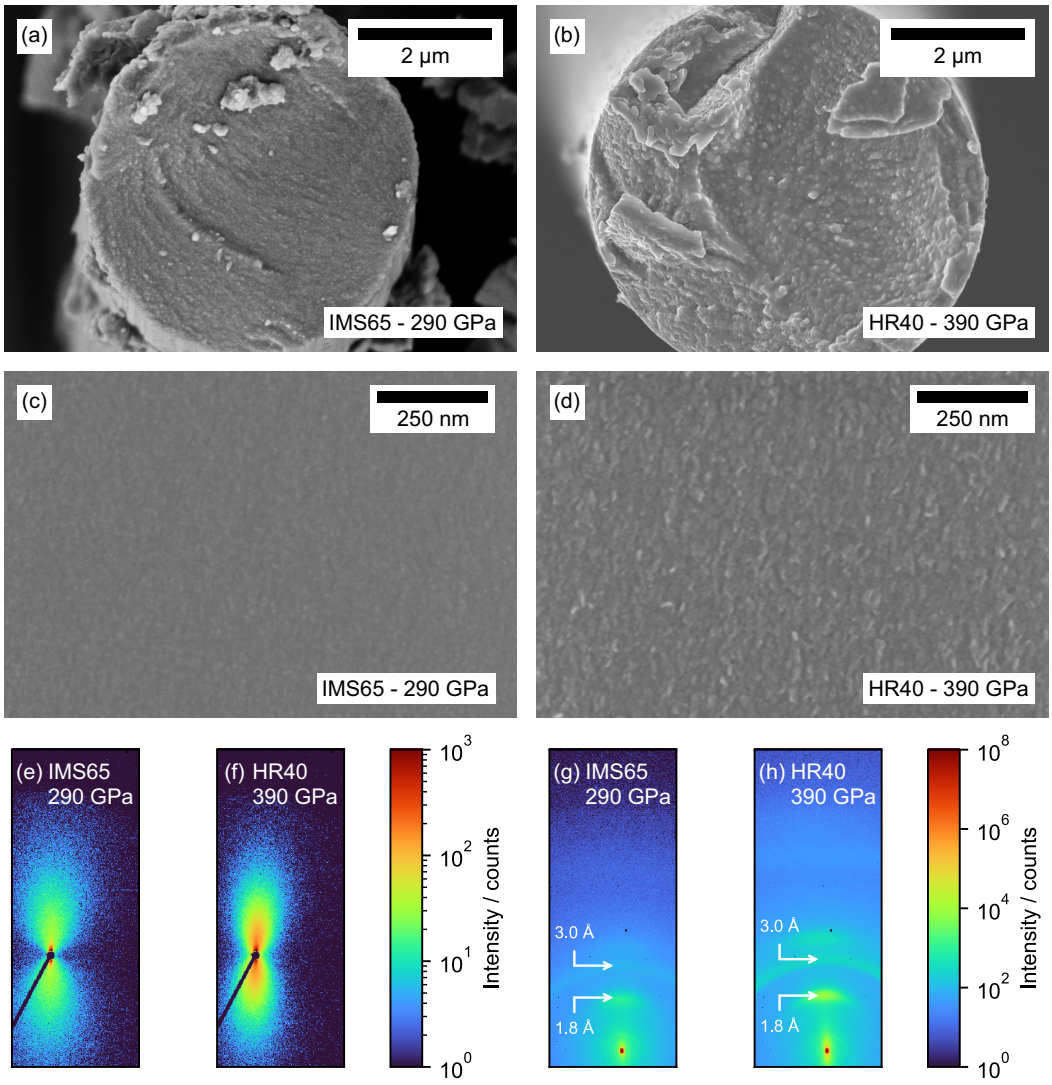

Figure 8.2.: Comparison of the fiber nanostructure. (a-d) SEM images of the cross sections of a high and low tensile modulus fiber with different magnifications. (e-f) WAXS and (g-h) SAXS scattering patterns of corresponding fiber bundles.

a Gaussian distribution, azimuthal averaging shows an orientation with a standard deviation of 15° to 19° (Figure 8.S2). The radially averaged data (Figure 8.S3) reveals a power law behavior of q^{-1} at an intermediate q-range with q being the scattering vector. This is characteristic for one-dimensional objects and suggests spindle-like voids. At lower values of q, a behavior of q^{-4} is visible. The crossing point between the two regimes, corresponds to a correlation length, l_p. Assuming

$$q \cdot l_p = 2\pi, \tag{8.5}$$

the correlation length is approximately 25 nm for HTS40 and IMS65, 30 nm for A49 and 45 nm for HR40. The second change of the power law behavior at $q \approx 0.14\,\text{Å}^{-1}$ hints to a feature size of about 4.5 nm. Assignment to pores or crystallites is inconclusive.

The WAXS data (Abbildung 8.2g-h and Figure 8.S1e-f) show that voids seen in SAXS coexist with an ordered arrangement of graphitic domains. As a simple model, we can imagine the fibers consisting of graphitic bands and voids (Abbildung 8.1). The fibrilar graphitic bands align parallel to the fiber orientation and are separated by the voids. Thus, we attribute the sharp, anisotropic Bragg spot at around $1.8\,\text{Å}^{-1}$ to the average thickness of the crystalline bands. The reflex at about $3.0\,\text{Å}^{-1}$ is isotropic and hints to a turbostratic orientation of the individual layers inside the crystalline bands. XRD measurements (Figure 8.S4) confirm these values and give additional insights into the graphitic structure. The (002) reflex position shifts with increasing tensile modulus from 25.2° (HTS40) to 26.1° (HR40). This indicates that the interlayer distance decreases sligthly from 0.35 nm (HTS40) to 0.34 nm (HR40). At the same time, the ratio of the reflex area to its height changes considerably. While HTS40, A49, and IMS65 have a ratio of about 2.8°, it is 5.6° for HR40. This indicates that there are bigger crystalline domains in the HR40 fibers. The area ratio of the (002) and (10) reflexes changes from roughly 36 (HTS40, A49, IMS65) to 57 (HR40), suggesting different shapes of the graphitic domains. A precise determination of the crystal size is not possible, because the anisotropy constant in the Debye-Scherrer equation is unknown for our samples. We roughly estimate the crystalline domain size to be 4 nm (HTS40, A49, IMS65) and 8 nm (HR40). Despite the absolute value being only a rough estimation, we can definitely say that HR40 has larger crystalline domains.

8.4.2 Thermal conductivity of laminates

The thermal conductivity, κ, can be calculated from the heat capacity, c_p, density, ρ, and thermal diffusivity, α, by the following equation:

$$\kappa = \rho \cdot c_p \cdot \alpha. \tag{8.6}$$

Abbildung 8.3a shows the transverse thermal conductivity of the fiber composites as a function of fiber type and fiber volume content. The fiber HR40 with a tensile modulus of 390 GPa also exhibits the highest transverse thermal conductivity, followed by IMS65 with a tensile modulus of 290 GPa. The two fiber types A49 and HTS40 with tensile moduli of 239 and 250 GPa, respectively, show only minor differences in tensile modulus and thermal conductivity. The overall trend is that the increasing tensile modulus of the fibers is accompanied by an increase in transverse thermal conductivity. This matches our expectations and can be described by the equation of Lewis and Nielsen[21]

(Abbildung 8.3a). An increased tensile modulus indicates higher processing temperatures. As shown in Abbildung 8.1, this correlates with larger crystalline domains in the through-plane cross sections facilitating better heat flow.

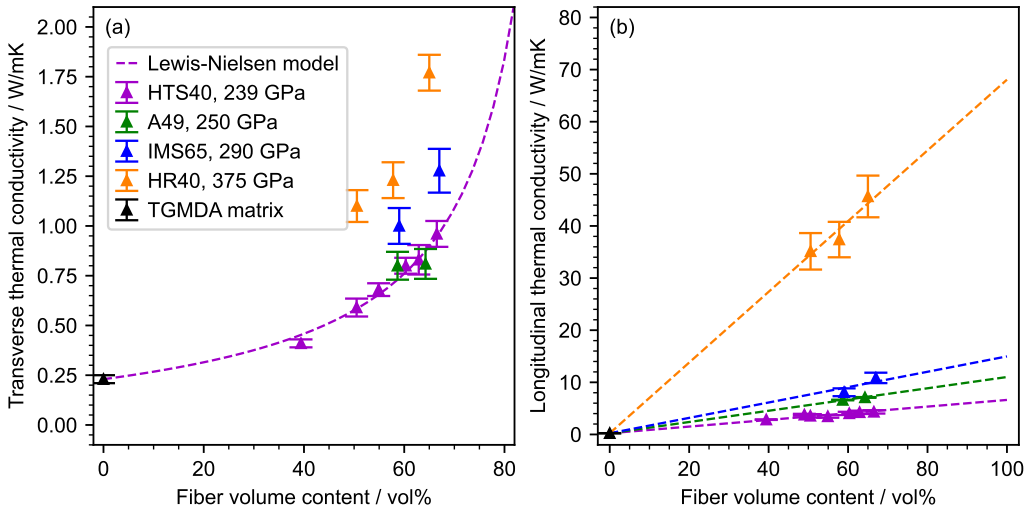

Figure 8.3.: Thermal conductivity in (a) transverse and (b) fiber direction versus fiber volume content depending on tensile modulus. In transverse direction, the thermal conductivity follows the model proposed by Lewis and Nielsen.[21] In longitudinal direction, the thermal conductivity follows a linear mixing model.[22]

At the same time, we expect a greater thermal conductivity parallel to the fiber direction. In addition to their increased size, the crystallites orient along the fiber. Therefore, the thermal conductivity is much higher in the longitudinal direction than in the transverse direction. This becomes clearly visible in Abbildung 8.3b. The thermal conductivity in the fiber direction of the high-modulus carbon fiber is 46 $\mathrm{W\,m^{-1}\,K^{-1}}$ at a fiber volume content of 65 % by volume, while in the transverse direction it is only 1.8 $\mathrm{W\,m^{-1}\,K^{-1}}$. In addition, a clear correlation of the tensile modulus and the thermal conductivity is evident here. The higher the tensile modulus, which likely occurs due to higher production temperatures, the greater the thermal conductivity in the fiber direction. As expected from our structural analysis of the fibers, the largest difference is visible between HR40 and the remaining fiber types.

An anisotropy factor can be calculated from the ratio of thermal conductivity in the fiber direction and in the transverse direction. This value is 4.8(6) for the fiber with a tensile modulus of 239 GPa and then increases to 8.3(2) (250 GPa), 8.5(2) (290 GPa), and 29.4(26) (390 GPa). Thus, the higher the tensile modulus, the better the thermal conductivity in the fiber direction compared to the transverse thermal conductivity. The increase in the anisotropy factor with increasing tensile modulus is likely caused by the crystalline domains.

8.4.3 Thermal conductivity of single fiber measurements

Parallel to the fabrication and analysis of the fiber reinforced composites, the thermal conductivity of neat fibers was measured in fiber direction.

We measured the thermal diffusivity of fibers by lock-in thermography as described in literature.[18,19] Details about the measurement conditions and principle are given in the Materials and methods section. For the fibers with the lowest tensile modulus, HTS40, we obtained a thermal conductivity of 8.8(7) $W\,m^{-1}\,K^{-1}$. With increasing tensile modulus, the thermal conductivity along the fiber direction increases steadily up to a value of 65.2(26) $W\,m^{-1}\,K^{-1}$ for HR40 fibers (Abbildung 8.4).

To compare the measurements to the fiber composites, a linear fit for the measured values of the composites was performed. Extrapolating the fiber volume content to 100 % should equal the values for the isolated fibers (Abbildung 8.4). Within the experimental uncertainties, the directly measured values of the fibers and the extrapolated values of the composites match very well.

Overall, an increasing trend of the thermal conductivity in respect to the tensile modulus is visible. This shows that the fiber nanomorphology, mainly determined by the interplay between voids and graphitic domains, correlates with both the tensile modulus and the thermal conductivity.

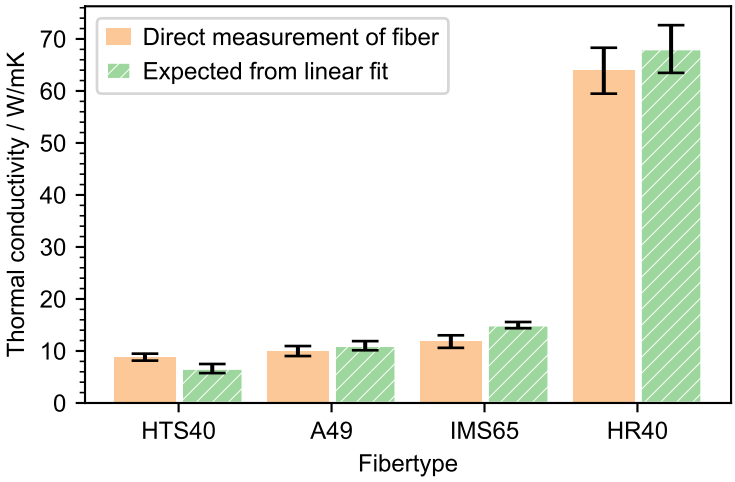

Figure 8.4.: Comparison of direct measurements of the thermal conductivities of fibers and the values derived from linear fitting of the laminates.

8.5 Conclusions

The aim of this work was to investigate the relationship between the morphology of carbon fibers, their tensile modulus, and their thermal conductivity in C-fiber composites with a resin matrix. The most important findings on the influence of the morphology of the carbon fibers under investigation on the thermal conductivity and morphology of the C-fiber can be summarized as follows:

- The investigation of the carbon fibers by SAXS, WAXS and XRD showed differences in the microstructure of the carbon fiber from different producers. We could link differences in the crystalline domains with the tensile modulus provided by the manufacturer.
- The microstructure of the fibers controls the composite thermal conductivity. The effect is particularly pronounced in the direction of the fibers, where the thermal conductivity with a fiber volume content of 65 % was 46 $\mathrm{W\,m^{-1}\,K^{-1}}$ when using the high-modulus fibers and 7 $\mathrm{W\,m^{-1}\,K^{-1}}$ when using the fibers with the lowest tensile modulus. In the transverse direction, the thermal conductivity of the composites with 65 vol% fibers was 1.77 $\mathrm{W\,m^{-1}\,K^{-1}}$ and 0.96 $\mathrm{W\,m^{-1}\,K^{-1}}$ for the high- and low-modulus fibers, respectively.
- The anisotropy of the carbon fibers is retained in fiber-epoxy composites. The transverse thermal conductivity increases disproportionately with increasing fiber volume content. It ranges below 2 $\mathrm{W\,m^{-1}\,K^{-1}}$ and can be described by the equation of Lewis and Nielsen. In the in-plane direction parallel to the fibers, a linear relationship with regard to volume content was observed. We find a maximum anisotropy between parallel and transversal thermal conductivity for the HR40 fibers.
- The direct measurements of the thermal conductivity of individual carbon fibers are in good agreement with the extrapolated values from the composite analysis. This proves that a simple linear mixing model can be used to predict the thermal conductivity along the fiber direction.

8.6 Acknowledgements

The authors kindly thank the German Ministry of Economy and Energy (BMWi) for the funding of the Lufo Project TELOS (FKZ 20Y1516D). We thank the Bavarian Polymer Institute and its keylab for mesoscale characterization for the SAXS, WAXS, and XRD measurements.

8.7 References

[1] N. Sheng, T. Nomura, C. Y. Zhu, H. Habazaki, T. Akiyama, *Solar Energy Materials and Solar Cells* **2019**, *192*, 8–15.

[2] R. Rolfes, U. Hammerschmidt, *Composites Science and Technology* **1995**, *54*, 45–54.

[3] G. Zhang, *Thermal transport in carbon-based nanomaterials*, Elsevier, Amsterdam, Netherlands, **2017**.

[4] S. Bard, M. Demleitner, M. Haublein, V. Altstadt in 22nd European Conference on Fracture (ECF) - Loading and Environmental Effects on Structural Integrity, **2018**, pp. 1442–1446.

[5] S. Bard, F. Schonl, M. Demleitner, V. Altstadt, *Materials (Basel)* **2019**, *12*, DOI 10.3390/ma12071084.

[6] S. Bard, F. Schonl, M. Demleitner, V. Altstadt, *Polymers (Basel)* **2019**, *11*, DOI 10.3390/polym11050823.

[7] A. A. Campbell, Y. Katoh, M. A. Snead, K. Takizawa, *Carbon* **2016**, *109*, 860–873.

[8] D. D. L. Chung, *Carbon Fiber Composites*, 1st ed., Butterworth-Heinemann, Newton, MA, **1994**.

[9] S.-J. Park, *Carbon Fibers*, Springer, Dordrecht, Netherlands, **2015**.

[10] P. Morgan, *Carbon Fibers and their Composites*, 1st ed., CRC Press, Boca Raton, FL, **2005**.

[11] X. Y. Qin, Y. G. Lu, H. Xiao, Y. Wen, T. Yu, *Carbon* **2012**, *50*, 4459–4469.

[12] G. W. Ehrenstein, *Faserverbund-Kunststoffe: Werkstoffe - Verarbeitung - Eigenschaften*, 2nd ed., Carl Hanser Verlag, München, **2006**.

[13] F. Campbell, *Structural Composite Materials*, ASM International, Materials Park, OH, **2010**.

[14] C. Cherif, *Textile Materials for Lightweight Constructions*, 1st ed., Springer, Berlin, **2016**.

[15] K. Dong, K. Liu, Q. Zhang, B. H. Gu, B. Z. Sun, *International Journal of Heat and Mass Transfer* **2016**, *102*, 501–517.

[16] DIN 16459:2021-06, Determination of the fiber volume content of fiber-reinforced plastics by thermogravimetric analysis (TGA), Standard, **2021**.

[17] ASTM E1269-11, Standard test method for determining specific heat capacity by differential scanning calorimetry, Standard, **2011**.

[18] T. Tran, C. Kodisch, M. Schöttle, N. W. Pech-May, M. Retsch, *The Journal of Physical Chemistry C* **2022**, *126*, 14003–14010.

[19] A. Mendioroz, R. Fuente-Dacal, E. Apinaniz, A. Salazar, *Rev Sci Instrum* **2009**, *80*, 074904.

[20] C. Ho, R. Powell, P. Liley, *Journal of Physical and Chemical Reference Data* **1974**.

[21] T. B. Lewis, L. E. Nielsen, *Transactions of the Society of Rheology* **1968**, *12*, 421–443.

[22] Q. Song, M. Schöttle, P. Ruckdeschel, F. Nutz, M. Retsch in *Functional Materials from Colloidal Self-Assembly*, (Eds.: G. Zhao, Q. Yan), **2022**, pp. 493–538.

8.8 Supplemental Information

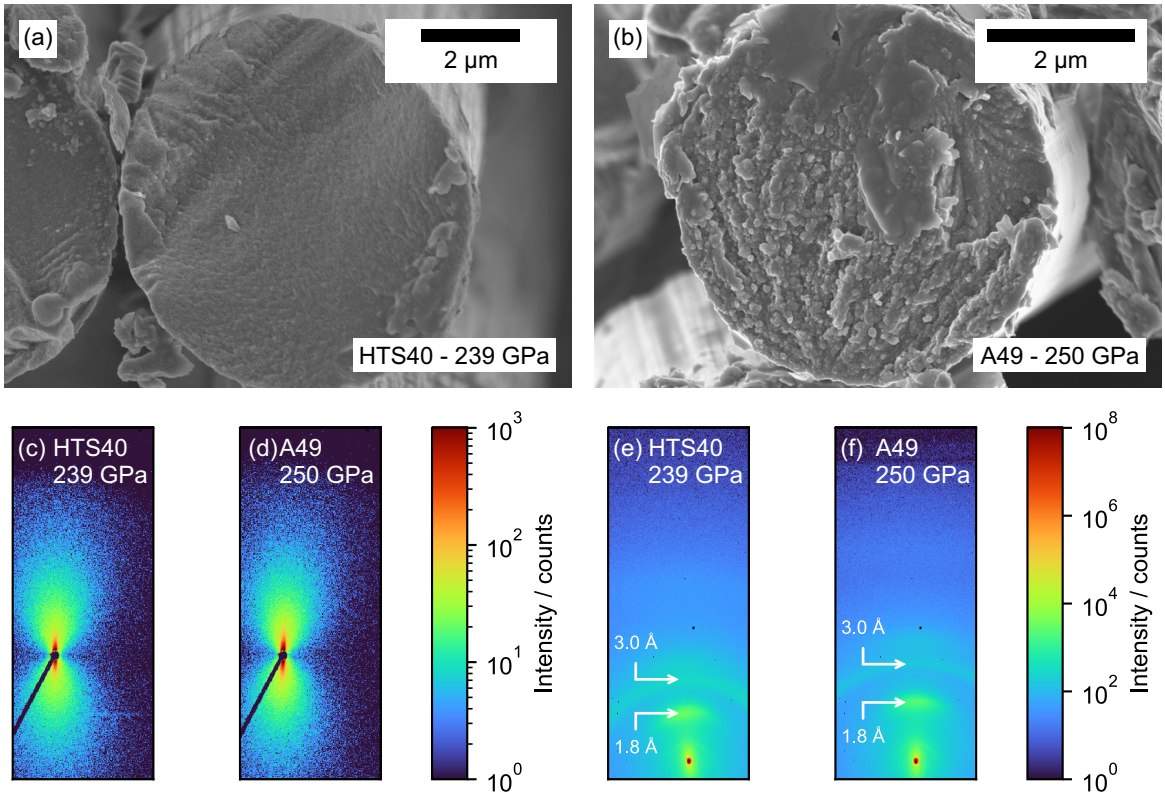

Figure 8.S1.: (a–b) SEM images of the cross sections of different carbon fibers. (c–d) WAXS and (e–f) SAXS scattering patterns of corresponding fiber bundles.

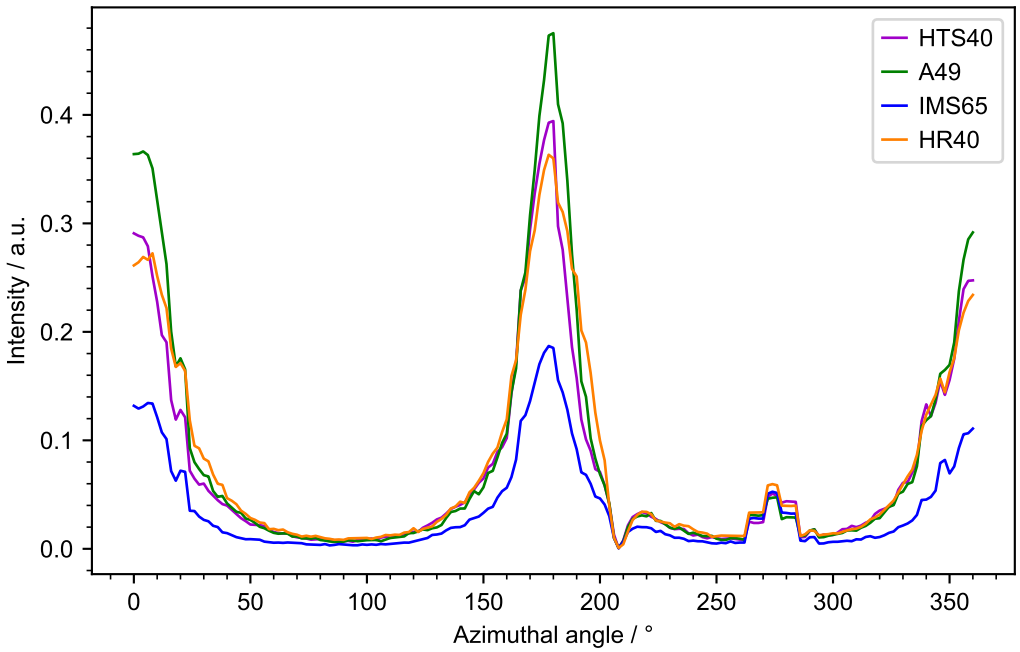

Figure 8.S2.: Azimuthally averaged SAXS data of different fiber bundles. The reflex between 150° and 200° can be fit with a Gaussian shape.

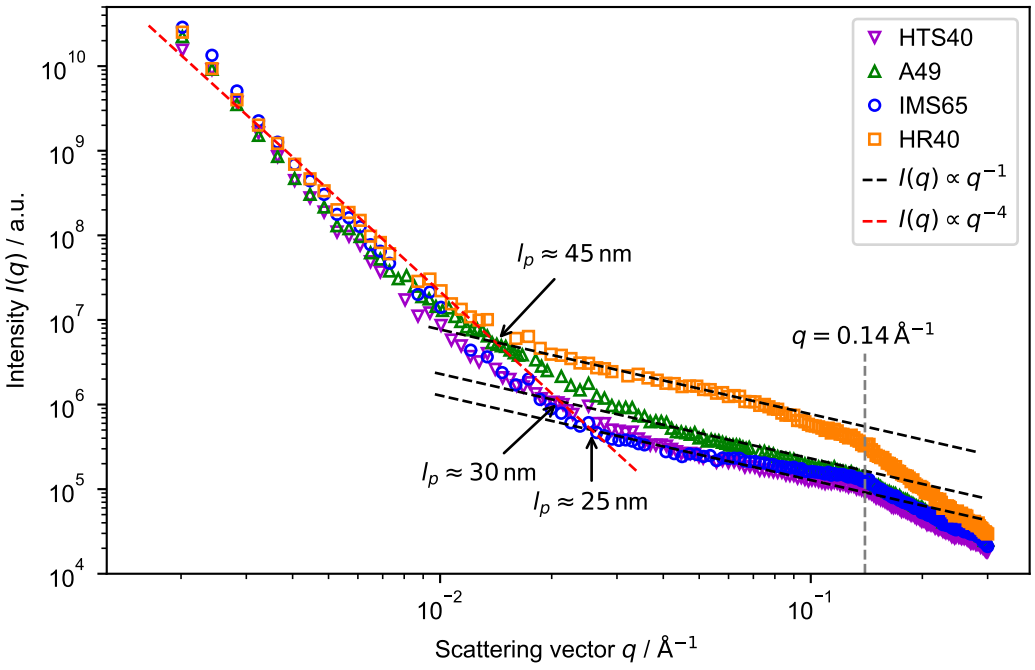

Figure 8.S3.: Radially averaged SAXS data of different fiber bundles. The transitions between different power law behaviors are marked.

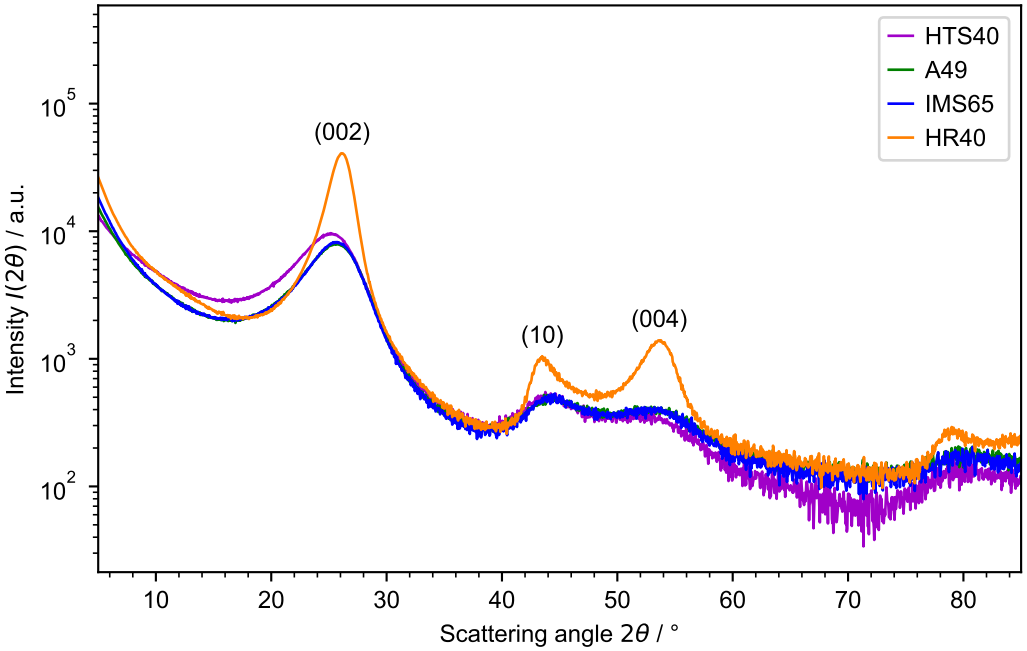

Figure 8.S4.: XRD data of different fiber bundles. All fibers show reflexes characteristic for graphitic domains. HR40 has the most pronounced reflexes.

9 Time-Temperature Integrating Optical Sensors Based on Gradient Colloidal Crystals

Marius Schöttle,[1] Thomas Tran,[1] Tanja Feller,[1] and Markus Retsch[1, 2, *]

1 Department of Chemistry, Physical Chemistry I, University of Bayreuth, Universitätsstraße 30, 95447 Bayreuth, Germany

2 Bavarian Center for Battery Technology (BayBatt), Bavarian Polymer Institute, and Bayreuth Center for Colloids and Interfaces, University of Bayreuth, Universitätsstraße 30, 95447 Bayreuth, Germany

* Corresponding author

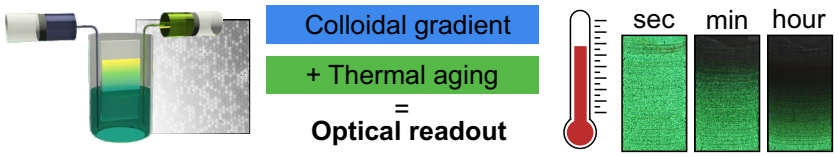

Published in *Advanced Materials*, **2021**, *33*(40), 2101948.

9.1 Abstract

Manipulation-free and autonomous recording of temperature states for extended periods of time is of increasing importance for food spoilage and battery safety assessment. An optical readout is preferred for low-tech visual inspection. Here, a concept for time–temperature integrators based on colloidal crystals is introduced. Two unique features in this class of advanced materials are combined: 1) the film-formation kinetics can be controlled by orders of magnitude based on mixtures of particles with distinct glass transition temperatures. 2) A gradual variation of the particle mixture along a linear gradient of the colloidal crystal enables local readout. Tailor-made latex particles of identical size but different glass transition temperatures provide a homogenous photonic stopband. The disappearance of this opalescence is directly related to the local particle ratio and the exposure to a time and temperature combination. This sensing material can be adjusted to report extended intermediate and short excessive temperature events, which makes it specifically suitable for long-term tracing and threshold applications.

9.2 Introduction

Particle-based colloidal crystals (CCs) and inverse opals have been subject to extensive research for a long time.[1] For homogeneous and patterned colloidal assembly structures a wide range of fabrication techniques has been investigated and established, which render such nanostructured films a mature area of research.[2] The intricate nanostructure on a length scale of a few to hundreds of nanometers raised interest in fields such as granular mechanics,[3,4] heat transport,[5,6] phononics,[7] and catalysis,[8,9] to name a few. By far most prominent is, however, their periodic refractive index modulation, resulting in vivid structural colors. Consequently, colloidal crystals are predestined for sensing, where significant color changes can often be recognized with the bare eye.[10–12]] A shift of the optical stopband, as well as a change of the opalescence intensity, can serve as an indicator for changes inflicted to the colloidal ensemble. Such changes can be caused by temperature,[13,14] force,[15,16] humidity,[17–19] pH,[20,21] ionic strength/complexation,[22] wettability,[23,24] or biodegradation[25] and either alter the refractive index contrast (change in intensity), the periodicity of the structure (change in bandgap), or both. The sensing performance can be further tuned, for example, by the introduction of fluorescence for organic vapor detection.[26–28]

An important and general distinction of sensors is their classification into reversible and irreversible ones. Reversible sensors indicate the actual condition of a system in real-time. Temperature-dependent color changes of liquid crystals are a wide-spread example of

this. In the case of monitoring certain predefined limits, irreversible sensors are more suitable as they allow judging the history of a certain state. Irreversible sensors are especially relevant in food or drug transportation and storage.[29,30] When the readout response changes in a gradual and slow manner, irreversible sensors can also indicate the degree to which a certain state has been exceeded. This provides additional information either regarding the time or intensity that a certain state has been reached. Considering the role of colloidal crystals in the field of irreversible sensors, the loss of opalescence at the film-forming temperature is obvious. This process is also called dry-sintering and has been studied already.[31–33] The onset of dry-sintering is related to the glass transition temperature (T_g) in the case of polymer colloidal crystals. At this point, the optical and thermal properties change abruptly, corresponding to the structural degradation process. The concomitant loss of contrast and periodicity diminishes both photonic opalescence and thermal insulation properties.[34,35] Introduction of additives can alter the kinetics and reversibility of this film formation process, which allows correlating time and temperature processes.[36] Random mixtures of two monodisperse particle types with different glass transition temperatures allowed to change the abrupt jump in thermal conductivity at the glass transition temperature to a gradual one.[37] An even more elaborate microstructural design with locally controlled film formation kinetics was introduced by Lee et al.[38] Polymer inverse opals with locally varied cross-linking densities allowed to determine the temperature and exposure time simultaneously.

The aforementioned work is an excellent example of the emerging possibilities of future functional materials, where unconventional properties can be realized by a local control on the fundamental material properties. Lithographic (micro)patterning of colloidal structures has been investigated by various groups already.[39] Much fewer systems have been reported in the case of CCs and inverse opals, where the structure or composition is gradually altered. First examples for tuning the lattice spacing have been realized by means of diffusion,[40,41] compression,[42,43] wrinkling,[44,45] or an external magnetic field.[46] Ultracentrifugation has also been used for the preparation of colloidal gradients.[47–49]

In this work, we demonstrate how a controlled spatial variation of the colloidal crystal composition allows realizing a time–temperature integrator. We introduce two new aspects to the field of colloidal materials. First, we elaborate a logarithmic dry-sintering kinetic behavior based on random binary CCs consisting of high- and low-T_g polymer particles. Second, we introduce a method to fabricate thin-film colloidal crystals with a compositional gradient. The synergistic combination of composition-dependent kinetics and local composition control results in an adjustable time–temperature integrating sensor with a position-dependent optical readout.

9.3 Results and Discussion

The dry-sintering kinetic properties of a homogeneous CC consisting of purely low-T_g particles are well known (Figure 9.1a). We, therefore, fabricated homogeneous colloidal crystals comprising monodisperse poly[(methyl methacrylate)-*random*-(butyl acrylate)] (PMMA-*r*-nBA) colloids via dip-coating from aqueous dispersions. As a larger contact area between neighboring particles is formed and the air is expelled from the structure, the periodic variation of the refractive index is lost. Concomitantly, the structural color vanishes and the cracks between crystalline domains become larger to accommodate shrinkage, which can be seen in the microscopy images from top to bottom (Figure 9.1a). Transmission UV–vis spectra (Figure 9.1b) show a slight blueshift of the photonic stopband of approximately 10 nm and an even more pronounced decrease of the intensity (purple to yellow color). The normalized stopband intensity can be used as a measure for the kinetics of the film formation process (Figure 9.1c, details in Figures 9.S1 and 9.S2, Supporting Information). We use a semi-logarithmic scale for a clearer representation of the temporal evolution of the sintering behavior. For the specific case shown here ($T_g = 49\,°C$, sintering temperature $T = 60\,°C$), the film formation process is complete after about 4 min (normalized intensity decayed to ≈ 0). Scanning electron microscopy (SEM) images of the colloidal crystal before and after sintering at 60 °C for 100 min (Figure 9.1d,g) confirm the expected loss of porosity during the film formation.

Adding various amounts of a second latex bead of the same size but with a different glass transition temperature ($T_g = 94\,°C$, Figure 9.S3, Supporting Information) to the dip-coating dispersion does not compromise the colloidal crystal formation, but it strongly influences the film formation process. When 50 % high-T_g particles are added, the hexagonal lattice structure is retained, but only half of the particles experience deformation during sintering at 60 °C (Figure 9.1e,h). This leads to particle patches with retained shape and interstitial space. The surface impression provided by SEM is confirmed by the bulk behavior of the stopband, where a blue structural color is retained (Figure 9.1h, inset). Heating a CC composed purely of high-T_g particles at 60 °C shows no effect, and the structure remains unaltered (Figure 9.1f,i).

Analogous to the pure low-T_g system, we quantified the sintering kinetics of various binary CC compositions by in situ UV–vis measurements at 60 °C. Figure 9.1k summarizes the time-dependent decay of the normalized stopband intensity for these systems. Quite strikingly, the binary compositions shift the film formation kinetics by orders of magnitude to longer time scales with an increasing amount of high-T_g particles. Each individual system follows an exponential decay at first glance. We, nevertheless, want to stress that this optical analysis is not sufficient to unravel the detailed mechanics of this process.

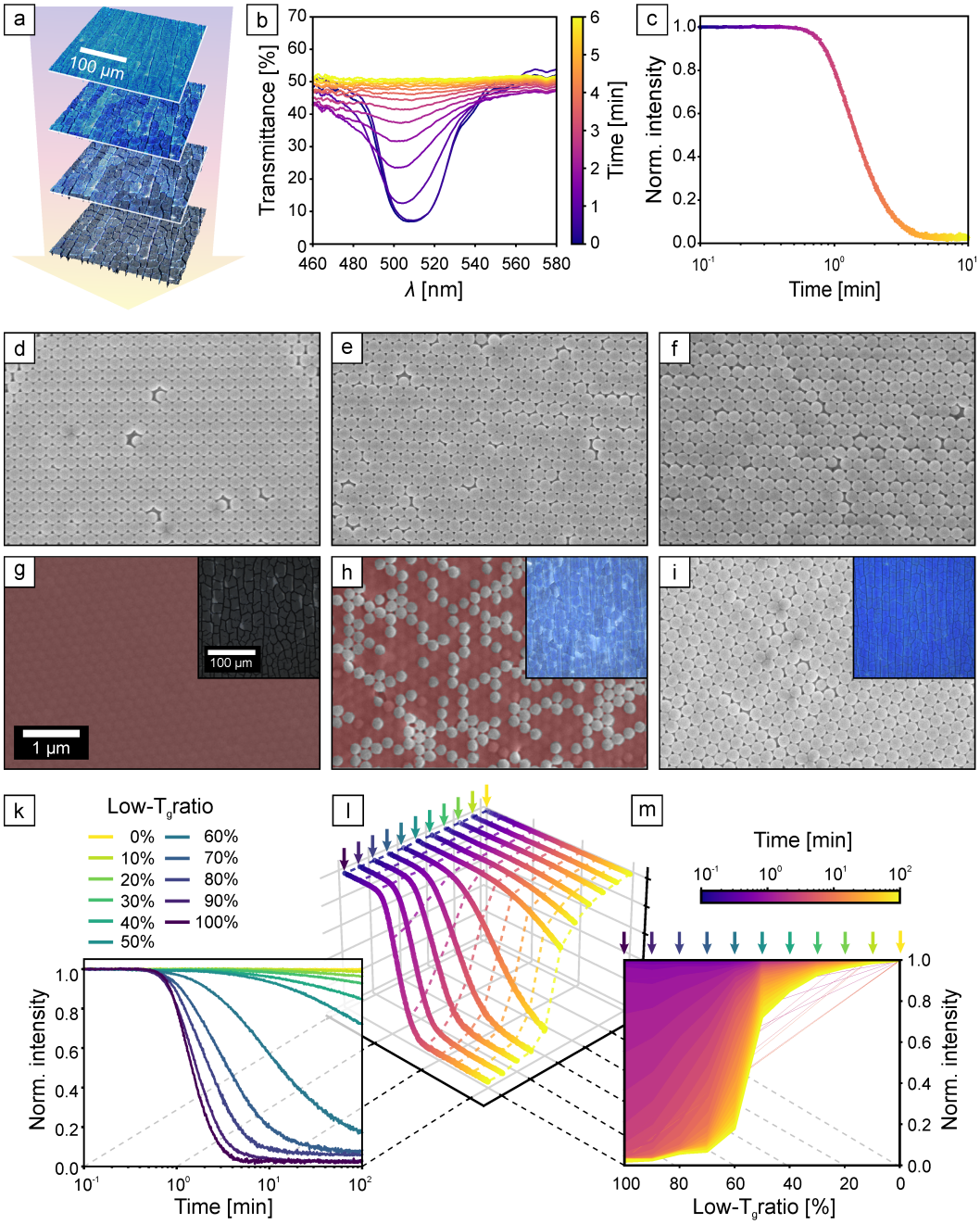

Figure 9.1.: Characterization of the film-formation of colloidal crystals at 60 °C. a) Optical microscopy images show the simultaneous color fading (blue to gray) and crack formation (thin dark lines) during the film-formation of 100 % low-T_g particles. b) In situ transmission UV–vis spectra showing the temporal change of the photonic stopband during the film-formation process shown in (a). c) Time-dependent decay curve calculated from the normalized stopband intensity shown in (b) to quantify the loss of opalescence. d–f) Scanning electron microscopy images of pristine colloidal crystals consisting of 100 %, 50 %, and 0 % low-T_g particles, respectively. g–i) Images of the same samples after 100 min at 60 °C. Dense, sintered regions are color-coded in red, original SEM images are shown in Figure 9.S4, Supporting Information. Insets show light microscopy images, where a loss of the photonic stopband and the appearance of cracks is visible when transitioning from a pristine to a sintered film. k) Stopband decay curves of various compositions between 100 % and 0 % low-T_g particles. (l) and (m) show how the data in (k) can be transformed to convert the time-dependent measurement into a composition-dependent analysis.

Dry-sintering of polymer colloids takes place in a number of different steps, including, for example, contact area formation.[32] The underlying refractive index matching is presumed to arise from viscous polymer flow of the low-T_g component and capillary infiltration of cavities between non-sintered particles. Each step most likely shows a unique temperature dependence, and we will therefore compare these results only qualitatively. One may infer a jump in decay kinetics between the 50 % and 60 % low-T_g particle composition in Figure 1k. We rationalize this by examining SEM images of all sample compositions sintered at 60 °C (Figure 9.S4, Supporting Information). A gradual change in composition results in a transition from a continuous low-T_g particle network to isolated domains. This is most evident between 40–60 % low-T_g particles, where the majority phase inverts. The presence of islands of one particle type is not an effect of phase separation. In Figure 9.S5, Supporting Information, SEM images of partially sintered CCs are compared to a 2D-simulation of a random distribution of two particle types. An analysis of the mean absolute number of neighboring, non-sintered particles in the first, second, and third generation is performed for both the measured and simulated images. The relative intensities as well as the absolute values show a significant overlap between the experimental and simulated data. This comparison confirms the statistical distribution expected due to the same size and surface chemistry of the two particle types.

The observed sintering behavior is rather intriguing as it allows an adjustment of the thermal response simply by mixing particles at a defined ratio with two distinct glass transition temperatures. The dependence of time, composition, and normalized stopband intensity result in a wide parameter space that can be difficult to grasp. We, therefore, introduce an alternative way to visualize the film formation kinetics (Figure 9.1l,m). Here, the normalized intensity is plotted versus the composition and color-coded with respect to the sintering time. Each line represents one specific composition. Figure 9.1l connects the time-scale to the crystal composition. It also helps to understand the representation in Figure 9.1m, from which the expected stopband intensity can be derived for any sintering time and any particle composition. For the sake of clarity, we point out to the reader that throughout this work, the color scheme shown in Figure 9.1k (yellow to turquois) corresponds to a change in composition, while a time dependency is indicated by the color scheme in Figure 9.1m (yellow to purple).

Further in situ measurements of the various particle ratios are conducted at temperatures of 50, 70, and 90 °C (Figure 2a–c). As 50 °C is close to the lower glass transition temperature, the observable effect is comparatively small. None of the samples showed complete thermal degradation during 100 min of measurement time. A gradual change from 100–50 % low-T_g particles is present beyond which none of the curves exhibit a discernible decay. Increasing the temperature to 70 °C causes the low-T_g dominated

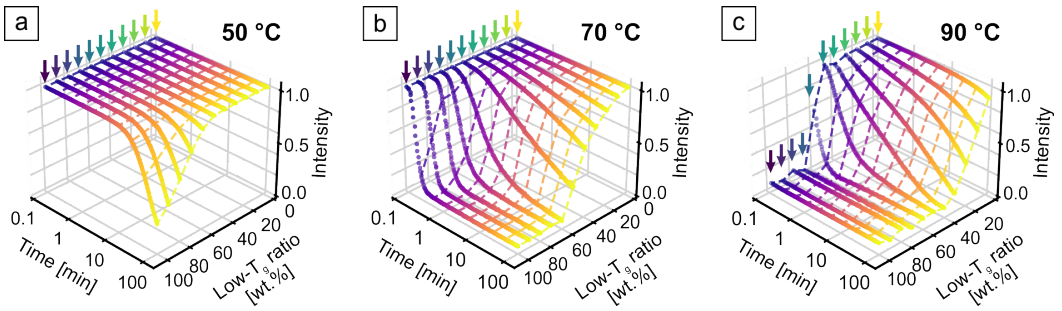

Figure 9.2.: Three-dimensional representation of stopband decay curves. Several compositions are measured at temperatures of 50 °C (a), 70 °C (b), and 90 °C (c). The dashed lines are guides to the eye. They represent the composition-dependent intensity profile expected for the sintering behavior after certain time steps.

samples to degrade in a matter of seconds to minutes. The perceptible change of the profile shape at longer sintering times is shifted to the range between 70–20 %. This is amplified when the temperature is raised further to 90 °C. Here, a slight degradation even of the pure high-T_g particles sets in. In total, the temperature and time-dependent behavior shows how binary CCs could be used as time–temperature integrators. The combination of various compositions and their normalized intensities correlate to certain combinations of the sintering time at a certain temperature. Limits of this particular system are given by a lower temperature where no effect is observed at approximately 45 °C and an excessively fast film formation of all particles above 100 °C (Figure 9.S6, Supporting Information).

To fully exploit the potential of this composition-dependent film formation behavior, we demonstrate now how to arrange the binary particles in a gradient colloidal crystal. For this, we took inspiration from infusion-withdrawal-coating (IWC), which has been reported for sol–gel-derived gradients.[50–53] This method is based on dip-coating by the use of two syringe pumps (Figure 9.3a). A glass substrate is dipped in a dispersion of one particle type, which is extracted with a syringe pump. Simultaneously, a second syringe pump infuses a dispersion of the second particles at a slower rate. The water level, thereby, decreases continuously, mimicking dip-coating, while the composition changes in a slow and gradual fashion. This time-dependent concentration change translates directly into a compositional gradient along the coated substrate. Similar to dip-coating, this produces a continuous thin-film with a strong iridescent color throughout the entire sample. Figure 9.3b also shows a typical colloidal crystal with a film thickness between 4–8 µm. The periodic roughness, especially on the top half of the sample, is a consequence of meniscus pinning and stick-slip behavior.[54] Transmission UV–vis spectra in Figure 9.3c measured at equidistant points along the coating axis corroborate the successful colloidal assembly. The stopband of this photonic crystal is distinct at all points. Peak intensities vary slightly, which is attributed to the observed thickness modulation. Peak position and

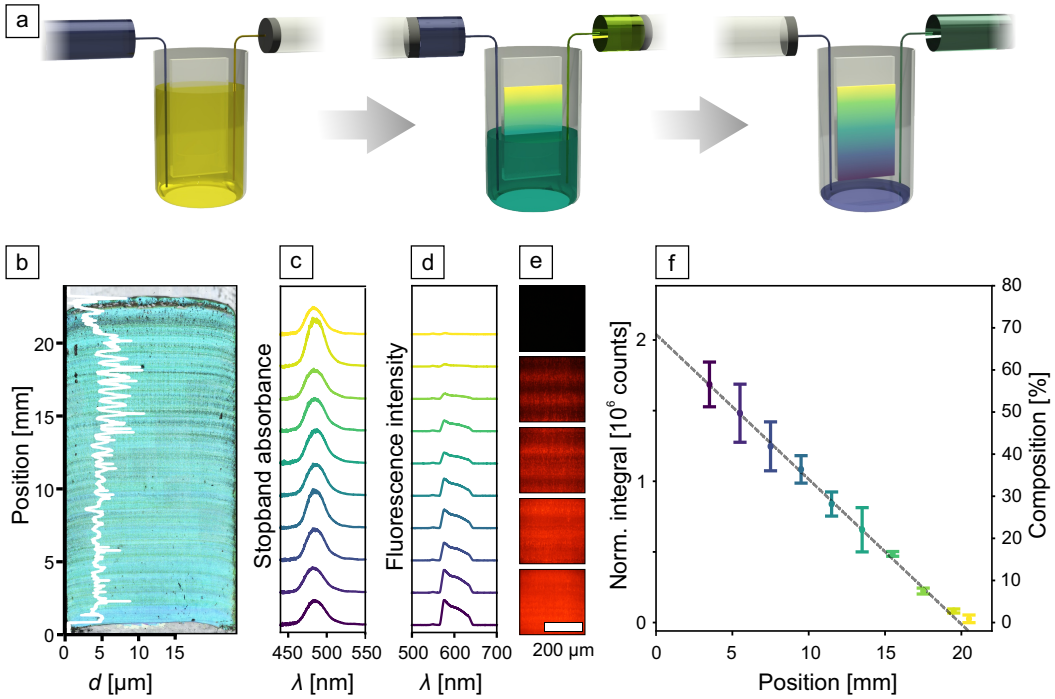

Figure 9.3.: Infusion withdrawal coating technique to fabricate gradient colloidal crystals. a) Simultaneous infusion and extraction of the colloidal dispersion at different rates leads to a continuous composition gradient. This gradient is coated on the submerged glass substrate by continuous extraction of the mixed dispersion. b) Stitched light microscopy image of a colloidal crystal prepared via infusion withdrawal coating. The overlay (white line) shows the thickness of the colloidal film measured along the coating axis. This sample comprises a gradient of fluorescently labeled tracer particles. c,d) Stopband absorbance and fluorescence intensity at various gradient positions, respectively. e) Example fluorescence microscopy images taken along the gradient. f) Change of the normalized fluorescence intensity versus gradient position. A linear profile of the change in composition is obtained. The error bars result from measurements on three individual samples.

FWHM by and large remain constant, emphasizing the homogeneity and high quality of the gradient colloidal crystal. To visualize and quantify the gradual composition change, we introduced red-fluorescent polystyrene particles to the infusion dispersion. These fluorescent tracer beads (100 nm diameter) are small enough to theoretically occupy octahedral gaps in the structure and were added in a trace amount of 1 wt% with respect to the PMMA/nBA particles.

Fluorescence microspectroscopy (Figure 9.3d,e) confirms the targeted composition gradient. A gradual increase of the fluorescence intensity is spectroscopically measured and corroborated by microscopy images exhibiting a transition from black to red. Modulation of the layer thickness can also be observed in the microscopy images. The fluorescence intensity is expected to be proportional to the number of tracer particles and to the film thickness. Quantification of the gradient is, therefore, performed by integration of the fluorescence signal between 560–650 nm. The integrated fluorescence is then corrected

to the local layer thickness by normalization to the stopband intensity measured at the same position. The validity of this analytic procedure is assessed by measuring homogeneously dip-coated samples with defined tracer particle concentrations between 0–1.0 wt% (Figure 9.S7, Supporting Information). The expected linear trend of the tracer particle concentration could be reconstructed when normalizing to the stopband intensity. This analysis confirms the direct relation between fluorescence particle concentration and fluorescence intensity. We use this direct relationship to measure the normalized fluorescence integral at identical positions along three individual gradient samples. Figure 9.3f shows that the composition profile follows a linear trend. Despite the homogeneous photonic stopband of this binary system, we were able to prepare a linear gradient of the tracer particle incorporation. Due to some limitations inherent to the IWC setup, we can access gradients ranging from 0–60 % composition.

Using this approach, we prepared CCs with a gradually changing ratio of high- and low-T_g particles. Two identical gradients are subjected to sintering temperatures of 70 and 90 °C, respectively (Figure 9.4a,b). In both cases, dry-sintering and loss of structural color sets in first at the bottom of the sample where the amount of low-T_g particles is highest. While the temperature persists, the threshold between the colorful and degraded regions moves along the gradient. As expected, this film-forming process proceeds faster at a higher temperature. To better quantify these observations, we evaluate the normalized peak intensity along the gradient sintered at 90 °C (Figure 9.3c). This data is obtained from ex situ UV–vis measurements (Figure 9.S8, Supporting Information) after the gradient structure has been subjected to the respective time and temperature. The stopband decay correlates well with the aforementioned observations. It becomes especially clear how sintering times on a logarithmic scale can be distinguished. The profiles at 1 and 10 min are just as well separated as those of 10 and 100 min. We further corroborate the reproducibility of the kinetic behavior by including the expected composition-dependent intensity decay derived from Figure 9.2c as dotted lines in Figure 9.4c. This is possible by translating the position along the gradient into a low-T_g ratio via the results from the fluorescence measurements. Expected and measured data overlap quite well and substantiate the controlled and predictable sintering behavior of the nanostructure. Measurements along the same gradient heated to 70 °C in Figure 9.S9, Supporting Information, show a profile where dry-sintering is primarily observed at the bottom of the sample where more low-T_g particles are present. This is corroborated by SEM images of the partially sintered gradient (Figure 9.S10, Supporting Information). In this case, distinguishing sintering times between 1, 10, and 100, and even 103 and 104 min is possible. Further examination shows that similar intensity profiles can be reached by various time–temperature combinations. For the case shown here, annealing at 70 °C for 100 min and 90 °C for 1 min result in comparable measurements. This behavior portrays the expected sensitivity to both temperature and time. We point out that a

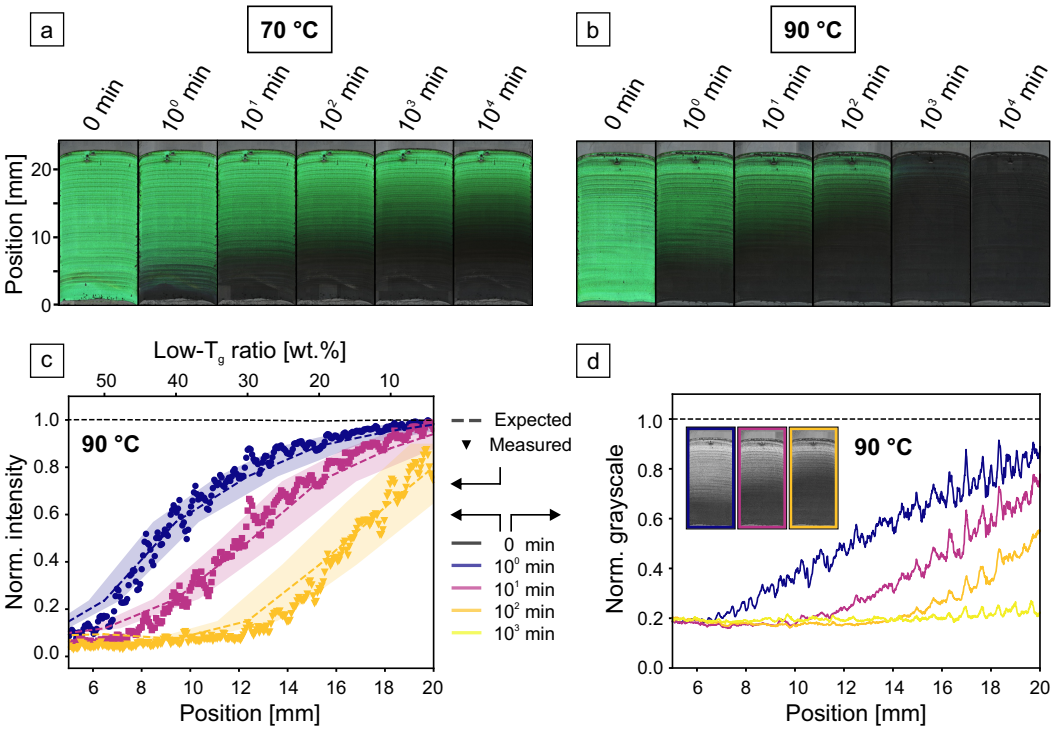

Figure 9.4.: Colloidal crystals with a gradual change of the ratio of high- and low-T_g particles. (a) and (b) show identically prepared gradients and the sintering procedure at 70 and 90 °C, respectively. Images are obtained via stitching of light microscopy images and ex situ during the sintering process. The respective sintering times increase on a logarithmic scale. c) Normalized intensity obtained from ex situ UV–vis transmission measurements along the gradient axis. The dotted lines correspond to expected profiles originating from in situ measurements shown in Figure 9.2c. The shaded areas arise from the errors in the linear fit in Figure 9.3f, which is needed to correlate distance and composition. d) The inset shows green-channel images after color-channel separation of the pictures in (b). Profile analysis normalized to the measurement of the pristine gradient shows analogous results to the ex situ UV–vis measurements.

correction coefficient is applied to the expected data to shift the axis of the particle composition relative to the position on the substrate in Figure 9.4c. This is necessary due to subtle and non-systematic variations during the individual coating processes. Such variations are likely caused by inconsistent pinning of the meniscus, variations of the substrate wettability, and the relative humidity during coating. The correction is done by optimizing a shift parameter to overlap the expected and measured data at a sintering time of 1 min. In the case of the 90 °C measurement, the axis is shifted by 0.8 mm. This is a reasonably small variability given the dynamic position of the wetting meniscus. Profiles of ensuing measurements at longer sintering times then all show a good agreement between the expected and measured intensity profiles.

The simplest method of analyzing the sintering behavior is the observation of the structural color at different degrees of sintering. The sintering difference along the composition gradient is obvious to the bare eye (Figure 9.4a,b). Simple image analysis is

sufficient to obtain a more quantitative analysis, which reaches a comparable significance compared to the spectral analysis shown in Figure 9.4c. The separation of the color channels and profile analysis of the green channel image is shown in Figure 9.4d. The distinction of sintering times on the same logarithmic time-scale is clearly visible. To provide a benchmark, the accuracy of temperature and time determination by green-channel evaluation is provided in Figures 9.S11 and 9.S12, Supporting Information, respectively. These experiments show that, depending on the absolute temperature region, temperature steps between 5–10 °C can clearly be distinguished. Regarding the temporal evaluation, approximately 1–2 steps can be resolved between each decade. Despite the uniquely simple measurement and evaluation, reproducibility is not impaired as shown in Figure 9.S13, Supporting Information. Identically prepared colloidal crystal gradients show green-channel profiles with a strong overlap when subjected to the same thermal history.

This method of evaluation requires no elaborate equipment and works with a low-level software realization. We expect that given correct lighting conditions and a reference region on each sample, this analysis could be readily achieved by modern smartphones. This provides the context for a potential application of such gradient-based time–temperature integrators. These structures operate autonomously and cannot be restored nor refreshed once the film formation sets in and are, therefore, not susceptible to manipulation. The distinct property of this gradient sensor is its sensitivity to prolonged moderate temperature exposures and short high-temperature excesses. The temperature can be imposed by the environmental conditions or caused by an operating device serving as heat source. Hence, a continuous monitoring of, for example, the thermal history of high-power batteries is readily conceivable, where heat management is gaining increased attention. High operating temperatures have pronounced negative effects regarding, for example, capacity fading.[55,56] Batteries that experience excessive temperatures can additionally become a safety hazard.[57] As batteries are an ubiquitous part of everyday life, it is of great importance to make an assessment of the thermal history as simple as possible. The colloidal gradients introduced here provide a visual way to judge on the time–temperature history based on the position-dependent stopband intensity. Beyond a certain threshold of local film formation, either the desired life expectancy would have been surpassed, or an undesired high-temperature excursion appeared. In either case, a thorough analysis of the battery state would be required before further usage. For such potential applications the current model system needs to be improved by a specific design of the required sensitive temperature range. This can be achieved by fine-tuning the composition range, by realizing non-linear composition gradients, and by creating gradient strips with particles of different, pre-defined T_g.

9.4 Conclusion

We have demonstrated a novel approach to functional colloidal crystals, which can be used as time–temperature integrators. Two key advancements in colloidal material fabrication made this sensor based on structural color detection possible. First, mixing of two equally sized, monodisperse latex particles with distinct glass transition temperatures provides access to composite colloidal crystals with specific time-dependent film formation properties. The film formation kinetics at a certain temperature can be varied from a few seconds to hours, days, and weeks by choosing the right particle composition. Second, the fabrication of gradient colloidal crystals allows the translation of the particle composition to a local position. We, therefore, introduced infusion-withdrawal coating for the fabrication of linear composition gradients at a retained optical stopband. The gradient structures exhibit the expected film-formation kinetic behavior and, consequently, change the intensity of the optical stopband locally. The gradual and local transition can be analyzed spectroscopically or through simple image analysis and provides a simple, autonomous, and manipulation-free way to assess the colloidal gradient's thermal history. Our contribution demonstrates how space-specific material engineering allows fabricating structures that exceed their individual components' properties.

9.5 Experimental Section

Details on the particle synthesis, coating procedures, and characterization methods, as well as details regarding the data evaluation of UV–vis spectroscopy, fluorescence spectroscopy, and scanning electron microscopy images can be found in the Supporting Information.

9.6 Acknowledgements

This project was supported by the Bavarian Center for Battery Technology (BayBatt). The help from the Keylab Electron Microscopy is appreciated. Tobias Lauster is thanked for discussions on the optical characterization, Celina Bräutigam is thanked for help with the microscopy images. M.S. and T.T. acknowledge support from the Elite Network Bavaria (ENB). This project has received funding from the European Research Council (ERC) under the European Union's Horizon 2020 research and innovation programme (grant agreement No 714968).

9.7 References

[1] A. Stein, F. Li, N. R. Denny, *Chemistry of Materials* **2008**, *20*, 649–666.

[2] N. Vogel, M. Retsch, C.-A. Fustin, A. Del Campo, U. Jonas, *Chemical reviews* **2015**, *115*, 6265–6311.

[3] J. Yin, M. Retsch, E. L. Thomas, M. C. Boyce, *Langmuir* **2012**, *28*, 5580–5588.

[4] N. Boechler, J. Eliason, A. Kumar, et al., *Physical review letters* **2013**, *111*, 036103.

[5] J. Ma, B. R. Parajuli, M. G. Ghossoub, et al., *Nano letters* **2013**, *13*, 618–624.

[6] M. T. Barako, A. Sood, C. Zhang, et al., *Nano letters* **2016**, *16*, 2754–2761.

[7] W. Cheng, J. Wang, U. Jonas, G. Fytas, N. Stefanou, *Nature materials* **2006**, *5*, 830–836.

[8] C. M. Parlett, K. Wilson, A. F. Lee, *Chemical Society Reviews* **2013**, *42*, 3876–3893.

[9] A. Stein, B. E. Wilson, S. G. Rudisill, *Chemical Society Reviews* **2013**, *42*, 2763–2803.

[10] Z. Li, Y. Yin, *Advanced Materials* **2019**, *31*, 1807061.

[11] J. Hou, M. Li, Y. Song, *Nano Today* **2018**, *22*, 132–144.

[12] Y. Yu, S. Brandt, N. J. Nicolas, J. Aizenberg, *ACS applied materials & interfaces* **2019**, *12*, 1924–1929.

[13] M. Tsuchiya, Y. Kurashina, H. Onoe, *Scientific reports* **2019**, *9*, 1–10.

[14] J. M. Weissman, H. B. Sunkara, A. S. Tse, S. A. Asher, *Science* **1996**, *274*, 959–963.

[15] W. Wohlleben, F. W. Bartels, S. Altmann, R. J. Leyrer, *Langmuir* **2007**, *23*, 2961–2969.

[16] A. C. Arsenault, T. J. Clark, G. von Freymann, et al., *Nature Materials* **2006**, *5*, 179–184.

[17] E. Tian, J. Wang, Y. Zheng, et al., *Journal of Materials Chemistry* **2008**, *18*, 1116–1122.

[18] R. A. Barry, P. Wiltzius, *Langmuir* **2006**, *22*, 1369–1374.

[19] Y. Wang, D. Aurelio, W. Li, et al., *Advanced Materials* **2017**, *29*, 1702769.

[20] S. Jia, Z. Tang, Y. Guan, Y. Zhang, *ACS applied materials & interfaces* **2018**, *10*, 14254–14258.

[21] M. Chen, Y. Zhang, S. Jia, et al., *Angewandte Chemie International Edition* **2015**, *54*, 9257–9261.

[22] J. H. Holtz, S. A. Asher, *Nature* **1997**, *389*, 829–832.

[23] I. B. Burgess, L. Mishchenko, B. D. Hatton, et al., *Journal of the American Chemical Society* **2011**, *133*, 12430–12432.

[24] Y. Heo, H. Kang, J.-S. Lee, Y.-K. Oh, S.-H. Kim, *Small* **2016**, *12*, 3819–3826.

[25] J.-W. Kim, J.-S. Lee, S.-H. Kim, *Advanced Materials Interfaces* **2018**, *5*, 1701658.

[26] M. Pelton, *Nature Photonics* **2015**, *9*, 427–435.

[27] J. F. Olorunyomi, M. M. Sadiq, M. Batten, et al., *Advanced Optical Materials* **2020**, *8*, 2000961.

[28] F. Fleischhaker, R. Zentel, *Chemistry of Materials* **2005**, *17*, 1346–1351.

[29] B. Liu, P. A. Gurr, G. G. Qiao, *ACS sensors* **2020**, *5*, 2903–2908.

[30] A. Saha, Y. Tanaka, Y. Han, et al., *Chemical Communications* **2012**, *48*, 4579–4581.

[31] F. A. Nutz, P. Ruckdeschel, M. Retsch, *Journal of colloid and interface science* **2015**, *457*, 96–101.

[32] E. A. Sulyanova, A. Shabalin, A. V. Zozulya, et al., *Langmuir* **2015**, *31*, 5274–5283.

[33] G. Herzog, M. M. Abul Kashem, G. Benecke, et al., *Langmuir* **2012**, *28*, 8230–8237.

[34] F. A. Nutz, M. Retsch, *Physical Chemistry Chemical Physics* **2017**, *19*, 16124–16130.

[35] F. A. Nutz, A. Philipp, B. A. Kopera, M. Dulle, M. Retsch, *Advanced materials* **2018**, *30*, 1704910.

[36] I. Jurewicz, A. A. King, R. Shanker, et al., *Advanced functional materials* **2020**, *30*, 2002473.

[37] F. A. Nutz, M. Retsch, *Science advances* **2017**, *3*, eaao5238.

[38] S. Y. Lee, J.-S. Lee, S.-H. Kim, *Advanced Materials* **2019**, *31*, 1901398.

[39] T. Ding, Q. Zhao, S. K. Smoukov, J. J. Baumberg, *Advanced optical materials* **2014**, *2*, 1098–1104.

[40] S.-H. Kim, W. C. Jeong, H. Hwang, S.-M. Yang, *Angewandte Chemie* **2011**, *123*, 11853–11857.

[41] C. Zhu, J. Qiu, S. Pongkitwitoon, S. Thomopoulos, Y. Xia, *Advanced Materials* **2018**, *30*, 1706706.

[42] H. Ding, C. Liu, B. Ye, et al., *ACS applied materials & interfaces* **2016**, *8*, 6796–6801.

[43] H. Ding, C. Liu, H. Gu, et al., *ACS Photonics* **2014**, *1*, 121–126.

[44] A. E. Schedl, I. Howell, J. J. Watkins, H.-W. Schmidt, *Macromolecular Rapid Communications* **2020**, *41*, 2000069.

[45] A. E. Schedl, C. Neuber, A. Fery, H.-W. Schmidt, *Langmuir* **2018**, *34*, 14249–14253.

[46] J. Chi, C. Shao, Y. Zhang, et al., *Nanoscale* **2019**, *11*, 12898–12904.

[47] A. Spinnrock, D. Schupp, H. Cölfen, *Small* **2018**, *14*, 1803518.

[48] M. Chen, K. Hagedorn, H. Cölfen, S. Polarz, *Advanced Materials* **2017**, *29*, 1603356.

[49] J. Bahner, N. Klinkenberg, M. Frisch, L. Brauchle, S. Polarz, *Advanced Functional Materials* **2019**, *29*, 1904058.

[50] K. M. Ashraf, M. R. K. Khan, D. A. Higgins, M. M. Collinson, *Langmuir* **2018**, *34*, 663–672.

[51] K. M. Ashraf, C. Wang, S. S. Nair, et al., *Langmuir* **2017**, *33*, 4207–4215.

[52] D. Giri, C. N. Hanks, M. M. Collinson, D. A. Higgins, *The Journal of Physical Chemistry C* **2014**, *118*, 6423–6432.

[53] F. Ye, C. Cui, A. Kirkeminde, et al., *Chemistry of Materials* **2010**, *22*, 2970–2977.

[54] J. Huang, R. Fan, S. Connor, P. Yang, *Angewandte Chemie* **2007**, *119*, 2466–2469.

[55] J. Shim, R. Kostecki, T. Richardson, X. Song, K. A. Striebel, *Journal of power sources* **2002**, *112*, 222–230.

[56] F. Leng, C. M. Tan, M. Pecht, *Scientific reports* **2015**, *5*, 1–12.

[57] J. Hou, M. Yang, D. Wang, J. Zhang, *Advanced Energy Materials* **2020**, *10*, 1904152.

9.8 Supplemental Information

9.8.1 Experimental Section

Materials

Methyl methacrylate (MMA), n-butyl acrylate (nBA), 3-styrenesulfonic acid sodium salt hydrate (NaSS, ≥ 99 %), and potassium persulfate (KPS, ≥ 99 %) were obtained from Sigma-Aldrich. MMA and nBA are destabilized over Alox B prior to use. Sulfate-modified, fluorescent red polystyrene particles (100 nm diameter) were obtained from Sigma-Aldrich as an aqueous suspension, diluted to 0.025 wt %, and sonicated for 20 minutes

before further use. Water is taken from a Millipore Direct Q3UV unit for all experiments.

Particle synthesis Monodisperse polymer colloids are prepared via an emulsifier free emulsion polymerization. 13 mL monomer mixture (MMA/nBA, either 70:30 or 90:10) are added to 250 mL water and heated to 80 °C. After stirring at 850 rpm for 60 minutes under nitrogen flow, 10 mg NaSS and subsequently 100 mg KPS, both dissolved in 5 mL water, are added quickly. After 15 minutes, the stirring speed is reduced to 650 rpm. The reaction is left to proceed over-night and terminated by exposure to ambient oxygen.

Substrates Glass substrates are cleaned carefully prior to all coating procedures. Ultrasonication proceeds twice in 2 vol % aqueous Hellmanex III solution and once in ethanol (p.a.). Subsequently, substrates are immediately dried under a nitrogen stream. Directly before coating, the surface is hydrophilized via oxygen plasma treatment.

Dip-coating Homogeneous colloidal crystals are prepared via dip-coating. Several dispersions with varying ratios of particle types are prepared. Mixtures are adjusted to 1.0 total wt % and stirred over-night to ensure statistical distribution of the two particle types. Clean glass substrates are inserted, and dip-coating proceeds with a velocity of $0.25\,\mu m\,s^{-1}$ and a controlled atmosphere of 25 °C and 75 % relative humidity.

Infusion-withdrawal-coating Gradient colloidal crystals are prepared via an infusion-withdrawal-coating process. A clean glass substrate is dipped in a 10 mL PTFE-beaker filled with 8.7 mL of the starting dispersion and equipped with a stirrer bar. The stirring speed is set to 80 rpm. Two cannulas are inserted vertically on opposite sides of the beaker, and each is connected to a syringe pump. One injects the second dispersion at $0.6\,mL\,h^{-1}$, the other extracts the resulting mixture at $1.1\,mL\,h^{-1}$. Taking into account a determined evaporation rate of $0.1\,mL\,h^{-1}$, this ensures that the extraction rate is twice the infusion rate. The first part of the colloidal crystal is especially subject to pinning and defect formation. Therefore, before the infusion is started, extraction is set to $0.5\,mL\,h^{-1}$ for one hour. The corresponding top part of the sample is not regarded in the evaluation. The concentration of both dispersions is 1.3 wt %, and the ambient conditions lie between 19–21 °C and 25–35 % relative humidity. For the fluorescence measurements, one PMMA/nBA type is used, and 1.0 wt % (with respect to PMMA/nBA) red-fluorescent polystyrene particles are added to the infusion dispersion.

Methods

Differential scanning calorimetry Measurements are conducted using a TA Instruments Discovery DSC 2500. The second of two heating cycles is used for the evaluation. Samples are measured between −20–200 °C at 10 K min^{-1} and in a nitrogen atmosphere.

Imaging microscopy 2D color images and 3D reconstructed images are obtained using a laser scanning microscope (Olympus, LEXT). High magnification images are taken using a 50× lens with N.A. 0.95. Overview images are obtained by stitching several domains with a 5× lens with N.A. 0.15.

UV-Vis/Fluorescence microscopy The setup is based on an Olympus IX71 inverted microscope. Throughout all measurements, a 4× lens with N.A. 0.10 is used. UV-Vis spectra are obtained in transmission geometry with a halogen light source. An OceanOptics USB4000 spectrometer is coupled via fiber optics. In-situ measurements are conducted by using an Instec HCS622HV heating stage with a silver heating block and transmission capability to the setup. The lid of the stage is lifted briefly while the sample is placed on the preheated silver block, and the measurement is immediately started. Spectra are obtained every 500 ms over a period of 100 minutes. Ex-situ measurements are performed by externally heating samples on the same heating stage for a defined amount of time. Subsequently, a motorized µm-stage is used to automatically measure spectra at defined positions along the samples. Fluorescence spectroscopy is performed with the same setup but with a mercury vapor lamp in reflection geometry. A Chroma 49005 Cy3 filter cube is used, allowing excitation between 530–560 nm and emission detection between 590–650 nm. The integration time is set to 2 seconds, and 10 scans are measured for averaging. Gradients are measured at defined positions using a µm-stage. Thereby, fluorescence and transmission UV-Vis spectra can be measured at the same position.

Scanning electron microscopy Images were taken with a Zeiss Ultra plus (Carl Zeiss AG, Germany) at an operating voltage of 3 kV and with in-lens detection after sputtering of 2–4 nm platinum.

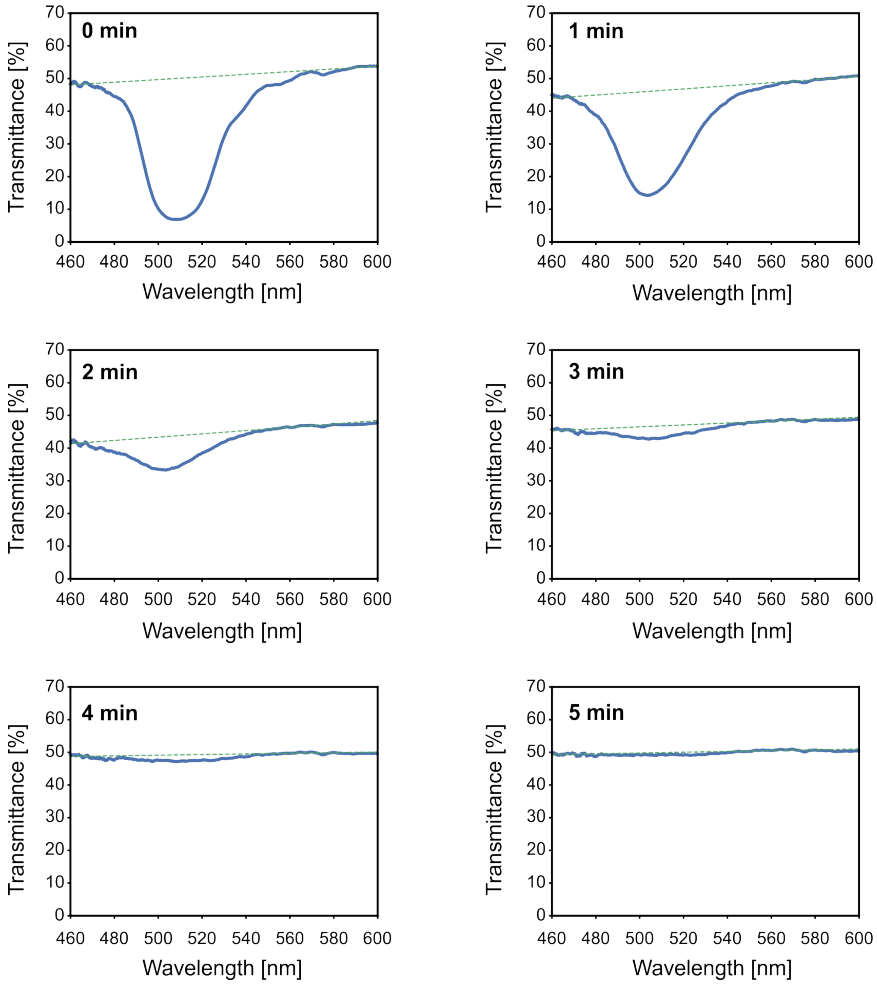

Figure 9.S1.: Transmission UV-Vis spectra during the film-formation of a 100 % low-T_g colloidal crystal at 60 °C. Dotted green lines show the baseline used for the evaluation. Division of the spectrum by the baseline and subsequent normalization to the stopband intensity at 0 minutes leads to the decay curve in Figure 9.1c.

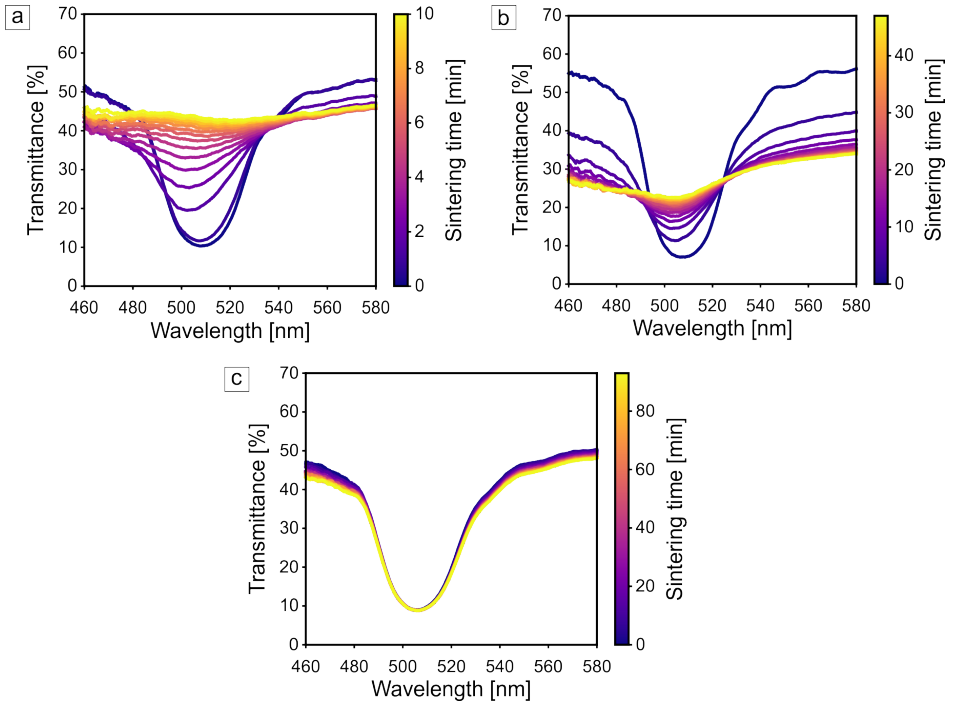

Figure 9.S2.: Exemplary in-situ UV-Vis measurements of samples with a) 80, b) 60, and c) 10 % low-T_g particles at 60 °C. After 5 minutes, the spectra in a) show slight minima and maxima that arise from thin-film interference. This cannot accurately be distinguished from the stopband and is therefore not corrected. As an effect, the normalized intensity decays to a value slightly above zero.

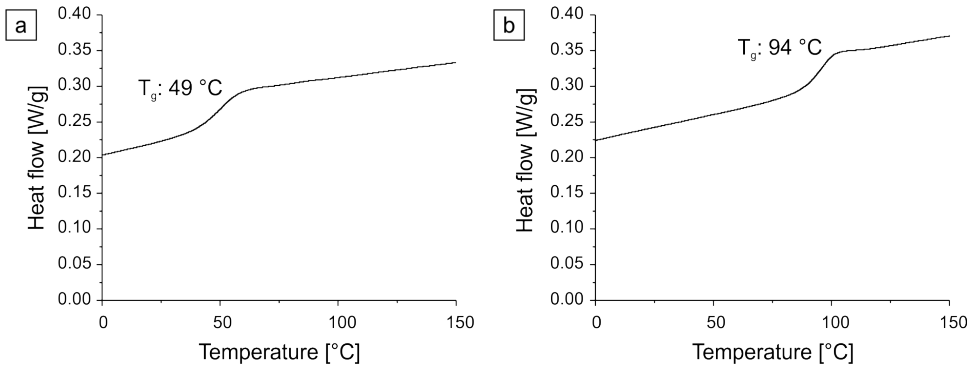

Figure 9.S3.: The second heating curve of DSC measurements of PMMA/nBA particles with a monomer ratio of a) 70:30 and b) 90:10.

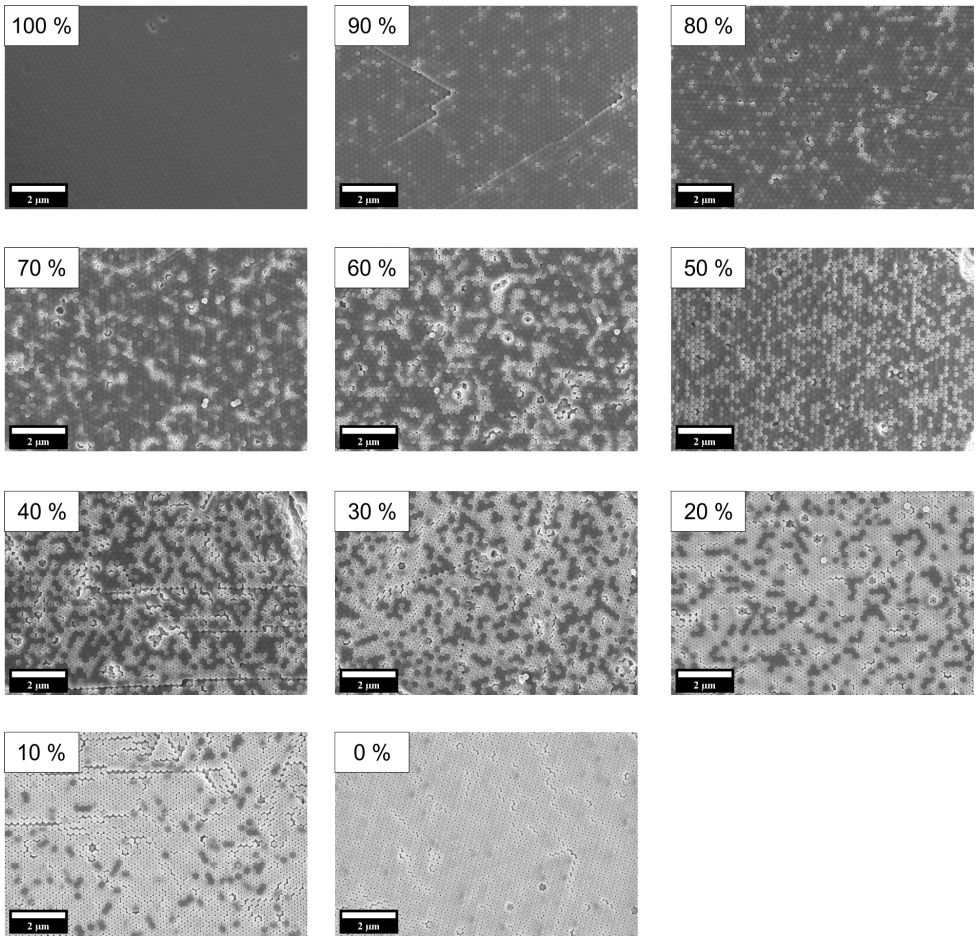

Figure 9.S4.: Scanning electron microscopy images of colloidal crystals after film formation for 100 minutes at 60 °C. Different compositions are labeled with the amount of low-T_g particles in the mixture.

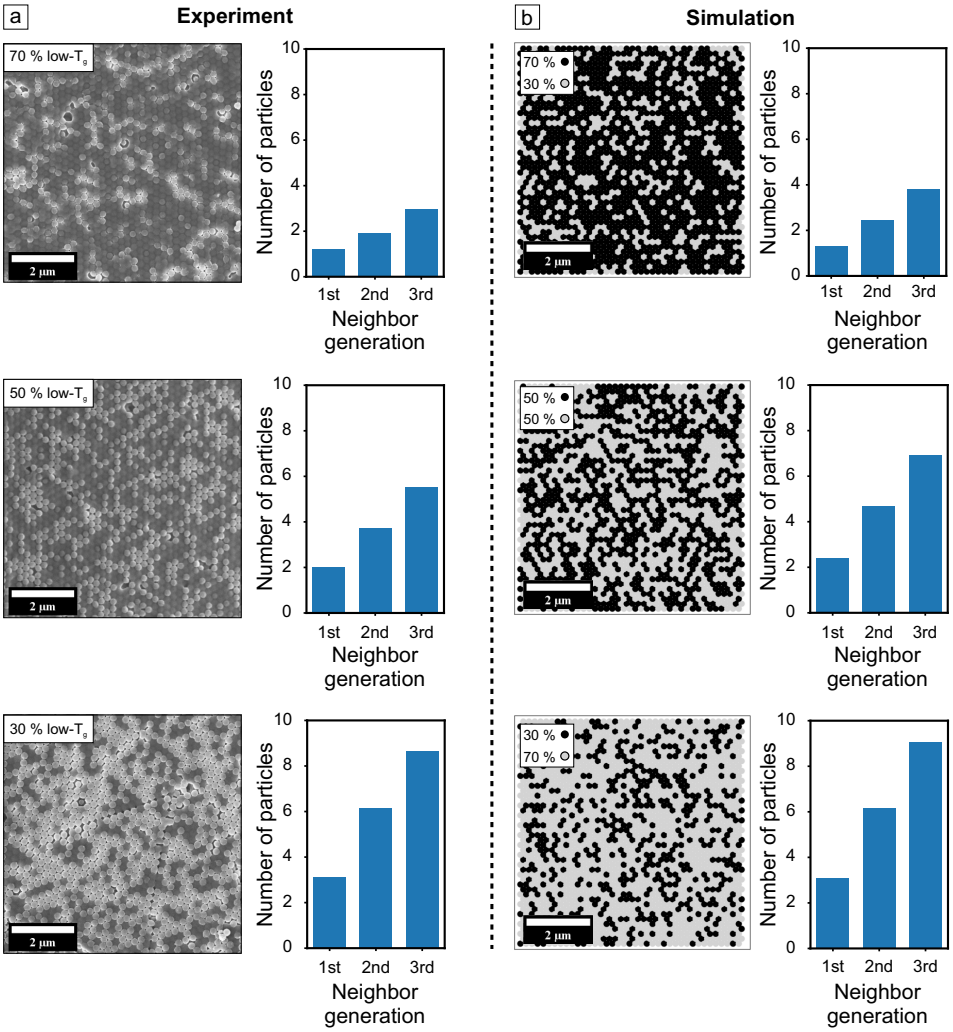

Figure 9.S5.: a) Scanning electron microscopy images of colloidal crystals with a different amount of low-T_g particles after film formation. b) Simulated distributions of two different particle types randomly mixed in a 2D-hexagonal structure. The images are calculated by randomly assigning each particle with a black or grey color. The probability of each color is chosen according to the particle ratio in the SEM counterpart. For the quantitative evaluation, the positions of non-sintered particles in the SEM images and grey particles in the simulations are examined. The mean number of neighbors is evaluated in both cases. First generation neighbors are integrated between 0–0.3 µm distance between particle centers, second generation between 0.3–0.5 µm and third generation between 0.5–0.7 µm. The distributions of experiments and simulations correlate very well. Relative intensities of the three generations as well as the absolute values are comparable. This concludes that the particles are indeed randomly distributed in the colloidal crystals. The lack of phase separation and prevention of heterogeneous film formation kinetics is a prerequisite for the characterization shown in this work.

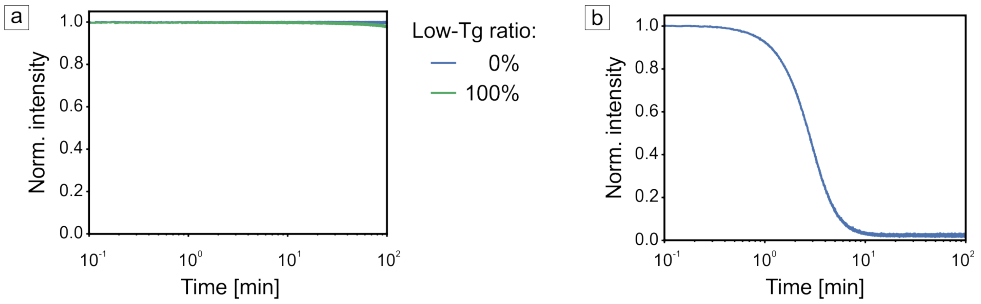

Figure 9.S6.: a) Stopband decay curves of colloidal crystals consisting purely of high- and low-T_g particles, respectively, at 45 °C. b) Stopband decay curve of 100 % high-T_g particles at 100 °C. These measurements show the temperature limits accessible with the present combination of copolymer colloids.

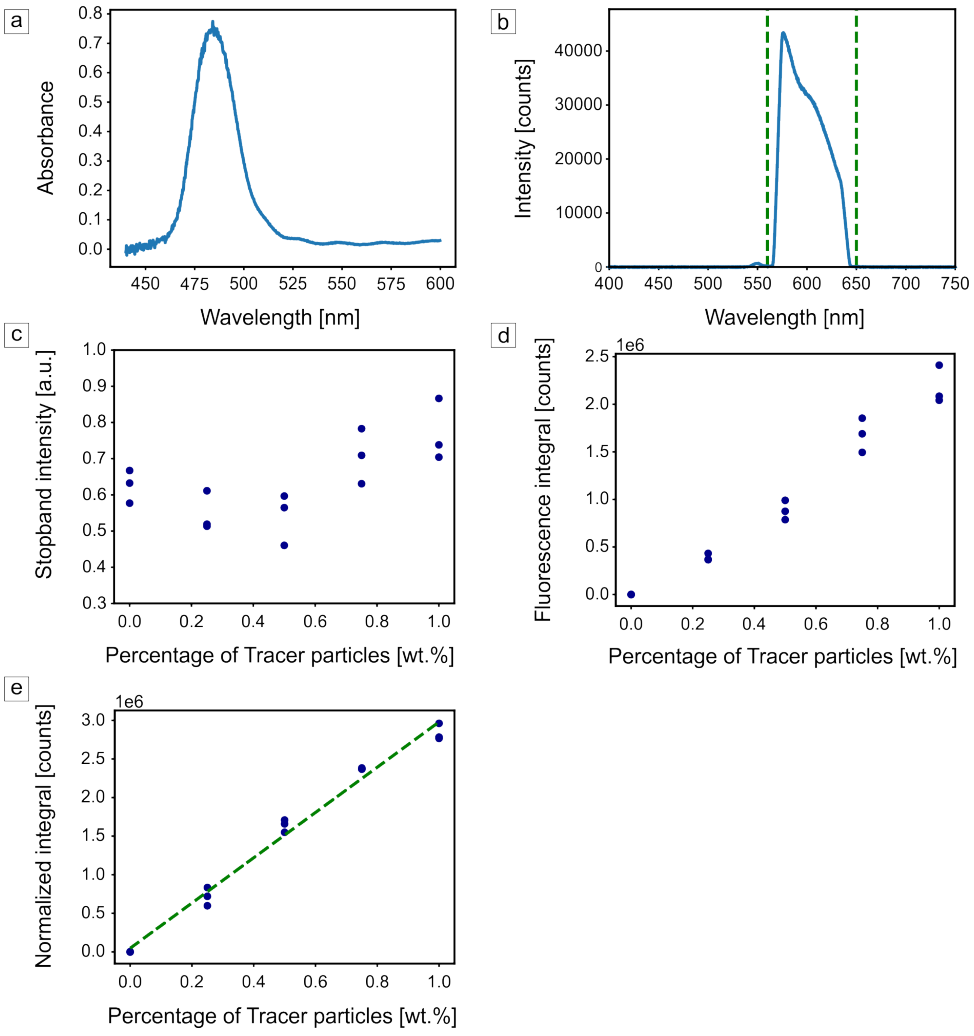

Figure 9.S7.: Exemplary a) baseline-corrected transmission UV-Vis and b) fluorescence emission spectra of a PMMA/nBA colloidal crystal prepared via dip-coating with 1.0 wt % red-fluorescent polystyrene particles. Green lines in b) show the integration boundaries required for further evaluation. c) Determined stopband intensity and d) fluorescence integral of all measurements. e) Normalized fluorescence integral obtained for the various percentages of tracer particles. The green dotted line represents the linear fit used for the correlation of position and composition of the gradient in Figure 9.3f.

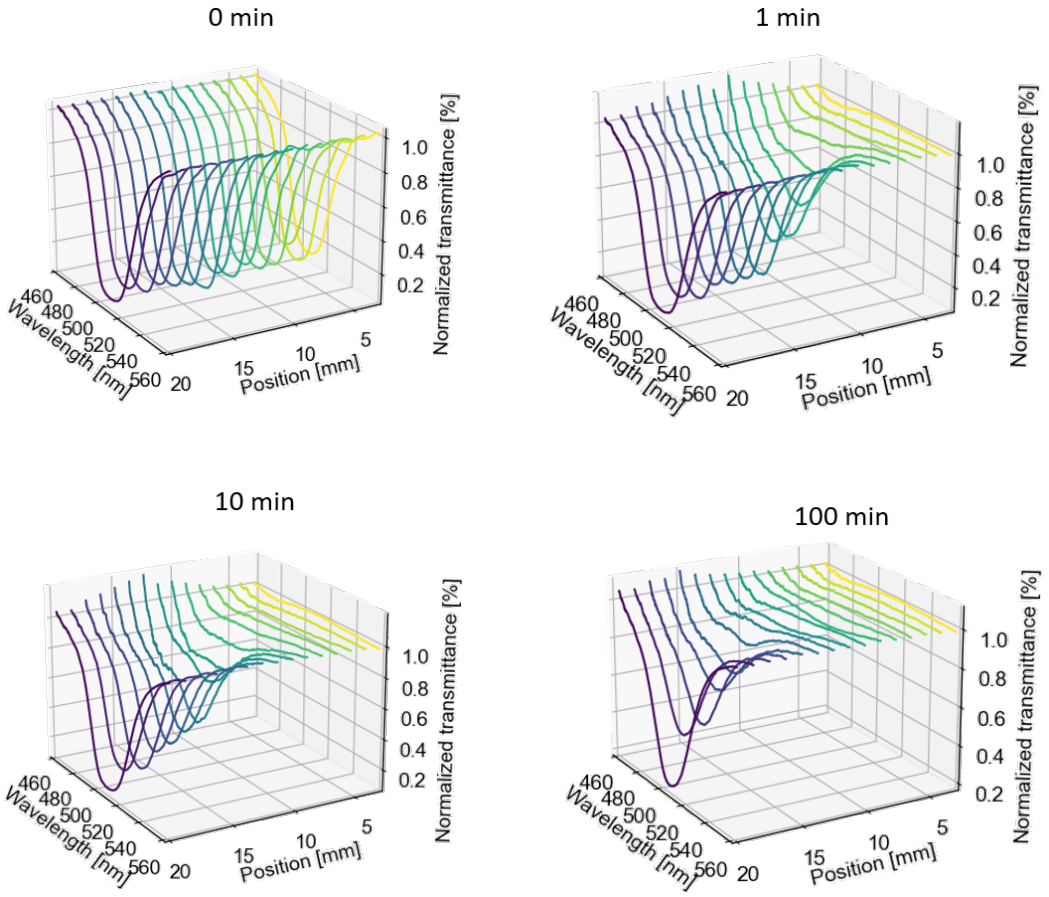

Figure 9.S8.: Baseline corrected transmission UV-Vis spectra measured ex-situ along a gradient colloidal crystal. These show the film formation process at 90 °C and how the degradation proceeds along the gradient.

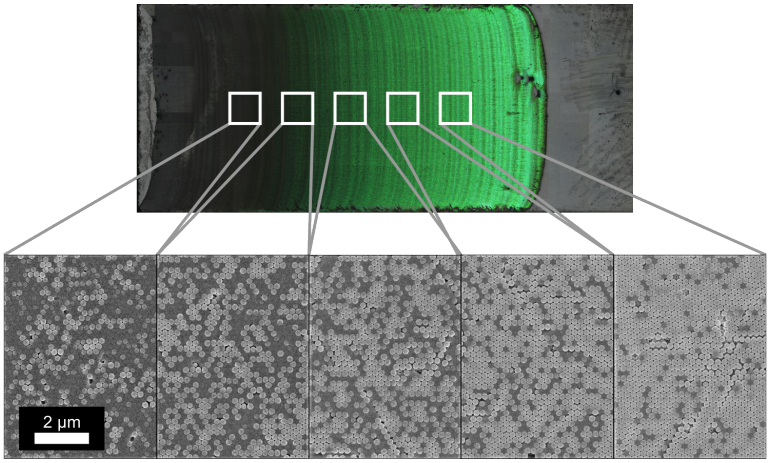

Figure 9.S9.: Measurements of the colloidal crystal gradient after different sintering times at 70 °C. a) Greyscale profile analysis via green channel separation of photographs shown in Figure 9.4a. b) Ex-situ UV-Vis results of a gradient sintered at 70 °C (large symbols) and 90 °C (small symbols) at equivalent sintering-times. The near overlap of the time-temperature pairs 100 min / 70 °C and 1 min / 90 °C shows the mutual influence of both time and temperature on the local film formation.

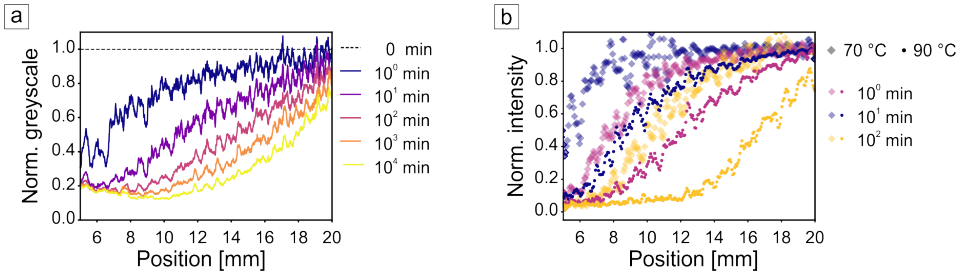

Figure 9.S10.: Scanning electron microscope images of a colloidal crystal gradient sintered at 70 °C for 100 minutes. A gradual decrease in the percentage of low-T_g particles is observed from left to right. The random particle distribution corresponds well to the individually prepared mixtures shown in Figure 9.S4.

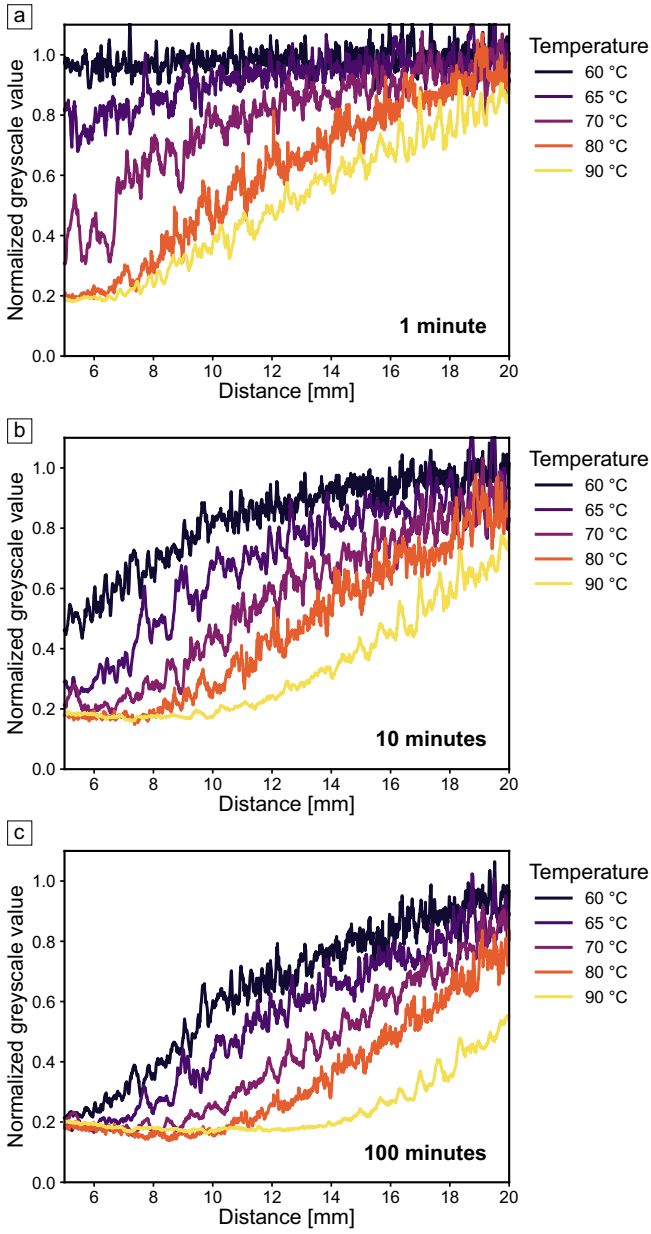

Figure 9.S11.: Temperature accuracy evaluation. Five gradient colloidal crystals are subjected to temperatures between 60–90 °C and the respective profiles are determined via green-channel image analysis. Three sintering times of a) 1 minute, b) 10 minutes and c) 100 minutes are presented. Temperature difference of 5 °C and higher can be distinguished.

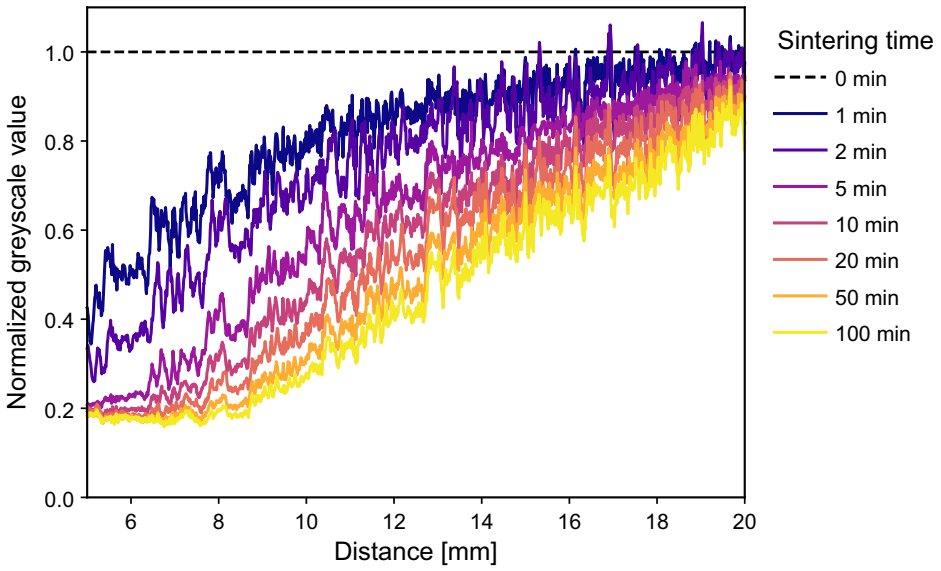

Figure 9.S12.: Time accuracy evaluation. A gradient colloidal crystal is subjected to a temperature of 70 °C and ex-situ profiles are obtained at various sintering times. The respective time decades (1 min, 10 min, 100 min) are well separated, inferring a temporal accuracy of a fraction of the sintering time of interest.

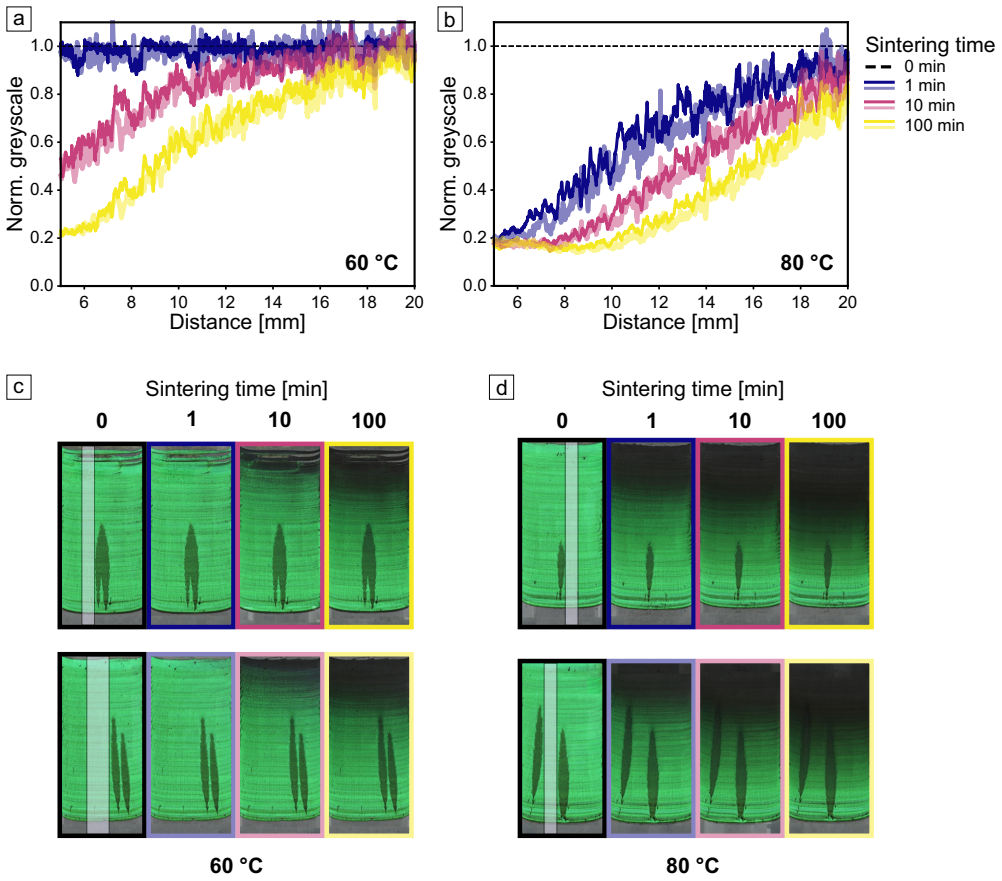

Figure 9.S13.: Reproducibility evaluation. Gradient colloidal crystals are subjected to sintering temperatures of a) 60 °C and b) 80 °C and profiles are determined via green-channel image analysis. Two samples are measured at each temperature and the resulting profiles are presented together (shown as an overlay of dark and light curve for each sintering time). The corresponding samples at the given sintering times are shown in c) and d), respectively. The high agreement between the two samples at both temperatures showcases the reproducibility of the time-temperature integrator. The green-channel profile analysis is conducted in regions of the samples (white shaded area) unaffected by the dark-green defects.

10 Machine Learning Enabled Image Analysis of Time-Temperature Integrating Colloidal Arrays

Marius Schöttle,[1, 4] Thomas Tran,[1, 4] Harald Oberhofer,[2, 3] and Markus Retsch[1, 3, *]

1 Department of Chemistry, Physical Chemistry I, University of Bayreuth, Universitätsstraße 30, 95447 Bayreuth, Germany
2 Department of Physics, Theoretical Physics VII, University of Bayreuth, Universitätsstraße 30, 95447 Bayreuth, Germany
3 Bavarian Center for Battery Technology (BayBatt), University of Bayreuth, Universitätsstraße 30, 95447 Bayreuth, Germany
* Corresponding author

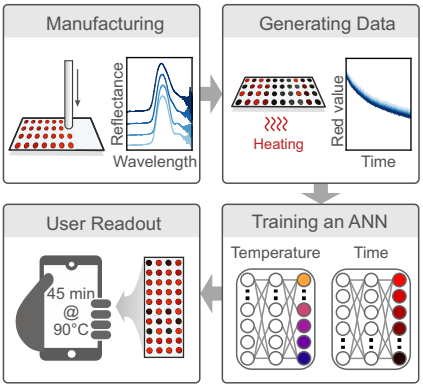

Published in *Advanced Science*, **2023**, *10*(8), 2205512.

10.1 Abstract

Smart, responsive materials are required in various advanced applications ranging from anti-counterfeiting to autonomous sensing. Colloidal crystals are a versatile material class for optically based sensing applications owing to their photonic stopband. A careful combination of materials synthesis and colloidal mesostructure rendered such systems helpful in responding to stimuli such as gases, humidity, or temperature. Here, an approach is demonstrated to simultaneously and independently measure the time and temperature solely based on the inherent material properties of complex colloidal crystal mixtures. An array of colloidal crystals, each featuring unique film formation kinetics, is fabricated. Combined with machine learning-enabled image analysis, the colloidal crystal arrays can autonomously record isothermal heating events — readout proceeds by acquiring photographs of the applied sensor using a standard smartphone camera. The concept shows how the progressing use of machine learning in materials science has the potential to allow non-classical forms of data acquisition and evaluation. This can provide novel insights into multiparameter systems and simplify applications of novel materials.

10.2 Introduction

Autonomous sensing has become increasingly important for various aspects of everyday life. For example, lifetime monitoring of batteries, food, and medicine requires tamper-proof sensors independent of an external power supply.[1–3] Color-coded systems are advantageous since they allow user-friendly readout.[4] This prerequisite is often realized using the responsive photonic properties of nanostructured (often polymeric) materials.[5,6] These can react to external stimuli by changing the spacing, effective refractive index, or via loss of order.[7–9] Beside the sensing of, e.g., pH-value[10] and (bio-)analytes,[11] temperature monitoring plays a key role in tracking degradation and spoilage.[12,13] Depending on the application, both reversible sensors and irreversible indicators have been shown.[14,15] More intricate systems can provide further information regarding the thermal history. Time-temperature integrators (TTIs) additionally provide temporal readout, which is highly relevant for establishing the safety of products.[16–18] Often, this is achieved by controlling the kinetics of the deformation process in structured polymeric materials.[19] A system shown by Lee et al. even allows the independent evaluation of time and temperature.[20] This was possible by semi-analytical characterization of the creep-deformation process in polymeric inverse opals using local UV-vis spectroscopy. Recently, we showed a related material class: mixed colloidal crystals.[21] These make use

of adjustable dry-sintering kinetics[22,23] and show great potential regarding evaluation using simple image analysis.

Sensing via RGB channels of images obtained with digital cameras greatly enhances the applicability compared to a spectral analysis. Examination using commercial, hand-held devices rather than expensive (micro-)spectrometers makes these appliances much more user-friendly and more easily distributable. Research on such methods has been shown for, e.g., pH-sensing[24] and water-content determination.[25] Other materials for smartphone-based temperature sensing allow readout via luminescence thermography.[26–29] Another path towards combining materials science with digital advancements is beginning to evolve in the form of machine learning.[30] The application of these tools stretches from the prediction of optical properties[31] to optimizing synthetic parameters to create the desired materials.[32] For sensors, machine learning allows automated readout of complex, multiparameter systems that often cannot be described analytically. Examples comprise biomolecular sensing,[33] ethanol content,[34] and temperature.[35,36]

Here, we introduce a TTI based on multicomponent colloidal crystals, using smartphone-based image acquisition and machine learning analysis for the data evaluation. Four monodisperse polymer particle types are synthesized with varying glass transition temperatures to span a quaternary phase diagram. We use a fast, automated, and reproducible drop-casting method to fabricate colloidal crystal arrays of mixed compositions. The composition correlates to the dry-sintering kinetics and concomitantly to the loss of structural color. However, the quaternary particle system is too complex to allow an analytical description. Instead, we demonstrate that an artificial neural network can accurately measure our colloidal crystal arrays' time and temperature history. A system that initially is too intricate for conventional characterization is thereby made applicable for multiparameter sensing. Our analysis demonstrates a general approach to improve the sensing capabilities of well-established photonic structures drastically. Due to the scalable fabrication process, the modular adjustment to other sensing tasks by a specific particle selection, and the user-friendly, low-tech characterization method, this TTI concept opens the pathway toward cheap multiparameter sensors.

10.3 Results and Discussion

We aim to fabricate a sensor enabling a simple readout of two independent parameters: time and temperature. One main difficulty, thereby, is designing a system that is complex enough to over-determine the parameter space yet remains feasible to analyze. The concept presented here is based on an array of polymer colloidal crystals (CCs). The first

step, therefore, is the realization of a suitable self-assembly process. Prerequisites for sample preparation are site selectivity, reproducibility, automation, and a fast preparation rate. Consequently, we apply a combination of array-printing and drop-casting that meets these criteria and additionally is scalable, resource-efficient, and non-toxic.

A spring-loaded pin with a hydrophilic, round tip is dipped into a particle suspension that adheres via wetting. When brought into contact with a glass substrate, a defined dispersion volume is deposited and subsequently forms a CC via evaporative self-assembly (Figure 10.1a). The interplay of capillary and Marangoni flow in these sessile droplets at room temperature results in a pronounced coffee-stain effect (Figure 10.1b).[37] Structural colors appear faint and far from homogeneous, and the droplet itself shows an irregular shape. When heating the substrate to 70 °C, the interactions favor a homogeneous layer of particles, facilitated by the formation of a 'milk-skin' like particle layer during the accelerated evaporation.[38] Additionally, evaporation occurs at the edges immediately after contact, forcing the assembly to occur in a well-defined circular area. This greatly enhances the reproducibility and, thereby, the readability of the sensor during the analysis described later. Scanning electron microscopy (SEM) images of the surface show large domain sizes of densely packed, monodisperse particles, corroborating the vivid structural colors observed via light microscopy (Figure 10.1c). Another significant feature of this process is efficiency, as almost none of the suspension is wasted. Therefore, a given laboratory-scale batch of particles (typically a few 100 mL with 5 wt % particle concentration) can theoretically be used to prepare several thousand samples.

Having established a robust array fabrication method, we now present the cornerstones of the particulate system. The polymer latex particles used in this work consist of random copolymers of methyl methacrylate (MMA) and n-butyl acrylate (nBA). Four different particle types are prepared with varying comonomer volume ratios between 85:15 and 100:0 while maintaining a consistent particle diameter of 320 ± 5 nm. Self-assembly of all four particle types and subsequent UV-vis spectroscopy (Figure 10.1d) show an optical stop band at 635 ± 3 nm in each case. Both the assembly behavior and the periodicity of the resulting nanostructure are thereby proven to be uniform. The differences between the four particle types are elucidated via differential scanning calorimetry (DSC). Heating curves show the glass transition temperature (T_g) shifting towards higher temperatures when increasing the MMA content (Figure 10.1e). This dependency of T_g and comonomer composition is linear (Figure 10.1f).

The key aspects of these building blocks are the same size and surface chemistry of the particles with different thermal properties. This allows the fabrication of multicomponent yet crystalline nanostructures from mixed particle suspensions. Depending on the number of components in an ensemble, the film formation process can be tailored to a specific temperature range. The thermal parameter space, we apply for sensing, can be

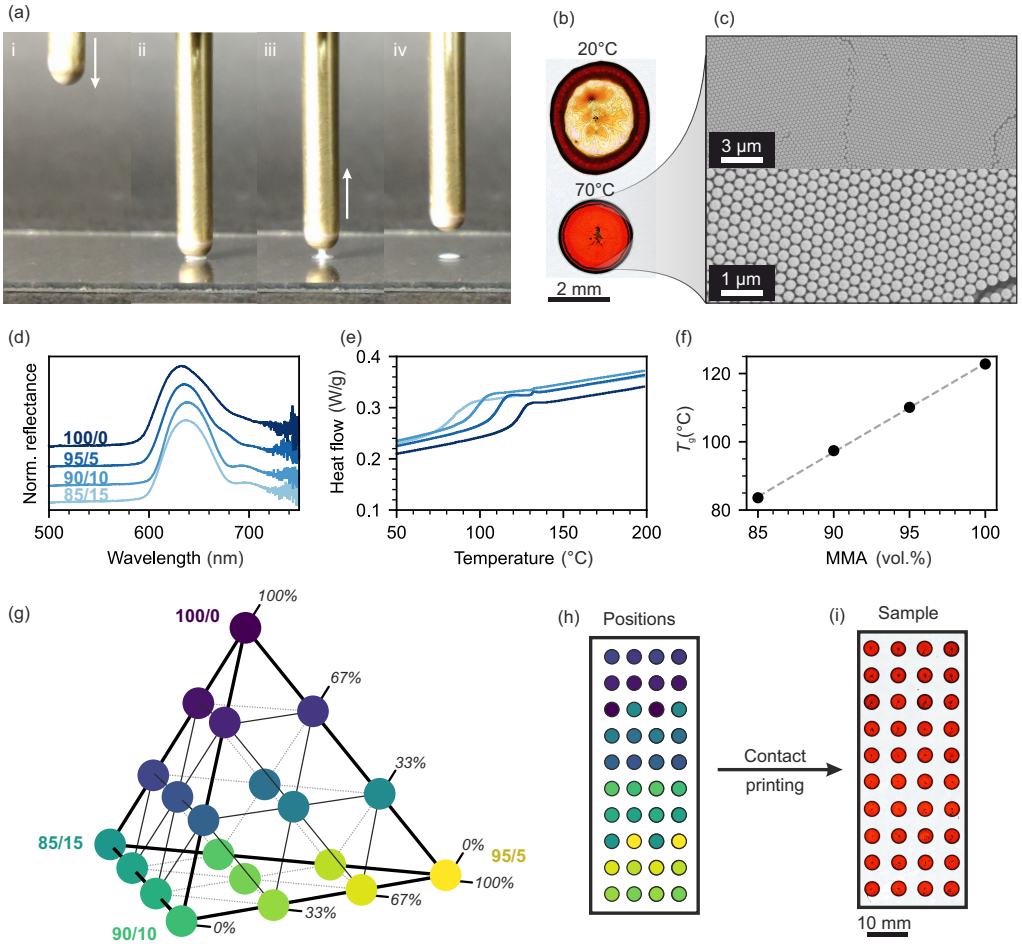

Figure 10.1.: Fabrication process of multi-spot colloidal crystal sensors. a) Snapshots of the array-printing procedure, showing the (i) advancing, loaded tip, (ii, iii) the tip in contact with the substrate, and (iv) the receding pin. b) Microscopy images of spots prepared at different substrate temperatures, elucidating the importance of accelerated evaporation during self-assembly. c) SEM images of the colloidal crystal shown in panel (b). d) UV-vis reflectance spectra of four spots prepared from copolymer particles of identical size but different comonomer compositions. e) DSC heating curves of the four different copolymers. f) Glass transition temperatures obtained from panel (e), showing a linear dependence regarding the comonomer composition. g) Quaternary phase diagram of all particle mixtures obtained from mixing the four different particle types. h) Positions of these mixtures on the substrates. i) Microscopy image of a substrate prepared via the array-printing of the mixed particle suspensions shown in panels (g) and (h).

elucidated in a quaternary phase diagram (Figure 10.1g) showing all utilized particle mixtures. The automated array-printing setup facilitates the realization of this large parameter space. We, therefore, drop-cast a total of 20 different particle mixtures onto defined positions on a glass substrate (Figure 10.1h). Two spots are prepared with each composition to introduce some redundancy and improve later readout. The setup allows reproducible fabrication of samples with circular spots of CCs, all with the same vivid, red structural coloration due to a consistent periodicity, geometry, and effective refractive index (Figure 10.1i). Differences can later be observed at elevated temperatures, where the thermal response of each composition is tracked.

The question now is how to characterize such a sample appropriately. Classic laboratory characterization methods can be divided into two groups: 1) Methods that exhaustively cover the entire sample but can only be measured ex situ. 2) In-situ methods that are, however, limited to one spot at a time. An example of ex situ characterization is scanning light and electron microscopy (Figure 10.2a–d). A pristine sample (RT), as well as three samples subjected to isothermal sintering at different temperatures between 83 and 112 °C for 120 min, are shown. Depending on the thermal history, specific CCs remain (nearly) pristine, while others show various degrees of discoloration. We examine three representative positions post-sintering via SEM to corroborate the expected structural change (Figure 10.2b–d). The respective CCs consist of particles with 90 %, 95 %, and 100 % MMA and show compositions of 0:1:2 (spot i), 1:1:1 (spot ii), and 2:1:0 (spot iii). When the CC consists of only high-T_g particles (spot i), the structure remains intact after heating (blue-shaded particles). When only the minority phase is affected by the temperature increase, and these particles deform (spot ii), an interconnected nanostructure of periodically arranged particles remains. As the temperature persists, these voids are slowly filled by the creeping polymer. The overall refractive index contrast between spheres and voids is concomitantly reduced, and the saturation diminishes. If the majority of particles are heated above their T_g (spot iii), only small islands remain and (nearly) all symmetry and periodicity are lost. No discernable color remains.

Complementary to this ex situ evaluation, in situ UV-vis spectroscopy provides temporal information regarding the sintering process. Three spots are measured, one after the other (Figure 10.2e–g). The spectrum of spot i shows little to no change during 60 min at an elevated temperature. Spot ii, however, shows a slow and consistent degradation of the stop-band to approximately half of its previous reflectance. Spot iii shows a fast response, with almost complete loss of any indication of a photonic stop-band during the first 10–15 min. Quantifying the time-dependent UV-vis spectra is possible, e.g., in the form of the normalized stop-band intensity (Figure 10.2h). However, it is unfeasible to perform this measurement at all 40 spots at once. Spectroscopic methods, therefore, fail to provide a holistic evaluation of the sensor's response to thermal events. Additionally,

while similar optical studies of inverse polymeric opals have been conducted by applying, e.g., the Kelvin-Voigt model and WLF theory,[20] our system is difficult to be studied (semi-)analytically.[21] Sintering of particulate systems, in general, is a multi-step process,[39,40], and the binary and ternary mixtures increase this intricacy. Besides the polymer and particle composition, the surface chemistry may influence the film formation kinetics. All this renders an analytical description of the film formation increasingly difficult.

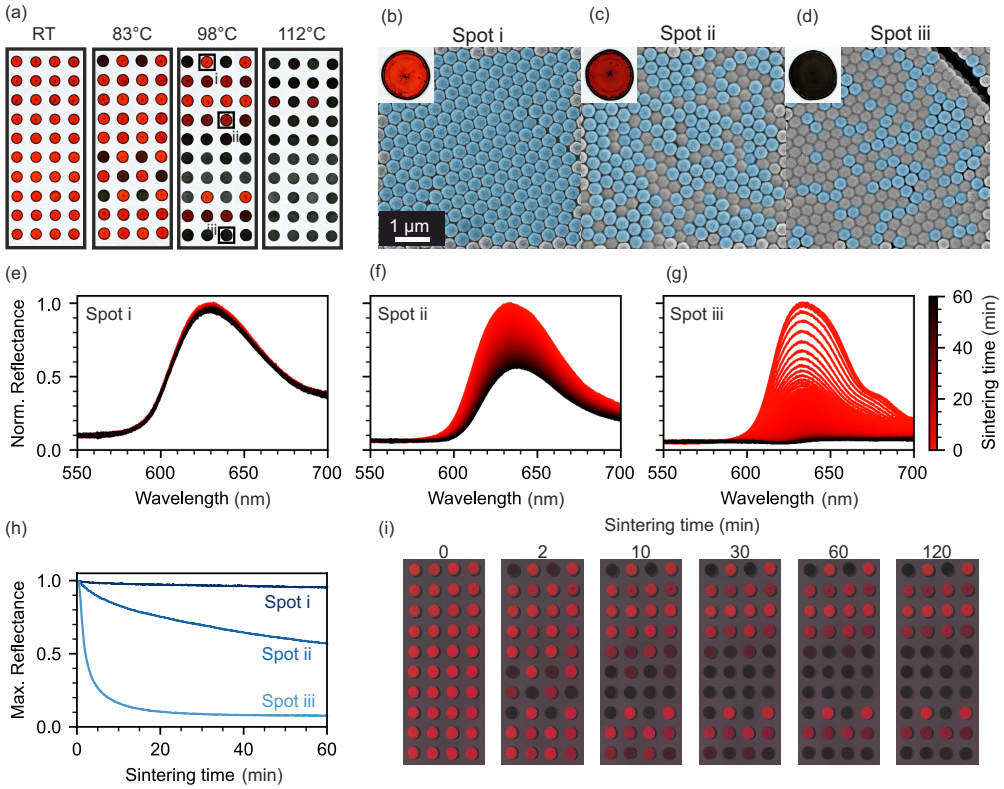

Figure 10.2.: Thermal response of the sensors. a) Light microscopy images of samples held at different temperatures for 120 min. The width of each image is 27 mm. b–d) SEM images of the spots indicated in (a). The blue overlay shows intact, non-sintered particles. e–g) In-situ UV-vis spectra of equivalent spots during the sintering process at 98 °C showing the gradual stop-band degradation. These, however, have to be measured consecutively. h) Time-dependent decrease of the normalized stop-band intensity. i) Photographs taken in situ of a sample during the sintering process at 98 °C with a smartphone camera.

Machine learning lends itself as a prime candidate for evaluating the behavior of our sensors. It can describe nonlinear behavior without requiring extensive physical modeling. Instead, a prerequisite for machine learning is a large amount of data. We acquire the necessary data by capturing the time-dependent optical response of the sensor using a smartphone camera. This unconventional yet convenient method has the additional benefit of being widely applicable and providing a user-friendly and non-expert evaluation. Capturing the response with a smartphone combines the time-resolution of the in situ

UV-vis spectroscopy with the ability to measure the entire sensor of scanning microscopy (Figure 10.2i).

An evaluation of the full images is computationally expensive and includes many pixels of the substrate background that contain no relevant information. Furthermore, slight differences between spot sizes will complicate the training process. We, therefore, determine the mean red value of each spot by dividing every image into 40 sub-images containing one spot each (Figure 10.3a). We use the mean brightness of the 5 %, 10 %, 15 %, 20 %, and 25 % of pixels with the highest red value for the evaluation (Figure 10.3b). For each substrate, 40 spots with five mean values each correspond to 200 inputs for a given image. Compared to the RGB images with a size of 420×1060 pixels, the number of inputs is reduced by a factor of ≈ 6700, significantly speeding up computations. The mean red value of each spot (Figure 10.3c) changes similarly to the stop-band intensity shown in Figure 10.2h. Spots i and ii both show little to no change during 120 min of isothermal heating. Also, the absolute red value of the two spots is nearly identical, corroborating the homogeneity and structural integrity of the CCs. The mean red value of spot iii decreases continuously throughout the measurement, while spot iv shows a fast degradation during the first 10 min. Combining these different response types to an elevated temperature is important for making a reasonable readout possible. For comparison, we also show analogue plots for samples measured 5 K above and below this temperature (Figure 10.S1). The influence of the change in temperature on the sintering kinetics is clearly visible in each decay curve. Therefore, we conclude that thermal and temporal information is hidden in the 200 inputs and continue to establish a model capable of deciphering the results.

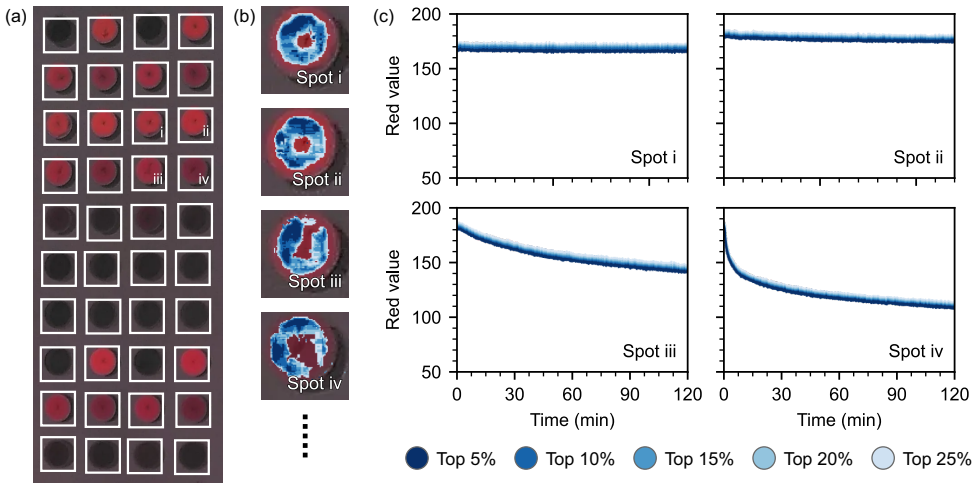

Figure 10.3.: Preprocessing of the image data for the neural network. The shown image was taken after heating the sample for 80 min at 98 °C. a) The digital image of the sensor is divided into 40 sub-images containing one spot each. b) For each sub-image, the pixels with the highest red value are used for further evaluation. c) The mean red values follow the same trend as the stop-band decay.

We use artificial neural networks (ANNs) with ten hidden layers to predict the time and temperature of a single image. The design idea for our ANN is to model the distinct sintering kinetics of each particle composition at each temperature. Therefore, the model consists of two parts (Figure 10.4). First, the model estimates the probability of an image being taken at a specific temperature by detecting the pattern of spots with no, little, and high red intensities. The resulting probability density and the mean red values are the inputs for the time prediction layer. Finally, the model reports the most probable temperature and predicts the time as a continuous variable. A detailed description of the network architecture and training procedure is in the Experimental Section.

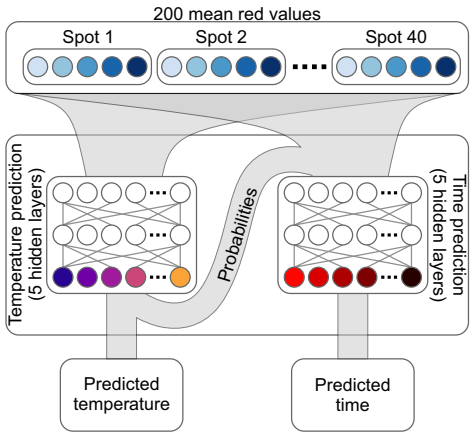

Figure 10.4.: Artificial neural network architecture. The model consists of two parts. The first half predicts the temperature by using only the mean red values. The second half predicts the heating time, with the inputs being the mean red values and the temperature probabilities.

We trained the ANN with nine different temperatures between 100 and 140 °C. Here, we report the hot plate set point as the temperature for better readability. The set point is slightly higher than the actual sensor temperature (Figure 10.S2). At each temperature, we measured eight samples for 2 h at intervals of 5 s, corresponding to $>$ 94000 training images. Supervised training optimizes the model parameters, and after 20 training epochs, the model assigns 96.7 % of training images to the correct temperature (Figure 10.S3a). The predicted time also correlates very well with the measured time. More than 80 % of training inputs deviate $<$ 10 min from the correct value (Figure 10.S3b). We notice that the wrong assignment of temperatures occurs primarily at short times and that the incorrectly predicted temperature is directly below the correct temperature (Figure 10.S3c).

Next, we investigate the generalization of our ANN by predicting the time and temperature for two validation samples per temperature. Our model has never seen these samples before and is unaware of the correct values. We can validate our system over the whole time-temperature regime because both the sensor creation and the sensor evaluation are automated. In total, the validation set consists of $>$ 23000 images. As

shown in Figure 10.5, the resulting predictions resemble the training results well. Temperature predictions are correct for the most part (96.4 %). If images are mislabeled, the temperature error is mainly only 5 K (3.3 %). Concerning the time, the majority of the predictions closely follow the correct value (Figure 10.5b). However, some predictions deviate from expectations. The large number of validation images allows us to investigate these deviations in more detail by grouping the time predictions by the correct temperature.

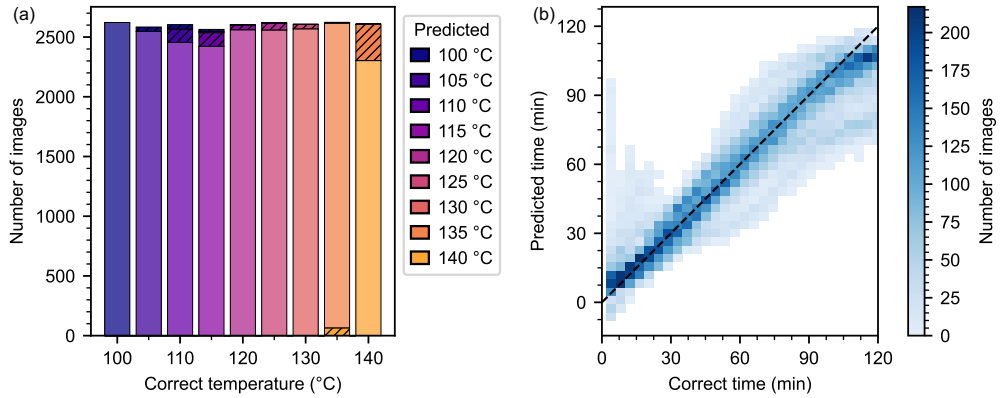

Figure 10.5.: Prediction results for two samples per temperature, corresponding to > 23000 validation images. a) Correlation of correct and predicted temperatures. Incorrect predictions (hatched areas) are minimal and mostly show a deviation of only 5 K from the correct value. Underestimations are shown at the top, and overestimations at the bottom. b) Correlation between correct and predicted time values.

Figure 10.6a shows how the prediction quality varies with the correct sensor temperature. Each point in the graphs corresponds to one validation image. For most temperatures, no difference between the two used validation samples is visible, demonstrating that both the creation and evaluation of our sensors are highly reproducible. While predictions at temperatures below 135 °C are very accurate, some images at the highest temperatures show incorrectly predicted time values. As the same phenomenon occurs in the training data (although less pronounced), this is not a generalization issue but a limitation of the applied system itself.

Without a large amount of validation data, it is impossible to identify the prediction capabilities in the distinct areas shown above. Previous publications about TTIs validated their system with a small number of validation samples,[15,18,20,21] thus, not covering the whole time-temperature regime. Our large amount of validation data allows us to state individual uncertainties for each pair of predicted temperature and time (Figure 10.7). The mean absolute difference between the predicted and the measured time is generally below 10 min for temperatures below 135 °C. For high temperatures, the uncertainty is larger. These individual errors can be used as an output for the end user. Examples of single images as recorded by a potential user are shown in Figure 10.6b.

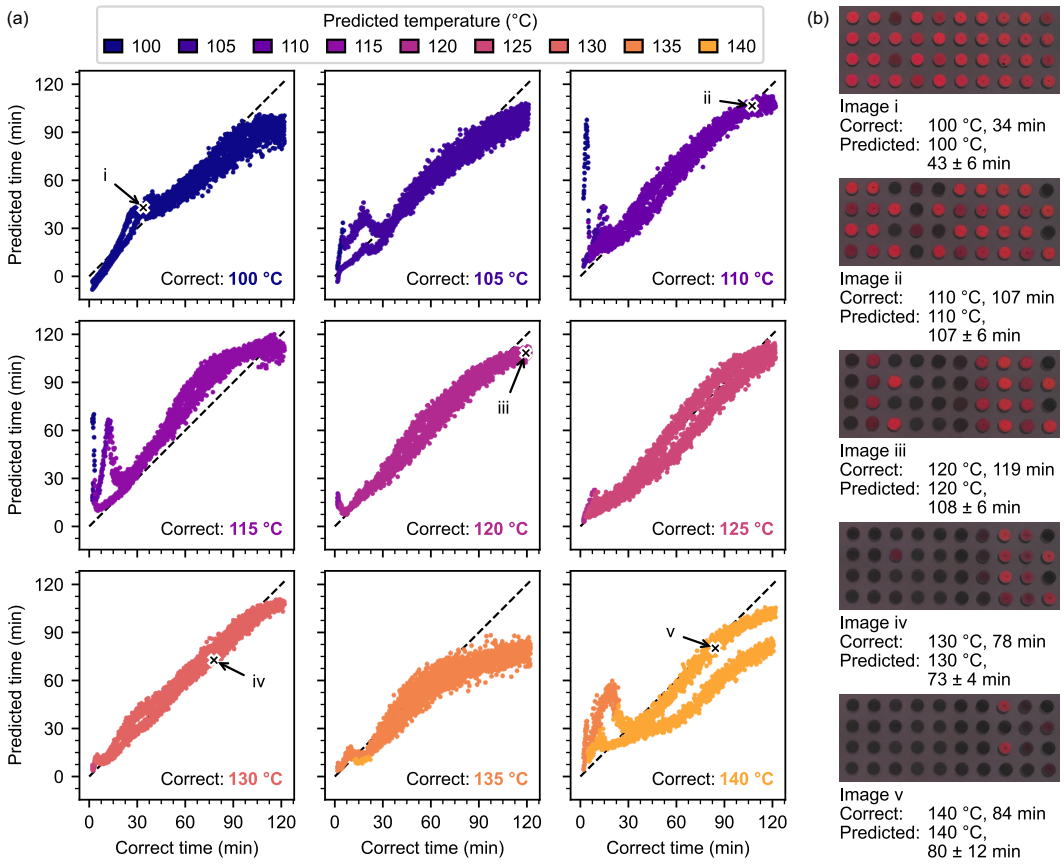

Figure 10.6.: Detailed prediction results for the validation images. a) Predictions for the first seven temperatures are very close to the true values. At higher temperatures, the time predictions begin to deviate. b) Input images of five validation points from (a) with their corresponding predictions.

Further examples are in Figure 10.S4–10.S6, showing how our integrators behave with multiple temperature steps. As expected, if the sensors cool down between two isothermal heating steps, the predicted time is the sum of the two heating durations (Figure 10.S4). If multiple heating events in the temperature range of the sensors occur, the prediction refers to the higher temperature and further heating at lower temperatures does not affect the readout (Figure 10.S5). For small temperature differences, a slight overestimation of the time is possible (Figure 10.S6). Consequently, this type of TTI sensor is most suitable and applicable for the recording of the highest temperature events, which are, in many cases, the most relevant ones to judge on safety or spoilage issues.

The evaluation of a single photograph takes < 1 s and is based solely on an image taken by a smartphone camera. No knowledge of photonic systems or the underlying physical processes is necessary to utilize our system. The software will immediately predict the time and temperature of the photographed sensor and state the corresponding uncertainty. Consequently, non-specialists can employ our system effortlessly. This concept can

conceivably be adjusted to adapt the prerequisites to various applications. The time and temperature ranges that can be determined are related only to the thermal properties of the respective polymer particles. Changing the glass transition temperature of these can easily be done by varying the monomer composition. Alternatively, high-temperature applications can be made possible by adding inorganic components such as silica colloids to the phase diagram. Since the process is irreversible, tamper-proof monitoring of goods such as food or batteries becomes a simple process. Further advancements can be readily implemented by miniaturizing the colloidal arrays down to the image resolution limit of commercial cameras. Thereby, an even larger number of CC spots and, consequently, particle mixtures could be examined at once. Increasing the number of CC spots will also provide flexibility to include particle mixtures with different stop-bands allowing for a multi-color analysis specific to certain temperature ranges.

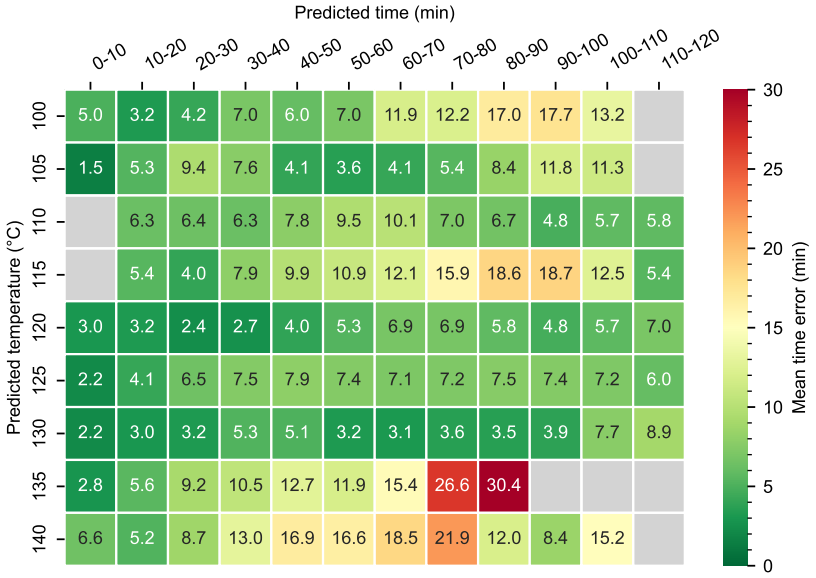

Figure 10.7.: Mean errors between predicted and correct time. The validation over the whole time-temperature regime allows estimating uncertainties precisely. Lower temperatures show a smaller deviation from the correct value. For high predicted temperatures, the uncertainty increases.

10.4 Conclusion

We established a concept that applies a combinatorial approach to add significant functionality to the well-known material class of polymer colloidal crystals. Mixed photonic systems described by a quaternary phase diagram were assembled using a scalable and efficient array-printing method. This allowed us to examine the thermal response of numerous samples, which formed a solid training set for our measurement evaluation.

The sensor state can be optically read out by digital photography using a standard smartphone. The evaluation was performed using an artificial neural network. Using only the photograph of a sample subjected to isothermal heating, the model correctly predicts time and temperature independently. Our concept can be readily transferred to specific sensing applications comprising photonic structures and integrating sensing capabilities. The case demonstrated here is particularly simple owing to the robust array fabrication procedure and the optical readout, which make this sensor useful for non-expert users. Overall, we showed how the combination of materials chemistry and advanced computational methods are starting to enable a multiparametric analysis from complex colloidal systems.

10.5 Experimental Section

Materials Methyl methacrylate (MMA), n-butyl acrylate (nBA), 3-styrenesulfonic acid sodium salt hydrate (NaSS, 99 %), and potassium persulfate (KPS, 99 %) were obtained from Sigma-Aldrich. Before further use, both MMA and nBA were destabilized over Alox B. Water of MilliQ quality was used throughout all experiments. Glass substrates were cleaned via sonication in an aqueous 2 vol % Helmanex III solution and in ethanol.

Particle Synthesis Monodisperse particles were prepared via a surfactant-free emulsion polymerization. 240 mL water were heated to 80 °C and degassed in a 250 mL three-necked flask for 75 min. While stirring at 600 rpm, 19 mL of the respective monomer mixture were added, together with 10 mg NaSS dissolved in 5 mL water. After 5 min, the polymerization was initiated by adding 200 mg KPS dissolved in 5 mL water. The reaction was left to proceed overnight and terminated by exposure to ambient oxygen. The different particle dispersions were each filtered over a 125 µm mesh and otherwise used directly for preparing the binary and ternary mixtures. The concentration of all dispersions was 5.7 ± 0.1 wt %.

Self-Assembly via Array-Printing The printing procedure was fully automated using an XYZ stage to ensure full reproducibility. A clean glass substrate was placed on a hot-plate set to 70 °C. A spring-loaded, rounded brass pin with a diameter of 5 mm was dipped into a dispersion and then brought in contact with the substrate for a duration of 1 s. The pin was then mechanically cleaned in a water bath and dried with a non-woven fabric. The process then repeated with the next dispersion.

Characterization Methods Microscopy images were obtained using a laser scanning confocal microscope (Olympus, OLS5000) with a white light source as well as a 405 nm laser with a 5×-magnification lens and stitching of 7×18 images.

Scanning electron microscopy images were obtained with a Zeiss Leo 1530 (Carl Zeiss AG, Germany) at an operating voltage of 1 kV and both in-lens as well as secondary electron detection after sputtering of 2 nm platinum. Images, where a false-colored overlay was applied, are shown in their original form in Figure 10.S7.

UV-vis spectra of drop-cast suspensions were measured on an Olympus IX71 inverted microscope with a 10× lens in reflection geometry and a halogen light source. An OceanOptics USB4000 spectrometer is coupled via fiber optics. In-situ measurements were conducted using an Instec HCS622HV heating stage with a silver heating block set to 110 °C. Samples were attached to the stage using double-sided carbon tape, and the sample was heated to 98 ± 3 °C. Spectra were obtained at intervals of 2 s.

Differential scanning calorimetry was conducted using a TA Instruments Discovery DSC 2500. The second of two heating cycles was used for the evaluation. Samples were measured between 20 and 200 °C at 10 K min^{-1} and in a nitrogen atmosphere.

The hydrodynamic diameter was measured using diluted dispersions with a Zetasizer (Malvern) with 175° backscattering geometry.

Image Acquisition and Feature Extraction Each sample was placed on a black-coated hot plate (PZ 28-2, Harry Gestigkeit GmbH). A full-spectrum lamp (Walimex pro LED Niova 600 Plus Daylight) with a light diffuser illuminated the sample at an angle of 10° and a distance of 30 cm. A smartphone (Fairphone 3+) took photographs (ISO 100, 1/10647 s exposure time) of the sample at an angle of 10° and a distance of 10 cm every 5 s, stored in the WebP format. The full 3000×4000 pixel images were cut into 40 squares of 75×75 pixels at pre-defined positions. The cropped images are available online.[41] For each square, the 5 %, 10 %, 15 %, 20 %, and 25 % pixels with the highest red value were used to determine five distinct mean values used as the input for the ANN. Each input vector of length 200 is standardized by z-score normalization using the mean and standard deviation of the training set.

ANN Architecture PyTorch[42] was used for the network creation and we made the code available online.[43] To choose a suitable model structure, different architectures were compared. Details are in the Supporting Information. The final machine learning approach encompasses two almost identical, sequential models for temperature and time. They consist of an initial batch normalization layer and five hidden, linear layers each. The hidden layers have node sizes of 8192, 2048, 2048, 2048, and 512, respectively.

Each hidden layer uses a leaky ReLU function[44] as its activation. After the final hidden layer, a dropout layer with a dropout probability of 50 % was introduced to improve generalization. For the temperature module, the output layer was a softmax function creating a probability density for the nine temperature categories. For the time module, the output layer was a final linear layer of size one.

Training Process The time series images of eight samples per temperature were labeled and used for training. The initial 2 min of each sample were discarded due to temperature equilibration (Figure 10.S2). Prior to training, the time labels were scaled by min-max normalization with a minimum time of 2 min and a maximum of 122 min. Stochastic gradient descent was employed. Different hyperparameters were tested (Table 10.2). The final model was trained with a batch size of 32, a learning rate of 5×10^{-4}, a Nesterov momentum of 0.9 and a weight decay of 1×10^{-3}. The loss function is the sum of the cross-entropy loss for the temperature prediction and the mean squared error for the time predictions. The training concluded after 20 epochs.

Statistical Analysis The errors indicated for the predicted times are mean deviations between the correct and predicted times of the validation data. To determine those, predictions were grouped into the temperature and time bins shown in Figure 10.7. For each bin, the mean absolute difference between the correct and predicted value is shown. The training set consists of 94 032 and the validation set of 23 433 images. Preprocessing of the photographs is explained in the subsection *Image Acquisition and Feature Extraction*. The data and software are available online.[41,43]

10.6 Acknowledgements

M.S. and T.T. contributed equally to this work. The authors thank the keylabs of the Bavarian Polymer Institute (BPI) for access to the scanning electron microscopy. H.O. acknowledges support by the DFG within the Heisenberg scheme (grant no. OB425/9-1). T.T. and M.S. appreciate the support by the Elite Network Bavaria (ENB). Funded by the Deutsche Forschungsgemeinschaft (DFG, German Research Foundation) – 491183248. Funded by the Open Access Publishing Fund of the University of Bayreuth. Open Access funding enabled and organized by Projekt DEAL.

10.7 References

[1] R. A. Barry, P. Wiltzius, *Langmuir* **2006**, *22*, 1369–74.

[2] L. H. J. Raijmakers, D. L. Danilov, R. A. Eichel, P. H. L. Notten, *Applied Energy* **2019**, *240*, 918–945.

[3] B. Liu, P. A. Gurr, G. G. Qiao, *ACS Sensors* **2020**, *5*, 2903–2908.

[4] Z. Li, Y. Yin, *Advanced Materials* **2019**, *31*, e1807061.

[5] J. H. Holtz, S. A. Asher, *Nature* **1997**, *389*, 829–32.

[6] M. Tsuchiya, Y. Kurashina, H. Onoe, *Scientific Reports* **2019**, *9*, 17059.

[7] J. Hou, M. Li, Y. Song, *Nano Today* **2018**, *22*, 132–144.

[8] I. B. Burgess, L. Mishchenko, B. D. Hatton, et al., *Journal of the American Chemical Society* **2011**, *133*, 12430–12432.

[9] S. Jia, Z. Tang, Y. Guan, Y. Zhang, *ACS Applied Materials & Interfaces* **2018**, *10*, 14254–14258.

[10] M. Chen, Y. Zhang, S. Jia, et al., *Angewandte Chemie International Edition* **2015**, *54*, 9257–61.

[11] Z. Ma, P. Chen, W. Cheng, et al., *Nano Letters* **2018**, *18*, 4570–4575.

[12] M. Weston, S. Geng, R. Chandrawati, *Advanced Materials Technologies* **2021**, *6*, 2001242.

[13] J. Reichstein, S. Mussig, H. Bauer, S. Wintzheimer, K. Mandel, *Advanced Materials* **2022**, *34*, e2202683.

[14] K. Ueno, K. Matsubara, M. Watanabe, Y. Takeoka, *Advanced Materials* **2007**, *19*, 2807–2812.

[15] I. Jurewicz, A. A. K. King, R. Shanker, et al., *Advanced Functional Materials* **2020**, *30*, 2002473.

[16] C. Zhang, A. X. Yin, R. Jiang, et al., *ACS Nano* **2013**, *7*, 4561–8.

[17] S. Choi, Y. Eom, S. M. Kim, et al., *Advanced Materials* **2020**, *32*, e1907064.

[18] J.-W. Kim, J.-S. Lee, S.-H. Kim, *Advanced Materials Interfaces* **2018**, *5*, 1701658.

[19] Y. Foelen, A. Schenning, *Advanced Science* **2022**, *9*, e2200399.

[20] S. Y. Lee, J. S. Lee, S. H. Kim, *Advanced Materials* **2019**, *31*, e1901398.

[21] M. Schottle, T. Tran, T. Feller, M. Retsch, *Advanced Materials* **2021**, *33*, e2101948.

[22] F. A. Nutz, M. Retsch, *Science Advances* **2017**, *3*, eaao5238.

[23] F. A. Nutz, M. Retsch, *Physical Chemistry Chemical Physics* **2017**, *19*, 16124–16130.

[24] P. Das, S. Paul, S. S. Bhattacharya, P. Nath, *IEEE Sensors Journal* **2020**, *21*, 2839–2845.

[25] J. Othong, J. Boonmak, F. Kielar, S. Youngme, *ACS Applied Materials & Interfaces* **2020**, *12*, 41776–41784.

[26] J. F. C. B. Ramalho, S. F. H. Correia, L. Fu, et al., *Advanced Science* **2019**, *6*, 1900950.

[27] W. Piotrowski, K. Trejgis, K. Maciejewska, et al., *ACS Applied Materials & Interfaces* **2020**, *12*, 44039–44048.

[28] J. F. C. B. Ramalho, L. D. Carlos, P. S. André, R. A. S. Ferreira, *Advanced Photonics Research* **2021**, *2*, 2000211.

[29] J. F. C. B. Ramalho, L. M. S. Dias, L. Fu, et al., *Advanced Photonics Research* **2021**, *3*, 2100206.

[30] J. Kimmig, S. Zechel, U. S. Schubert, *Advanced Materials* **2021**, *33*, e2004940.

[31] S. Xu, X. Liu, P. Cai, et al., *Advanced Science* **2022**, *9*, 2101074.

[32] J. Kimmig, T. Schuett, A. Vollrath, S. Zechel, U. S. Schubert, *Advanced Science* **2021**, *8*, 2102429.

[33] S. Pandit, T. Banerjee, I. Srivastava, S. Nie, D. Pan, *ACS Sensors* **2019**, *4*, 2730–2737.

[34] A. Döring, A. L. Rogach, *ACS Applied Nano Materials* **2022**, *5*, 11208–11218.

[35] C. Lewis, J. W. Erikson, D. A. Sanchez, et al., *ACS Applied Nano Materials* **2020**, *3*, 4045–4053.

[36] Y. Zhang, L. Yu, Z. Hu, et al., *Journal of Lightwave Technology* **2021**, *39*, 1537–1543.

[37] A. Gencer, C. Schutz, W. Thielemans, *Langmuir* **2017**, *33*, 228–234.

[38] J. Zhang, Z. Zhu, Z. Yu, et al., *Materials Horizons* **2019**, *6*, 90–96.

[39] G. Herzog, M. M. Abul Kashem, G. Benecke, et al., *Langmuir* **2012**, *28*, 8230–7.

[40] E. A. Sulyanova, A. Shabalin, A. V. Zozulya, et al., *Langmuir* **2015**, *31*, 5274–83.

[41] M. Schöttle, T. Tran, H. Oberhofer, M. Retsch, *Experimental Data for: Machine learning enabled image analysis of time-temperature sensing colloidal arrays*, Zenodo, **2022**.

[42] A. Paszke, S. Gross, F. Massa, et al. in *Advances in Neural Information Processing Systems 32*, (Eds.: H. Wallach, H. Larochelle, A. Beygelzimer, et al.), Curran Associates, Inc., **2019**, pp. 8024–8035.

[43] The source code for our software is available at `https://github.com/thomas-tran-de/tti-analysis`, including the preprocessed data, model, and training scripts.

[44] B. Xu, N. Wang, T. Chen, M. Li, Empirical Evaluation of Rectified Activations in Convolutional Network, **2015**.

10.8 Supplemental Information

10.8.1 ANN Architecture

We compared five different model and chose the best one to be our final architecture (Tab. 10.1).

Full images The input for this model are the RGB images of our sensors instead of the average red values. Multiple convolutional layers preceed the fully connected layers.

Single model Instead of splitting the model into parts dedicated to the temperature and time prediction, we use the outputs of the second to last layer to one independent layer for time and temperature, each.

Small model The number of nodes of this model is reduced to 1/16th of the final model.

Medium model The model architecture described in the main text.

Large model The number of nodes of this model is four times larger than that of the final model.

Table 10.1.: Comparison between different network architectures. The final model is highlighted.

Model	Traning loss	Validation loss
Full images	1.38	1.62
Single model	1.45	1.48
Small model	1.52	1.54
Medium model	1.41	1.42
Large model	1.43	1.49

Table 10.2.: Comparison between different training parameters. Shaded parameters are used to train our model.

Batch size	Learning rate	Momentum	Weight decay	Traning loss	Validation loss
32	5×10^{-4}	0.7	1×10^{-3}	1.56	1.54
32	5×10^{-4}	0.98	1×10^{-3}	1.44	1.49
32	5×10^{-4}	0.9	1×10^{-4}	1.45	1.42
32	5×10^{-4}	0.9	5×10^{-3}	1.53	1.50
16	5×10^{-4}	0.9	1×10^{-3}	1.46	1.44
64	5×10^{-4}	0.9	1×10^{-3}	1.50	1.49
32	1×10^{-4}	0.9	1×10^{-3}	1.61	1.54
32	5×10^{-4}	0.9	1×10^{-3}	1.41	1.42
32	1×10^{-3}	0.9	1×10^{-3}	1.44	1.44

10.8.2 Supporting Figures

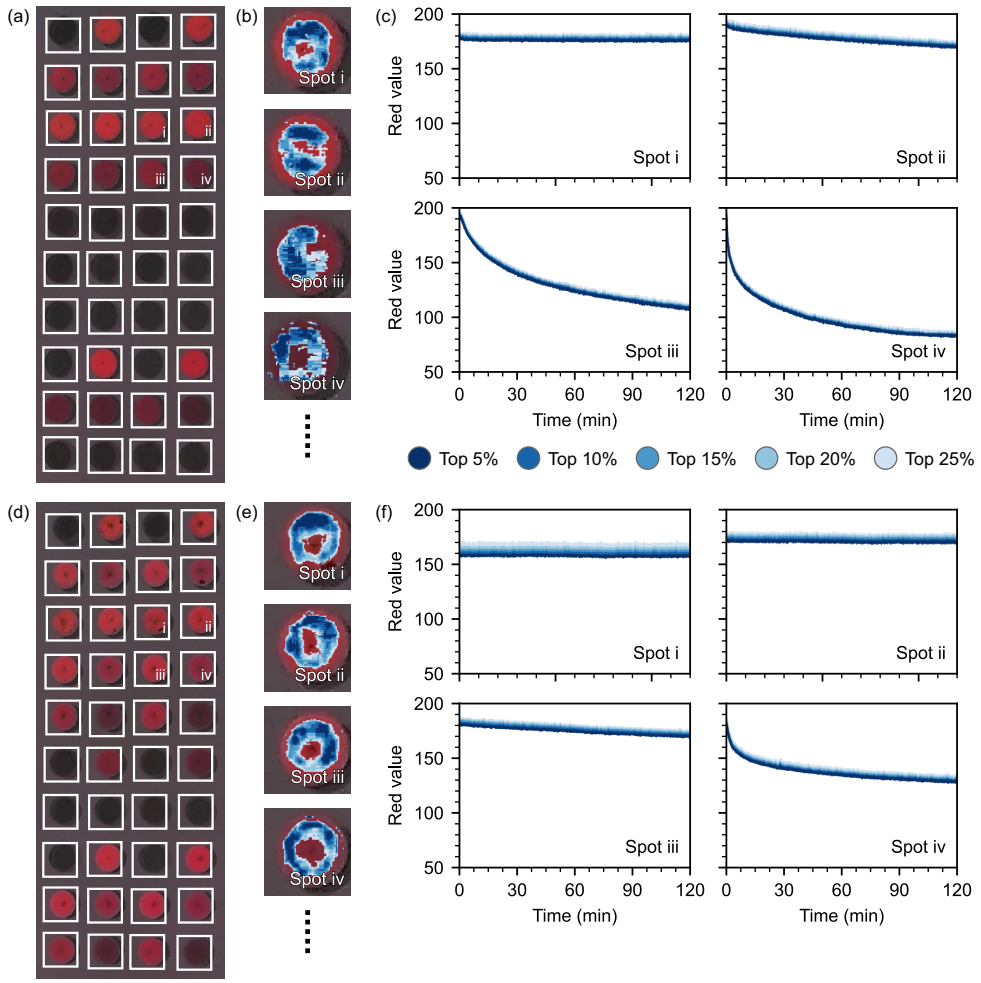

Figure 10.S1.: Detection of mean red values for samples at different temperatures. (a–c) 125 °C, (d–f) 115 °C.

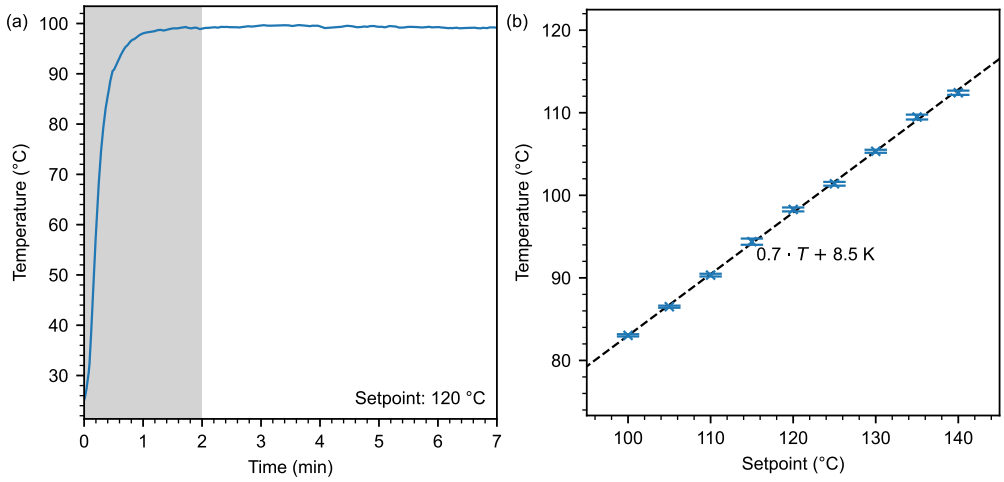

Figure 10.S2.: Sample temperature on the hotplate. The true temperature was measured by a Pt-100 placed on top of a glass substrate. (a) During the first two minutes (shaded area), the sample reaches thermal equilibrium. (b) Due to the experimental setup, the sample temperature is lower than the setpoint of the hotplate.

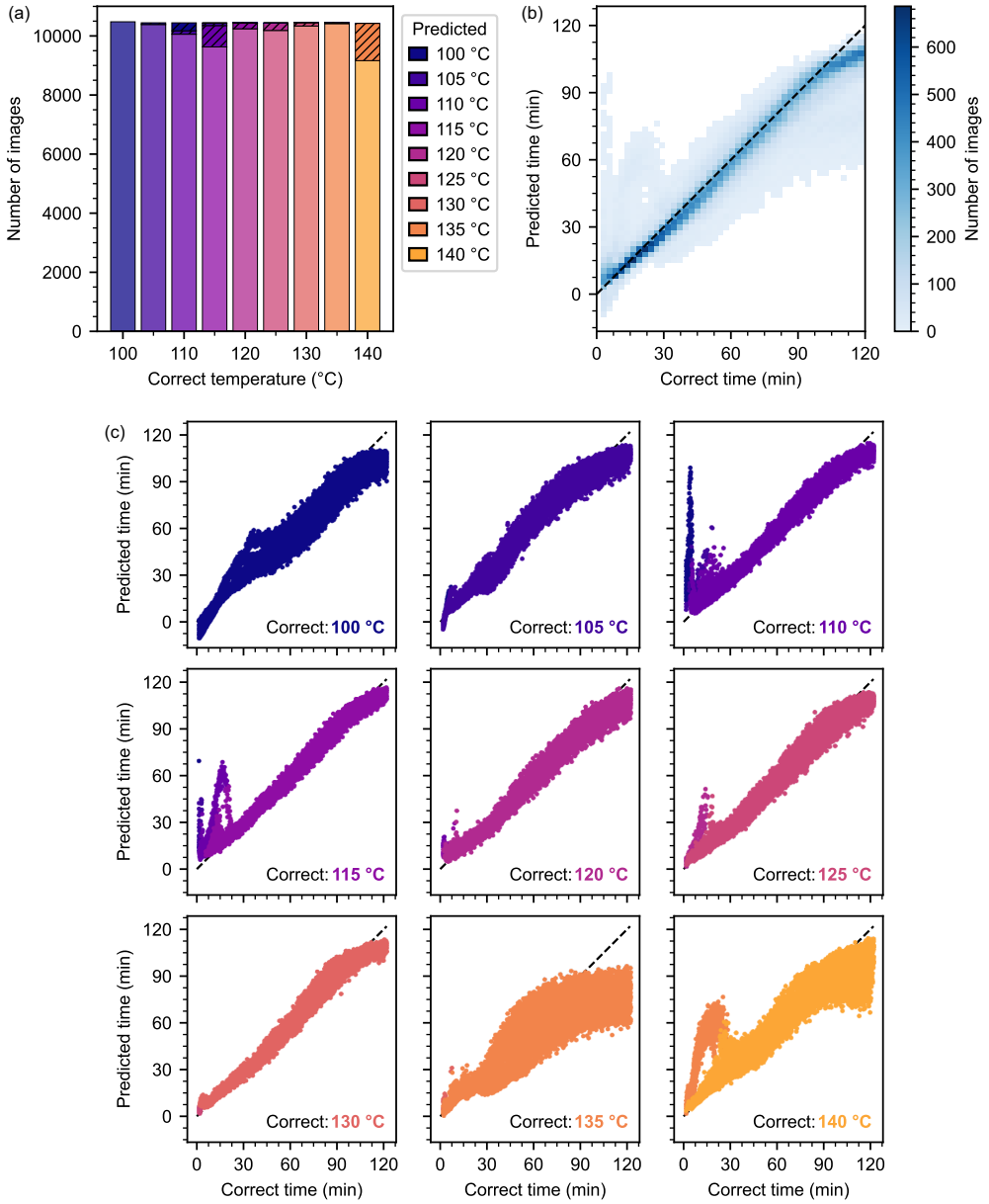

Figure 10.S3.: Prediction results for the training data. (a) Temperature prediction. (b) Correlation between predicted and correct time. (c) Detailed view of time and temperature prediction.

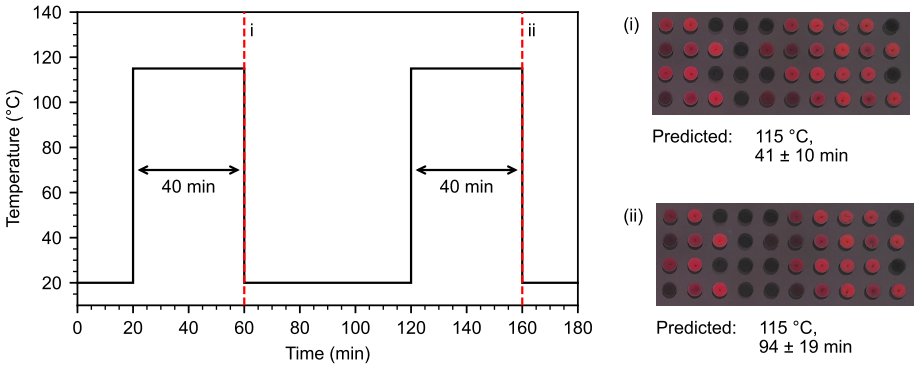

Figure 10.S4.: Prediction results with complete cooldown. The graph shows the applied temperature profile. Evaluation of the sensor after both heating steps shows is as expected. The sensors integrate the total time at the elevated temperature.

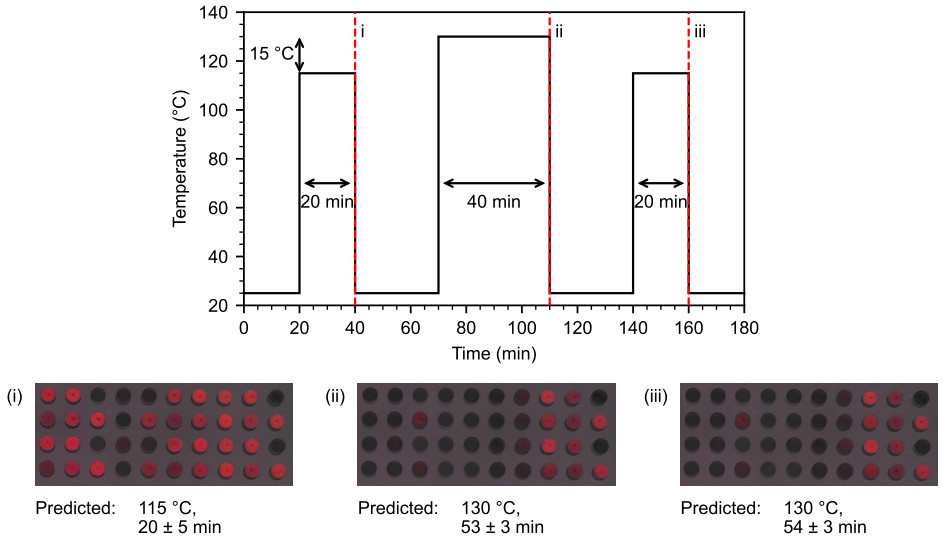

Figure 10.S5.: Multiple heating events inside the operating range of the sensor. The sensor reports the highest detected temperature and the corresponding heating time.

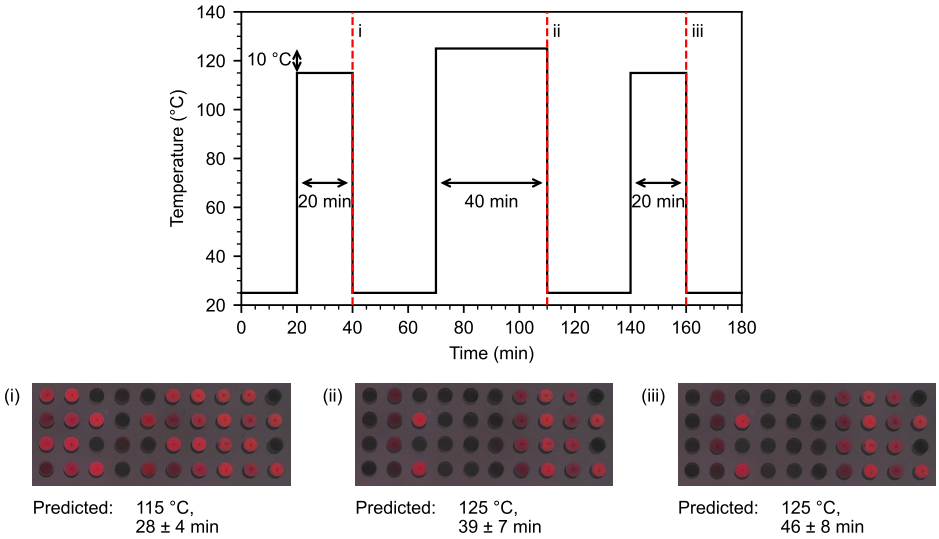

Figure 10.S6.: Multiple heating steps with a small temperature difference. Our sensor shows the expected result after the first and second heating step. After the third heating step, the predicted time slightly increases.

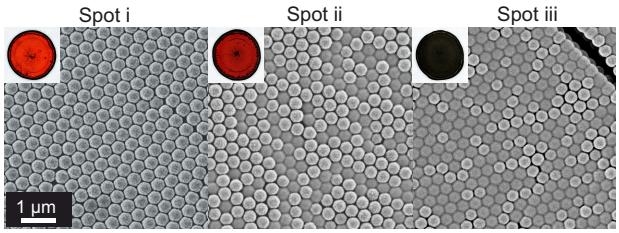

Figure 10.S7.: Original SEM images of partially sintered colloidal crystals shown in Fig. 10.2b–d.

Eidesstattliche Versicherungen und Erklärungen

§ 8 Satz 2 Nr. 3 PromO Fakultät für Biologie, Chemie und Geowissenschaften

Hiermit versichere ich eidesstattlich, dass ich die Arbeit selbstständig verfasst und keine anderen als die von mir angegebenen Quellen und Hilfsmittel benutzt habe (vgl. Art. 64 Abs. 1 Satz 6 BayHSchG).

§ 8 Satz 2 Nr. 3 PromO Fakultät für Biologie, Chemie und Geowissenschaften

Hiermit erkläre ich, dass ich die Dissertation nicht bereits zur Erlangung eines akademischen Grades eingereicht habe und dass ich nicht bereits diese oder eine gleichartige Doktorprüfung endgültig nicht bestanden habe.

§ 8 Satz 2 Nr. 4 PromO Fakultät für Biologie, Chemie und Geowissenschaften

Hiermit erkläre ich, dass ich Hilfe von gewerblichen Promotionsberatern bzw. –vermittlern oder ähnlichen Dienstleistern weder bisher in Anspruch genommen habe noch künftig in Anspruch nehmen werde.

§ 8 Satz 2 Nr. 7 PromO Fakultät für Biologie, Chemie und Geowissenschaften

Hiermit erkläre ich mein Einverständnis, dass die elektronische Fassung der Dissertation unter Wahrung meiner Urheberrechte und des Datenschutzes einer gesonderten Überprüfung unterzogen werden kann.

§ 8 Satz 2 Nr. 8 PromO Fakultät für Biologie, Chemie und Geowissenschaften

Hiermit erkläre ich mein Einverständnis, dass bei Verdacht wissenschaftlichen Fehlverhaltens Ermittlungen durch universitätsinterne Organe der wissenschaftlichen Selbstkontrolle stattfinden können.

Bayreuth, 09.01.2023

Thomas Quang Vinh Tran

Method Development and Data-Driven Analysis for Thermal Management and Heat Monitoring

Dissertation, 2023

University of Bayreuth
Physical Chemistry I
Faculty of Biology, Chemistry & Earth Sciences
Universitätsstraße 30
95447 Bayreuth